Physico-thermal Properties of TiO_2 Nanoparticles Using Molecular Dynamics Simulations with Relevance to Thermal Conductance of Nanofluids

George Obiora Ugochukwu Okeke

Submitted in accordance with the requirements for the degree of
Doctor of Philosophy

The University of Leeds
Institute of Particle Science and Engineering
School of Process, Environmental and Materials Engineering

October 2013

The candidate confirms that the work submitted is his own, except where work which has formed part of jointly authored publications has been included. The contribution of the candidate and the other authors to this work has been explicitly indicated below. The candidate confirms that appropriate credit has been given within the thesis where reference has been made to the work of others.

Chapter 3, 5 and 6 of the thesis contain some materials from the eight jointly-authored publications given below;

Okeke, G., Hammond, R. & Joseph Antony, S. 2013. Influence of size and temperature on the phase stability and thermophysical properties of anatase TiO_2 nanoparticles: molecular dynamics simulation. *Journal of Nanoparticle Research,* 15**,** 1-9.

Okeke, G., Hammond, R. B. & Antony, S. J. 2013. Molecular Dynamics Simulation of Anatase TiO_2 Nanoparticles. *Journal of Nanoscience and Nanotechnology,* 13**,** 1047-1052.

Okeke, G., Hammond, R. B. & Antony, S. J. 2012. Molecular Dynamics Study of Antase TiO_2 Nanoparticles in Water. *Proceedings of the ASME 2012 International Mechanical Engineering Congress & Exposition, Texas, USA.*

Okeke, G., Hammond, R. & Antony, S. J. 2012. Analysis of Structural and Surface Properties of TiO_2 Nanoparticles in Water and Vacuum Using Molecular Dynamics Modeling and Simulations. *Journal of Nanofluids,* 1**,** 21-27.

Okeke, G., Hammond, R. & Antony, S. J. 2011. Molecular Dynamics Simulation of Anatase TiO_2 nanoparticles. *International Conference on Nanoscience & Technology, China 2011.*

Okeke G., Witharana, S., Antony, S. & Ding, Y. 2011. Computational analysis of factors influencing thermal conductivity of nanofluids. *Journal of Nanoparticle Research,* 13**,** 6365-6375.

Amanbayev, T., Okeke, G., Afzal, M. & Antony, S. J. 2010. Modelling of Bacterial Growth in Nano Liquids. *Proceedings of the Seventh International Conference on Engineering Computational Technology. Civil-Comp Press, Stirlingshire, UK, Paper 118.*

Okeke, G., Witharana, S., Antony, S. & Ding, Y. 2009. A Sensitivity Analysis of Factors Influencing Thermal Conductivity of Nanofluids. *UKHTC 2009. The Eleventh UK National Heat Transfer Conference, London, UK.*

The work presented in the eight publications above was carried out by the candidate (George Okeke). The top five publications were carried out under the supervision of Dr S. J. Antony and Dr R. B. Hammond (co-authors, supervisors). The last three publications were carried out under the supervision of Dr S. J. Antony, with contributions from Prof. Y. Ding, Dr W. Sanjeeva, Dr T. Amanbayev, and M. Afzah (co-authors), who were involved in manuscript preparation. The candidate is also the lead author of the 1st to 6th, and the 8th publications.

In memory of

Mercillin Okeke

Dedicated to

Dr Eric Obiora Okeke
Joshua Okeke
Peter Okeke
Ifeyinwa Okeke

Acknowledgement

I would like to show appreciation to the School of Process Environmental and Materials Engineering at the University of Leeds, for partly funding my school fees during my PhD programme. I would like to express my sincere gratitude to my supervisors, Dr Simon J. Antony and Dr Robert Hammond for their outstanding supervision and guidance throughout the period of this research. My appreciation is also extended to Professor Rick Brydson, Dr Andrew Scott and Trevor Hardcastle of the Institute of Materials Science, University of Leeds who gave me access to their elastic constant values from *ab initio* calculations.

I would also like to thank my colleagues, Babatunde Arowosola, Saeed Albaraki, Grace Adeola Olugbenga, Saleh Alzahrani, Akinola Falola, Derrick Njobuenwu, Chidi Efika, Bala Fakandu, Yousef Faraj, Jiabin Jha and Kelechi Anyikude for their valuable support and moral contribution. I am also thankful to my friend, Seyi Ayinla who supported me during this research.

Abstract

Nanoparticles have attracted the attention of researchers in a number of multidisciplinary fields as they possess enhanced structural and physical properties, which make them desirable to a wide range of industries. These enhancements have mostly been attributed to nanoparticles possessing large surface area-to-volume ratio. The concept of engineered nanofluids refers to making stable suspension of nanoparticles in base fluids to provide more efficient and thermally enhanced effective thermal conductance in a number of engineering applications involving heat transfer processes. Although experimental and computational studies have shown significant enhancement of thermal conductivity of nanofluids compared to the conventional heat transfer fluids, the underlying mechanism behind this enhancement is still not well understood. Out of the several mechanisms which have been proposed in the literature to be behind this enhancement of thermal conductivity, nanoparticle clustering seems to evolve as a relatively more significant factor for the enhancement of effective conductance of nanofluids and hence requires more detailed investigation in the future.

In this study, initially, numerical investigations are conducted to study the effect of particle clustering on thermal conductivity of nanofluids. The degree of thermal enhancement is analysed for different factors that capture particle clustering, such as aggregate size, particle concentration, interfacial thermal resistance, and fractal and chemical dimensions. This analysis is conducted for three model water-based nanofluids of aluminium oxide (Al_2O_3), copper oxide (CuO) and titanium dioxide (TiO_2) nanoparticles in which particle concentrations are varied up to 4 volume %. Results from the numerical work are validated using available experimental data. Studies showed that predicted and experimental data for thermal conductivity enhancement are in good agreement as particle clustering is seen to influence effective thermal conductance of the model nanofluids. Considering this observation and to further understand the mechanism behind particle clustering, particle scale properties such as thermodynamic, structural, surface and interaction force properties are investigated in vacuum and liquid environments at different temperatures, using Molecular Dynamics (MD) simulations. These simulations are carried out on TiO_2 nanoparticles (with particle sizes ranging between 2 – 6nm) as a model system owing to their wide industrial applications, with a particular focus on two mostly encountered forms of TiO_2 namely; anatase and rutile. From MD simulations, the Radial Distribution Function (RDF) plots of the particles in vacuum revealed much higher crystallinity with peaks of almost an order higher than that of the nanoparticles in water. For anatase, surface energy of the particles in vacuum is seen to be higher than that of the particles in water by about 100% for the smaller size particles (especially for 2 and 3nm), and about 60% for relatively larger particles (especially for 4 to 6 nm). In both environments, surface energy of anatase nanoparticles is also seen to increase with particle size to a maximum value of critical particle size (i.e. 4 nm) after which no further significant increase in surface energy is observed. Finally, force – displacement analysis which captures interaction force relations is conducted for different particle sizes in vacuum and water environments, using MD simulations. This analysis provides interaction force information which is vital in studying particle interactions. In this study, the nanoparticles are seen to be more attractive at a smaller size and the attraction increases as the particle size increases. Particles are also seen to become repulsive at initial contact.

Overall, this thesis presents vital information on particle scale properties of TiO_2 nanoparticles (as a model system) under different environments. These properties are known to influence clustering of nanoparticles which in turn influence thermal enhancement of nanofluids. In the near future, knowledge of these particle scale properties will aid in the development of more enhanced nano and bulk systems with better physico-thermal properties, to meet the ever growing requirement for technological advancement.

Table of Contents

Acknowledgement v

Abstract vi

Table of Contents viii

List of Figures xii

List of Tables xxi

Nomenclature xxiii

Chapter 1 1

1 Introduction to the Project 2

- 1.1 Introduction 2
- 1.2 Aim of Thesis 5
- 1.3 Structure of theThesis 7

Chapter 2 9

2 Thermal Conductivity of Nanofluids: Background and Recent Development 10

- 2.1 Introduction 10
- 2.2 Nanofluid background 10
- 2.3 Applications of nanofluids 12
  - 2.3.1 Transportation 12
  - 2.3.2 Micromechanical Systems 12
  - 2.3.3 Refrigeration and air-conditioning 13
  - 2.3.4 Chemical, petroleum and pharmaceutical industries 13
  - 2.3.5 Medicine 13
- 2.4 Thermal conductivity of nanofluids 13
  - 2.4.1 Interfacial thermal resistance 17
- 2.5 Possible mechanisms for thermal conductivity enhancement in nanofluids.. 21
  - 2.5.1 Brownian motion 22
  - 2.5.2 Interfacial layering 23
  - 2.5.3 Ballistic transport mechanism 24
  - 2.5.4 Particle aggregation or clustering 26
- 2.6 Mean field model 27
  - 2.6.1 Series and parallel bounds 27
  - 2.6.2 Hashin and Shtrikman (HS) bounds 29
  - 2.6.3 Similarities with solid composites 30
- 2.7 Computational background of the present numerical modelling approach 36

2.7.1 The concept of Fractal theory 36
2.7.2 Relationship between Fractal and Chemical dimensions 38
2.7.3 The aggregation model 39
2.8 Conclusion 43
Chapter 3 45
3 Predictions of Effective Thermal Conductivity of Nanofluids using Numerical Modelling 46
3.1 Introduction 46
3.2 Summary of nanofluid model system specification and parameters used in the thermal conductivity investigation 46
3.3 Effect of Interfacial thermal resistance (α) 48
3.4 Effect of Aspect ratio and Particle volume fraction 50
3.5 Effect of Fractal and Chemical dimensions 52
3.6 Validation of numerical results with experimental data 55
3.7 Effective thermal conductivity of model systems 58
3.8 Conclusion 60
Chapter 4 62
4 Theoretical Background of TiO_2 and Molecular Modelling 63
4.1 Introduction 63
4.2 Titania (TiO_2) nanoparticles 63
4.3 General applications of TiO_2 67
4.3.1 Bactericidal disinfection processes 67
4.3.2 Chemical/Bio treatments 67
4.3.3 Sensors 68
4.3.4 Solar Cells and Photonic Devices 68
4.4 General overview of crystals 68
4.4.1 Lattice and Unit Cells 69
4.4.2 Planes and Directions 70
4.4.3 Mechanical properties of crystals 71
4.4.4 Prediction of crystal shape (morphology) 74
4.5 Characteristics and properties of crystalline phases of TiO_2 85
4.5.1 Rutile 85
4.5.2 Anatase 91
4.5.3 Brookite 95
4.6 Computational background of the Molecular modelling approach 97
4.6.1 Coordinate systems 97
4.6.2 Potential energy surfaces 98

4.6.3 Molecular Surfaces 98
4.7 Molecular mechanics: Force field models 99
4.7.1 Bond stretching 101
4.7.2 Angle bending 103
4.7.3 Torsional terms 103
4.7.4 Non-bonded interactions 104
4.7.5 The concept of force field fitting/parameterisation 116
4.7.6 The concept of energy minimization 117
4.8 Conclusion 118
Chapter 5 119
5 Computational Methods of Molecular Modelling 120
5.1 Introduction 120
5.2 Why Molecular modelling? 120
5.3 Molecular modelling packages used 120
5.3.1 The General Utility Lattice Program (GULP) Package 121
5.3.2 Structural information and input data 124
5.3.3 TiO_2 Nanoparticle Simulation Technique: The DL_POLY Package 124
5.3.4 Creation of nanoparticles 127
5.3.5 Creation of water molecules 128
5.3.6 The Force Field Selection 129
5.4 Conclusion 136
Chapter 6 138
6 Properties of TiO_2 Crystals and Nanoparticles Predicted by Molecular Modelling 139
6.1 Introduction 139
6.2 Properties of TiO_2 crystal structure 139
6.2.1 Surface and attachment energy calculation of TiO_2 bulk crystalline phases 141
6.2.2 Prediction of morphology structures and surfaces of TiO_2 crystalline phases 148
6.3 Conclusion of results on properties of TiO_2 crystalline phases 159
6.4 Properties of TiO_2 nanoparticles 160
6.4.2 Particles in Water 190
6.5 Conclusion 198
Chapter 7 200
7 Prediction of Particle Interactions Forces using Molecular Modelling 201
7.1 Introduction 201

7.2 The AFM Concept 201
7.3 Molecular Dynamics Simulation Concept 203
7.3.1 Particle interaction in vacuum 206
7.3.2 Particle interaction in water 210
7.4 Relating interparticle interactions to effective thermal conductivity 214
7.5 Conclusion 215
Chapter 8 217
8 Conclusion and Recommendations for Future work 218
8.1 Conclusion 218
8.1.1 Investigations on Effective thermal conductivity of model based nanofluids and the relevance of their single-particle scale properties (Chapter 3) 218
8.1.2 Performance testing of the force field for conducting molecular modelling of TiO_2, using force fitting (Chapter 5) 219
8.1.3 Bulk properties of TiO_2 crystals using GULP for molecular modelling (Chapter 6, section 6.2 – 6.3) 220
8.1.4 Physico-thermal properties of TiO_2 nanoparticles using DL_POLY for molecular dynamics simulations (Chapter 6, section 6.4 – 6.5) 221
8.1.5 Force distance analysis of TiO_2 interacting nanoparticles using DL_POLY for molecular dynamics simulations (Chapter 7) 223
8.2 Recommendation for future work 224
References 226
List of Publications 243
A. Appendix A 244
B. Appendix B 250

List of Figures

Figure 1.1 Structure of the thesis 6

Figure 2.1 Comparison of the thermal conductivity of different materials. 11

Figure 2.2 Prediction of thermal conductivity ratio ($keff/kf$) for volume fractions of water based (a) iron-oxide (Fe_3O_4) and (b) titania (TiO_2) nanofluids using the Maxwell and Hamilton-Crosser (HC) model 16

Figure 2.3 Thermal enhancement due to liquid layering around the particles forming a liquid/particle interface (Keblinski et al., 2002) 24

Figure 2.4 Ballistic and diffusive phonon transport in a particle (Wang and Mujumdar, 2007) 25

Figure 2.5 Thermal conductivity enhancement due to particle clustering/aggregation, i – iv represents the degree of packing volume in reducing order (Keblinski et al., 2002) 27

Figure 2.6 Series (a) and parallel (b) modes of conduction paths for nanofluids (Eapen et al., 2010) 28

Figure 2.7 Nanofluid configuration for the (a) lower HS bound and (b) upper HS bound (Eapen et al., 2010) 29

Figure 2.8 HS bounds for solid composites. Comparison with experimental data for; (a) Polypropylene – Al, (b) Polyethylene – Al_2O_3, and (c) ZnS – Diamond. (Eapen et al., 2010) 32

Figure 2.9 HS bounds for nanofluids. Comparison with experimental data for water based (a) Al_2O_3, (b) CuO and (c) TiO_2 nanofluid. (Eapen et al., 2010) 35

Figure 2.10 Small pieces of self-similar fractals to form two distinct structures. 37

Figure 2.11 Shortest possible path between two points illustrating Chemical dimension 38

Figure 2.12 DLCCA and RLA limits for fractal dimension 39

Figure 2.13 Schematic diagram of a single aggregate comprising the backbone (black particles) and weak ends (grey particles). The aggregate is decomposed into weak ends with the base fluid and the backbone. Thermal conductivity of the aggregate with only particles belonging to the weak ends is k_{nc}, with the linear chains embedded inside a medium with effective conductivity of k_{nc}. (Evans et al., 2008). 40

Figure 2.14 An aggregate (within the sphere) characterised by the radius of gyration (Rg) and an individual particle characterised by its own radius. 40

Figure 3.1 Dependence of enhancement ratio (k_{eff} /k_f) with aspect ratio and the interfacial resistance data for water-based (a) Alumina, (b) CuO and (c) Titania nanofluids. On each plot the bottom set of lines represent 0.5 volume %, the top set is for 4 volume % (Okeke et al., 2011) 49

Figure 3.2 Effect of aspect ratio and particle volume fraction on the enhancement ratio for α = 1 for water-based (a) Alumina, (b) CuO and (c) Titania nanofluids (Okeke et al., 2011). 52

Figure 3.3 Effect of fractal dimension (d_f) (Erdin et al.) on enhancement ratio (k_{eff} / k_f) for water based Alumina nanofluid for d_l = 1.4 and α = 1 (Okeke et al., 2011). 53

Figure 3.4 Effect of chemical dimension (d_l) on enhancement ratio (k_{eff} / k_f) for water based Alumina nanofluid for d_f = 1.8 and α = 1 (Okeke et al., 2011) 54

Figure 3.5 Experimental data and model prediction for alumina-water nanofluid for d_l = 1.4 and α = 1 (Okeke et al., 2011) 57

Figure 3.6 Comparison of enhancement ratio (k_{eff} / k_f) obtained in the present work with literature data for water-based (a) Alumina, (b) CuO and (c) Titania nanofluids. d_f = 1.8, d_l = 1.4 and α = 1. The dotted lines represent data from the present model while thick lines represent experimental data from the literature (Okeke et al., 2011). 59

Figure 4.1 The Bravais lattices (Galasso, 1970) 69

Figure 4.2 Miller indices for planes in cubic cells (Douglas, 2006) 71

Figure 4.3 Definition of (a) Extension and (b) Shear (Kelly et al., 2000)............. 72

Figure 4.4 Schematic representation of the classical Wulff plot for the derivation of equilibrium form (Docherty, 1990) 76

Figure 4.5 The two region surface simulation cell viewed at right angles to the surface normal, where the solid vertical lines represent the boundaries between 2D periiodic images of the cell and the dash lines represent the boundary between region 1 and the stagnant region 2. 78

Figure 4.6 Schematic diagram showing the partition of slice and attachment energies. The figure was obtained from (Docherty, 1990)..................................... 80

Figure 4.7 Schematic representation of (a) unrelaxed surface, including (b) normal, and (c) lateral relaxation of the upper atomic layer of a crystal (Hermann, 2011). 81

Figure 4.8 Schematic representation of relaxed surfaces showing a localised symmetry set of (a) balanced forces, and (b) unbalanced forces 82

Figure 4.9 Schematic representation of *fcc* (a) (1 0 0), (b) (1 1 0) and (c) (1 1 1) bulk surfaces with square, rectangular and hexagonal Bravais unit lattices respectively. 82

Figure 4.10 Schematic representation of an *fcc* (1 0 0) bulk surface with an adsorbate unit cell and surface unit cell embedded on it. 83

Figure 4.11 Schematic representation of *fcc* (1 0 0) and (1 1 1) bulk surfaces with unit cells represented by Woods notations 84

Figure 4.12 Crystal structure of rutile. The grey and red atoms represent the Ti and O atoms respectively. (sourced from the Inorganic Crystal Structure Database (ICSD) (http://cds.dl.ac.uk/icsd/index.html)). Structure generated using Materials Studio 86

Figure 4.13 Atomic arrangement of tetragonal crystal structure of rutile. Small circles represent Ti, and large circles represent O. The figures refer to the bond types (*) listed in Table 4.3 (Grant, 1959). 87

Figure 4.14 Predicted morphology for rutile obtained using the BDFH method of the morphology module in Accelrys Materials Studio 5.2 software. 89

Figure 4.15 Rutile (1 1 0) surface obtained using the cleaved surface builder module in Accelrys Materials Studio 5.2 software. 89

Figure 4.16 Rutile (1 0 0) surface obtained using the cleaved surface builder module in Accelrys Materials Studio 5.2 software. 90

Figure 4.17 Rutile (0 0 1) surface obtained using the cleaved surface builder module in Accelrys Materials Studio 5.2 software 90

Figure 4.18 Crystal structure of anatase. The grey and red atoms represent the Ti and O atoms respectively. (sourced from the Inorganic Crystal Structure Database (ICSD) (http://cds.dl.ac.uk/icsd/index.html)). Structure generated using Materials Studio 92

Figure 4.19 Predicted morphology structure for anatase using the BDFH method of the morphology module in Accelrys Materials Studio 5.2 software. 93

Figure 4.20 Anatase (1 0 1) surface obtained using the cleaved surface builder module in Accelrys Materials Studio 5.2 software 94

Figure 4.21 Anatase (0 0 1) surface obtained obtained using the cleaved surface builder module in Accelrys Materials Studio 5.2 software..................................... 95

Figure 4.22 Crystal structure of brookite. The grey and red atoms represent the Ti and O atoms respectively. (sourced from the Inorganic Crystal Structure Database (ICSD) (http://cds.dl.ac.uk/icsd/index.html)). Structure generated using Materials Studio 96

Figure 4.23 Predicted morphology for brookite using the BDFH method of the morphology module in Accelrys Materials Studio 5.2 software. 96

Figure 4.24 The van der Waals, molecular and accessible surfaces of a molecule. (Leach, 2001) 99

Figure 4.25 Schematic representation of the four main contributions to a molecular mechanics force field: bond stretching, angle bending, torsional terms and non-bonded interactions. (Leach, 2001)... 101

Figure 4.26 Variation in bond energy with interatomic separation. (Leach, 2001). 101

Figure 4.27 Comparison of the simple harmonic potential (Hooke's law) with the Morse curve. (Leach, 2001) 102

Figure 4.28 Torsional potential varies as shown for different values of V_n, n and γ. (Leach, 2001). 104

Figure 4.29 The electrostatic potential due to two point charges. (Leach, 2001) 106

Figure 4.30 The relative orientation of two dipoles. (Leach, 2001) 106

Figure 4.31 The most favourable orientations of various multipoles. (Leach, 2001) 107

Figure 4.32 The Drude model for dispersive interactions. (Leach, 2001).......... 108

Figure 4.33 The interaction energy and the force between two argon atoms. (Leach, 2001) 110

Figure 4.34 The Lennard-Jones potential. (Leach, 2001).......... 111

Figure 4.35 Diagram showing the Lennard-Jones potential constructed from a repulsive component $\alpha r - 12$and an attractive component $\alpha r - 6$. (Leach, 2001) 112

Figure 4.36 A setback of the Buckingham potential is that it becomes steeply attractive at short distances. (Leach, 2001).......... 113

Figure 4.37 The three types of surface as grouped by Tasker (a) type I, where each layer consists of coplanar anions and cations and all planar cuts lead to a non-polar surface; (b) type IIa, where the anions and cations containing the layers are not coplanar but permits the cuts of some surface to split the layers in a way as to produce no dipole; (c) type IIb, which is almost similar to type IIa, except that some ions are moved from the surface to the bottom of region 2 in order to derive zero dipole; (d) type III, where there are alternating layers of cations and anions, and all possible planar cuts result in a surface with a dipole moment (Tasker, 1979). 115

Figure 5.1 Schematic diagram of a mid-sectional view of a 3-dimensional cuboidal simulation cell with size *4d* containing a nanoparticle of size *d (periodic conditions apply to all boundaries of the box)* 125

Figure 5.2 Image of typical structure generated for 3 nm (a) rutile and (b) anatase TiO_2 nanoparticle created using Materials Studio. Ti and O atoms in red and blue colours respectively 127

Figure 5.3 Wateradd utility of the DL_POLY Java GUI 128

Figure 5.4 Image of a 3 nm TiO_2 anatase nanoparticle in water (Ti, red; O, blue; HW, grey; OW, pink) 129

Figure 6.1 Screenshot of a the GDIS software containing a Model Editing window (left) for defining 3 X 3 transformation matrix and 3 X 1 translational offset, and rutile crystal structures (right). (a) normal structure, and (b) structure with translated/inverted atom coordinates. ... 143

Figure 6.2 Screenshot of the surface builder of GDIS showing a list of rutile cleaved surfaces without dipoles. ... 144

Figure 6.3 Prediction of the calculated and experimental equilibrium morphology rutile structure (a) BFDH model, (b) unrelaxed morphology using surface energies, (c) relaxed morphology using surface energies, (d) unrelaxed morphology attachment energies, (e) relaxed morphology attachment energies and (f) experimental data (Kostov, 1968). Structures predicted using the surface builder module in GDIS. ... 149

Figure 6.4 Cleaved (a) unrelaxed and (b) relaxed (0 0 1) surface of rutile. Surfaces were obtained using the surface builder module in GDIS. Ti and O atoms are in green and red respectively ... 150

Figure 6.5 Cleaved (a) unrelaxed and (b) relaxed (1 1 0) surface of rutile. Surfaces were obtained using the surface builder module in GDIS. Ti and O atoms are in green and red respectively ... 150

Figure 6.6 Cleaved (a) unrelaxed and (b) relaxed (0 1 1) surface of rutile. Surfaces were obtained using the surface builder module in GDIS. Ti and O atoms are in green and red respectively ... 151

Figure 6.7 Cleaved (a) unrelaxed and (b) relaxed (1 0 0) surface of rutile. Surfaces were obtained using the surface builder module in GDIS. Ti and O atoms are in green and red respectively ... 151

Figure 6.8 Cleaved (a) unrelaxed and (b) relaxed (2 2 1) surface of rutile. Surfaces were obtained using the surface builder module in GDIS. Ti and O atoms are in green and red respectively ... 152

Figure 6.9 Prediction of the calculated and experimental equilibrium morphology anatase structure (a) BFDH model, (b) unrelaxed morphology using surface energies, (c) relaxed morphology using surface energies, (d) unrelaxed morphology attachment energies, (e) relaxed morphology attachment energies and (f) experimental data (Kostov, 1968). Structures predicted using the surface builder module in GDIS. ... 153

Figure 6.10 Cleaved (a) unrelaxed and (b) relaxed (0 0 1) surface of anatase. Surfaces were obtained using the surface builder module in GDIS. Ti and O atoms are in green and red respectively ... 154

Figure 6.11 Cleaved (a) unrelaxed and (b) relaxed (0 1 1) surface of anatase. Surfaces were obtained using the surface builder module in GDIS. Ti and O atoms are in green and red respectively ... 154

Figure 6.12 Prediction of the calculated and experimental equilibrium morphology brookite structure (a) BFDH model, (b) unrelaxed morphology using surface energies, (c) relaxed morphology using surface energies, (d) unrelaxed morphology attachment energies, (e) relaxed morphology attachment energies and (f) experimental data (Kostov, 1968). Structures predicted using the surface builder module in GDIS. 156

Figure 6.13 Cleaved (a) unrelaxed and (b) relaxed (0 0 1) surface of brookite. Surfaces were obtained using the surface builder module in GDIS. Ti and O atoms are in green and red respectively 157

Figure 6.14 Cleaved (a) unrelaxed and (b) relaxed (1 1 1) surface of brookite. Surfaces were obtained using the surface builder module in GDIS. Ti and O atoms are in green and red respectively 157

Figure 6.15 Cleaved (a) unrelaxed and (b) relaxed (1 0 0) surface of brookite. Surfaces were obtained using the surface builder module in GDIS. Ti and O atoms are in green and red respectively 158

Figure 6.16 Cleaved (a) unrelaxed and (b) relaxed (0 1 0) surface of brookite. Surfaces were obtained using the surface builder module in GDIS. Ti and O atoms are in green and red respectively 158

Figure 6.17 Cleaved (a) unrelaxed and (b) relaxed (2 1 0) surface of brookite. Surfaces were obtained using the surface builder module in GDIS. Ti and O atoms are in green and red respectively 159

Figure 6.18 Temperature and Total Energy (ETOT) plotted against time for 2nm anatase TiO_2 nanoparticles 161

Figure 6.19 Temperature and Total Energy (ETOT) plotted against time for 3nm anatase TiO_2 nanoparticles 162

Figure 6.20 Temperature and Total Energy (ETOT) plotted against time for 2nm rutile TiO_2 nanoparticles 163

Figure 6.21 Temperature and Total Energy (ETOT) plotted against time for 3nm rutile TiO_2 nanoparticles 164

Figure 6.22 Total Energy (ETOT) as a function temperature for 2 – 6 nm nanoparticles 165

Figure 6.23 RDF’s for anatase Ti – Ti, Ti – O and O – O pairs for 2 nm 169

Figure 6.24 RDF’s for rutile Ti – Ti, Ti – O and O – O pairs for 2 nm 170

Figure 6.25 Surface disordering of anatase nanoparticles with increase in temperature 172

Figure 6.26 Surface energy of anatase nanoparticles as a function of particle size and time step at different temperatures 174

Figure 6.27 Surface energy of anatase and rutile nanoparticles from present study and literature at 300 K 175

Figure 6.28 Structural change of anatase nanoparticles before and after MD simulation at 300 K 177

Figure 6.29 Structural change of rutile nanoparticles before and after MD simulation at 300 K 178

Figure 6.30 TEM images showing rutile TiO_2 nanorods (Ribeiro et al., 2007). 178

Figure 6.31 Rutile nanorod from simulation, showing the crystal surfaces upon visual inspection. 179

Figure 6.32 Structural change of 2 nm rutile nanoparticle after MD simulation at different temperatures..... 180

Figure 6.33 Comparison of surface energy for anatase and rutile nanoparticles at different temperatures as a function of particle size 181

Figure 6.34 Surface energy of (a) anatase and (b) rutile nanoparticles at the final stages of simulation time, as a function of temperature..... 182

Figure 6.35 Schematic representation of a spherical shaped nanoparticle with different layers representing cut-off distances from the centre. Oxygen and titanium atoms are red and grey colours, respectively. 184

Figure 6.36 Degree of shift or change in structure for different anatase TiO_2 nanoparticle sizes with respect to its optimised structure. Optimisation simulation was conducted at 0 K 185

Figure 6.37 Degree of shift of atoms of anatase from their original positions. (a) 2 nm particle before optimisation, (b) 2 nm particle after optimisation, (c) 6 nm particle before optimisation, (d) 6 nm particle after optimization. Oxygen and titanium atoms are in red and blue colours, respectively. Optimisation simulation was conducted at 0 K. 186

Figure 6.38 Atom shifts at the (a) bulk or core (b) intermediate and (c) surface, of 5 nm anatase nanoparticle. Oxygen and titanium atoms are in red and blue colours, respectively 186

Figure 6.39 Degree of sphericity of anatase as a function of (a) temperature for different nanoparticle sizes and (b) nanoparticle size for different temperatures .. 188

Figure 6.40 Degree of sphericity of rutile as a function of (a) temperature for different nanoparticle sizes and (b) nanoparticle size for different temperatures .. 189

Figure 6.41 Degree of sphericity as a function of simulation time for 2 nm anatase and rutile nanoparticle at 300 K. 190

Figure 6.42 Validation of SPC/E water RDF plots (i.e. H and O atom pairs) with literature at 300 K. OW and HW represents water oxygen and hydrogen respectively (Okeke et al., 2012) 191

Figure 6.43 Comparison of energies of water slab in the tetragonal box (U_T) to the energies of water molecules in fully period cubic box (U_C) (HW, grey and OW, pink). Simulation was carried out at 300 K (Okeke et al., 2012) 192

Figure 6.44 Radial distribution function for Ti – O, Ti – Ti and O – O pairs of the particle in water and vacuum at 300 K for anatase (a) 2nm and (b) 3nm nanoparticles (Okeke et al., 2012). 194

Figure 6.45 Radial distribution function for anatase Ti – OW, Ti – HW, O - OW and O – HW pairs at 300 K (Okeke et al., 2012). 195

Figure 6.46 Simulation environments with TiO_2 and water in one box, and bulk water alone in the other. 196

Figure 6.47 Surface energy of anatase TiO_2 nanoparticles in water and vacuum environments at 300 K (Okeke et al., 2012) 197

Figure 7.1 A typical AFM set up using an optical deflection technique (Leung et al., 2012). 202

Figure 7.2 A typical force-displacement curve showing the non-contact, attractive and repulsive regimes (Giessibl, 2003). 203

Figure 7.3 Schematic representation of a typical force-displacement curve showing (i) two particles separated from each other by centre-centre distance, (ii) two particles in contact... 206

Figure 7.4 Force-displacement curves for 2nm anatase and rutile nanoparticles simulated in vacuum. Molecules in the particles were treated as rigid body units. 207

Figure 7.5 Force-displacement curves for 3nm anatase and rutile nanoparticles simulated in vacuum. Molecules in the particles were treated as rigid body units. 208

Figure 7.6 Force-displacement curves for 4nm anatase and rutile nanoparticles simulated in vacuum. Molecules in the particles were treated as rigid body units. 208

Figure 7.7 Force-displacement curves for 5nm anatase and rutile nanoparticles simulated in vacuum. Molecules in the particles were treated as rigid body units. 209

Figure 7.8 Force-displacement curve for 2nm anatase nanoparticles simulated in vacuum. Particles were constrained at their centre of masses and their atoms were allowed to rotate and distort. 210

Figure 7.9 Schematic representation of a typical force-displacement curve showing two particles with water molecules around them and (i) separated from each other by centre-centre distance, (ii) two particles in strong contact............. 211

Figure 7.10 Force-displacement curves for 2nm anatase and rutile nanoparticles simulated in water. Molecules in the particles were treated as rigid body units. ... 212

Figure 7.11 Force-displacement curves for 3nm anatase and rutile nanoparticles simulated in water. Molecules in the particles were treated as rigid body units. ... 213

Figure 7.12 Force-displacement curves for 2nm anatase nanoparticles simulated in bulk water. Particles were constrained at their centre of masses and their atoms were allowed to rotate and distort. 214

Figure 7.13 Cluster of loosely packed anatase nanoparticles with water molecules around particle surfaces and heat (in red) flowing across the effective volume. 215

Figure A.1 Temperature and Total Energy (ETOT) plotted against time for 4nm anatase TiO_2 nanoparticles 244

Figure A.2 Temperature and Total Energy (ETOT) plotted against time for 5nm anatase TiO_2 nanoparticles 245

Figure A.3 Temperature and Total Energy (ETOT) plotted against time for 6nm anatase TiO_2 nanoparticles 246

Figure A.4 Temperature and Total Energy (ETOT) plotted against time for 4nm rutile TiO_2 nanoparticles 247

Figure A.5 Temperature and Total Energy (ETOT) plotted against time for 5nm rutile TiO_2 nanoparticles 248

Figure A.6 Temperature and Total Energy (ETOT) plotted against time for 6nm rutile TiO_2 nanoparticles 249

Figure B.1 RDF’s for anatase Ti – Ti, Ti – O and O – O pairs for 3 nm 250

Figure B.2 RDF’s for anatase Ti – Ti, Ti – O and O – O pairs for 4 nm 251

Figure B.3 RDF’s for anatase Ti – Ti, Ti – O and O – O pairs for 5 nm 252

Figure B.4 RDF’s for anatase Ti – Ti, Ti – O and O – O pairs for 6 nm 253

Figure B.5 RDF’s for rutile Ti – Ti, Ti – O and O – O pairs for 3 nm 254

Figure B.6 RDF’s for rutile Ti – Ti, Ti – O and O – O pairs for 4 nm 255

Figure B.7 RDF’s for rutile Ti – Ti, Ti – O and O – O pairs for 5 nm 256

Figure B.8 RDF’s for rutile Ti – Ti, Ti – O and O – O pairs for 6 nm 257

List of Tables

Table 1.1 Tasks and descriptions for Thesis 5

Table 2.1 Conventional models for effective thermal conductivity of solid/liquid suspensions (Eapen et al., 2010) (Choi et al., 2001, Hamilton and Crosser, 1962).15

Table 3.1 System description outlining the type of investigation and parameters used in the present thermal conductivity investigation 47

Table 4.1 Typical physical and mechanical properties of the rutile phase of titania (sourced from www.azom.com/details.asp) 65

Table 4.2 Crystal systems and the 14 Bravais Lattices (Douglas, 2006)........... 70

Table 4.3 Bond distances and angles of rutile crystal structure (Grant, 1959) .. 87

Table 4.4 Some mechanical properties of rutile 88

Table 4.5 Some mechanical properties of anatase 92

Table 4.6 Summary of characteristics of the three crystalline phases of titania 97

Table 5.1 Potentials available in GULP 122

Table 5.2 Keywords in GULP 124

Table 5.3 Experimental unit cell parameters and fractional coordinates for rutile, anatase and brookite. (Naicker et al., 2005).. 124

Table 5.4 Size of nanoparticles and the corresponding number of TiO_2 units for anatase and rutile 127

Table 5.5 Size of anatase nanoparticles and corresponding water molecules and water density in each simulation box.. 128

Table 5.6 Potential parameters for TiO_2. (Oliver et al., 1997, Matsui and Akaogi, 1991) 130

Table 5.7 SPC/E water potential parameters (Bandura and Kubicki, 2003, Předota et al., 2004) 130

Table 5.8 Parameters for interaction between water molecules and TiO_2 nanoparticles (Bandura and Kubicki, 2003)... 130

Table 5.9 Observables: Elastic constants (Units in GPa)............................... 132

Table 5.10 Sources of elastic constants used in force field fitting and their corresponding refined force field identity... 133

Table 5.11 Force field parameters derived using elastic constants in Table 5.9. Refined force field 1 derived from *ab initio* (IMR group). Refined force field 2 derived from experiments (Isaak et al., 1998)... 133

Table 5.12 Properties of bulk TiO_2 phases predicted using the Matsui – Akaogi force field, the refined force field 1 derived from *ab initio* (IMR group), and the refined force field 2 derived from experiments (Isaak et al., 1998) 134

Table 5.13 Comparison of predicted elastic constants for the three TiO_2 phases with elastic constants in Table 4.4 and 4.5 from literature. The elastic constants were predicted using the Matsui – Akaogi force field, the refined force field 1 derived from ab initio (IMR group), and the refined force field 2 derived from experiments (Isaak et al., 1998). 135

Table 5.14 Comparison of cell parameters predicted from Matsui – Akaogi and the refined force fields, to Table 4.6 from literature 136

Table 6.1 Results for the three phases of TiO_2 calculated using GULP 140

Table 6.2 Surface energies for the three phases of TiO_2 calculated using GULP. Simulation data obtained from (Oliver et al., 1997). 145

Table 6.3 Differences between the surface energies of the unrelaxed and relaxed surfaces for the three phases of TiO_2. Simulation data obtained from (Oliver et al., 1997) 145

Table 6.4 Attachment energies for the three phases of TiO_2 calculated using GULP. Simulation data obtained from (Oliver et al., 1997). (Note: $\Delta Uatt$ per atom) 147

Table 6.5 Differences between the attachment energies of the unrelaxed and relaxed for the three phases of TiO_2. 147

Table 6.6 Size of cuboidal simulation box and their corresponding containing nanoparticle sizes. 160

Table 6.7 Coordination number for corresponding particle size, bond length/position of the first peak, rij, and temperature for anatase and rutile TiO_2 nanoparticles (Okeke et al., 2013) 167

Table 6.8 Surface energy (in Jm^{-2}) of rutile and anatase nanoparticles for different temperatures.. 180

Table 6.9 Surface area (in $Å^2$) of anatase nanoparticles in vacuum and water environments. 197

Nomenclature

Roman Letters

a	radius of primary nanoparticles
ak	Kapitza radius
cp	Specific heat
D	Particle diffusion constant
d	Particle diameter
d_l	chemical dimension
d_f	fractal dimension
JQ	Thermal flux
k	Thermal conductivity
kB	Boltzmann constant
l	Mean free path
n	shape factor
N	number of particles
R_b	Interfacial thermal resistance
Rg	radius of gyration
T	Temperature
t	Time
$U(r^N)$	Potential energy
ΔU_{SE}	Surface energy
U_{bulk}	Bulk energy

Greek Characters

η	Fluid viscosity
ρ	Density
τ_D	Time required for a particle to move a distance equal to its size
τ_H	Time required for heat to move at the same distance in the liquid
χ	Thermometric conductivity, given as $\chi = k/\rho c_P$
β	Ratio of particle to fluid thermal conductivity given as $\beta = k_p/k_f$
α	Non-dimensional interfacial thermal resistance, given as $\propto = 2R_b k_f/d$
Ø	Particle volume fraction

Subscripts

a	aggregate
c	backbone
eff	effective
f	fluid

nc	dead ends
p	particle
f	Fluid
HC	Hamilton and Crosser theory
m	melting
M	Composite matrix
p	particle
SE	Surface energy

Acronyms

GULP	General Utility Lattice Program
RLA	Reaction Limited Aggregation
DLCCA	Cluster Limited Cluster-Cluster aggregation

Chapter 1

Introduction to Project

1 Introduction to the Project

1.1 Introduction

Recently, nanofluids are reported to possess enhanced properties that can be harnessed for a wide variety of applications. Nanofluids are base liquids containing suspended nanoparticles, usually formulated for the purpose of enhanced heat transfer. These fluids are shown to have enhanced thermal/heat transfer properties compared to their conventional counterparts (Keblinski et al., 2002). Early studies were carried out by Maxwell (Maxwell, 1881) on solid particle suspensions of magnetic metallic oxides, most of which were on millimetre to micrometer size particles. However, it is highly desirable to develop nano solid-particle suspensions with enhanced heat transfer properties as the surface area to volume ratio of particles increases significantly for decrease in particle size.

It has been experimentally shown in many instances that nanofluids have displayed higher thermal conductivity and convective heat transfer in comparison to host conventional liquids (Chen et al., 2008, Ding et al., 2010, Garg et al., 2009, Li and Peterson, 2006, Wen et al., 2006). For example, 30% increase in thermal conductivity of water (base fluid) containing a suspension of 13 nm size Al_2O_3 nanoparticles at 4.3% volume fraction was observed (Keblinski et al., 2002). An even higher increase of about 40% was observed when 10 nm size Cu nanoparticles at 0.3% volume fraction were suspended in similar base fluid (Keblinski et al., 2002). However, when the particle concentration is very low (< 0.1%), the enhancement in thermal conductivity is generally negligible (Kim et al., 2007, Putnam et al., 2006, Witharana et al., 2010). This observation was confirmed by the recently concluded international benchmarking exercise for nanofluids which was conducted by 34 organizations participating from around the world (Buongiorno et al., 2009). The main objective of this exercise was to compare thermal conductivity data obtained from various experimental approaches for similar samples of different types of nanofluids. Their main finding was that thermal conductivity enhancement of the tested nanofluids increased with increasing particle volume fraction. This finding was consistent when thermal conductivity measurements of the base fluids and nanofluids were taken using the same measurement techniques. Negligible systematic differences in thermal conductivity measurements were observed for different measurement techniques. Following this, the experimentally observed heat transfer enhancement caused by suspended nanoparticles prompted deeper investigations into this subject. It was recognised that clearer understanding of the underlying mechanisms behind the observed enhancement was required and would pave the way to develop better nanofluids for enhanced heat transfer purposes. Hence, the experiments were followed by numerical modelling. These numerical models were aimed at predicting thermal enhancement of nanofluids similar to those observed from experiments. However, most of the developed models such as the effective medium theories of Maxwell, Bruggeman, and Hamilton and Crosser (Maxwell, 1881, Bruggeman, 1936, Hamilton and Crosser, 1962), were found to be unable to predict the experimental data very well, as the experimental results have shown much higher effective thermal conductivity of nanofluids (even up to an order of magnitude greater) (Xie et al., 2005). One of the main reasons for this discrepancy is that these models were originally developed to predict the effective thermal conductivity of composites and mixtures based on a continuum-level approach which basically incorporates only the particle shape and volume fraction as variables and assume diffusive heat transport in both liquid and solid phase. They do not take into account important parameters such as particle size, interparticle interactions and particle aggregation. They also lack any account of some mechanisms which are key in predicting effective thermal conductivity of nanofluids. In order to develop a more comprehensive model with the ability to potentially predict the effective thermal conductivity of nanofluids, four possible mechanisms behind the observed thermal enhancement were proposed (Keblinski et al., 2002). These mechanisms laid the foundation for the development of most of the thermal conductivity prediction models recently published (Jang and Choi, 2004, Koo and Kleinstreuer, 2004, Kumar et al., 2004). These mechanisms are; Brownian motion of nanoparticles in the liquid, formation of liquid layers around nanoparticles, ballistic nature of heat transport within nanoparticles, and formation of nanoparticle clusters (Wen et al., 2009). Among these mechanisms, the formation of nanoparticle clusters is believed to be the mechanism that is most likely behind the observed thermal enhancement (Wen et al., 2009). In this research, three model water-based nanofluids consisting of alumina, copper oxide and titanium dioxide respectively, were initially used to study the influence of particle aggregation (clustering) on the effective thermal conductivity of nanofluids. Results from these investigations showed that particle aggregation enhanced the effective thermal conductivity of the model nanofluids used in the analysis, and this justified an in depth research on the physical mechanism behind particle aggregation within the base liquid. To study particle aggregation, an investigation into their particle scale properties would be of great interest as these properties have been known to influence their bulk/macroscopic transport behaviour (Okeke et al., 2011, Okeke et al., 2012). This gave the main motivation for this research, which is to conduct a thorough investigation into thermodynamic, structural, surface and interaction force properties which are known to influence particle interactions (Dunphy Guzman et al., 2006). In this research and with regards to TiO_2 nanoparticles as a model system, molecular dynamics simulation packages have been used to study how their physico-thermal properties evolve under vacuum and liquid environments for different temperatures.

Titanium dioxide nanoparticles are widely applied in the industry due to their enhanced physical, chemical and electrical properties. These unique and enhanced properties they possess have made them widely researched, providing a wide selection of literatures. There are three main polymorphic forms of titanium dioxide which are; rutile, anatase and brookite. Of the three forms, rutile has been found to be the most stable polymorph in the bulk form while anatase and brookite transform irreversibly to rutile under high temperature (Banfield et al., 1993, Yang et al., 2001, Ovenstone, 2001). Experimental evidence further suggests that anatase is the most thermodynamically stable in the nanocrystalline form (Koparde and Cummings, 2008). The current research focuses on two mostly encountered forms of TiO_2 for industrial applications namely; anatase and rutile. The present results provide a strong platform for future studies on their clustering behaviours for under different environments.

1.2 Aim of Thesis

The main aim of this thesis is to fully investigate the role of particle scale properties on transport properties of nanofluids. The following tasks and descriptions provided in Table 1.1 and Figure 1.1 will aid in carrying out this investigation.

Table 1.1 Tasks and descriptions for Thesis

Task	Description
Transport Properties: Effective thermal conductivity of nanofluids	Detailed study on effective thermal conductivity of nanofluids and the reason for the use of nano-systems rather than conventional heat transfer systems.
Possible mechanisms behind effective thermal conductivity	Outline and discuss possible mechanisms behind effective thermal conductivity that have been proposed so far from the literature
Role of particle aggregation	Investigations on the influence of aggregate size, volume fraction, interfacial thermal resistance, and fractal and chemical dimensions on effective thermal conductivity of nanofluids. Furthermore, results obtained from current investigations are validated, where possible, with those from literature. This motivates to perform in-depth analysis of how thermo-physical properties evolve at molecular level using molecular dynamics simulations on TiO_2 nanoparticles as model system.
Molecular dynamics simulation of TiO_2 nanoparticles	Predict atomic scale properties of TiO_2 nanoparticles while in both liquid and vacuum environments. Properties predicted are; structural, thermodynamic, surface and interparticle interaction properties, using molecular dynamics software packages such as GULP and DL_POLY. These key properties could be accounted further in developing higher-order models of clustering of TiO_2 nanoparitcles under different environment and their link to heat transport properties

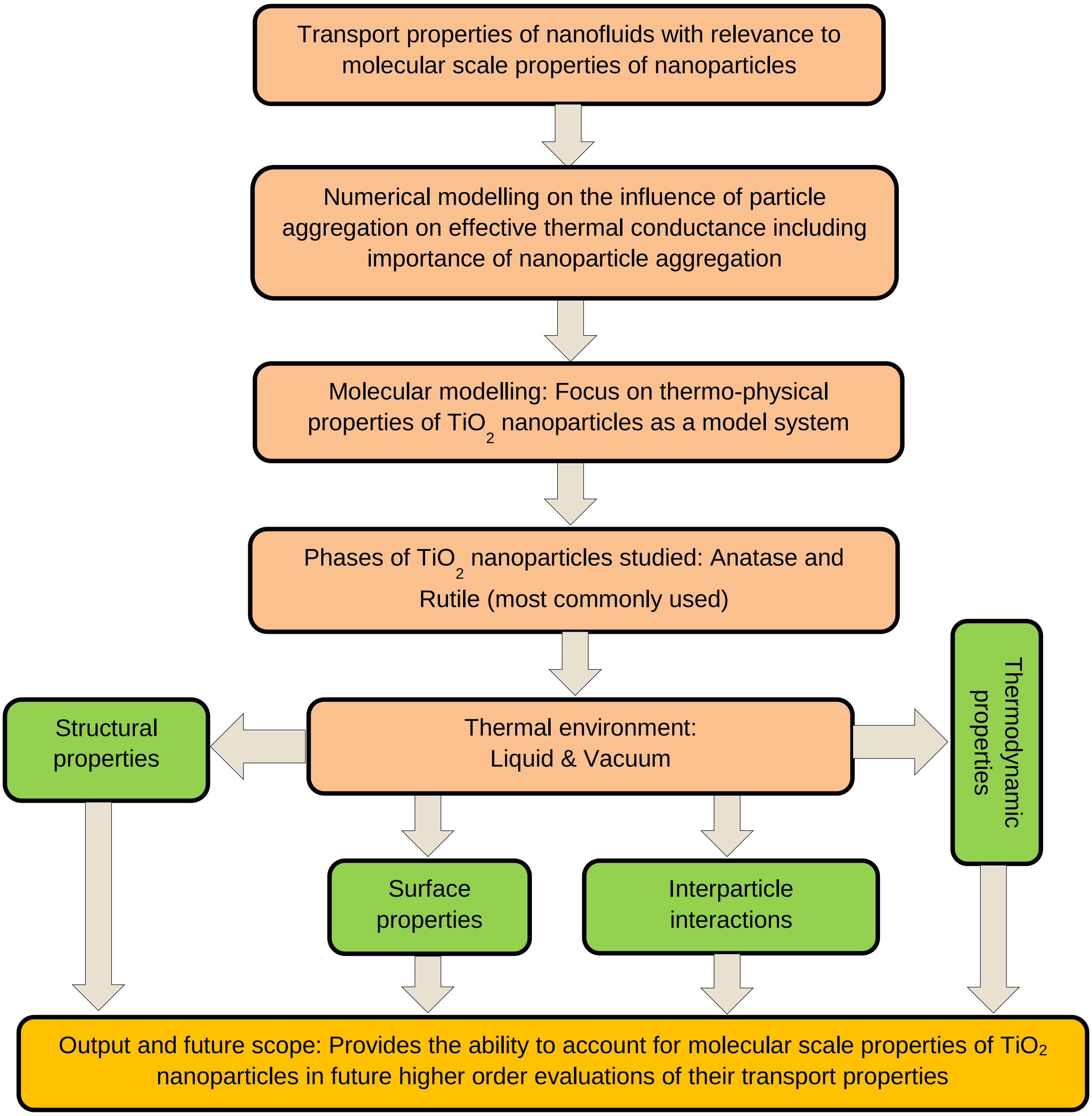

Figure 1.1 Structure of the thesis

1.3 Structure of theThesis

This thesis is composed of eight chapters in total. The general introduction to the project is contained in ***Chapter 1***. ***Chapter 2*** gives an introduction to the thermal conductivity of nanofluids including information about recent developments and its applications. Possible mechanisms behind the observed thermal enhancement in nanofluids that have been proposed by researchers are also discussed in this Chapter. Furthermore, the concept of a numerical modelling approach used in predicting the influence of particle aggregation on effective thermal conductivity of nanofluids is discussed here. In ***Chapter 3*, ** predictions of effective thermal conductivity of nanofluids using numerical/computational and sensitivity analysis are shown, to provide more insight into why particle aggregation is thought to be the most influential mechanism behind thermal conductivity enhancement, and to give a basis to carry out further investigation into the physico-thermal properties of nanoparticles. Here, numerical investigations have been conducted in detail to study the effect of particle clustering on thermal conductivity of nanofluids. The degree of enhancement has also been analysed for increasing aggregate size and particle concentration. The numerical work has been validated with experimental data on water-based nanofluids of metals and metal oxide nanoparticles. On top of this, studies have been conducted on the effect of the fractal and chemical dimensions of nanoparticle clusters. The concept of fractal dimension has been used in the past to study the aggregation process of particles. Using this concept it has been ascertained that aggregate structures can be characterized by fractal and chemical dimension of objects as these structures are usually complex (Xuan et al., 2003). ***Chapter 4*** gives a general background on TiO_2 including its molecular properties. It also provides in depth information about the characteristics and properties of its three crystalline phases. Here the main surfaces (with low index and known for their thermodynamic stability) of the crystalline phases are discussed. It also introduces the theoretical concept of molecular mechanics and force field models. ***Chapter 5*** provides information on the computational methods for the molecular modelling. A description of the molecular dynamics simulation package used in this research is also presented here, including the type of force field used. Results obtained from molecular modelling of TiO_2 nanoparticles on their atomic scale properties are shown and discussed in ***Chapter 6***. Here, lattice, attachment and surface energies have been initially calculated for the three phases of typical TiO_2 crystal structure using the General Utility Lattice Program (GULP) (Gale and Rohl, 2003). Afterwards, molecular dynamics simulations have been carried out for anatase TiO_2 nanoparticles ranging from 2 to 6 nm at 300 K, in both water and vacuum conditions using a classical molecular dynamic code DL_POLY. Later for both conditions, temperature effects on surface and structural properties of TiO_2 nanoparticles have been evaluated for temperatures ranging from 300-2500K. Further investigation has been conducted to study interparticle interaction forces in relation to separation distance between TiO_2 nanoparticles. ***Chapter 7*** provides results on interaction forces in relation to separation distance for different sizes of nanoparticles. These forces are known to influence the self-assembly and mechanical strength of nanoparticles which leads to particle aggregation and clustering. Finally, the entire project is concluded in ***Chapter 8***, and lessons learnt and recommendations for future work are discussed.

Chapter 2

Thermal Conductivity of Nanofluids:
Background and Recent Development

2 Thermal Conductivity of Nanofluids: Background and Recent Development

2.1 Introduction

This chapter provides a background introduction on thermal conductivity of nanofluids including its applications and recent developments that have so far been reported in the literature. Here, the possible mechanisms behind the observed thermal enhancement in nanofluids which have been proposed by researchers such as; Brownian motion, interfacial layering, ballistic transport and particle aggregation, are also discussed. Furthermore, the numerical modelling method used in this research which presents the concept of the aggregation model used in predicting effective thermal conductivity of nanofluids, is also discussed. This model incorporates parameters such as particle clustering, interfacial layer thickness, Kapitza radius and fractal and chemical dimensions which will be used to predict the degree of thermal enhancement.

2.2 Nanofluid background

A nanofluid is a stable suspension of metal oxide nano-metre sized particles in conventional heat transfer fluids or base fluids. The nanoparticles are usually well dispersed in the base fluid during the synthesis of nanofluids. Although the concept of a nanofluid was investigated a long time ago by Michael Faraday who in 1857 for example, first studied the synthesis and colours of colloidal gold, it gained more prominence when badged as nanotechnology (Stephan, 1985). Nanotechnology refers to the study of matter at the atomic or molecular scale and is experiencing rapid technological advancement. The scope of nanotechnology is across most areas of nature including engineering, medicine, pharmacology and biotechnology. It is envisaged to enhance industrial and technological growth which will have an impact on all walks of life. The inadequacy of conventional heat transfer fluids to perform in increased thermal loadings and a variety of thermal systems has led researchers, scientist and engineers to search for fluids with better heat transfer properties. With the advancement in technology, most systems and devices used in many transportation and manufacturing industries are designed to have more efficient features such as smaller sizes and increased power output. Miniaturization of these devices has brought about increased thermal energy demand in order to produce the desired power output (Murshed et al., 2008).

For optimum performance of these devices, proper thermal management incorporating heat transfer process and reduced energy loss is required. The control and removal of heat is of great importance in high thermal output systems such as microelectronics, nuclear fission and fusion, and micro chemical reactions. Among heat transfer fluids, water is known to have the highest thermal conductivity of about 0.6 W/mK at room temperature. Metal oxide particles (millimetre or micrometre size) (Figure 2.1) generally possess far higher thermal conductivity than conventional base fluids, hence their use in the synthesis of better heat transfer fluids (Eapen et al., 2010, Choi et al., 2001). However, setbacks such as poor stability of the suspended particles leading to sedimentation of particles, and clogging of flow micro-channels are being observed (Murshed et al., 2008). With enhanced thermal conductivity, nanofluids have exhibited better thermal properties including other features. This is as a result of the unique characteristics which nanoparticles possess such as high surface area for conduction of heat, and high surface to volume ratio for stability of the suspension in fluids (Kim et al., 2007). Other advantages of nanofluids over the previous fluid suspensions are; reduced clogging of micro-channels, adjustable properties such as thermal conductivity by varying particle volume fraction or concentration, and improved pumping ability thereby reducing pump power and energy consumption (Wen et al., 2009).

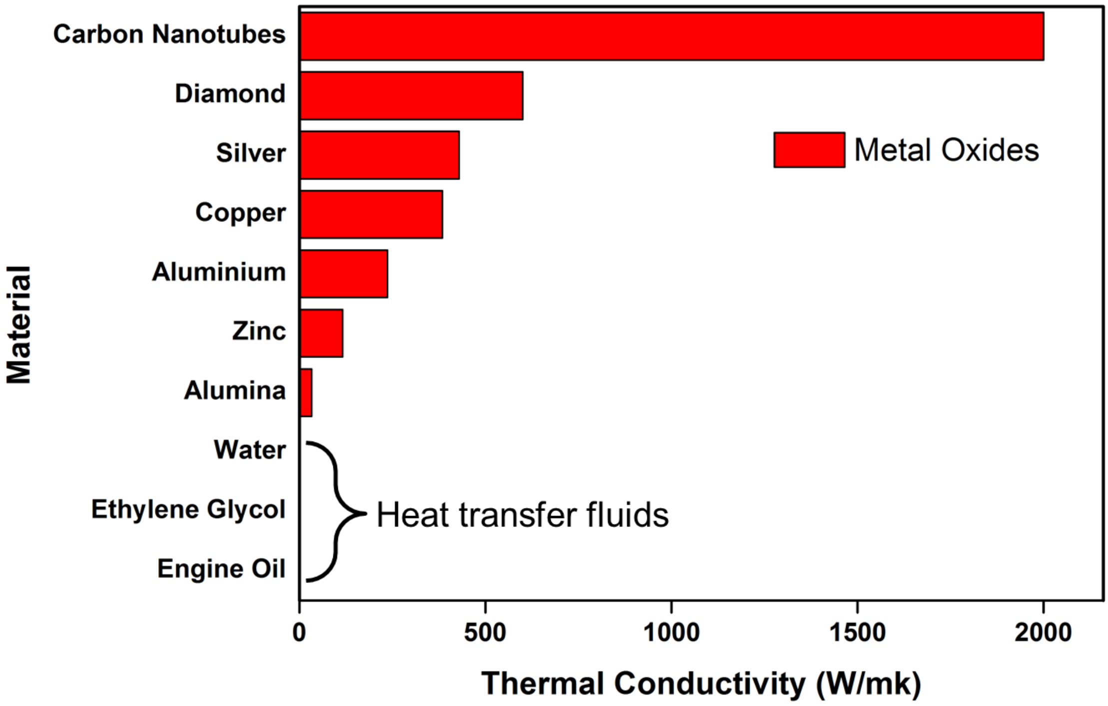

Figure 2.1 Comparison of the thermal conductivity of different materials.

The presence of the extremely small sized nanoparticles (usually < 100 nm) in nanofluids will aid the drive for system miniaturization since smaller heat exchangers will be designed creating innovative technological improvements, better systems performance, and enhanced heat transfer management leading to reduced operation cost. With the observation of increased thermal conductivity for heat transfer purposes, exploiting the full potential of these nanofluids for new applications will be of immense benefit in areas such as manufacturing, transportation, microelectronics, medical etc.

2.3 Applications of nanofluids

Due to the improved thermophysical properties which nanofluids exhibit, areas such as engineering and medicine will benefit immensely from the use of nanofluids (Franks, 1987). Nanofluids can be applied in industries such as;

2.3.1 Transportation

The use of nanofluids will improve heating and cooling applications in vehicles. Compared to current conventional vehicle heat transfer fluids (e.g. coolants, engine oil, etc) which usually have poor heat transfer abilities, nanofluids possess higher thermal conductivity potentials. The design of smaller engines, radiators and other vehicle components which require heat transfer fluids, will aid in manufacture of lighter vehicles with increased energy efficiency and less fuel consumption. This will promote the green initiative of saving the earth's climate as vehicles will produce lower emissions with reduced environmental pollution (Murshed et al., 2008).

2.3.2 Micromechanical Systems

Cooling of systems and units has been proven to show the greatest challenge in industries. A conventional method used for this purpose is the extension of surface area available for heat transfer which constitutes unnecessary increase in the size of systems for managing heat (Murshed et al., 2008). This contradicts the aim of system miniaturization which is a major stimulant for industrial and technological growth. Increased generation of heat and thermal loading which microelectromechanical systems (MEMS) exhibit, requires improved cooling backup compared to conventional cooling systems available. Apart from enhanced thermal conductivities, the small nanometer size of the suspended particles in nanofluids will enable easy and smooth flow of the fluid across microchannels within these MEMS's and other systems. Products such as electric/mechanical motors and pumps, heat pumps, valves, sensors, heat pipes, heat exchangers, medical devices, fuel cells and aircrafts can all be manufactured on a miniature scale (Choi, 1998). Heat exchangers of miniature sizes will exhibit features such as enhanced thermal properties, high heat transfer surface area, light weight, small size and low amount of required heat transfer fluid, which will require nanofluids with minimal micro channel clogging for optimum performance and improved durability of the system.

2.3.3 Refrigeration and air-conditioning

Heat transfer in heating, ventilating and air-conditioning systems (HVAC) will be enhanced with the use of nanofluids. With the reduction in sizes of refrigeration and HVAC units, pumping of coolants will be made easier. This will increase pump and energy efficiency while also establishing a cost effective system (Murshed et al., 2008).

2.3.4 Chemical, petroleum and pharmaceutical industries

Many processes which occur in these industries involve heat transfer which takes place in heat exchangers. Due to the adjustable thermal properties of nanofluids by varying particle concentration, its use in the pharmaceutical industry will improve the quality of products brought about by thermal control during product synthesis. Also, nanofluids with good particle suspension can be used in this industry without resulting in sedimentation (Keblinski et al., 2002).

2.3.5 Medicine

Efficient drug delivery can be made possible with the use of magnetic nanoparticles in body fluids for cancer treatment (Murshed et al., 2008). Unlike the side effects such as damage of DNA caused by present radiation therapies, magnetic nanoparticles which are more adhesive to cancer cells compared to normal cells, can replace the former therapy. This is a promising venture for cancer treatment as nanofluids can be used for drug delivery in body fluids (Murshed et al., 2008).

2.4 Thermal conductivity of nanofluids

The main rationale behind the suspension of nanoparticles in base fluids is the enhancement of the thermal conductivity of the resulting nanofluid (Buongiorno et al., 2009, Wen and Ding, 2004, Wen et al., 2006, Xuan and Li, 2000). Thermal conductivity generally refers to the property of a material that shows its ability to conduct heat. It measures the ability of heat transfer fluids to conduct heat. For a material, Fourier’s Law of heat conduction theoretically describes this property. Given that the formula for Fourier’s Law is;

$$\vec{q} = -k\nabla T \tag{2.1}$$

Where $\vec{q}$ is the heat flux density, *k* is the thermal conductivity and *T* is the temperature field (Eapen et al., 2010). This reveals that heat flows across different gradients such as temperature and those resulting from concentration (Kumar et al., 2004). Tentatively, thermal conductivity measurement for nanofluids may depend on the diffusion and chemical reaction effects within the fluid medium. A diffusion equation (Keblinski et al., 2002) describing heat transport in composite materials in terms of temperature field *T* in each composite material, can be based on the assumption given by (Keblinski et al., 2002);

$$\frac{\partial T}{\partial t} = \nabla(\chi \nabla \mathrm{T}) \tag{2.2}$$

where χ is the thermometric conductivity defined as (Keblinski et al., 2002). ∇ represents a differential operator which depends on the number of spatial dimensions.

$$\chi = {}^{k}/_{\rho c_P} \tag{2.3}$$

where *k* is thermal conductivity, $\mathrm{c_p}$ is the specific heat and *ρ* is the density. Equation 2.2 forms a basis for formulation of models for effective thermal conductivity such as those by Hamilton and Crosser, Maxwell medium theory (Maxwell, 1881) amongst others. Equation (2.2) can be simplified into the form of a Laplace equation with boundary conditions for continuity of thermal flux J_Q given by, (Keblinski et al., 2002).

$$\overrightarrow{J_Q} = -k\vec{\nabla} t \tag{2.4}$$

Below are conventional models for effective thermal conductivity of solid/liquid suspensions.

Table 2.1 Conventional models for effective thermal conductivity of solid/liquid suspensions (Eapen et al., 2010) (Choi et al., 2001, Hamilton and Crosser, 1962).

Models		Main features/expressions	Remarks
1.	Maxwell	$k_{eff}/k_f = 1 + \frac{3(\beta-1)\emptyset}{(\beta+2)-(\beta-1)\emptyset}$ (2.5)	Spherical particles are considered. Applicable to ∅ <<1 or |β-1|<<1
2.	Hamilton-Crosser (HC)	$\frac{k_{eff}}{k_f} = \frac{\beta+(n-1)-(n-1)(1-\beta)\emptyset}{\beta+(n-1)+(1-\beta)\emptyset}$ (2.6)	For spherical and non-spherical particles, n=3 for spheres and n=6 for cylinders. Applicable to ∅<<1 or |β-1|<<1
3.	Bruggeman	$1-\emptyset\left[\frac{k_f-k_{eff}}{k_f+2k_{eff}}\right]+\left[\frac{k_p-k_{eff}}{k_p+2k_{eff}}\right]=0$ (2.7)	Effective medium theory predicting thermal conductivity in the implicit form

where k_{eff} is the effective thermal conductivity of the solid/liquid suspension, k_p is the thermal conductivity of a nanoparticle, k_f is the thermal conductivity of the base fluid, $\beta = k_p/k_f$, particle shape factor is n, particle volume fraction is $\emptyset$.

The Maxwell theory was initially proposed for investigating the electrical conductivity and dielectric properties of composite materials. This theory can be referred to when predicting thermal conductivity enhancement of a matrix or nanofluid. The Maxwell theory is based on the assumption that the particles (i.e. spherical) are well-dispersed. The effective thermal conductivity is estimated by assuming that this set of well-dispersed particles is combined to make a single particle (Gao et al., 2006). Predicting effective thermal conductivity using other theories such as Hamilton and Crosser etc. is also based on the assumption of dispersion of particles. Interfacial thermal resistance, R_b, caused by temperature discontinuity between the nanoparticle and fluid can be taken as $\propto = 2R_b k_f/d$, and can be incorporated into the Maxwell theory (Nan et al., 1997). Figure 2.2 shows effective thermal conductivity predictions for water based (a) iron oxide and (b) titania nanofluids using the Maxwell and Hamilton-Crosser models.

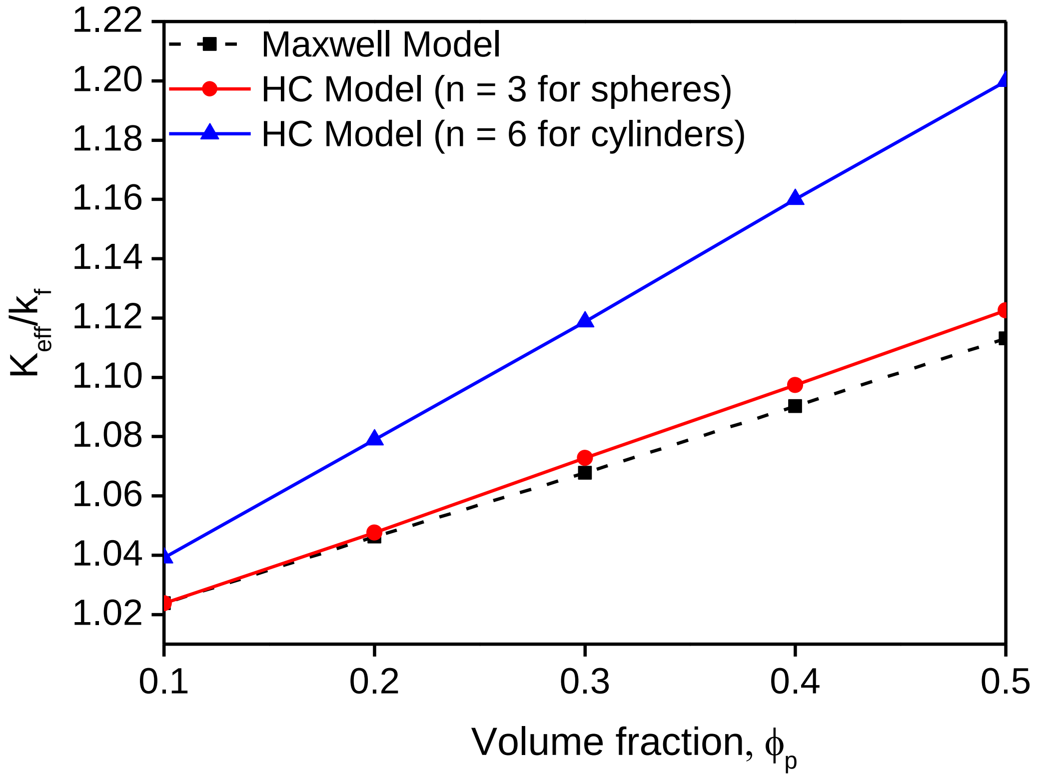

(a)

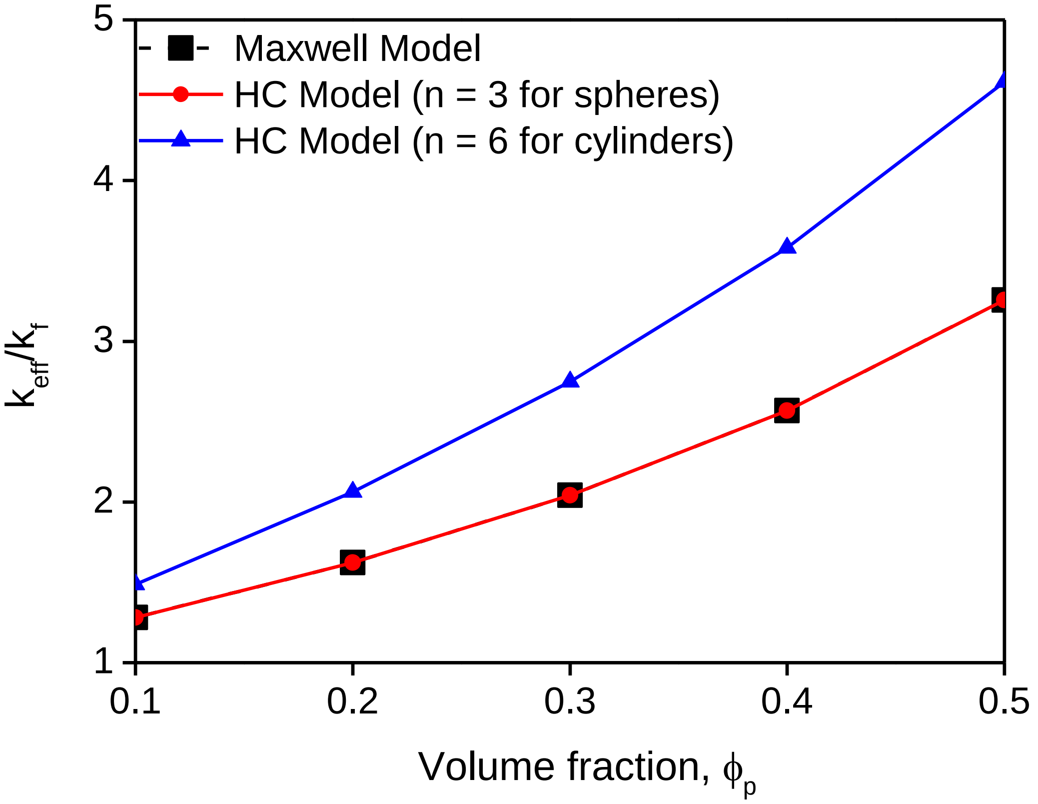

(b)

Figure 2.2 Prediction of thermal conductivity ratio (k_{eff}/k_f) for volume fractions of water based (a) iron-oxide (Fe_3O_4) and (b) titania (TiO_2) nanofluids using the Maxwell and Hamilton-Crosser (HC) model

Thermal conductivity amongst other properties such as density, viscosity, specific heat and surface tension are underlying thermo-physical properties which influence heat transfer abilities of heat transfer fluids. The heat transfer coefficient *h*, which is a function of these properties, depicts the intensity and capacity of heat transfer. Generally for heat transfer fluids, the heat transfer coefficient increases with effective thermal conductivity, density and specific heat but decreases for viscosity (Wen et al., 2009, Chen et al., 2008, He et al., 2007b). Nanoparticle suspensions in a base fluid can influence these properties thereby affecting heat transfer ability of the resulting nanofluid (Garg et al., 2009, Murshed et al., 2005).

Several studies and experiments have reported an enhancement in effective thermal conductivity for nanofluids compared to conventional heat transfer fluids that is dependent on the particle volume fraction or loading (Pak and Cho, 1998, Putnam et al., 2006). For example, for a particle loading of 1% the resulting nanofluid can have an increase in thermal conductivity of about 10% which is a desirable and favourable enhancement (Wen et al., 2009). Although this has been predicted, as seen from several studies, there are still some contradictions following some other studies. An in depth understanding of the reason behind this enhancement is still unknown. Knowledge and understanding of this will initiate and boost the commercialization of nanofluids. Negating the property of an ideal heat transfer fluid, nanofluids tend to exhibit increased viscosity on addition of nanoparticles. Although, this may be due to the structure and morphology of the particles added, stabilizers can be used to suppress this effect since high viscosity affects the effectiveness of heat transfer fluids (Wen et al., 2009, Ding et al., 2010). However, the enhanced thermal conductivity of nanofluids might make up for the increased viscosity observed.

2.4.1 Interfacial thermal resistance

As thermal conductivity enhancement is achieved depending on the ability of heat to flow rapidly across the aggregates, interfacial thermal resistance tends to pose a barrier to this heat flow. This boundary resistance, R_b which induces temperature discontinuity, ΔT, across the interface, is also defined in terms of the heat flux, Q, given by (Every et al., 1992);

$$\mathrm{Q} = \frac{\Delta T}{R_b} \tag{2.8}$$

Knowledge of the thermal boundary resistance gives information about thermal conductivity and vice versa for both particulate composites and nanofluids. Thermal boundary resistance was usually measured with initial measurements carried out by Kapitza in 1941 (Every et al., 1992). With his experiments on metal-liquid helium interfaces, the thermal boundary resistance R_b is now theoretically evaluated based on the Kapitza boundary (Every et al., 1992). His work which was mainly on solid-liquid interfaces can be related to the interfaces between nanoparticles and the base fluid in which they are suspended. Therefore the Kapitza radius is the thickness of the base fluid (in the case of nanofluids) or matrix (in the case of solid composites) over which the drop in temperature in a planar geometry is similar to that at the interface (Evans et al., 2008). Further investigation into experiments carried out on the thermal resistance of solid-solid metal-ceramic interface showed the measurement of the resistance as a function of temperature beginning from temperatures below the Debye temperatures for either material that make up the interface (i.e. solid-solid or solid-liquid), as fully capable of portraying the mechanisms of thermal conduction (Every et al., 1992). The acoustic mismatch model was developed to explain this phenomenon in which thermal resistance will become temperature independent after it gets to a temperature below the Debye temperature of the two materials that make up the interface. This model incorporates acoustic waves refracted at the interface with boundary conditions of continuity of displacement and traction force which depicts phonon propagation across an interface (Every et al., 1992). The diffuse scattering model which is a modified version of the acoustic mismatch model deals with randomly scattered phonons which arrive at the interface with directions depending on the available density of states in both materials (Every et al., 1992).

Generally, experimental investigations of thermal boundary/interfacial resistance are carried out on planar interfaces which can be compared to experiments for particle composites with interfaces which depend on the microstructure. This can aid in the evaluation of the thermal conductivity for a system matrix containing evenly dispersed particles using R_b. This can be related to the influence of interfacial thermal resistance on thermal properties of nanofluid system. This influence will depend on the size of the particles for dispersed individual or aggregated particles provided there is high boundary resistance in which case the surface to volume ratio of the particles will increase with smaller particles. In this analysis, a non-dimensional parameter, $\propto$, is used to represent the interfacial thermal resistance and is given as follows (Every et al., 1992);

$$\propto = {}^{a_k}/_{a} \tag{2.9}$$

Where a is the radius of the dispersed particles, and a_k is the Kapitza radius which is defined as; (Every et al., 1992)

$$\propto = R_b k_f \tag{2.10}$$

where k_f is the thermal conductivity of the base fluid.

A Debye model for R_b which takes into account a_k in terms of the acoustic mismatch theory is given by (Every et al., 1992);

$$R_b = \frac{4}{\rho C \upsilon \eta} \tag{2.11}$$

where ρ is the density, C is the specific heat, υ is the Debye velocity of the base fluid and η is the average probability for the movement of the phonons across the interface into the particles (Every et al., 1992). Considering this Debye model approximation, the thermal conductivity of the base fluid k_f, can be taken as, (Every et al., 1992)

$$k_f = \frac{1}{3} \rho C l \tag{2.12}$$

where l is taken as the phonon mean free path.

These illustrations for both R_b and k_f can further aid in elaborating on the model which takes into consideration the thermal conductivity of the fluid suspension in terms of α and the volume fraction of the dispersed phase (i.e. particles and aggregates) (Every et al, 1992). As a follow up, combination of 2.10, 2.11 and 2.12 will yield, (Every et al, 1992)

$$a_k \approx \frac{l}{\eta} \tag{2.13}$$

Equation 2.13 above reveals that for large Kapitza radius greater than the mean free path of phonons in the base fluid, the probability with which the phonons will move across the interface will be low. Since from the relation between $\propto$ and a_k in Equation 2.9, low probability will mean large a_k and therefore large $\propto$ which accounts for the interfacial thermal resistance (Every et al., 1992).

2.4.1.1 Estimation of the Kapitza radius for the interface of nanofluid compositions

In estimating the Kapitza radius for nanofluid composition (materials of which nanofluids are composed e.g. Water - CuO, Ethylene glycol – TiO_2) interface, it is necessary to note that the value of R_b estimated at room temperature for the particular nanofluid interface should lie close to the Debye temperature for the suspended nanoparticles and far below the Debye temperature for the base fluid. For example, in the case of solid composites ZnS - Diamond, the estimated value of R_b for its interface at room temperature should lie close to the Debye temperature for ZnS (which is the composite with $\theta_D = 315\,K$) and far below the Debye temperature for diamond (which is the matrix with $\theta_D = 2230\,K$) (Every et al., 1992). There are basically two methods of estimating the Kapitza radius which are the semi-empirical estimate which is based on the acoustic mismatch theory for both solid-solid and solid-liquid interfaces, and the Debye model in Equation 2.11 which assumes only phonons around the interface within the critical angleθ_C from the side of the nanoparticle or composite (i.e. for solid-liquid nanofluid interface or solid-solid composite interface) will be able to contribute (Every et al., 1992). In the case of the former, the semi-empirical estimate gives;

$$R_b = \frac{A}{T^2} \tag{2.14}$$

where A is a constant which is determined by the acoustic properties of either the solid-solid or solid-liquid in contact and in rare cases, the boundary conditions assumed since they add only about 10% difference to the values (Every et al., 1992). Experimental results have further shown that predictions of the acoustic mismatch model suggest temperatures for which the boundary resistance above this temperature will be insignificant as the dominant phonons will be nearing the Debye cut-off temperature and the limit of the heat capacity, is approached (Every et al., 1992). This is in contrast with numerical investigations carried out by Swartz and Pohl (Swartz and Pohl, 1989) which reveals that the boundary resistance will become insignificant at a much higher value than expected (i.e. far above the Debye cut-off temperature) which was assumed to be due to the scattering of the higher frequency phonons by subsurface damage (Every et al., 1992).

In the case of the second method, since only the phonons around the interface are likely to move, a fraction q of the phonons around the interface is given as; (Every et al., 1992)

$$q\frac{1}{2}\sin^2\theta_C = \frac{1}{2}(\upsilon/\upsilon')^2 \tag{2.15}$$

where υ and υ' are the Debye velocity for the nanoparticles and the base fluid respectively (for nanofluid) or for the composites and matrix respectively (for solid composites).

Closely related calculations have been carried out by Young and Maris (Young and Maris, 1989) and Pettersson and Mahan (Pettersson and Mahan, 1990) which involves lattice dynamical calculations of the Kapitza resistance between dispersed fcc lattices and the nature of the interfacial bonding (Every et al., 1992). Their calculation results show that for increasing strength of bonding between atoms of the two lattices, only a small effect is observed on the Kapitza resistance, while for weak bonding, the movement of the higher frequency phonons is reduced thereby increasing the boundary or Kapitza resistance.

2.5 Possible mechanisms for thermal conductivity enhancement in nanofluids

It has been proposed that particle size, particle shape and volume fraction influence thermal conductivity. This can be observed in the effective thermal conductivity theories/models in Table 2.1, where particle shape *n* and volume fraction *ø* are incorporated into these equations. Some experimental results also show increased thermal conductivity for the same volume fraction but different particle sizes (Keblinski et al., 2002). Based on the models and since particles have higher thermal conductivity compared to base fluids, an increase in thermal conductivity can be observed. The highest conductivity can be reached when $k_p >> k_f$ which is given by (Keblinski et al., 2002);

$$k_{eff} = k_f\left[\frac{1+2\emptyset}{1-\emptyset}\right] \tag{2.16}$$

This is a form of the Maxwell model which acts as a limiting value in which case an increase in thermal conductivity above this will have a minor effect on the thermal conductivity of the composite or nanofluid depending on the medium. This is due to the fact that temperature across the particle becomes constant for thermal conductivity of about 10 times or more, greater than that of the base fluid (Keblinski et al., 2002).

Some possible mechanisms behind the observed thermal enhancement in nanofluids have been proposed by researchers (Chen et al., 2008). These include;

Brownian motion, interfacial or liquid layering at the liquid-particle interface, nature of heat transport in nanoparticles involving ballistic transport of energy carriers called phonons, interfacial resistance and more recently particle aggregation or clustering (Wen et al., 2009).

2.5.1 Brownian motion

Brownian motion is basically the random movement of liquid molecules or particles in a fluid medium. As the particles move through the fluid, their movement may instigate collision between them thereby promoting the transfer of heat within the fluid. This has been suggested as a reason behind thermal conductivity enhancement in nanofluids (Jang and Choi, 2004, Koo and Kleinstreuer, 2004, Prasher et al., 2006a). However, a background investigation comparing the time length of motion of particles, to the diffusion of heat in the fluid may provide more insight as to whether Brownian motion is a possible mechanism. Brownian motion is described by the Stokes-Einstein formula, given as (Keblinski et al., 2002):

$$D = K_B T / 3\pi\eta d \tag{2.17}$$

Where *D* is the particle diffusion constant which signifies Brownian motion, K_B is the Boltzmann constant, *d* is the particle diameter and η is the fluid viscosity (Keblinski et al., 2002). Equation (2.17) can form a basis for the estimation of the Brownian motion effect on thermal conductivity of the nanofluid by the comparison of time length of motion of particle to the diffusion of heat in the liquid. For a particle in motion, the time taken (τ_P) for it to move a distance that is equivalent to its size can be given as (Keblinski et al., 2002);

$$\tau_P = \frac{d^2}{6D} = \frac{3\pi\eta d^2}{6K_B T} \tag{2.18}$$

Also for heat diffusion, the time taken (τ_H) for heat to move within the fluid in the same distance can be given as;

$$\tau_H = \frac{d^2}{6\chi} = \frac{d^2 c_P \rho}{6k_f} \tag{2.19}$$

Where ρ is density, c_P is specific heat capacity, *d* is particle diameter

So, for water at room temperature with η = 0.01 g/cm s, ρ = 1g/cm^3, c_P = 4.2 J/g, $k_f = 0.4\ \mathrm{W/mK}$ and for particle *d* = 10nm, substituting these values into Equation 2.18 and 2.19 will give $\tau_P \approx 2 \times 10^{-7}\mathrm{s}$ and $\tau_H \approx 4 \times 10^{-10}\mathrm{s}$ respectively (Keblinski et al., 2002). This adequately shows that diffusion of heat is faster than motion of particles in a fluid medium. This can be related to motion of particles in a nanofluid, suggesting that Brownian motion has a negligible effect on thermal conductivity enhancement since it does not meet the time requirement for heat transport as particle motion is slow.

2.5.2 Interfacial layering

The interfacial layer assumes an ordered fluid layer structure around the solid interface of the nanoparticles which is more ordered than that of the bulk liquid. Since solid metallic and crystalline particles exhibit better thermal conductivity than base liquids, liquid layering of fluid around these particles will lead to enhanced thermal conductivity of the nanofluid.

Now assuming that the thermal conductivity for the particle and interfacial liquid are the same, then the resulting structure (i.e. the total or effective volume) would possess increased thermal conductivity. In fact, molecular dynamic simulations show that the effective thermal conductivity achieved for this interfacial structure is much higher than the prediction by thermal conductivity models such as Maxwell theory (Eapen et al., 2010). The Yan model provides an estimate for the interface thickness around a particle and is given as (Eapen et al., 2010);

$$h = \frac{1}{\sqrt{3}}\left[\frac{4M_f}{\rho_f N_a}\right]^{1/3} \tag{2.20}$$

Where $\mathrm{M_f}$ is the molecular weight, ρ_f is the density of the surrounding fluid medium around a cluster of nanoparticles and N_a is Avogadro's number which is 6.023×10^{23}. For a small cluster of particles in a nanofluid, with fluid layers around forming an interfacial fluid structure, thermal conductivity enhancement has been observed due to the formation of a network of conduction paths. As the size of the cluster increases, the conduction path is been tampered with, which reduces the thermal conductivity similar to that which can be achieved from Maxwell theory predictions (Eapen et al., 2010). For an enhancement of thermal conductivity to occur, the liquid layer around the particle surface has to be thick enough i.e. for example, for a particle of *d* = 10nm, a liquid layer thickness *h*, of about 2.5nm would be required for enhanced thermal conductivity (Figure 2.3) (Wang and Mujumdar, 2007, Keblinski et al., 2002). Experimentally, this is not the case as liquid layer thickness is usually not as thick as required, with interfacial diameter of about 1nm. This means that although liquid layering around particles may aid thermal transfer, it may not be the reason behind the thermal conductivity enhancement that has been observed in nanofluids as the liquid layer thickness around the particle is insufficient for such an enhancement. Some experiments have also shown little or no thermal conductivity enhancement for interfacial structures of about four ordered fluid layers around the particle surface (Eapen et al., 2010). They show that for increased cluster sizes of about hundreds of atoms, interfacial structures containing a percolating conduction path have been compromised thereby reducing thermal conductivity enhancement. This is completely unlike the case for cluster size of the order of ten atoms.

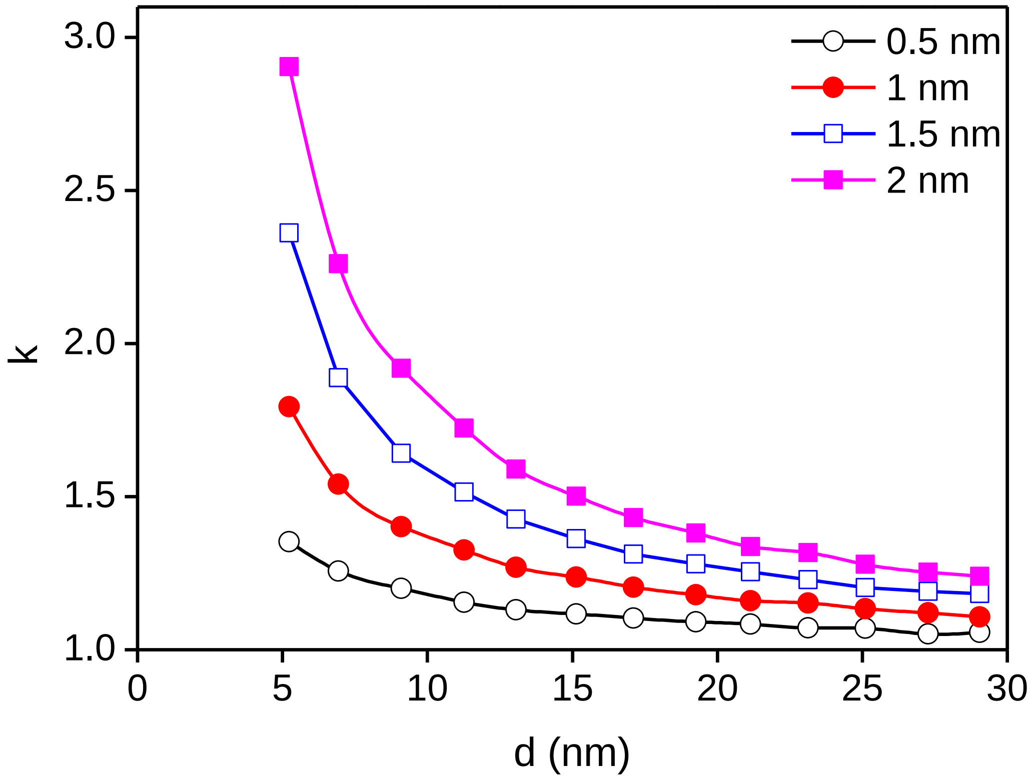

Figure 2.3 Thermal enhancement due to liquid layering around the particles forming a liquid/particle interface (Keblinski et al., 2002)

2.5.3 Ballistic transport mechanism

As in metals in which heat is transported by electrons, diffusive heat transport occurs in crystalline solids. In the case of diffusive heat transport, phonons transport heat in the form of vibrations in the crystal lattice of the crystalline solid. These phonons are randomly generated and move in different directions as they scatter and collide with each other. This random movement is assumed to transport heat effectively and thus increase thermal conductivity (Figure 2.4) (Wang and Mujumdar, 2007). The mean free path *l* of a phonon can be described by Debye theory given as (Keblinski et al., 2002);

$$l = {}^{10aT_m}/_{\gamma T} \tag{2.21}$$

where T_m is the melting point, γ is the Gruneisen parameter (of ≈ 1) and *a* is the lattice constant (≈ 0.5 nm) (Keblinski et al., 2002). Using this theory, an Al_2O_3 nanoparticle at room temperature will have a phonon mean free path *l* of about 35 nm, which makes phonon diffusion in the 10 nm particle size of Al_2O_3 impossible but rather a ballistic movement across the particle will occur.

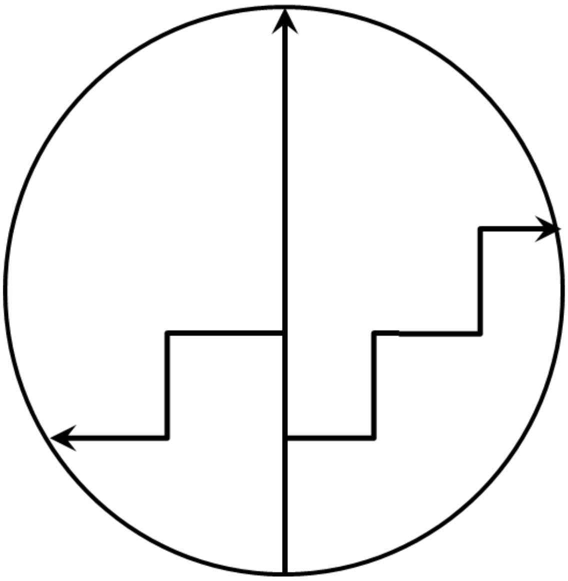

Figure 2.4 Ballistic and diffusive phonon transport in a particle (Wang and Mujumdar, 2007)

The restriction of phonon diffusion in the particle shows that the assumption of diffusion of heat transport in nanoparticles does not hold and so a more systematic theoretical analysis for the ballistic transport of phonon is required. A difficulty that could be experienced is the thermal conductivity enhancement achieved in comparison with diffusive phonon transport effects and ballistic phonon transport effects. In any case, temperature within the solid will be constant for either diffusive or ballistic phonon transport and so for a base liquid with low thermal conductivity heat flow will possess the same boundary condition (Keblinski et al., 2002). Apparently, but for the restriction of diffusion of phonons into the particle, phonon transport by diffusion would create better thermal conductivity enhancement compared to ballistic photon transport alone. This is due to the supposedly fast diffusive nature of phonon transport which would have transported heat suitable for massive thermal conductivity enhancement. Nevertheless, ballistic phonon transport could still offer some effects favourable for increased thermal conductivity. In the case where the time scale for ballistic phonons transported across a particle is long enough to remain in the liquid thereby reaching a nearby particle, thermal conductivity increase could be achieved. This will depend on the distance of the separation between particles as the phonon mean free path is far shorter in the liquid compared to that in the particle. Therefore, the particles need to be relatively close to each other for this case to occur. Closeness of particles may be achieved by the effect of Brownian motion due to the random motion of the particles. This closeness may assist easy and efficient phonon transport across particles thereby inducing thermal conductivity enhancement.

2.5.4 Particle aggregation or clustering

Clustering of particles has been considered to have an influence on thermal conductivity enhancement which is much higher than that predicted for homogenous dispersed particles (Xuan et al., 2003). This is still being investigated as clustered or aggregated particles formed will no longer suspend in the fluid after a certain period but will rather settle out. Also this aggregated structure may be destroyed during the impact of heat flow and heating conditions (Wen et al., 2009, Prasher et al., 2006b). However, it is assumed that physically for clustered nanoparticles formed, the resultant effective volume compared to that of single individual nanoparticles will be relatively larger and so an enhancement in thermal conductivity may be observed for this reason. Clustering of particles will aid easy heat transfer within the cluster which will enhance thermal conductivity. Clustered particles may be loosely or densely packed and larger enhancements could be observed for the more loosely packed clusters (Keblinski et al., 2005). Actually, for decreasing packing volume i.e. for loosely packed clusters, the effective volume of the cluster increases (Figure 2.5) (Wang and Mujumdar, 2007). This is because liquid fills the spaces in between these loosely packed particles within the cluster thereby increasing its effective volume compared to well dispersed nanoparticles. Since liquid intermediate clusters are formed, the idea of ballistic phonons transferring heat between particles with short separation distance may hold. The formation of loosely packed particle clusters resulting in liquid intermediate clusters will lead to an increase in effective volume and will aid in rapid heat flow within this

However, a major problem with clustering effects is the formation of large distances between clusters within the fluid which will leave large particle free regions. The isolation of clusters of particles within the fluid due to wide separation distances of these clusters may lead to high thermal resistance between clusters which will have a negative effect on thermal conductivity enhancement (Keblinski et al., 2002).

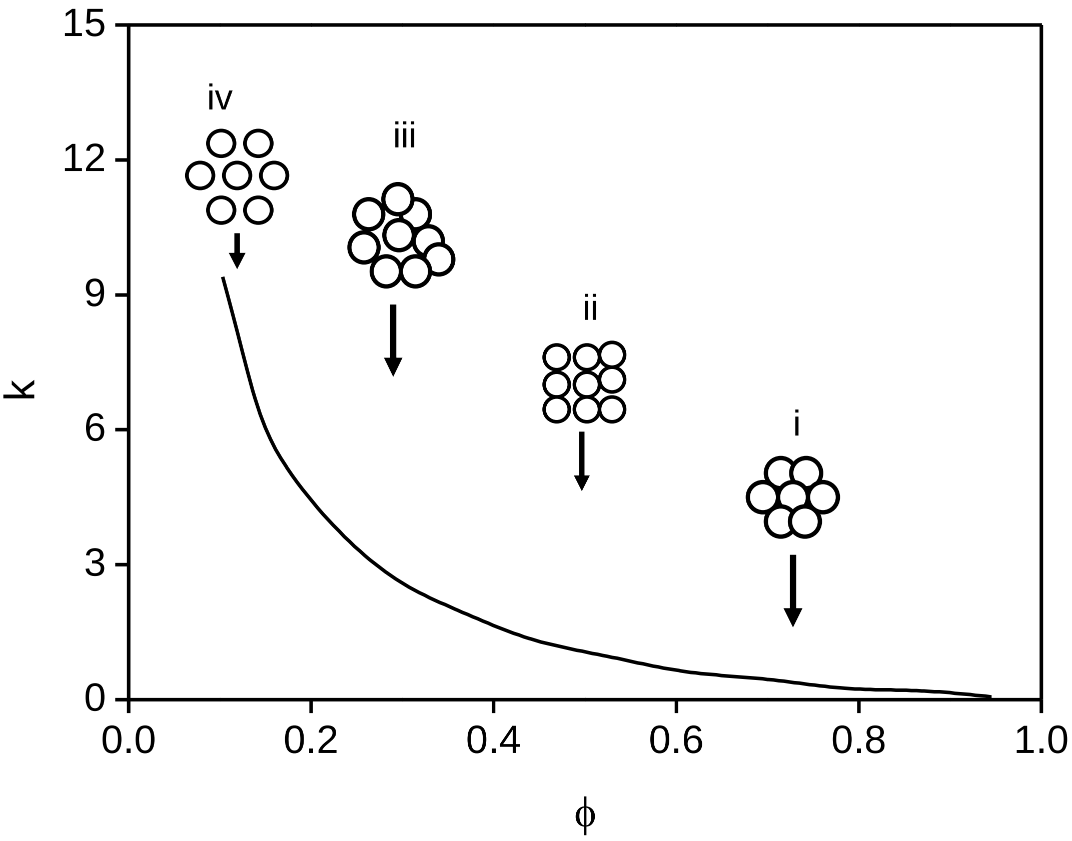

Figure 2.5 Thermal conductivity enhancement due to particle clustering/aggregation, i – iv represents the degree of packing volume in reducing order (Keblinski et al., 2002)

2.6 Mean field model

Mean field models have been created as an approach for the suggestion of possible mechanisms behind the thermal conductivity enhancement of nanofluid. There are basically two types of mean field models namely: the series and parallel bounds, and the Hashin and Shtrikman (HS) bounds.

2.6.1 Series and parallel bounds

The series and parallel models can be taken as conducting paths for thermal conduction. For these models as the name implies, the path of conduction that crosses through the nanoparticles and base fluid in series is the series mode while the one that crosses in parallel is the parallel mode (Figure 2.6). These models can describe the effective thermal conductivity of a nanofluid given by (Eapen et al., 2010)

$$\frac{1}{k_{eff}} = \frac{(1-\emptyset)}{k_f} + \frac{\emptyset}{k_p} \tag{2.22}$$

$$k_{eff}^{\parallel} = (1 - \emptyset)k_f + \emptyset k_p \tag{2.23}$$

Where $k_{eff}^{=}$ and $k_{eff}^{\parallel}$ are the series and parallel mode respectively

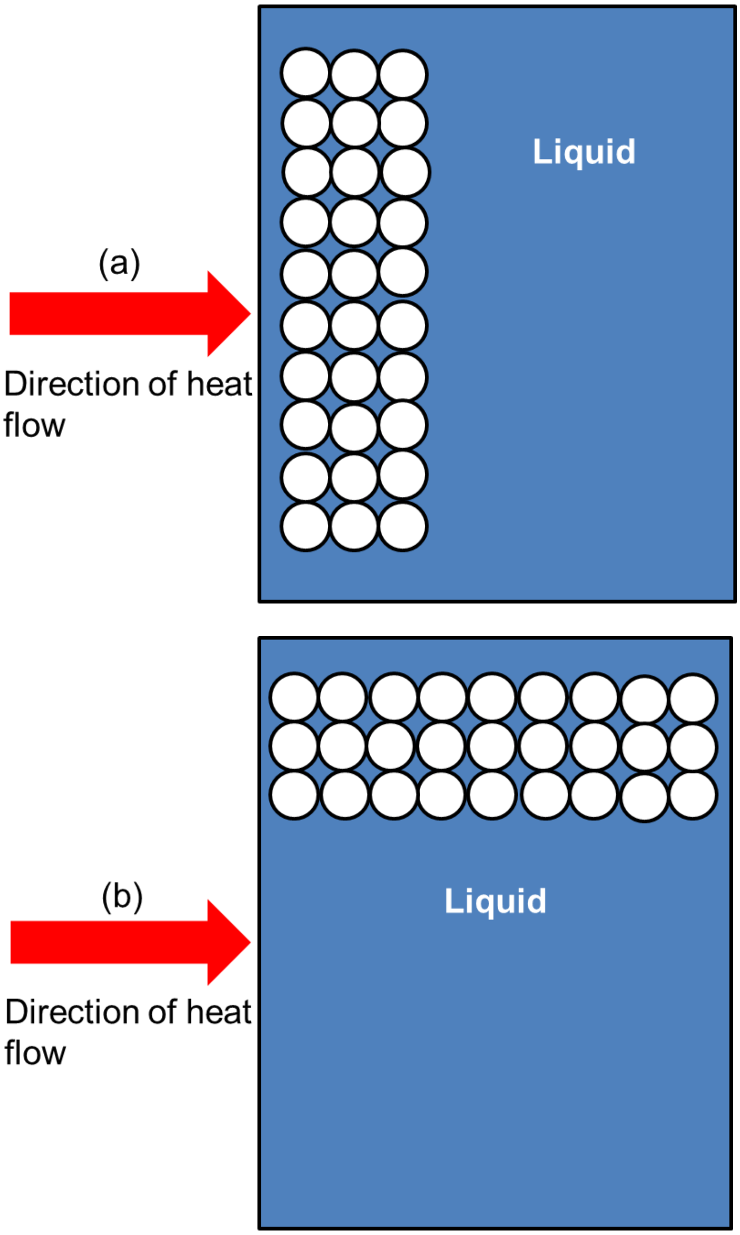

Figure 2.6 Series (a) and parallel (b) modes of conduction paths for nanofluids (Eapen et al., 2010)

From (Figure 2.6), for the series mode, the particle configuration is perpendicular to the direction of heat flow, while for the parallel mode, the particle configuration is in the same direction as heat flow. It is assumed that the parallel mode gives the best heat conduction path which leads to enhancement of thermal conductivity (Eapen et al., 2010) This is applicable to nanofluids, binary solid composites and liquid mixtures.

2.6.2 Hashin and Shtrikman (HS) bounds

The HS bounds set the most restrictive limits based on the idea of only volume fraction as a mean field approach for the prediction of possible mechanisms for thermal conductivity enhancement. The HS bounds for the thermal conductivity of a nanofluid can be given as (Eapen et al., 2010);

$$k_f = \left[1 + \frac{3\emptyset\left(k_p - k_f\right)}{3k_f + (1-\emptyset)\left(k_p - k_f\right)}\right] \leq k_{eff} \leq \left[1 - \frac{3(1-\emptyset)\left(k_p - k_f\right)}{3k_p - \emptyset\left(k_p - k_f\right)}\right] k_p \tag{2.24}$$

From Equation 2.24, the lower bound corresponds to the Maxwell model for well-dispersed nanoparticles in the nanofluid when $k_p > k_f$ while the upper bound corresponds to aggregated chain-like nanoparticles (Figure 2.7).

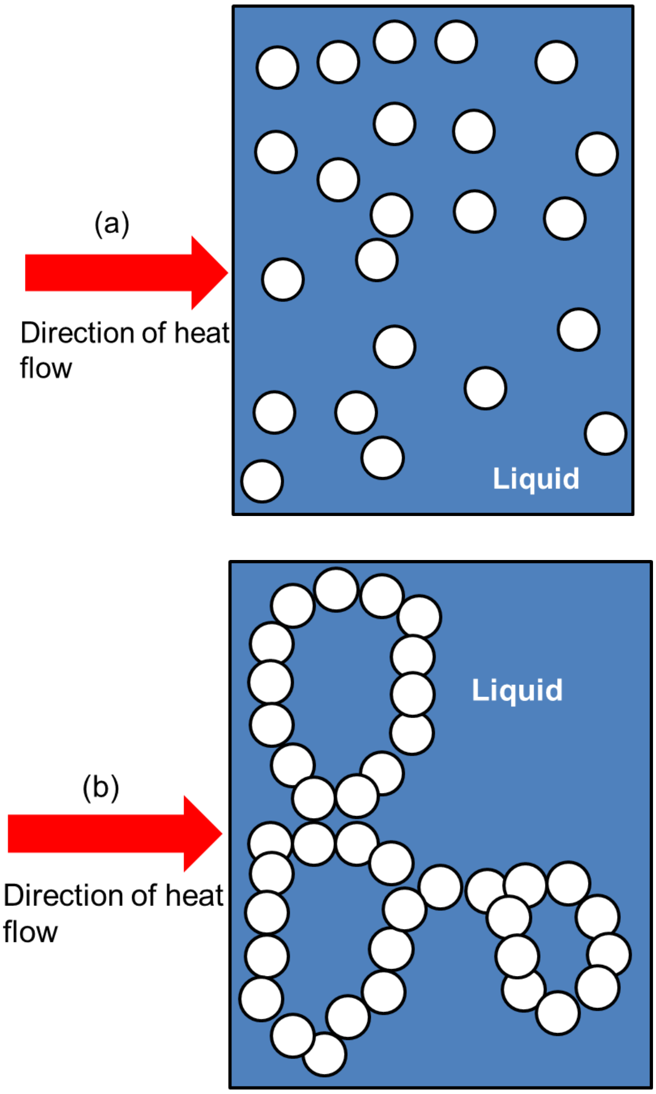

Figure 2.7 Nanofluid configuration for the (a) lower HS bound and (b) upper HS bound (Eapen et al., 2010)

The lower HS bound lies towards the series mode of thermal conduction (k_{eff}^{LHS}) while the upper HS bound lies towards the parallel mode of conduction (k_{eff}^{UHS}). In the case where the configuration neither lies towards the series nor parallel mode i.e. neutral, then the effective thermal conductivity (k^0) would be between the lower and upper HS bounds (Equation 2.25) (Eapen et al., 2010). Unlike the Maxwell model which is restricted only to well-dispersed nanoparticles in a nanofluid, the HS bounds incorporate a model both for well-dispersed and linear chain-like aggregated nanoparticles within the nanofluid system.

$$k_{eff}{}^{=} < k_{eff}^{LHS} < k^0 < k_{eff}^{UHS} < k_{eff}{}^{\parallel} \qquad (2.25)$$

Unlike well-dispersed nanofluid i.e. (for $k_p = k_f(1 + 3\emptyset)$ when $k_p/k_f > 1$), the effective thermal conductivity (k_{eff}) for aggregated nanofluids is a function of the nanoparticle thermal conductivity and more thermal conductivity enhancement is predicted when $k_p/k_f > 1$ (Eapen et al., 2010). In the case of models for aggregated nanoparticles in a nanofluid, higher thermal conductivity has been predicted compared to predictions by the Maxwell model. For this aggregation model, $k_{eff}/k_f = (\emptyset/3)\, k_p/k_f$ when $(\emptyset\, k_p/k_f) > 1$ which is similar to $(2\emptyset/3)\, k_p/k_f$ for the upper HS mode and $\emptyset\, k_p/k_f$ for the parallel mode. The aggregation model still possesses some disadvantages as it does not compare directly and completely to experimental results as regards enhancement of nanofluid thermal conductivity but conforms to numerical simulations for fractal clusters (Eapen et al., 2010).

With the above mentioned HS bounds, the thermal conduction of nanofluids and solid composites can be critically analysed theoretically. Predictions derived from the HS bounds for the particular nanofluid or solid composite analysed can be compared to their respective experimental result. This will show the adequacy and capability of the HS bounds and therefore the mean-field theories in explaining the reason behind the large thermal conductivity enhancement in nanofluids. Also this will show the similarity between solid composites and nanofluids in terms of increase in thermal conductivity.

2.6.3 Similarities with solid composites

2.6.3.1 HS bounds for solid composites

As aforementioned, the lower HS bound represents well-dispersed particles while the upper HS bound represents linear chain-like aggregated particles. These bounds will envelope the effective thermal conductivity derived from experiments which will aid in the theoretical analysis of thermal conductivity enhancement. For solid composites, most experimental results differ widely in terms of thermal conductivity (Eapen et al., 2010). The figures below represent effective thermal conductivity of some solid composites enveloped by HS bounds and experimental data (Boudenne et al., 2004, Agari and Uno, 1986, Every et al., 1992).

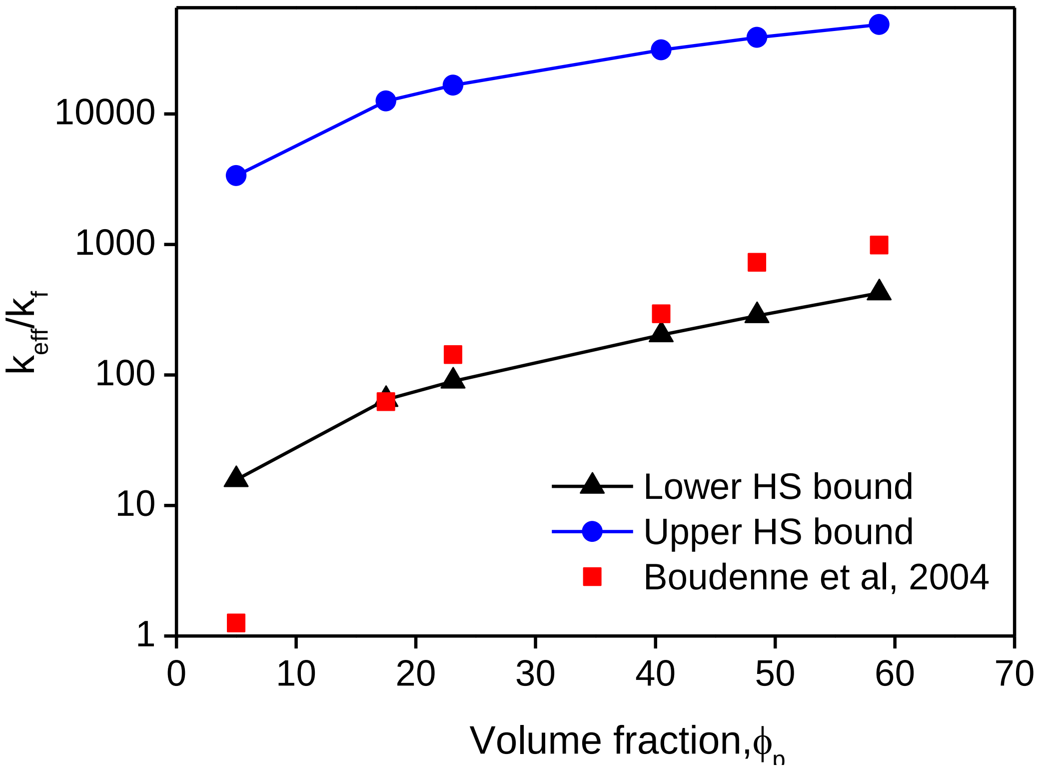

(a)

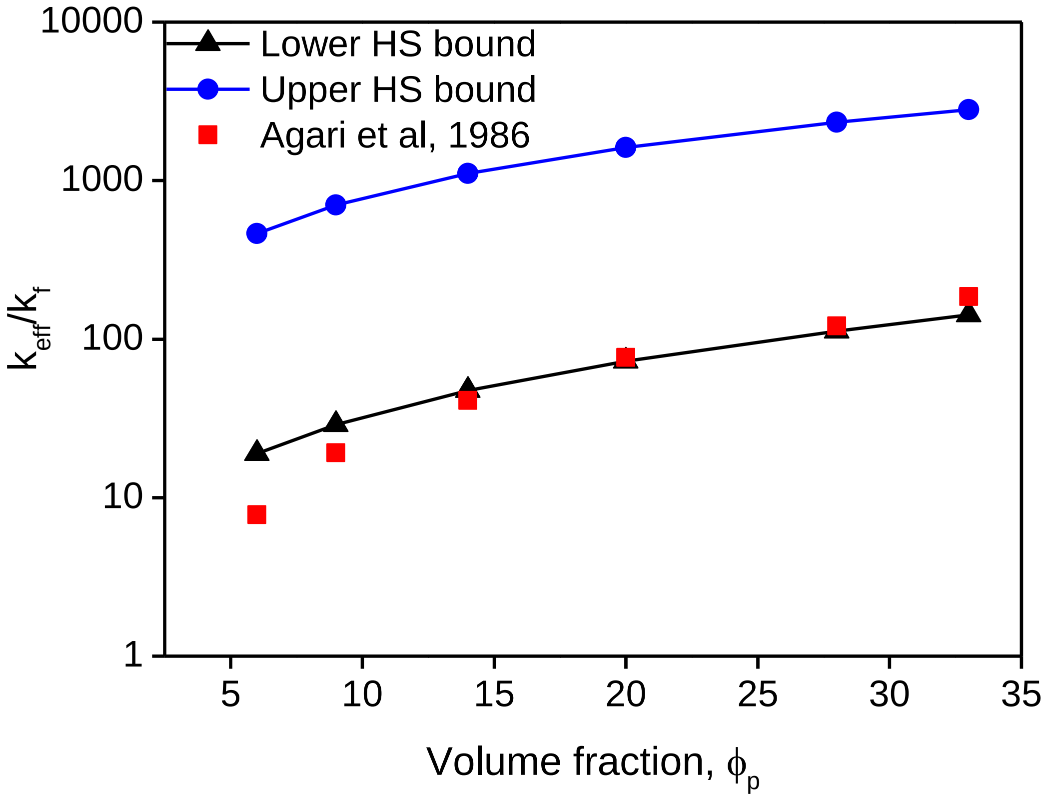

(b)

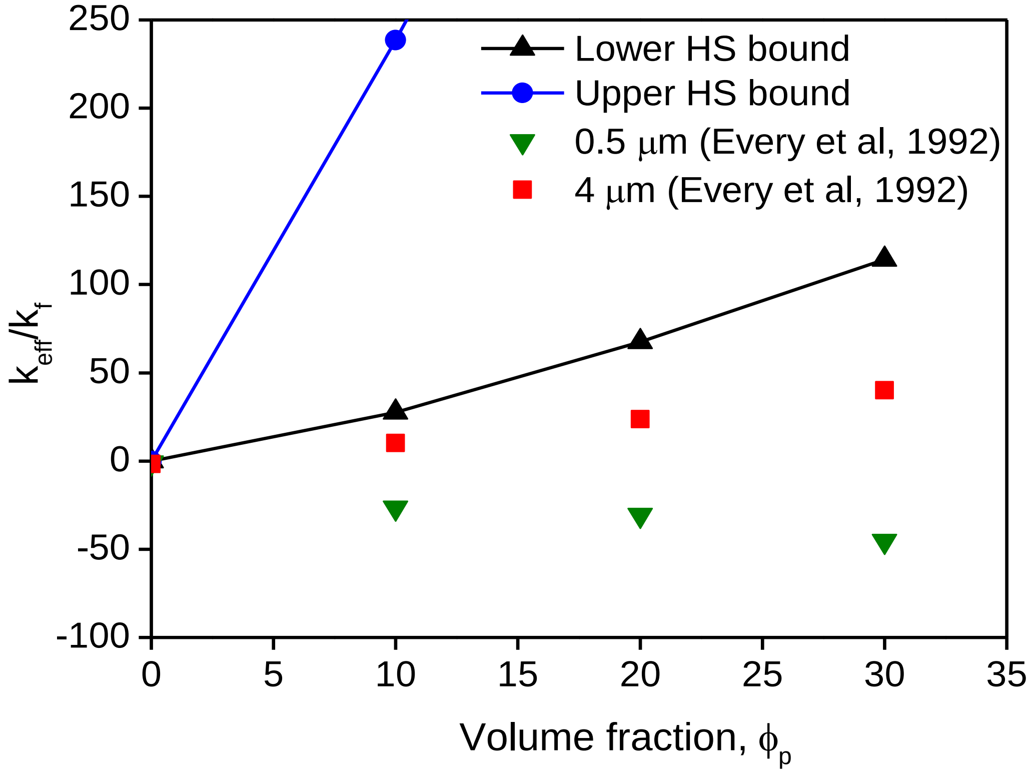

(c)

Figure 2.8 HS bounds for solid composites. Comparison with experimental data for; (a) Polypropylene – Al, (b) Polyethylene – Al_2O_3, and (c) ZnS – Diamond. (Eapen et al., 2010)

In Figure 2.8, thermal conductivity enhancement has been shown for different volume fractions of solid composites. For large volume fractions i.e.$\emptyset > 10\%$, the effective thermal conductivity represented by experimental data lies between the lower and the upper HS bound respectively. For volume fractions of $\emptyset \leq 10\%$, the thermal conductivity represented by experimental data falls below the HS bound. For ZnS - Diamond composites, it falls far below the lower HS bound and as the size of the particle increases the experimental thermal conductivity values increase. In this case, the thermal conductivity of 4 µm particle size is higher than that of 0.5 µm particle size, even though they are both still below the prediction of the lower HS bound which is similar to the Maxwell model. This agrees with the aforementioned analysis that for solid composites, particles of small sizes of about nanometer size will reduce the effective thermal conductivity even below the thermal conductivity of the base fluid in some cases. This is due to the effect of interfacial thermal resistance. The dimensionless interfacial thermal resistance is given by $\propto = 2R_b k_f / d$, which represents the temperature discontinuity at the interface of the particle filler (Eapen et al., 2010). When incorporated into the Maxwell model in the limit $k_p >> k_f$ (Eapen et al., 2010),

$$\frac{k_{eff}}{k_m} = \frac{(1 + 2\alpha) + 2\emptyset(1 - \alpha)}{(1 + 2\alpha) - \emptyset(1 - \alpha)} \tag{2.26}$$

where $k_m = k_f$ is the thermal conductivity of the base medium. From Equation 2.6, for smaller particle diameter d, interfacial thermal resistance α increases and therefore the effective thermal conductivity reduces. This agrees with the experimental data for ZnS – Diamond composites (Figure 2.8c) as the effective thermal conductivity is reduced even below the base fluid thermal conductivity for a 0.5 µm particle size.

2.6.3.2 HS bound for nanofluids

As like in the case of solid composites, the HS bounds can be estimated using theoretical data which will be compared to experimental data (Eastman et al., 1997, Das et al., 2003, Lee et al., 1999, Murshed et al., 2005, Zhang et al., 2006) for effective thermal conductivity of nanofluids. Plots of HS bounds for nanofluids compared with experimental data are shown in Figure 2.9.

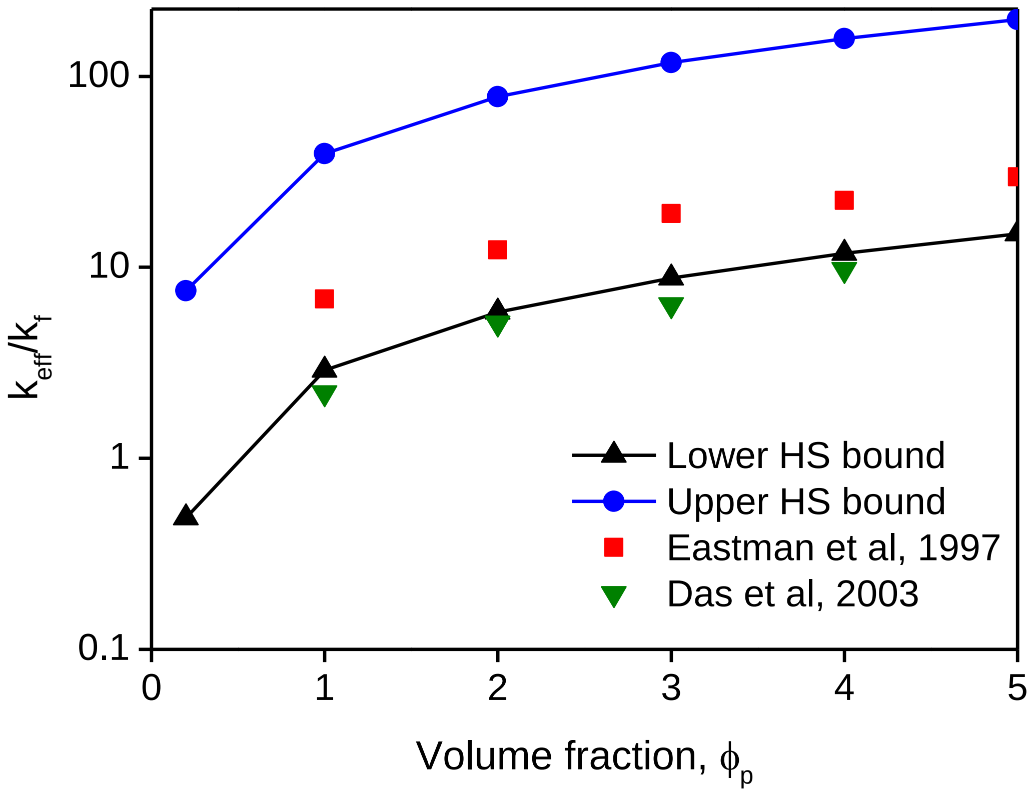
k_eff/k_f
100
10
1
0.1
0
1
2
3
4
5
Volume fraction, φ_p
Lower HS bound
Upper HS bound
Eastman et al, 1997
Das et al, 2003

(a)

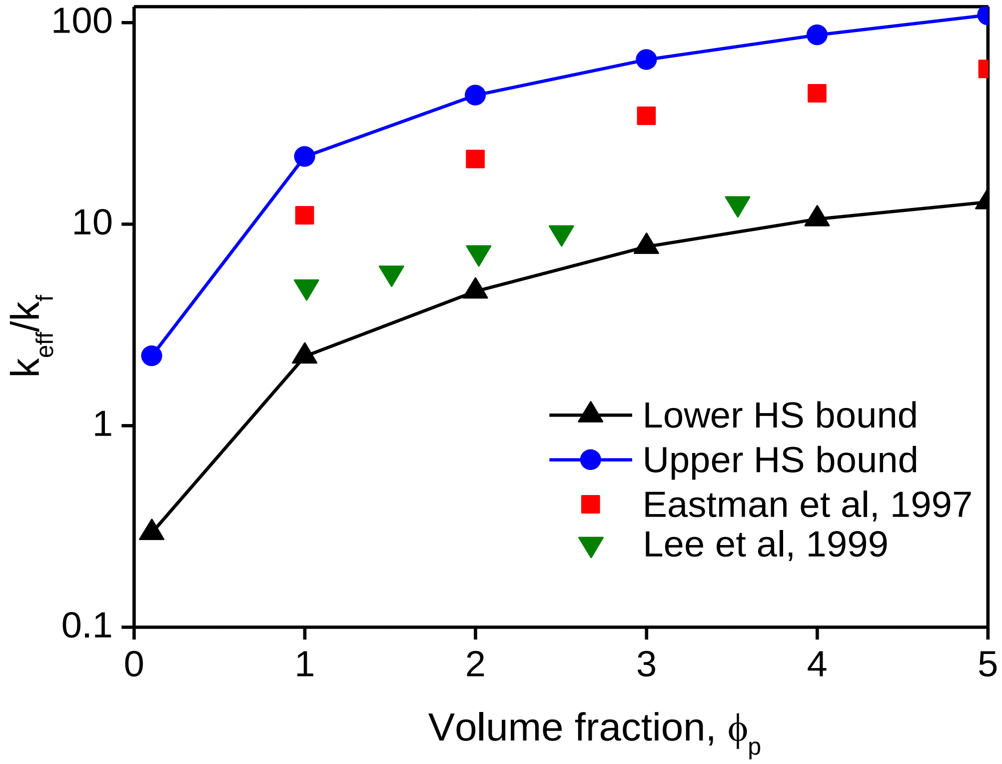
k_eff/k_f
100
10
1
0.1
0
1
2
3
4
5
Volume fraction, φ_p
Lower HS bound
Upper HS bound
Eastman et al, 1997
Lee et al, 1999

(b)

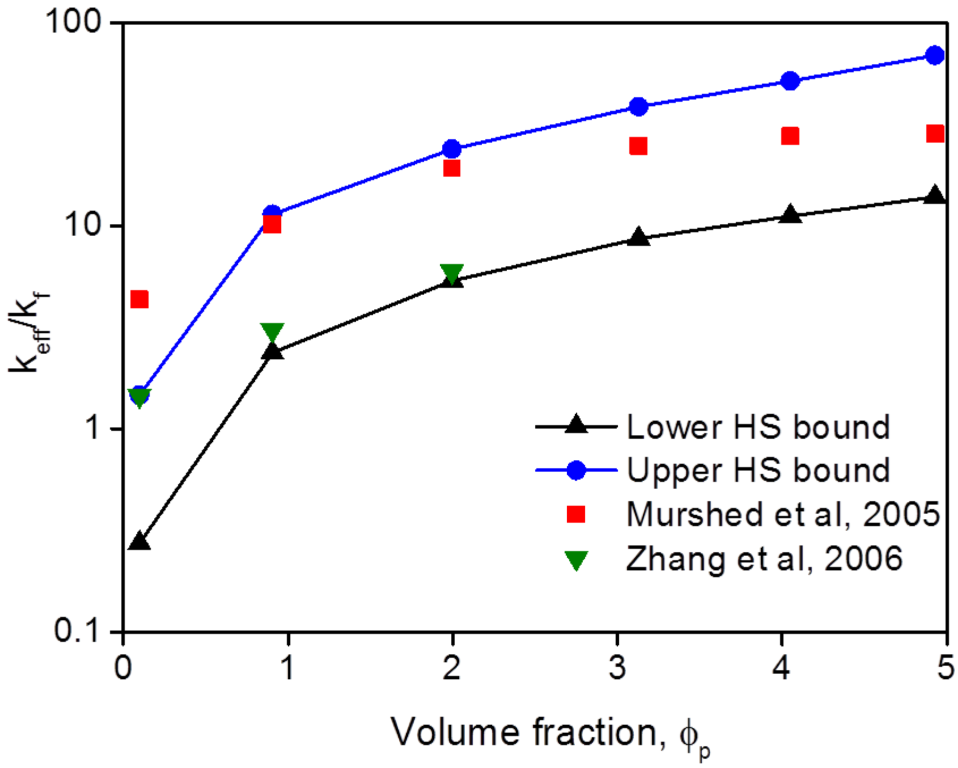

(c)

Figure 2.9 HS bounds for nanofluids. Comparison with experimental data for water based (a) Al_2O_3, (b) CuO and (c) TiO_2 nanofluid. (Eapen et al., 2010)

From Figure 2.9, since the experimental thermal conductivity data lies between the lower and upper HS bounds, the thermal conductivity behaviour of nanofluids can be compared to that of solid composites in terms of the mechanism behind thermal conductivity enhancement. It can be deduced that apart from a set of experimental thermal conductivity nanofluid data for water - Al_2O_3 which falls slightly below the lower HS bound for very low volume fractions, the other data lies comfortably between the upper and lower HS bounds. This is different for the case of solid composites where the experimental thermal conductivity data fell significantly below the lower HS bound. It can be seen that for nanofluids, the experimental effective thermal conductivity data shows better enhancement as compared to solid composites since it lies comfortably between the HS bounds almost close to the upper HS bound. Also, since the thermal conductivity enhancement for well-dispersed nanoparticles conforms with the lower HS bound or Maxwell theory and almost all the experimental thermal conductivity data are bounded by the lower HS bound from the bottom, interfacial thermal resistance can be taken to be negligible for nanofluids which means that $R_b = 0$ for nanofluids (Eapen et al., 2010). This is unlike the case of solid composites where interfacial thermal resistance plays a role in reducing effective thermal conductivity for smaller particle sizes.

2.7 Computational background of the present numerical modelling approach

In nanofluid systems, aggregates are formed when suspended nanoparticles move in a random manner in which the evolving stochastic motion leads to aggregation of nanoparticles. The concept of fractal dimension has been used in the past to study the aggregation process of particles. Using this concept, it has been suggested that aggregate structures can be related to complex fractal structures (Wang et al., 2003). Preliminary investigations have been carried out in this research to study the influence of particle aggregation on the effective thermal conductivity of nanofluids using an aggregation model which takes into account the concept of the fractal dimension including other parameters such as interfacial thermal resistance and particle volume fraction.

2.7.1 The concept of Fractal theory

The Fractal theory which was initially proposed by a French mathematician, Mandelbrot, can be used to describe the general mode of nanoparticle clustering and polarization within the of mesoscale range (Evans et al., 2008, Wang et al., 2003). In simple terms, the fractal dimension d_f can be taken as the measure of structures or fractals in their decomposed self-similar state (Figure 2.10). It reveals the collective but complex nature of self-similar and individual pieces of irregular curves or shapes as they repeat themselves to fill up space and form a single structure. Fractal profiles have the following characteristics; (i) they possess features that are repeated over multiple scales, (ii) they are continuous but may not be possible to differentiate, (iii) its features repeat in a self-similar manner with respect to scale over some range of scales, (iv) they may possess jagged or irregular curves (Leach, 2010). Most profiles are most easily measured due to their geometric nature, by fractal geometry rather than Euclidian geometry. The geometric properties of fractal structures such as profile length, surface area, inclination of the surface, and peak and valley radii, usually change with scale.

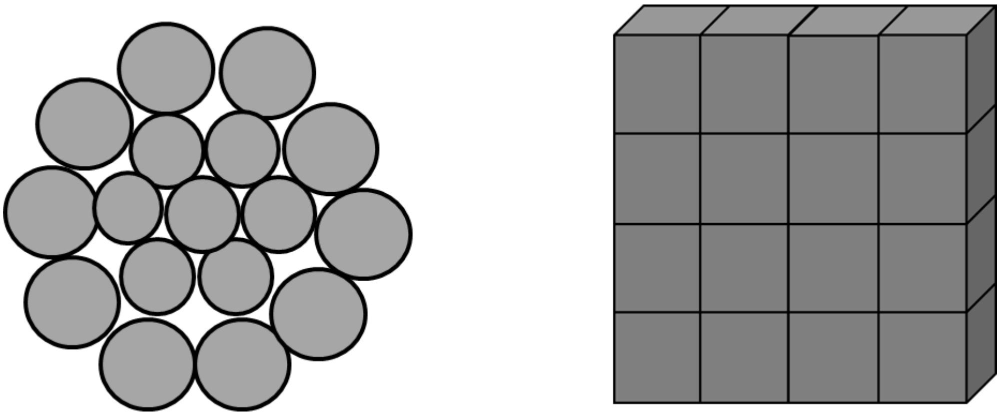

Figure 2.10 Small pieces of self-similar fractals to form two distinct structures

Fractal methods can be related to functional models of interactions with surfaces. They usually make use of information about the height and spacing of the surface. Fractals are characterised by a parameter (usually fractional, or fractal dimension) which is a measure of the complexity of the surface or profile of the structure (Leach, 2010). Mathematically, the fractal dimension for a line will be equal to or greater than 1 and less than 2, while that for a surface will be equal to or greater than 2 and less than 3. Fractal dimension can be insensitive to scaling during mathematical construction (Kirkby, 1979). However in engineering, surfaces are usually smooth when viewed at a significantly large scale, making the fractal dimension become sensitive to scaling. Fractal analysis can be implemented on engineering profiles and surfaces using two main approaches. One approach is to define a scaling exponent for the profiles that varies with scale (Shepard et al., 1995). The concept of this approach is known as self-affine topography. The other approach involves splitting the scales into regions. This approach can be used in situations where surfaces are rough at fine scales, and smooth at larger scales, in which case a boundary of smooth-rough crossover is defined between the rough and smooth surface (where the rough surface is described by fractal geometry and smooth surface, by Euclidean geometry) (Leach, 2010). The fractal dimension can be used to characterise the roughness of the rough region.

Theoretically, there are two methods usually used in measuring fractal dimension: linear fractal, and areal fractal analysis methods (Leach, 2010). Based on the linear fractal method, the fractal dimension and the length-scale fractal complexity are obtained from the slope of a log-log plot of relative lengths against scale (Brown and Savary, 1991). The relative length can give an indication of the amount of the surface that is available for interaction (Leach, 2010). There are two methods used in carrying out areal fractal analysis which are; the volume scale and area-scale methods. The volume-scale analysis which is also known as the variation method, gives an estimation of the volume between morphological opening and closing envelopes about a surface (Leach, 2010). Nominally square, structuring elements (with varied size) are used to estimate the volume. The lengths of the sides of the square structuring elements are used to plot the logarithm of the volume against the scale of the elements. This means that the both the scale and volume increase proportionally. Consequently, the fractal dimension is the slope of the plot, *d*, plus 2. Furthermore, the area-scale analysis is used to estimate the area of a rough surface as a function of scale. This uses repeated virtual tiling routines of the measured surface with triangles having an area representing the scale of the analysis. Area-scale analysis has a physical meaning for a wide range of applications. Most interactions with surfaces are associated with the area available to interact and with the surface inclinations (Leach, 2010).

2.7.2 Relationship between Fractal and Chemical dimensions

As fractal dimension d_f describes how a cluster mass scales with the cluster radius, chemical dimension d_l describes how the cluster mass scales within a chemical distance *l*. The chemical distance is the length of the shortest path on the fractal connecting two sites (Hong et al., 1985) and therefore the chemical dimension can be taken as the minimum cluster path between two points (Figure 2.11) (Margolina, 1985). Chemical dimension aids in better characterization of a cluster since the shortest possible path is considered.

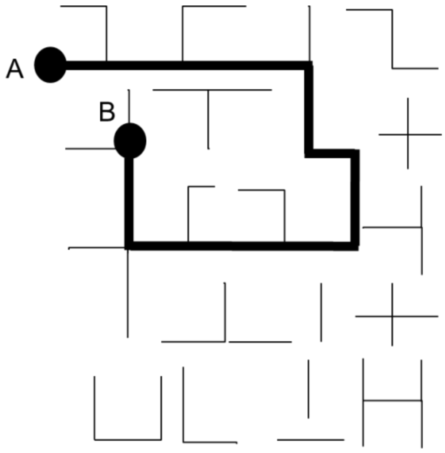

Figure 2.11 Shortest possible path between two points illustrating Chemical dimension

The chemical dimension can be related to the fractal dimension by incorporating d_{min} (i.e. fractal dimension of the minimum path) to get $d_l = d_f / d_{min}$, where d_f and d_l are fractal and chemical dimensions respectively. Previous study by (Hunter,

2001) shows that d_f ranges between 1.75 and 2.5. ((Hunter, 2001, Waite et al., 2001)) also carried out a detailed study on aggregated alumina nanoparticle suspensions and found the fractal dimension to range from 1.8 to 2.3. (Prasher et al., 2006c, Prasher et al., 2005) indicate that a fractal dimension of 2.5 signifies reaction-limited aggregation (RLA) and is a strong repulsive barrier while that of 1.8 signifies diffusion-limited cluster-cluster aggregation (DLCCA) and is a weak repulsive barrier. (Wang et al., 2003, Meakin, 1983, Meakin, 1987) suggest that aggregation in nanofluids has fractal dimensions close to 1.8 and therefore is DLCCA. Following these findings, studies in other literature such as (Prasher et al., 2006c) and (Evans et al., 2008) are based on a fractal dimension of 1.8. The same applies to the chemical dimension in which a value of 1.4 is fixed for studies conducted by (Evans et al., 2008).

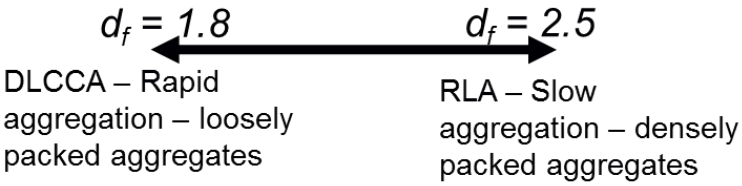

Figure 2.12 DLCCA and RLA limits for fractal dimension

2.7.3 The aggregation model

The aggregation model proposed is based on the simulation model of Prasher's work (Prasher et al., 2006c, Evans et al., 2008) which derives its understanding from the fractal morphology of nanoparticle clusters in colloids. Pitchumani and Yao have used this theory to determine the effective thermal conductivity for fibrous composites in single directions (unidirection) (Pitchumani and Yao, 1991). Similar work was done by Yu et al, who used the fractal theory including the conventional effective medium theory to determine the fractal characteristics of the effective dielectric coefficient of composite materials (Evans et al., 2008). Fractal theory has nevertheless not yet been employed to describe the influence of cluster morphology/particle aggregation of nanofluids on the effective thermal conductivity. The fractal dimension d_f, plays a major role in fractal description (Evans et al., 2008). In treating the particle scale/aggregation effect, it is assumed that the particular nanofluid consists of the base fluid and the resulting aggregates/cluster.

Figure 2.13 illustrates a possible application of fractal theory in ascertaining the clustering effect on the effective thermal conductivity of a nanoparticle suspension. A fractal cluster, which is composed of linear and side chains, is placed within a sphere of radius equal to the radius of gyration, R_g, (Figure 2.13) of the cluster (Kolb et al., 1983). The linear chains (chains of contacting primary particles giving a contiguous pathway across the sphere) which span the entire cluster are also referred to as backbones as they are mostly responsible for cluster-cluster transfer of elastic forces necessary for holding the clusters together (Evans et al., 2008). As the clusters are in patterns of percolation due to their connectivity, backbones for will be instrumental to thermal conductivity enhancement. The other particles, which do not span the entire cluster, are known as weak ends. They do not necessarily contribute much to the structure and therefore thermal conductivity of the system (Evans et al., 2008).

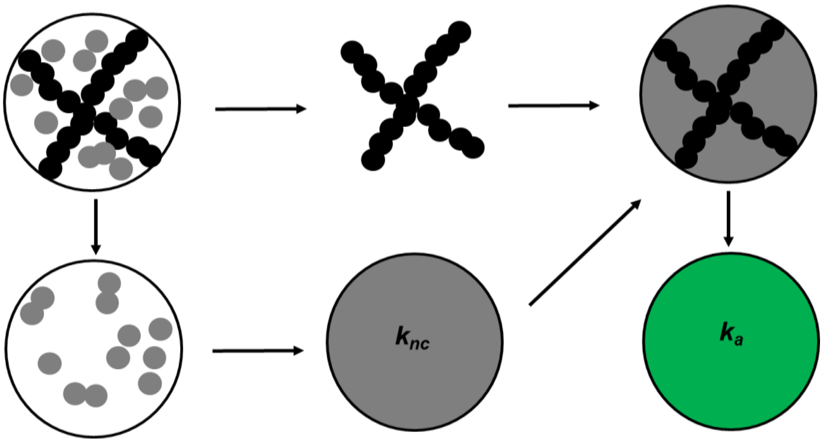

Figure 2.13 Schematic diagram of a single aggregate comprising the backbone (black particles) and weak ends (grey particles). The aggregate is decomposed into weak ends with the base fluid and the backbone. Thermal conductivity of the aggregate with only particles belonging to the weak ends is k_{nc}, with the linear chains embedded inside a medium with effective conductivity of k_{nc}. (Evans et al., 2008).

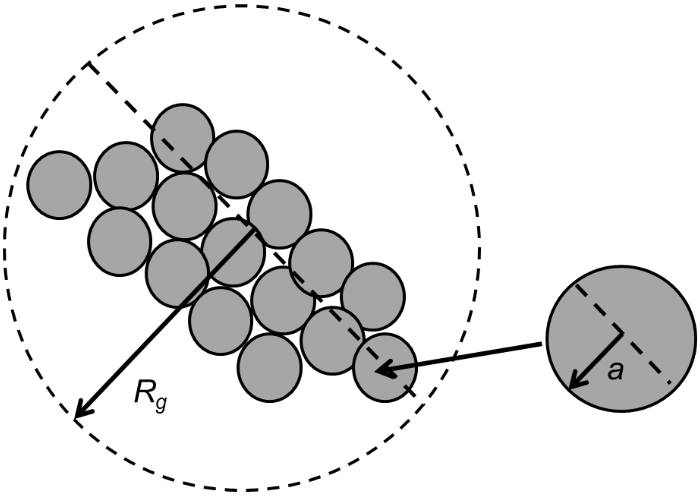

Figure 2.14 An aggregate (within the sphere) characterised by the radius of gyration ($\boldsymbol{R_g}$) and an individual particle characterised by its own radius.

Going further, the number of nanoparticles which are contained in the cluster is given as $N_{int} = (R_g/a)^{df}$ where a is the radius of the individual nanoparticle and R_g the size of the sphere (or radius of gyration) which describes the aggregate is larger than the radius of an individual nanoparticle (Evans et al., 2008, Prasher et al., 2006c). In this case where $\emptyset_p$ is the volume fraction of the individual nanoparticle, $\emptyset_{\text{int}}$ the volume fraction of the particles in the cluster or aggregates, and $\emptyset_a$ the volume fraction of the aggregates in the whole base fluid, then $\emptyset_p = \emptyset_{int}\emptyset_a$ (Prasher et al., 2006c). The relationship between $\emptyset_p$, $\emptyset_{int}$ and $\emptyset_a$, if $\emptyset_{int} = 1$, is for a well dispersed system since only one particle exists in each aggregate and therefore $\emptyset_a = \emptyset_p$. On the other hand if $\emptyset_a = 1$, then this is for a fully aggregated system and therefore $\emptyset_{int} = \emptyset_p$ (Prasher et al., 2006c). This relationship shows that the thermal conductivity will reach its peak between the limit for $\emptyset_{int} = 1$ and $\emptyset_a = 1$ (Prasher et al., 2006c).

Further analysis shows that $\emptyset_{int} = (R_g/a)^{df-3}$, and $(R_g/a)_{max} = (\emptyset_p)^{1/(d_f-3)}$ for the case of $\emptyset_a = 1$ (Evans et al., 2008). Also, the number of nanoparticles which are contained in the backbone N_c, is defined by the chemical dimension, d_l, and is given by, $N_c = (R_g/a)^{d_l}$, in which case d_l ranges between one and d_f (Evans et al., 2008). And so in the case where all particles are contained in the backbone without the presence of weak ends, $d_l = d_f$ (Evans et al., 2008). Judging by this, the volume fraction of the particles ($\emptyset_c$) which are contained in the backbone in the aggregates is given as $\emptyset_c = (R_g/a)^{d_l-3}$. Also, the volume fraction of the particles which are contained in weak ends, $\emptyset_{nc}$, is given as $\emptyset_{nc} = \emptyset_{int} - \emptyset_c$ (Evans et al., 2008).

Based on the above analysis, the model is developed initially only for the particles which are contained in the weak ends (Figure 2.10). Since in most cases, high volume fractions of highly conductive particles are involved, the Bruggeman model is used to estimate the thermal conductivity of the aggregate as a result of the particles which are contained in the weak end, and is given by, (Evans et al., 2008);

$$(1-\emptyset_{nc})(k_f-k_{nc})\Big/(k_f+2k_{nc}) + \emptyset_{nc}(k_p-k_{nc})\Big/(k_f+2k_{nc}) = 0 \qquad (2.27)$$

Where k_{nc} is the effective thermal conductivity of the aggregate sphere due to only the weak ends.

The effective thermal conductivity of the entire aggregate constituting the particles for both the weak ends and the backbone is estimated based on the assumption that the backbone is contained in a medium with an effective thermal conductivity of k_{nc} (Evans et al., 2008). Since the system contains aggregates and not completely dispersed particles (i.e. the aspect ratio of the chains is far larger than one), the model proposed by Nan et al for randomly cylindrical particles can be used (Evans et al., 2008). Following this model, the effective thermal conductivity of the aggregate sphere, k_a, consisting of both the backbone chains and the weak ends is given as, (Evans et al., 2008);

$$k_a = k_{nc}\frac{3+\emptyset_c[2\beta_{11}(1-L_{11})+\beta_{11}(1-L_{33})]}{3-\emptyset_c[2\beta_{11}L_{11}+\beta_{33}L_{33}]} \tag{2.28}$$

Where

$$L_{11} = \frac{0.5p^2}{(p^2-1)} - \frac{0.5p\cosh^{-1}p}{(p^2-1)^{1.5}} \tag{2.29}$$

$$L_{33} = 1-2L_{11} \tag{2.30}$$

$$\beta_{ii} = (k_{ii}^c - k_{nc})/[k_{nc}+L_{ii}(k_{ii}^c - k_{nc})]\,; \quad i = 1,3 \tag{2.31}$$

Where p is the aspect ratio which signifies clustering of particles in the aggregated state (i.e. cluster spanning chain) and is given as $p = R_g/a$, in which case the average is weighted by the number of particles in each aggregate. The interfacial resistance has been incorporated into this model and is accounted for in the term given by, (Evans et al., 2008);

$$k_{ii}^c = {k_p}\Big/{(1.0+\gamma L_{ii}\,k_p/k_f)} \tag{2.32}$$

Where $\gamma = (2+1/p)\alpha$

The effective thermal conductivity of the entire system is estimated using the Maxwell-Garnet (M-G) model which takes into consideration volume fraction and the thermal conductivity of the aggregates and is given as, (Evans et al., 2008);

$$k_{eff}\Big/k_f = \left([k_a+2k_f)]+2\emptyset_a[k_a-k_f]\right)\Big/\left([k_a+2k_f)]-\emptyset_a[k_a-k_f]\right) \tag{2.33}$$

As this model harnesses the knowledge of fractal morphology to aid in the study of cluster morphology in terms of aggregation, the incorporation of R_g/a into the above model will form a basis for the investigation of the influence of particle aggregation on the thermal conductivity of the nanofluid. By adjusting the value of R_g/a, a clearer view of its effect on effective thermal conductivity can be easily observed. Also, with the incorporation of the interfacial thermal resistance in the model, its influence on effective thermal conductivity will be analysed. By so doing, a sensitivity analysis on the influence of parameters such as R_g/a, $\emptyset_{\mathrm{p}}$ and α , will be carried out which will produce beneficial results linked to particle aggregation and effective thermal conductivity.

2.8 Conclusion

Nanofluids are undoubtedly required in most industries as research has shown that they possess tremendous thermal enhancement compared to conventional heat transfer fluids. The presence of metallic oxide nanoparticles in the base fluids has been shown to contribute to the observed thermal enhancement. Conventional models such as Maxwell, Hamilton-Crosser and Bruggeman have also been used to predict the effective thermal conductivity of nanofluids. These models (some of which are for spherical or non-spherical particles), are usually based on the assumption that the particles within the fluid are well dispersed. Possible mechanisms behind the observed thermal enhancement in nanofluids have been suggested by researchers, and include Brownian motion, interfacial layering, ballistic transport and particle aggregation. Particle aggregation or clustering has been widely speculated as a major mechanism behind thermal enhancement. Indications show that since individual and primary nanoparticles have a particular thermal conductivity that can induce an overall thermal enhancement in the nanofluid, an aggregate of these nanoparticles together (thereby contributing their individual thermal conductivities) will induce enhanced thermal conductivity. The thermal enhancement induced by aggregated nanoparticles can be taken as the effective thermal conductivity as this thermal property is more than that of the base fluid or fluid suspension with well-dispersed nanoparticles. It has also been suggested that the resultant effective volume of loosely packed clusters formed following particle aggregation will aid in easy heat transfer across the fluid. Furthermore, the meanfield bounds have been associated with particle aggregation. Investigations on H-S bounds (in which lower and upper bounds represent well-dispersed and aggregated chain-like nanoparticles respectively) reveal that experimental data from the literature were validated and were comfortably bounded within the field of the H-S bounds (i.e. for the case of nanofluids). In fact, for the water based nanofluid with CuO, by the experimental data close to the upper bound which shows that particle aggregation is influential in thermal enhancement. Also, the numerical model discussed above is based on the simulation model of Prasher's work which derives its concept from the fractal morphology of nanoparticle clusters in colloids. The model has been developed based on the fractal theory which takes into account the influence of particle clustering on effective thermal conductivity of nanofluids. Incorporation of parameters such as the aspect ratio and interfacial thermal resistance into the model will aid in the analysis of the influence of particle aggregation/clustering on effective thermal conductivity of nanofluids. The next chapter will present the results from preliminary investigations on the effective thermal conductivity of three model nanofluids systems using the aggregation model discussed in Section 2.7.3.

Chapter 3

Predictions of Effective Thermal Conductivity of Nanofluids using Numerical Modelling

3 Predictions of Effective Thermal Conductivity of Nanofluids using Numerical Modelling

3.1 Introduction

This chapter provides results obtained from the numerical modelling for predicting effective thermal conductivity of nanofluids, using the aggregation model discussed in Section 2.7.3 of Chapter 2. Here, preliminary investigations have been carried out on three model based nanofluid systems namely; CuO, Al_2O_3 and TiO_2. The model is seen to take into account factors such as fractal and chemical dimensions, aspect ratio (*Rg/*a) which captures aggregate size, particle volume fraction and interfacial thermal resistance. Results regarding each of these individual factors and their influence on thermal enhancement of nanofluids, are presented and discussed in detail, in this chapter.

3.2 Summary of nanofluid model system specification and parameters used in the thermal conductivity investigation

A summary of the parameters used in carrying out investigations on thermal conductivity enhancement in this study, are present in Table 3.1. From the table, the type of investigation refers to the parameters whose effects on thermal conductivity enhancement of the nanofluids have been investigated. The parameter description outlines the parameters (fixed and variable) used to carry out the types of investigations.

Table 3.1 System description outlining the type of investigation and parameters used in the present thermal conductivity investigation

Nanofluids	Type of Investigation	Parameter Description
Base fluid: Water **Nanoparticles:** CuO, Al_2O_3, TiO_2	Interfacial thermal resistance (α)	(1) α = 0.01, 0.1, 1, 5, 10 (2) Particle volume fraction ($\varnothing_p$) = 0.5 %, 4 % (3) Aspect ratio (Rg/a) = 2 – 70 (where 2 represents little aggregation)
	Particle volume fraction ($\varnothing_p$)	(1) Particle volume fraction ($\varnothing_p$) = 0.1 – 0.5 %, 1 – 4 % (2) Aspect ratio (Rg/a) = 2 – 70 (where 2 represents little aggregation) (3) α = 1 (fixed)
	Fractal dimension (d_f)	(1) Fractal dimension (d_f) = 1.75 – 2.5 (2) Particle volume fraction ($\varnothing_p$) = 1 – 4 % (3) α = 1 (fixed) (4) Chemical dimension (d_l) = 1.4 (fixed) (5) Aspect ratio (Rg/a) = 2, 5 - 8 (where 2 represents little aggregation)
	Chemical dimension (d_l)	(1) Chemical dimension (d_l) = 1.2 – 1.8 (2) Particle volume fraction ($\varnothing_p$) = 1 – 4 % (3) α = 1 (fixed) (4) Fractal dimension (d_f) = 1.8 (fixed) (5) Aspect ratio (Rg/a) = 2, 5 - 8 (where 2 represents little aggregation)

3.3 Effect of Interfacial thermal resistance (*α*)

As discussed in section 2.4.1 of Chapter 2, interfacial thermal resistance tends to pose a barrier to heat flow which might potentially help induce thermal conductivity. Here, the enhancement ratio (k_{eff}/k_f) was calculated for different cases of the average size of the nanoparticle cluster (in terms of *Rg/a*) for a range of interfacial thermal resistance (*α*) values; 0.01 ≤ *α* ≤ 10, for two typical cases of particle volume fractions, 0.5 % and 4 %. These are shown in Figure 3.1 below.

At 0.5 volume % concentration, the enhancement ratio is fairly independent of *Rg/a* as well as *α*. Moreover, as $Ø_p$ increases to 4 volume %, *α* ≥ 1 does not make a significant impact on the enhancement ratio and so results of *α* = 1 (i.e. the radius of the nanoparticles is the same as the Kapitza radius) is an average or median representation of this case of *α* (i.e. 0.01 ≤ *α* ≤ 10) being investigated. For the case of *α* = 1, the interfacial thermal resistance and therefore the Kapitza radius plays no major role in thermal enhancement of the contribution of the nanoparticles (Every et al., 1992). Overall, the enhancement ratio is seen to increase with reducing interfacial thermal resistance, irrespective of the aspect ratio or aggregate size.

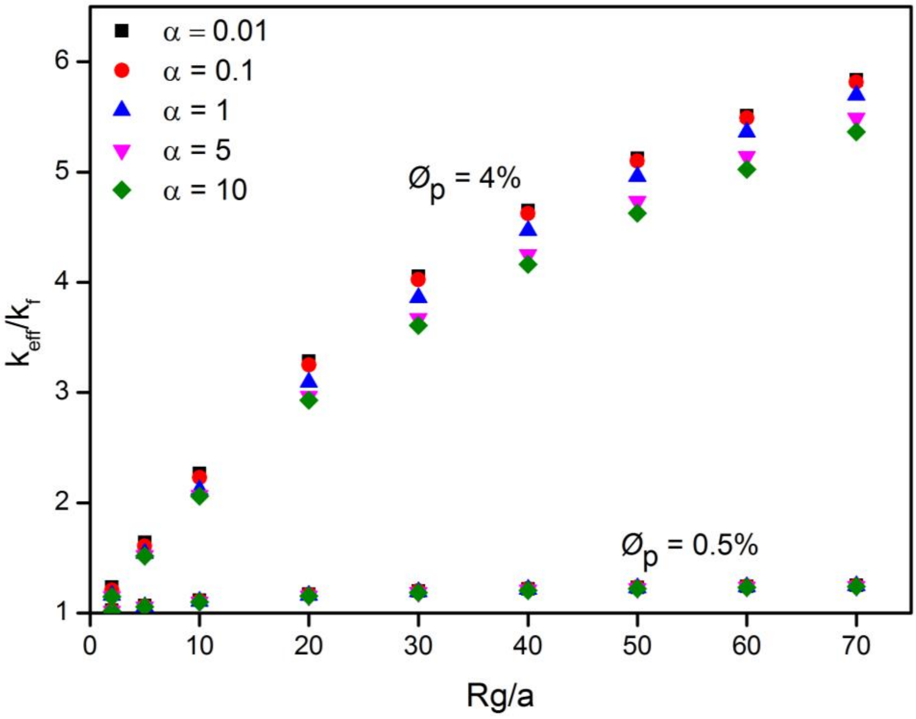

(a)

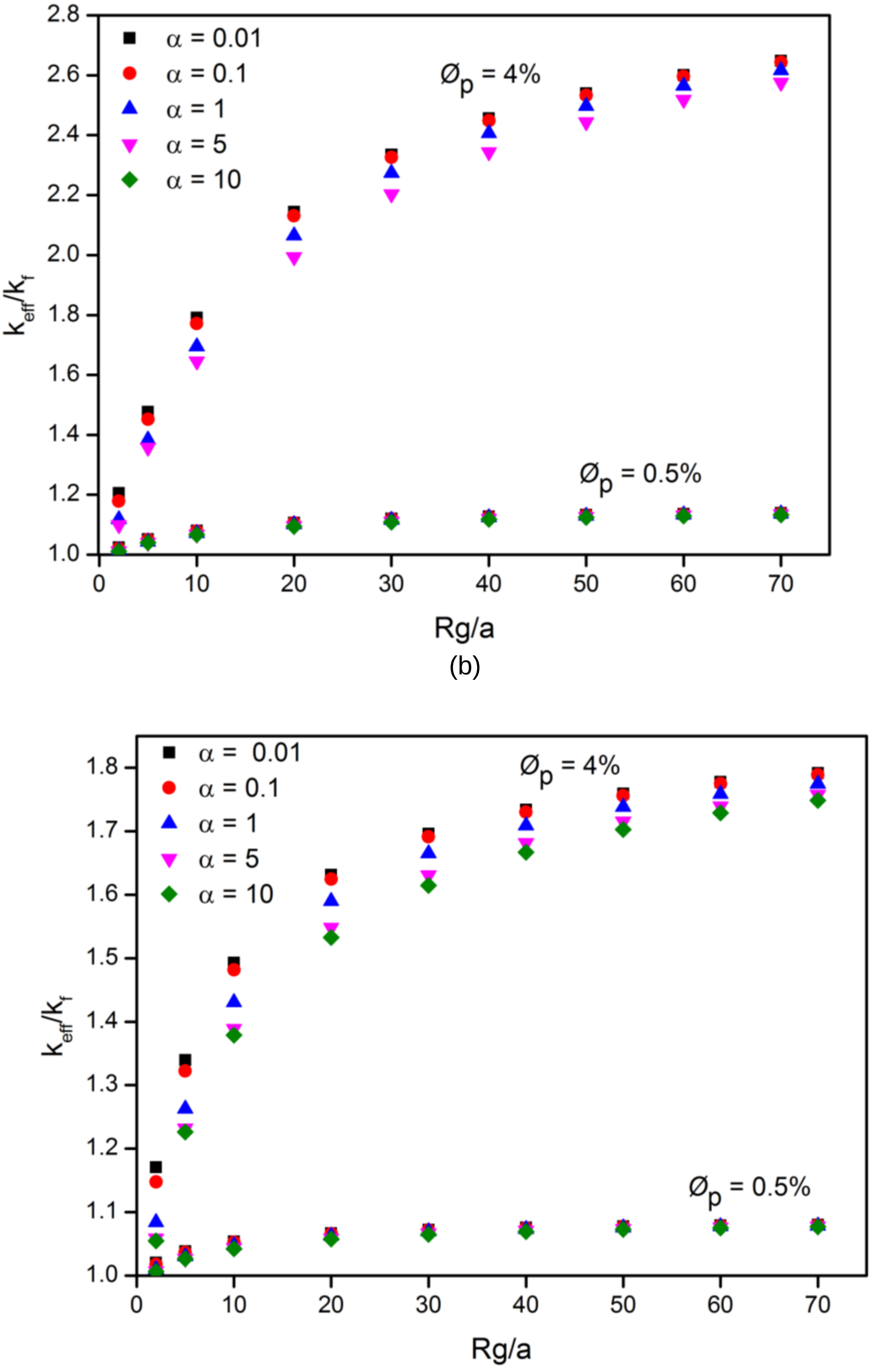

(b)

(c)

Figure 3.1 Dependence of enhancement ratio *(k_{eff} /k_f)* with aspect ratio and the interfacial resistance data for water-based (a) Alumina, (b) CuO and (c) Titania nanofluids. On each plot the bottom set of lines represent 0.5 volume %, the top set is for 4 volume % (Okeke et al., 2011)

A desirable nanofluid system is one which possesses very little or no interfacial thermal resistance to disrupt heat flow across the fluid system. (Evans et al., 2008) suggested that the interfacial thermal resistance poses more of a problem for small particles than large particles. This, they deduced from Equation 3.1 below, valid for effective medium theories which accounts for low volume fraction, and well dispersed nanoparticles.

$$\frac{k_{eff}}{k_f} - 1 = 3f\frac{a/a_k - 1}{a/a_k + 2} \tag{3.1}$$

Where a is the particle radius and a_k is the Kapitza radius. From Equation 3.1, the ratio of a/a_k is small for small particles. These observations are consistent for all the three types of nanofluids systems shown in Figure 3.1. Given this observation, the value for *α* was fixed to 1 in the following simulations.

3.4 Effect of Aspect ratio and Particle volume fraction

Presented in Figure 3.2 is the relationship between the enhancement ratio, aspect ratio and particle volume fraction. Note that *α* is set to 1.

The volume fractions used in Figure 3.2 were chosen to have an upper limit of 4%. In most practical applications, this is thought to be the limiting case, considering the clogging problem and pumping costs. It can be observed that for the three cases of nanofluid systems in Figure 3.2, a significant impact on the enhancement ratio begins when the volume % > 1. Moreover, there is a steep increase in enhancement ratio up to *Rg/a = 20*, after which the curves gradually flatten out. This can be seen to be the point of saturation at the level dependent on the volume fraction. The observed increase in enhancement ratio can be attributed to the fact that the size of the backbone (illustrated in section 2.7.3 of Chapter 2), increases to promote rapid conduction across the cluster (Evans et al., 2008). A maximum point (value) of enhancement ratio is reached which represents an interconnected network of nanoparticle clusters caused by the overlapping of the clusters. It is interesting to note that for stable nanofluids formulated from spherical primary particles, *Rg/a* is often less than 10 (He et al., 2007a, Wen and Ding, 2005).

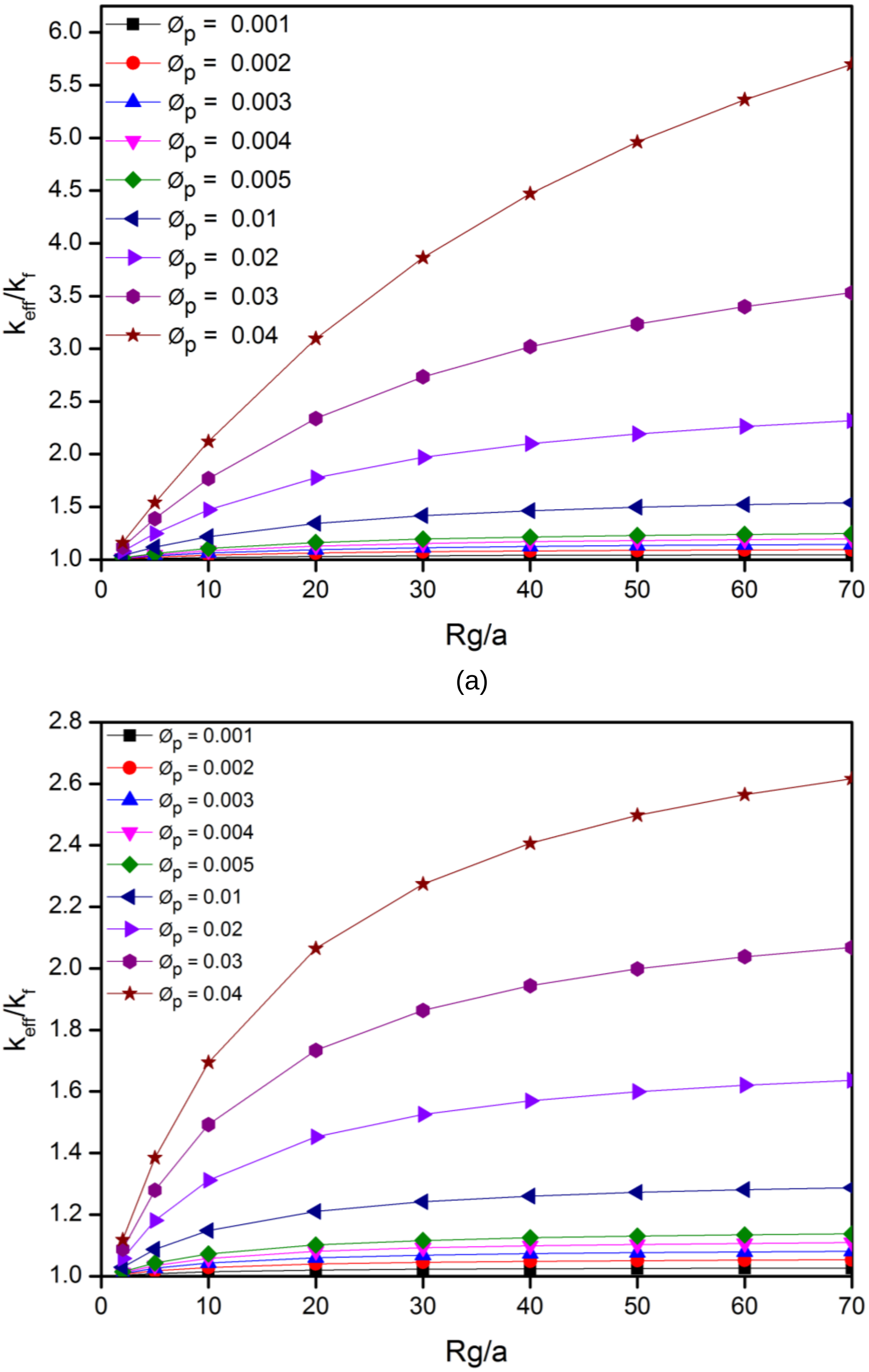
k_{eff}/k_f
Rg/a
$\varnothing_p$ = 0.001
$\varnothing_p$ = 0.002
$\varnothing_p$ = 0.003
$\varnothing_p$ = 0.004
$\varnothing_p$ = 0.005
$\varnothing_p$ = 0.01
$\varnothing_p$ = 0.02
$\varnothing_p$ = 0.03
$\varnothing_p$ = 0.04
1.0
1.5
2.0
2.5
3.0
3.5
4.0
4.5
5.0
5.5
6.0
1.2
1.4
1.6
1.8
2.2
2.4
2.6
2.8
0
10
20
30
40
50
60
70

(a)

(b)

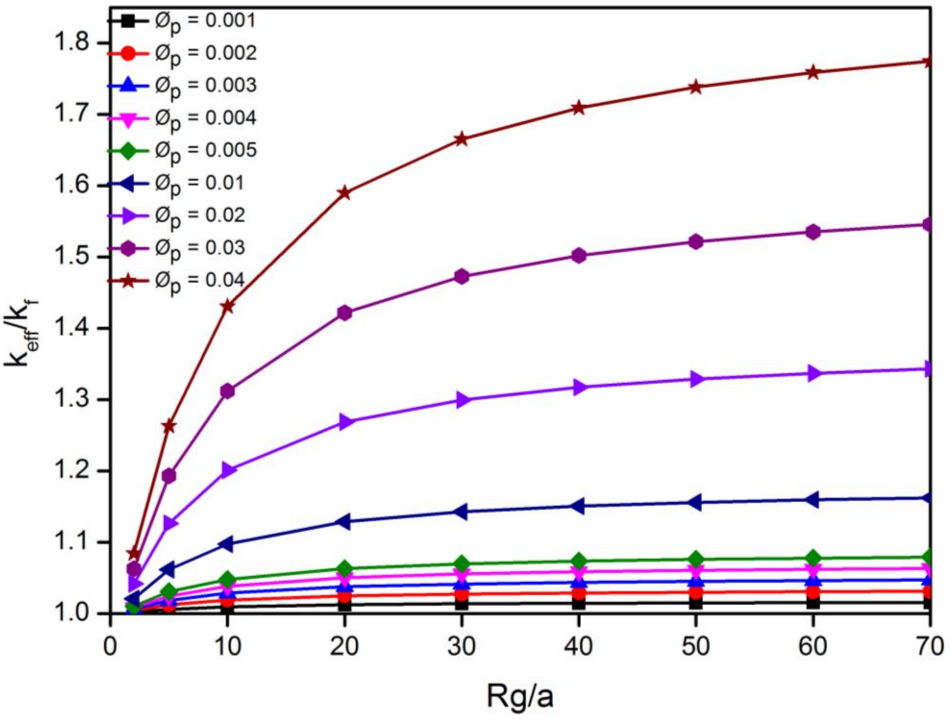

(c)

Figure 3.2 Effect of aspect ratio and particle volume fraction on the enhancement ratio for *α* = 1 for water-based (a) Alumina, (b) CuO and (c) Titania nanofluids (Okeke et al., 2011).

3.5 Effect of Fractal and Chemical dimensions

The effect of fractal and chemical dimension is been analysed for water based nanofluids of Alumina for each value of aspect ratio between 2 and 8. Based on previous observations, *α* which takes into account the interfacial thermal resistance is taken as 1. In the first instance from Figure 3.3 below, the plot of enhancement ratio against particle volume fraction for different fractal dimensions (I.e. ranging from about 1.8 to 2.5 and representing DLCCA for the lower limit and RLA for the upper limit of nanoparticles (Prasher et al., 2006b)) reveals an increase in thermal enhancement for reducing fractal dimension as particle volume fraction increases. (Wang et al., 2003) have shown that nanofluid aggregation is DLCCA since the fractal dimensions lie close to 1.8. In the case of DLCCA, the aggregation process is known to be rapid thereby leading to loosely packed aggregates while for RLA, the aggregation process is slower leading to the formation of densely packed aggregates (Waite et al., 2001).

Also considering the effect of chemical dimension, plots of enhancement ratio against particle volume fraction for different chemical dimension are shown below in Figure 3.4. .

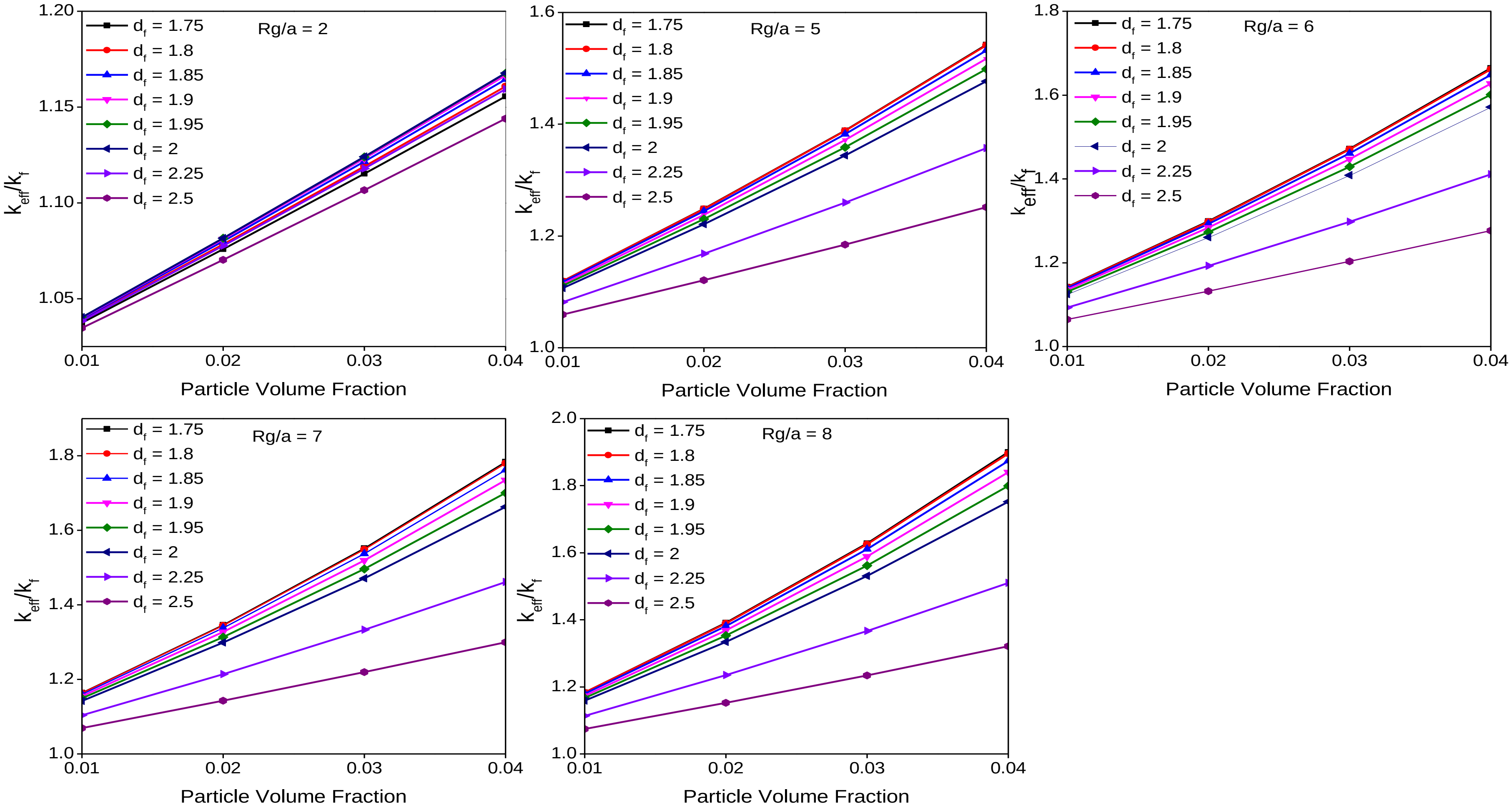

Figure 3.3 Effect of fractal dimension (d_f) (Erdin et al.) on enhancement ratio (k_{eff} / k_f) for water based Alumina nanofluid for d_l = 1.4 and α = 1 (Okeke et al., 2011).

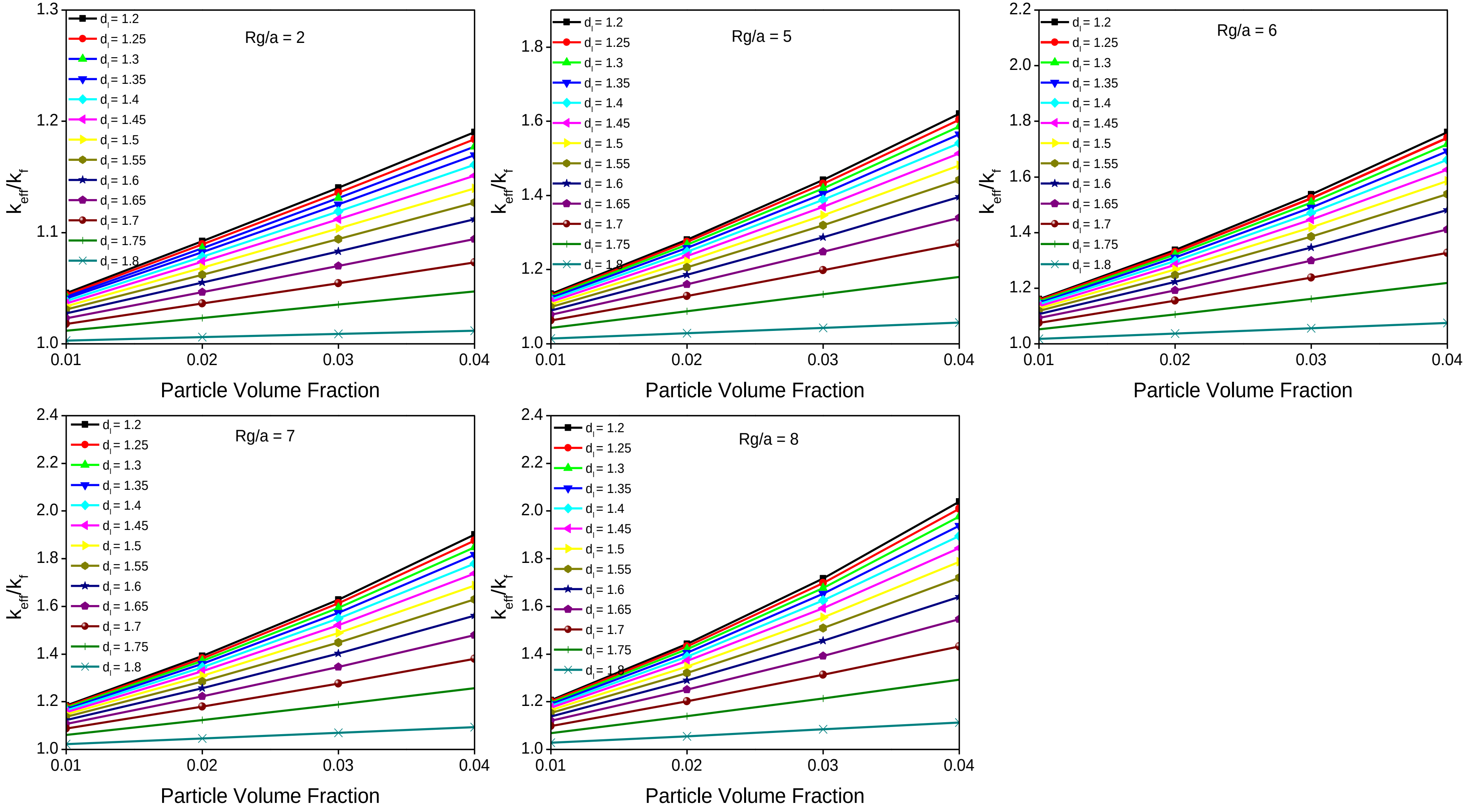

Figure 3.4 Effect of chemical dimension (d_l) on enhancement ratio (k_{eff} / k_f) for water based Alumina nanofluid for d_f = 1.8 and α = 1 (Okeke et al., 2011)

Following suit, as in the case of fractal dimension, an increase in thermal enhancement for reducing chemical dimension and increasing particle volume fraction is observed. With a wide range of values of chemical dimension plotted, enhancement also increases as the aspect ratio increases while chemical dimension still reduces. Similar to the analysed case of fractal dimension, high sensitivity to chemical dimension for lower values is observed (i.e. between 1.2 and 1.5) while higher values are less sensitive (i.e. between 1.5 and 1.8). The observed sensitivity is represented by the line plots for the chemical dimension which get closer to each other as the lower values of chemical dimension are approached. The backbone is mainly responsible for the thermal enhancement as particles form aggregates with the backbone rather than the dead ends to induce this enhancement (Evans et al., 2008). As the number of particles in the aggregated backbone increases, the chemical dimension reduces. A point is reached where all the particles are in the backbone which means that the chemical dimension is equal to the fractal dimension. This can be observed in Figure 3.4 as the enhancement ratio is seen to increase for increasing volume fraction, for a given chemical dimension.

3.6 Validation of numerical results with experimental data

To validate the present aggregation model, experimental data on alumina-water nanofluids was chosen. There have been numerous publications on alumina-water nanofluids (Avsec and Oblak, 2007, Wang et al., 2003, Yoo et al., 2007, Murshed et al., 2008, Wong and Kurma, 2008, Feng et al., 2007, Ren et al., 2005). However, only a few of them unambiguously specify primary particle size and the aggregate size. Datasets from (Wen and Ding, 2005) and (Leong et al., 2006) have been recruited for this purpose. Initially, the numerical and experimental values of the aspect ratio (*Rg/a*) of nanoaggregates responsible for enabling enhancement of thermal conductance of the commonly used alumina-water nanofluid system, were compared.

(Wen and Ding, 2005) formulated alumina-water nanofluids with particle loading up to 0.016 in volume fraction by dispersing alumina nanopowder in water, followed by ultrasonication and homogenising. SEM images had confirmed that the primary particles were ranging in sizes of 10 - 50 nm. After formulation, a Malvern Nano ZS instrument was used to measure particle sizes. They measured the aggregates' size and discovered that they had an average diameter of 167.5 nm. However for validation of the present model, values for *Rg/a* were specified. An estimated value range for primary particle size therefore has to be made. For this, the size range of

30 – 45 nm was chosen, which agrees with experiment. As a result, R_g/a will fall in an interval of 5.6 to 3.7 (Wen and Ding, 2005).

(Leong et al., 2006) had considered two particle sizes; 80 nm and 150 nm in their alumina-water nanofluids with particle volume fractions up to 0.005. Formulation details were not given but they presumably dispersed dry particles in water similar to their previous work (Murshed et al., 2005). Particle sizing methods were not clearly mentioned, but it is highly possible that they were referring to aggregate size. Assuming this, their experimental data for 150 nm aggregate size is to be used in the present study. Further assumptions are made for Leong's primary particle size for the interval of 30 – 45 nm.

Figure 3.5 demonstrates the model predictions and the experimental data as a function of d_f. for alumina-water nanofluid systems. For these cases, d_l is taken as 1.4.

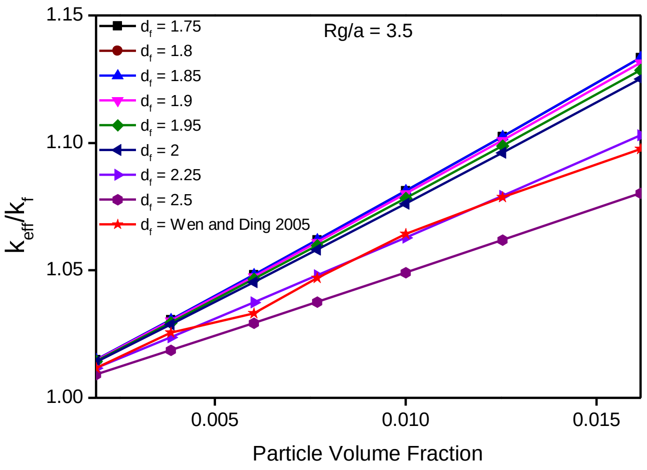

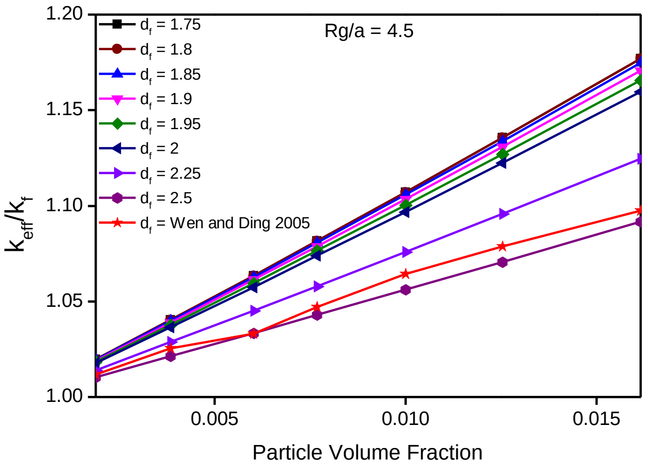

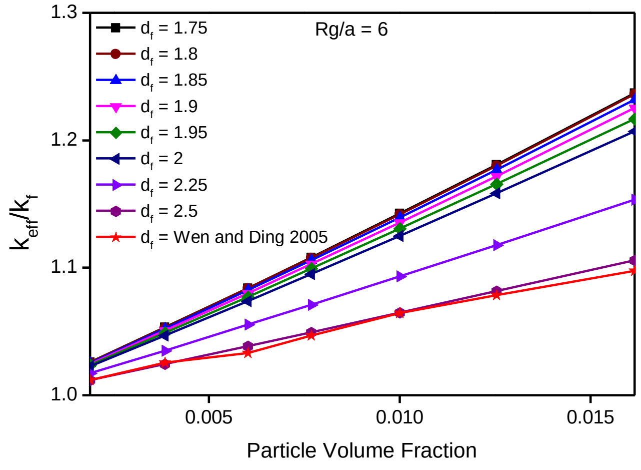

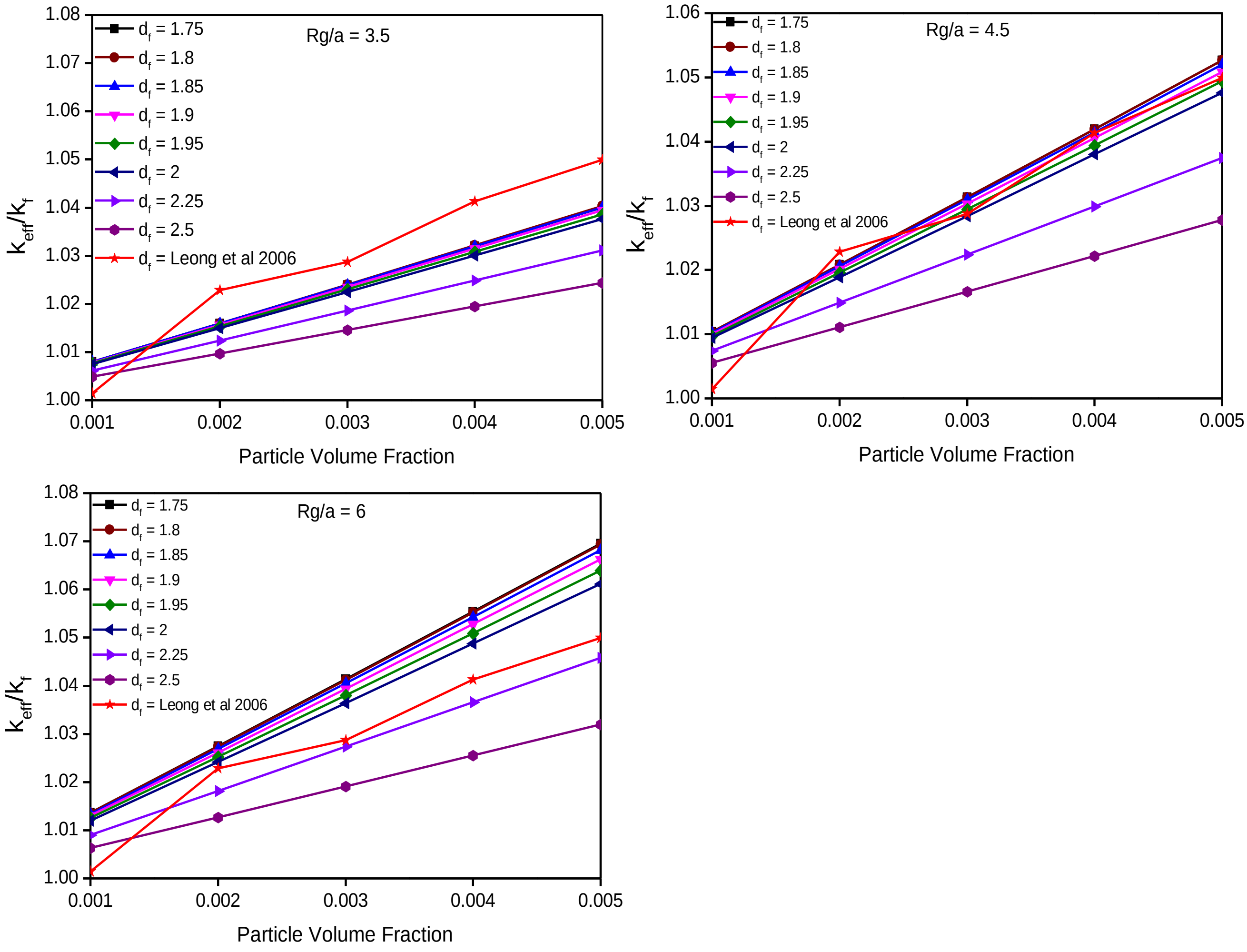

Figure 3.5 Experimental data and model prediction for alumina-water nanofluid for $d_l = 1.4$ and $\alpha = 1$ (Okeke et al., 2011)

It follows from Figure 3.5 that the model predictions agree very well with the experimental data. In particular, the agreement with Wen & Ding's data is excellent. Their experimental data falls within the interval of 2.25< d_f <2.5 while that for Leong et al, fell within 1.75 < d_f <2. It can be speculated that the aggregation process in Wen and Ding is likely to be RLA induced while that of Leong et al., DLCCA. Recall that this was the dataset where primary particle size was clearly specified. This observation could be linked to previous work of (Waite et al., 2001) where investigations were carried out on an alumina–water nanofluid system. Their study suggests that although the fractal dimensions obtained fell within the expected range of 1.8 – 2.3, it did not obey the conventional rule of DLCCA for lower fractal dimensions and RLA for higher fractal dimensions as they observed slightly higher fractal dimensions for higher aggregation rates. This could be the reason for the observed closeness in thermal enhancement ratio (< 1% difference) of experimental data. At the same time, these data fall at different regions of fractal dimensions. Furthermore, it is observed that the experimental data for Leong et al. approach the RLA interval as Rg/a increases. This may suggest that the aggregation process gets slower with increasing aggregate size.

3.7 Effective thermal conductivity of model systems

Based on the aggregation model, the accuracy of the present simulation technique is demonstrated by validating the present data with literature data for water based nanofluids of Alumina, CuO and Titania as shown in Figure 3.6. The aspect ratio (which captures particle aggregation) for nanoparticles (*Rg/a*) was fixed at a value of 2 assuming little aggregation (i.e. *Rg/a = 2*) among the particles, for Alumina-water system. This is to compensate for the often undisclosed primary particle sizes in literature as there is very limited information on the size of the primary particles for Alumina nanofluid systems. For the other systems (i.e. CuO and Titania), *Rg/a* varies between 5 to 8.

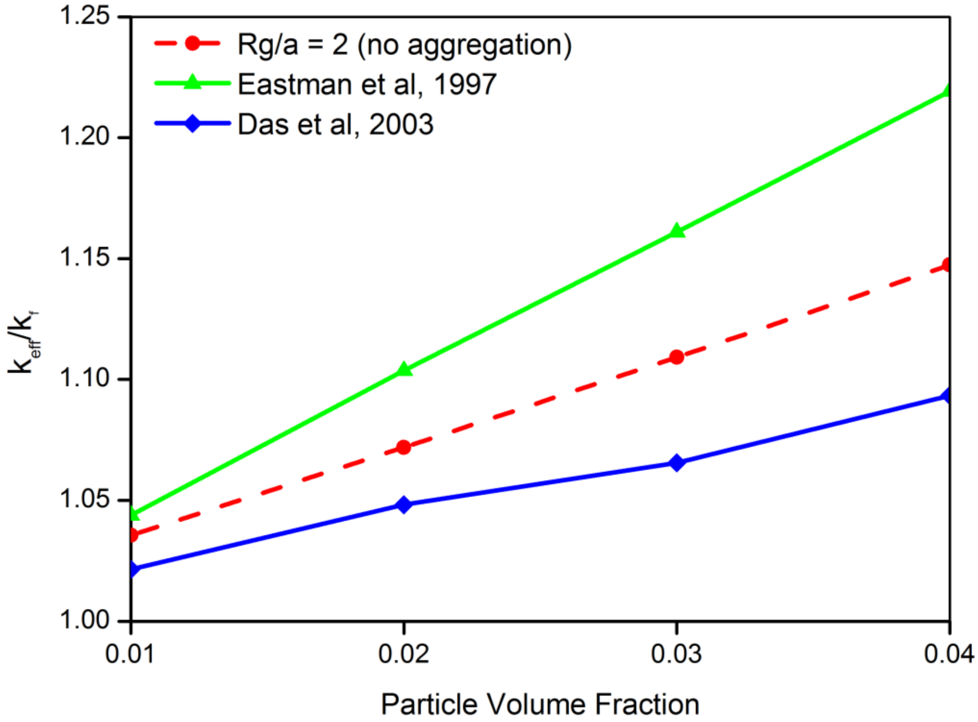

(a)

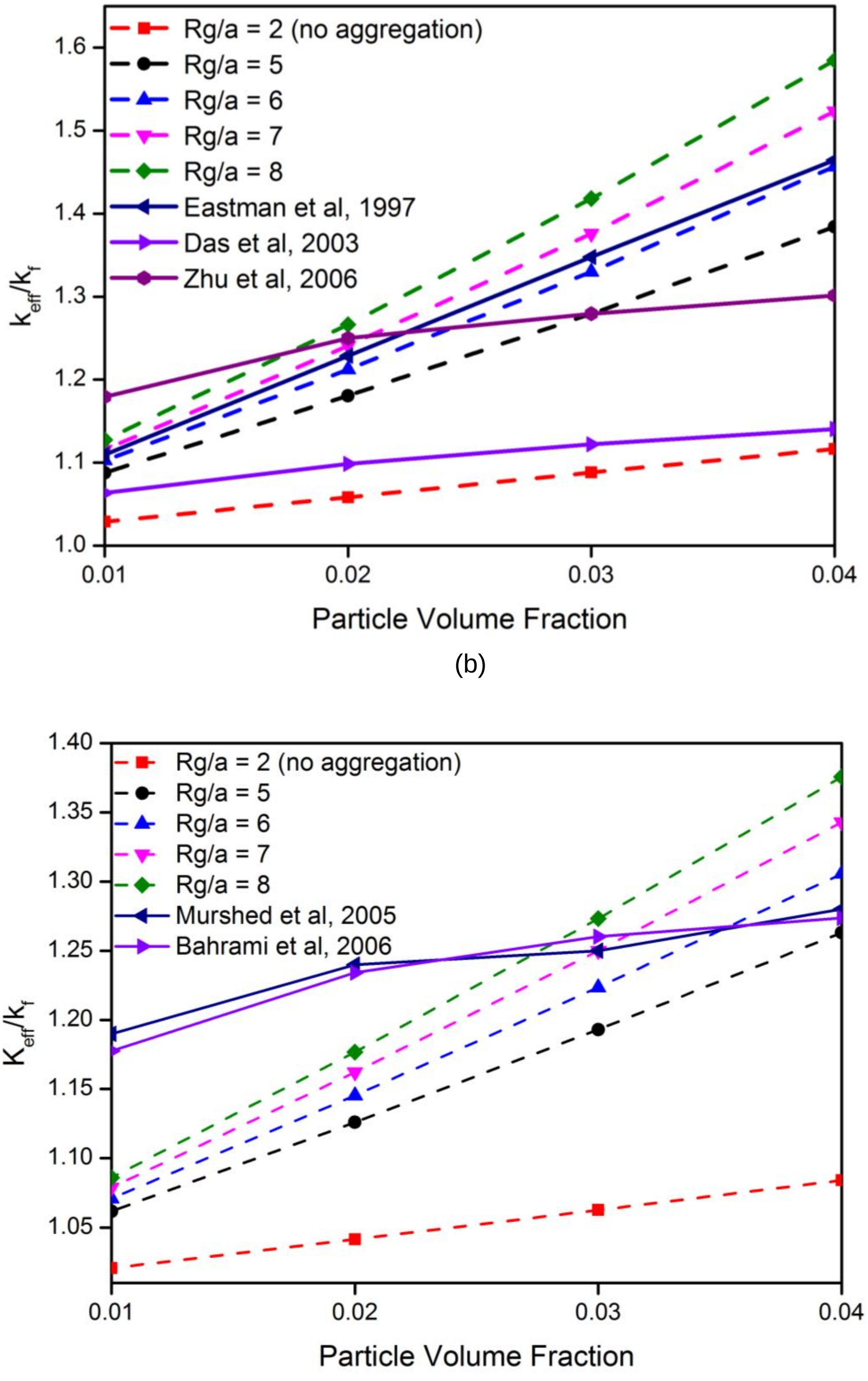

(b)

(c)

Figure 3.6 Comparison of enhancement ratio *(k_{eff} / k_f)* obtained in the present work with literature data for water-based (a) Alumina, (b) CuO and (c) Titania nanofluids. d_f = 1.8, d_l = 1.4 and α = 1. The dotted lines represent data from the present model while thick lines represent experimental data from the literature (Okeke et al., 2011).

It can be seen that the experimental data from the literature generally lie in the region of high *Rg/a* (i.e. *Rg/a* > 2). Apart from literature data of (Das et al., 2003), where the enhancement ratio is observed to fall below *Rg/a* = 2 for the case of alumina, and slightly above *Rg/a* = 2 for the case of CuO, an enhancement ratio within the range 5 ≤ *Rg/a* < 8 is observed for the other experimental data shown in plots for alumina, CuO and titania in Figure 3.6. This suggests that thermal enhancement of nanofluids is mostly influenced by aggregation of nanoparticles (represented by *Rg/a* > 2). Overall, for well-dispersed spherical shaped particles and at low volume fractions, the thermal conductivity of the nanofluid is usually dependent on the thermal conductivity of the particles (provided it is about 10 times or higher than that of the base fluid) (Evans et al., 2008). The reason for this condition is due to the fact that most of the resistance to heat flow within the nanofluid system will come from the base fluid, and as particles act as constant temperature regions, the particles would need to have high enough thermal conductivity to aid in heat flow.

3.8 Conclusion

The influence of particle aggregation on the effective thermal conductivity of nanofluids has been investigated using the aggregation model discussed in Chapter 2. Initially, preliminary investigations conducted using sensitivity analysis showed that results from the aggregation model were in good agreement with literature data for aqueous alumina, copper oxide and titania nanofluids. Further investigation also showed that other factors such as particle size, size of aggregates, particle volume fraction and interfacial thermal resistance play a major role in thermal enhancement. The study gave further insight into the effect of fractal and chemical dimensions on thermal conductivity. Results for water based alumina showed that both fractal and chemical dimensions reduce for increasing thermal enhancement. Validations conducted on fractal dimensions with data from the literature also showed that there is a link between aggregation mode, aggregate size and compactness of the aggregates.

Results achieved in this chapter have provided a solid foundation and shown that particle aggregation actually enhances thermal enhancement in nanofluids. Further investigations are to be carried out in the subsequent chapters to study particle scale properties from a molecular/atomic point of view, using molecular dynamics simulations. The nanoparticle which will be used to carry out investigations on the particle scale properties is titanium dioxide. They are widely applied in the industry due to their enhanced physical, chemical and electrical properties. An introduction to titanium dioxide nanoparticles is provided in Chapter 4. This includes its crystalline phases and their most important (low-index and thermodynamically stable) surfaces. An introduction to molecular mechanics and the concept of a force field is also provided in Chapter 4.

Chapter 4

Theoretical Background of TiO_2 and Molecular Modelling

4 Theoretical Background of TiO_2 and Molecular Modelling

4.1 Introduction

This chapter provides an in depth review of TiO_2 and its crystal phases. TiO_2 has been used in this study because it has been researched extensively. Also, it has many industrial applications mostly due to some aspects of its physical, chemical and electrical properties which are enhanced at the nanometer scale. Three crystalline phases of TiO_2 have been identified; rutile, anatase and brookite. Here, the applications of TiO_2, an overview of its crystalline structures, and the characteristics and properties of its three crystalline phases, will be discussed in detail. The surfaces (mostly the low index surfaces) for the crystalline phases of TiO_2 will also be discussed here. These low index surfaces are known to be most widely studied owing to their thermodynamically stable nature as they possess low surface energies (Pang et al., 2013). Furthermore, molecular modelling has been used in this research to investigate the physico-thermal properties of TiO_2 nanoparticles. Molecular modelling provides a better understanding of the atomic scale (from a microscopic perspective) properties and interactions. Surface properties such as surface energy influence the surface behaviour of the particles (from a macroscopic perspective) as atomic/molecular scale properties can greatly influence bulk scale properties. Hence, the next section of this chapter focuses on molecular modelling and how it was employed, to predict particle-scale properties including atomic scale and particle scale interactions.

4.2 Titania (TiO_2) nanoparticles

There is a growing interest among researchers in understanding why nanofluids containing, for example, TiO_2 nanoparticles exhibit unique and enhanced properties, such as enhanced thermal conductivity, in comparison with traditional heat-transfer fluids. Metal oxides expressed as particulates in the nanometer range possess a wide range of applicability in areas such as photonics, sensors, electronics and catalysis (Soo-Jin Park, 2010). Ceramic particles in the nanometre size range have a large surface area per unit mass ratio which may, potentially, underpin any enhancement in physical, chemical and electrical properties compared to the corresponding properties of the bulk states. Titania is an example of a ceramic material used in various applications such as photocatalysts, catalysts, microporous membranes and chemical sensors (Soo-Jin Park, 2010, Haverkamp, 2010). Understanding the behaviour of nanoparticles such as TiO_2 starting from their atomic scale structure through to their surface properties (such as surface energy as a function of different environmental conditions), may give further insight into their inter-particle interactions and aggregation characteristics which are fundamental to providing enhanced thermal conductance in nanofluids containing TiO_2 nanoparticles.

TiO_2 is widely used in research particularly due to its availability and the large amount of information present in the literature. Its key properties are its ease of production, cheapness, recyclability, and its ability to be synthesized into nanostructure forms more easily than most other materials employed in catalysts (A. Ahmad, 2006). It is also stable in aqueous media (i.e. in both acidic and alkaline solutions). A significant amount of research has been performed on TiO_2 over the last five decades and a number of reviews published (Gupta and Tripathi, 2011, Fujishima et al., 2000, Carp et al., 2004, Mor et al., 2006, Chen and Mao, 2007, Thompson and Yates, 2006, Linsebigler et al., 1995, Diebold, 2003). Synthesis of TiO_2 nanoparticles can be achieved using different methods such as the chloride process, sulphate process, impregnation, coprecipitation, hydrothermal methods (Oh et al., 2006), metal organic chemical vapour deposition methods, direct oxidation of $TiCl_4$ amongst other methods (A. Ahmad, 2006, Yang et al., 2001). In the midst of these methods, the sol-gel method has proved to be the most convenient way of synthesis due to its affordability, low processing temperatures as well as ease of production. The sol-gel method has been in existence since the mid 1800s (Akpan and Hameed, 2010) and has been used in the development of new materials for catalysis (Øye et al., 2006), chemical sensors (Carmona et al., 2007), and in solid state electrochemical devices (Skaarup et al., 1998). The sol-gel method is mainly used to produce thin film, powder catalysts (Akpan and Hameed, 2010), and nanosized metallic oxide materials (Su et al., 2004). TiO_2 synthesis by the sol-gel method involves the reactions of hydrolysis and polycondensation of titanium alkoxides, $Ti(OR)_n$ to form oxopolymers which are transformed into an oxide network (Su et al., 2004). Post-calcination, which is a thermal treatment process of ores in the presence air, is usually carried out during the sol-gel method and helps to improve the crystallinity of the nanoparticles (Shahini et al., 2011). The calcination temperature has been identified to be key in determining certain properties of TiO_2 nanoparticles such as structural, thermodynamic and photocatalytic properties. For example, an increase in the calcination temperature results in the aggregation and possible phase transformation of the resulting TiO_2 nanoparticle (Shahini et al., 2011). This affects the microstructure including thermodynamic and photocatalytic activities of the particles.

Some physical and mechanical properties of TiO_2 are given below;

Table 4.1 Typical physical and mechanical properties of the rutile phase of titania (sourced from www.azom.com/details.asp)

Property	**Value**
Density	4 gcm^{-3}
Porosity	0%
Modulus of Rupture	140 MPa
Compressive Strength	680 MPa
Poisson's Ratio	0.27
Fracture Toughness	3.2 $MPa.m^{-1/2}$
Shear Modulus	90 GPa
Modulus of Elasticity	230 GPa
Micro hardness (HV0.5)	880
Resistivity (25^0C)	10^{12} ohm.cm
Resistivity (700^0C)	$2.5x10^4$ ohm.cm
Dielectric Constant (1MHz)	85
Dissipation factor (1MHz)	$5x10^{-4}$
Dielectric strength	4 $KVmm^{-1}$
Thermal expansion (RT-1000^0C)	$9x10^{-6}$
Thermal Conductivity (25^0C)	11.7 WmK^{-1}

TiO_2 exists in three main crystalline forms namely rutile, anatase and brookite. The most important crystalline forms are rutile and anatase. Although anatase TiO_2 has been researched in recent years (due to its high photocatalytic activity), the number of research papers published on rutile TiO_2 has increased recently as it is observed to be the most active (in terms of photocatalysis) crystalline form (Wang et al., 2010). In the bulk form, the rutile phase is the most stable phase thermodynamically at room temperature, while both bulk anatase and brookite are metastable, transforming irreversibly to rutile at high temperature (in the range of 600 – 700^0C) (Hu et al., 2003b, Gupta and Tripathi, 2011). However, the phase stability differs for titania when comparing the bulk scale with the nanoscale (Koparde and Cummings, 2008). The thermodynamic stability observed for nanocrystalline rutile is dependent on the particle-size. As the size decreases (i.e. at particle diameters below about 14nm); anatase is more stable than rutile, and it has been suggested that anatase is the most stable phase when expressed in the nanocrystalline form (Zhang and F. Banfield, 1998). This may be the reason why anatase is usually synthesized in ultrafine sizes (Zhang and F. Banfield, 1998). Phase transformation processes occur where individual phases transform into other phases (like anatase to rutile). Understanding the factors that influence the order in which phase transformations take place may offer insights into how microstructures, phase composition and properties of titania-based materials can be controlled (Zhang and Banfield, 2000). Furthermore, research has shown that a synergy between the two important phases (i.e. anatase and rutile) can greatly influence certain properties of TiO_2 such as its photocatalytic properties. Anatase and rutile exhibit different physical properties at the nanoscale. The morphology of TiO_2 crystals can influence certain properties of TiO_2 crystals (such as photocatalytic ones). A decrease in the particle size of spherically-shaped crystals, for a given mass, results in a higher surface-to-volume ratio compared to the surface-to-volume ratio of non-spherically-shaped particles (Wang et al., 2010). It is important to note that particle shape can influence this ratio at a fixed volume.

From these perspectives (i.e. phase composition and TiO_2 morphology), controlling these crystal phases and their morphology is necessary to make them best suited for the desired and intended purposes. The rutile phase is known to grow mostly in the [110] direction leading to an elongated nanorod. This makes the synergy of both anatase nanoparticles and rutile nanorods favourable with the formation of a one-dimension/zero-dimension (1D/0D) heterogeneous nanostructure. These structures possess more desirable properties compared to conventional anatase/rutile nanocomposites (Wang et al., 2010). A proper control of this transition is important to get the desired phase from the transition process. It has been suggested that a coupling of anatase and rutile phases of TiO_2 is beneficial. As the control of the transformation process remains challenging especially under very high temperature, ultrasonic irradiation or high-pressure conditions (Testino et al., 2007), it is important to note that control of both the phase composition and size of TiO_2 are necessary for this purpose. However, inasmuch as certain inorganic oxide substrates or organic template molecules can aid in a desired phase control of the morphology, the important nanostructure and surface property may be affected under high temperature or pressure. This therefore requires the control of the phase and shaping of the morphology under mild process conditions (such as temperature and pressure) to achieve the desired heterogeneous nanostructure (Wang et al., 2010). Furthermore, for the purpose of phase transformation, a decrease in pH has been revealed to lead to anatase-to-rutile transformation within a solution medium while surface effects may disrupt the particle size below which anatase will be more stable than rutile and therefore influence anatase-to-rutile transformations (Hu et al., 2003a). Apart from particle size, physical and environmental factors can also be influential in controlling the phase stability of titania nanoparticles. High temperatures leading to an increase in particle size can enhance anatase-to-rutile transformation. In fact, experimental data derived at temperatures between 598 and 1023 K show that anatase is the most stable phase at particle sizes below 11 nm, brookite is the most stable at particle sizes between 11 nm and 35 nm and rutile is the most stable phase at all particle sizes above 35 nm (Ranade et al., 2002). This means that the transformation pathway for brookite would be directly to rutile and for anatase may be either directly to rutile or through brookite to rutile (Koparde and Cummings, 2008). It is believed that the surrounding environment can also influence phase transformations, for instance investigations carried out by *Ab initio* calculations (Barnard and Zapol, 2004) reveal that the cross-over diameter (i.e. particle size below which anatase is more stable than rutile) is smaller for particles in a vacuum than particles in water.

4.3 General applications of TiO_2

4.3.1 Bactericidal disinfection processes

Previous investigations have been conducted in a batch spiral reactor for the photocatalytic degradation of *E.coli* in water by Degussa P25 TiO_2 (Amanbayev et al., 2010). Also, photocatalytic disinfection studies have been carried out on *E.coli* by using the sol-gel method and annealing for the dip-coating on soda lime glass. Light-induced hydrophilicity, including high photocatalytic activity were observed in the sol-gel thin film (Haverkamp, 2010, Subba Rao et al., 2006). Generally, the destruction of cells observed can be related to first-order kinetics (Haverkamp, 2010, Subba Rao et al., 2006).

4.3.2 Chemical/Bio treatments

A common problem is the difficulty in degrading organic pollutants in wastewater by conventional method of biological treatments. This challenge can be overcome to a great extent using the method of photocatalytic oxidation. The latter mentioned method has been conducted on phenol in water using TiO_2 nanoparticles with different ratios of anatase-to-rutile showing high phenol degradation for samples with higher anatase-to-rutile ratios (Haverkamp, 2010, Subba Rao et al., 2006). Also, it has been observed that in aerobic conditions, sucrose and/or nitrate can undergo photodegradation in aqueous solution over nanoparticle haematite photocatalysts with TiO_2 coating in the presence of an UV irradiation (Haverkamp, 2010, Subba Rao et al., 2006). TiO_2 can also be used for photoelectrochemical reactions

4.3.3 Sensors

The sol-gel process can be used in the synthesis of MoO_3-TiO_2 nanocomposite thin films with varying content of Mo and Ti which can be used for gas sensing (Li et al., 2001). It can also be used in preparing V_2O_5-TiO_2 of nano-sizes for oxygen sensing (Zhuiykov et al., 2001).

4.3.4 Solar Cells and Photonic Devices

Photovoltaic cells which are usually used as solar cells, can be replaced with more efficient dye-sensitized solar cells made of nano-sized anatase TiO_2. It is thought that the presence of these TiO_2 films can enhance the performance of solar cells (Hart et al., 2004, Hart et al., 2005, Hart et al., 2007).

In a nutshell, the applications of TiO_2 cover a very wide range as this material possesses exceptional and unique properties especially at the nanoscale. Apart from those applications discussed above, TiO_2 is widely used as a metal-oxide semiconductor. It is also used as a white pigment in paints and papers as a result of its opacity. While it can be used in high temperature separations and photocatalytic applications, it can also be used as a raw material in electronic and structural ceramics (Koparde and Cummings, 2005). In recent times, nanosized TiO_2 has been used as a catalyst especially under ultraviolet light in many reactions including paint pigment degradation, dehydration of alcohol, reduction of nitrogen oxide, oxidation of aromatic compounds and toxic contaminant removal from waste water (Koparde and Cummings, 2005). It can also be used as a biocompatible material for bone implants as well as a spacer material for magnetic spin valve systems (Han et al., 2006).

Understanding the physico-thermal properties of TiO_2 nanoparticles (which is the main focus of this thesis) is of great importance as this will help in engineering these particles for improved use. For example, knowing its thermodynamic behaviour and properties will aid in understanding its use in high temperature applications and as a semiconducting material.

4.4 General overview of crystals

It is a well known fact that atomic scale properties of materials influence their bulk properties. Crystallography, which involves the study of the arrangement of atoms in solid materials, plays a major role in understanding properties such as thermodynamic, structural and surface properties, on an atomic scale. The subsequent sub-sections will provide an overview of crystals.

4.4.1 Lattice and Unit Cells

Atoms in crystals are organised in a three-dimensional periodic pattern in space (Galasso, 1970). A Bravais lattice which is a three-dimensional set of evenly spaced points in crystals, can be formed by using three non-coplanar directions emanating from one point (Galasso, 1970). The Bravais lattices which form a basis for all crystals can be seen in Figure 4.1 below;

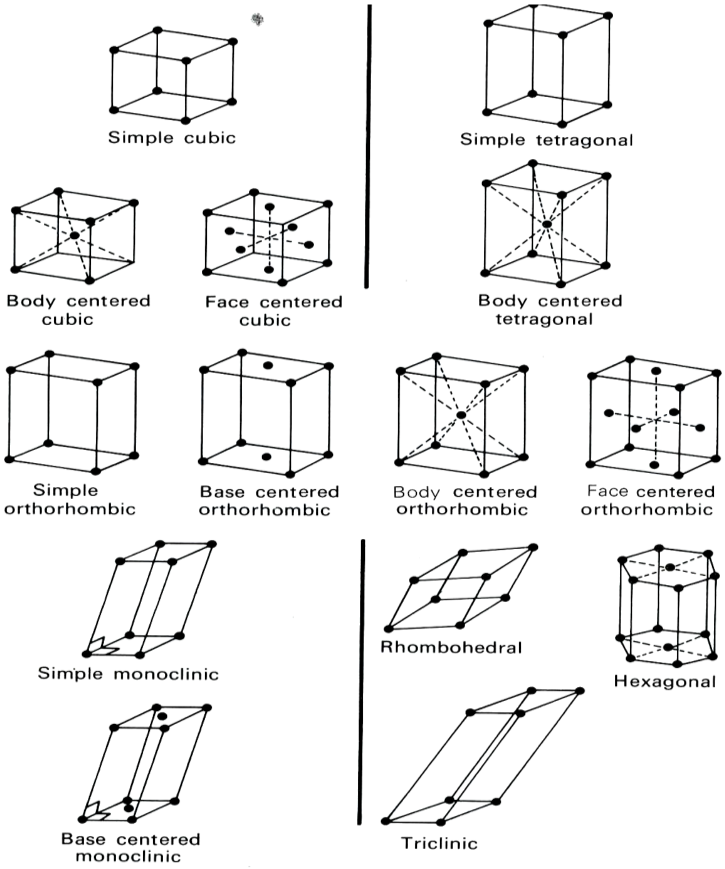

Figure 4.1 The Bravais lattices (Galasso, 1970)

The unit cells in crystals have dimensions of *a, b* and *c* and angles of *α, β* and *γ*. These angles represent the angles between *b* and *c*, *c* and *a*, and *a* and *b* respectively. Table 4.2 shows data which can be used to illustrate different types of unit cells.

Table 4.2 Crystal systems and the 14 Bravais Lattices (Douglas, 2006)

Seven systems	Axes and angles	14 Bravais Lattices	Lattice symbols
Cubic	$a = b = c$ $\alpha = \beta = \gamma = 90^0$	Primitive Body centred Face centred	P I F
Tetragonal	$a = b \neq c$ $\alpha = \beta = \gamma = 90^0$	Primitive Body centred	P I
Orthorhombic	$a \neq b \neq c$ $\alpha = \beta = \gamma = 90^0$	Primitive Body centred Base face centred Face centred	P I C F
Trigonal or rhombohedral	$a = b = c$ $\alpha = \beta = \gamma \neq 90^0$	Primitive	R
Hexagonal	$a = b \neq c$ $\alpha = \beta = 90^0$ $\gamma = 120^0$	Primitive	P
Monoclinic	$a \neq b \neq c$ $\alpha = \beta = 90^0 \neq \gamma$ or ($\alpha = \beta = 90^0 \neq \gamma$)	Primitive Base face centred	P B or C
Triclinic	$a \neq b \neq c$ $\alpha \neq \beta \neq \gamma \neq 90^0$	Primitive	P

4.4.2 Planes and Directions

The orientation of a plane in a crystal lattice is best described by the Miller index which is a set of reciprocals of the fractional intercepts that a plane makes with the crystallographic axes (Galasso, 1970). The Miller index is the reciprocal of the Weiss index which is constructed using an arbitrary lattice point as the origin and the intercept of the plane with three crystallographic axes in units of a, b and c (Douglas, 2006, Schaak, 2006). This means that it is necessary to express the intercepts in terms of the unit distances a, b and c along the three axes (Galasso, 1970). The use of the Miller index aids in simplification as it is zero for a plane parallel to an axis and so removes fractions and infinity. Basically, the Miller index for a face or a set of planes is hkl, where h is the number of equal divisions of a in the unit cell, k the divisions of b and l the divisions of c (Douglas, 2006, Schaak, 2006). The [hkl] direction is perpendicular to the (hkl) plane in the cubic system, but not in general. Examples of some planes and directions are shown in Figure 4.2

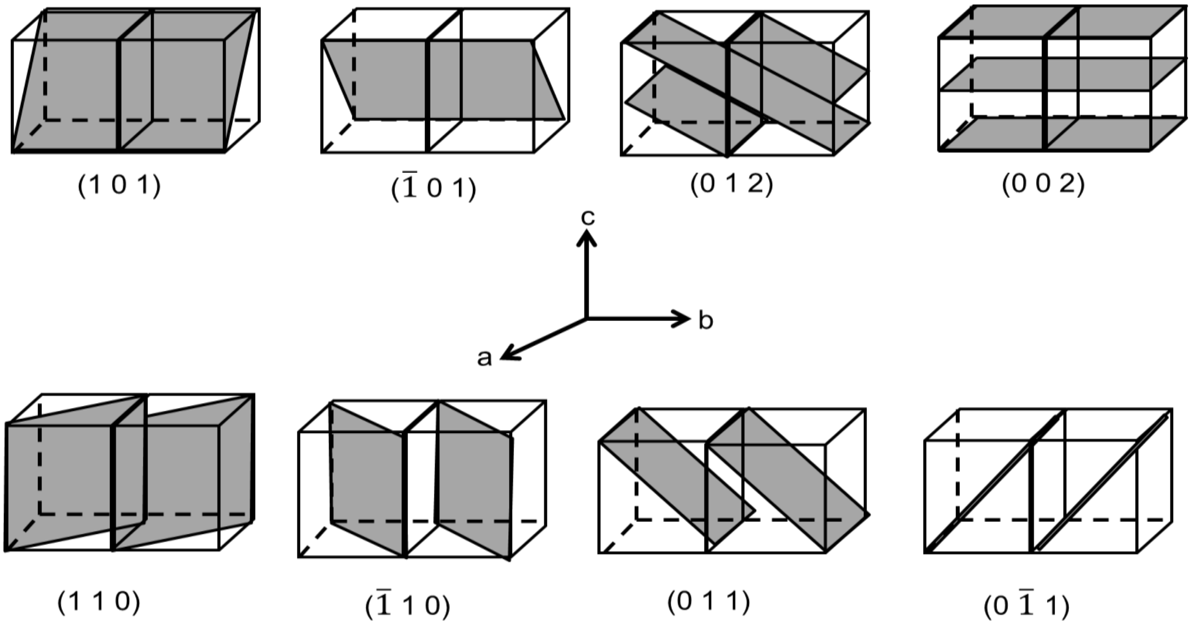

Figure 4.2 Miller indices for planes in cubic cells (Douglas, 2006)

4.4.3 Mechanical properties of crystals

As with materials in general, crystals possess mechanical properties. Examples of these properties are elastic moduli and tensor, stiffness constants, compressibility etc. Alterations in the arrangement and ordering of atoms within crystals can greatly influence these properties. Knowledge of these properties is important to help understand the behaviour of crystals. For example, the elastic modulus is a measure of the tendency of a crystal to deform elastically when a force is applied to it. Measuring or calculating the elastic modulus aids in the development of materials to suit various applications under different loading conditions.

Stress and strain are key in describing mechanical properties such as elasticity. Strain, relates to the change in the relative positions of atoms in crystals when forces are applied to the crystals or imperfections are formed in them. The concept of extension and shear best describe strain. Extension can be illustrated by considering a thin rod of length l (Figure 4.3 a) stretched to a length l' in the strained state. The extension, e, is the ratio of the change in length to the original length, as seen below (Kelly et al., 2000);

$$e = \frac{l' - l}{l} \tag{4.1}$$

Therefore

$$l' = l(1 + e) \tag{4.2}$$

Shear is a measure of the change in angle between two lines in a material when it distorts. Consider two perpendicular straight lines OX and OY in their original unstrained states, and their positions O'X' and O'Y' in their strained state (Figure 4.3 b), the shear strain γ related to these two directions at point O is defined as (Kelly et al., 2000);

$$\gamma = tan\left(\frac{\pi}{2} - \theta\right) \tag{4.3}$$

Where θ is the angle between O'X' and O'Y' in the strained state.

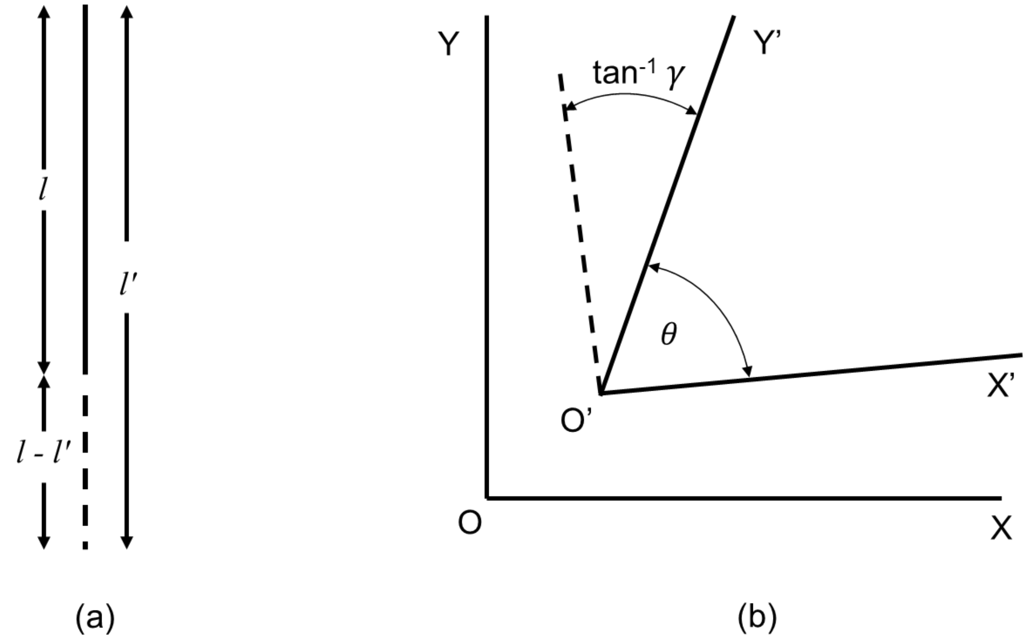

Figure 4.3 Definition of (a) Extension and (b) Shear (Kelly et al., 2000)

In crystals, when atoms are displaced relative to each other, forces act on them which tend to restore them to their normal spatial relationship (Kelly et al., 2000). Stress σ, is the ratio of the restoring force caused as a result of deformation to the area in which the force is applied and is defined as follows;

$$\sigma = \frac{F}{A} \tag{4.4}$$

Where *F* and *A* represent the force and area respectively.

4.4.3.1 Elastic modulus and stiffness constant

Elastic constants provide information about the stiffness of materials, and give understanding into their mechanical properties. In general, they provide a measure of the interatomic forces in materials (Westbrook and Fleischer, 2000). The elastic modulus is the mathematical description of the tendency of a material to be elastically deformed when a force is applied to it. The elastic modulus of a material is defined as the slope of its stress – strain curve in the elastic deformation region and is given as;

$$\lambda = \frac{\sigma}{\epsilon} \tag{4.5}$$

where λ is the elastic modulus and ϵ is the strain. The relationship between stress σ_{ij} and strain ϵ_{ij} (*i, j* = 1, 2, 3) for Cartesian coordinates is represented by Hooke's law (Westbrook and Fleischer, 2000). The symmetrical axis of a crystal structure is given below as;

$$\begin{bmatrix} \sigma_{11} \\ \sigma_{22} \\ \sigma_{33} \\ \sigma_{23} \\ \sigma_{31} \\ \sigma_{12} \end{bmatrix} = \begin{bmatrix} c_{11} & c_{12} & c_{13} & c_{14} & c_{15} & c_{16} \\ & c_{22} & c_{23} & c_{24} & c_{25} & c_{26} \\ & & c_{33} & c_{34} & c_{35} & c_{36} \\ & & & c_{44} & c_{45} & c_{46} \\ \multicolumn{4}{l}{symmetry} & c_{55} & c_{56} \\ & & & & & c_{66} \end{bmatrix} \begin{bmatrix} \epsilon_{11} \\ \epsilon_{22} \\ \epsilon_{33} \\ \epsilon_{23} \\ \epsilon_{31} \\ \epsilon_{12} \end{bmatrix} \tag{4.6}$$

where c_{ij} is the Voigt notation for the components of the elastic stiffness tensor. c_{11} is the appropriate elastic modulus *M*, determined from the velocity of the longitudinal wave in the [1 0 0] direction. c_{55} and c_{66} are determined from the velocity of the transverse wave in the [1 0 0] direction on (0 0 1) and (0 1 0) planes, respectively. There are 21 independent terms in the general elastic tensor. For the cubic class of crystals, three constants, c_{11}, c_{12} and c_{44} define the elastic properties (Kelly et al., 2000). An elastic stiffness constant $\{c_{ij}\}$, can be obtained by measuring the velocities of the elastic waves in a crystal. This can be carried out by sending shear and longitudinal waves into several planes of the crystal in specified orientations. This method of measuring stiffness constants is called the plane wave transmission method and is a widely used approach for this kind of measurement. Detection and measurement of these waves is usually done with piezoelectric transducers which are connected through the planes of the crystal sample (Zhu et al., 1998). Stiffness constants are usually written in the form of matrices with 21 independent terms as seen below;

$$\begin{matrix} c_{11} & c_{12} & c_{13} & c_{14} & c_{15} & c_{16} \\ c_{12} & c_{22} & c_{23} & c_{24} & c_{25} & c_{26} \\ c_{13} & c_{23} & c_{33} & c_{34} & c_{35} & c_{36} \\ c_{14} & c_{24} & c_{34} & c_{44} & c_{45} & c_{46} \\ c_{15} & c_{25} & c_{35} & c_{45} & c_{55} & c_{56} \\ c_{16} & c_{26} & c_{36} & c_{46} & c_{56} & c_{66} \end{matrix}$$

Any crystal has 21 different elastic constants. These constants can be chosen from the crystal axes based on its symmetry and type of lattice (i.e. cubic, hexagonal, tetragonal, orthorhombic, etc.). In a cubic crystal, the reference axes are usually chosen to be parallel to the crystal axes.

4.4.4 Prediction of crystal shape (morphology)

The morphology of crystals is key in determining the quality of most crystalline materials such as fertilizers, pharmaceutical drugs, speciality chemicals, cosmetics, food products, etc. (Singh and Ramkrishna, 2013). Understanding the morphology of crystals and the fundamental behaviour of their growth form, helps in ensuring better quality of crystals. The improved quality significantly influences production processes (e.g. separation, handling, packaging, storage etc.) of crystalline related materials. The external morphology of crystals has been observed to be closely related to their internal crystal structures, and this has attracted significant research interest (Docherty, 1990). Crystals (i.e. visible shape) have a variety of morphologies due to the relative growth rates of the crystal faces. Models of crystal morphology are often calculated based on either the surface or attachment energy, terms which are defined below. These are taken to represent, in a surface energy based model, crystals grown under a minimum driving force i.e. at conditions close to thermodynamic equilibrium and, in an attachment-energy based model, crystals grown under kinetic control. Structural models such as; the Wulff construction and the Bravais-Friedel-Donnay-Harker (BFDH) model have been developed for morphological predictions. The Wulff construction is closely related to a morphological model based on surface energy minimisation. The BFDH model is based on crystal lattice geometry. These models are discussed below.

4.4.4.1 The Wulff construction - Equilibrium form

The symmetry of the external shape of most naturally occurring crystalline solids has been attributed to the orderliness of the internal arrangement of its atoms or molecules (Docherty, 1990). Crystals usually grow in a non-equilibrium form and their resulting shape are mainly influenced by many factors which contribute to the kinetics of growth (Dobrushin et al., 1992). The measure of the driving force for crystal growth is, in the case of crystals grown from solution, solution supersaturation, and in the case of crystals grown from the melt it is the undercooling, and for crystals grown from the vapour it would be over-pressure. The closer the crystal remains to being in equilibrium with its growth environment during the growth period (i.e. the smaller the driving force) the more closely the shape or morphology will correspond to that predicted using a surface energy model. (Hauy, 1792) suggested that polyhedral crystal shapes could be built up by stacking cubes (i.e. unit cells) in a variety of three-dimensional sequences. Also, (Gibbs, 1875) suggested that the polyhedral shape of a crystal is governed by the principle of minimisation of free energy and can be taken as;

$$\sum_i U_i \, A_i = minimum \tag{4.7}$$

Where U_i and A_i are the surface energies and areas of the *i*th face respectively. Wullf (Wullf, 1901) suggested that the equilibrium form would comprise of faces located at distance from the growth origin proportional to the surface energies of the faces. This, can be further used to generate a Wulff plot (Figure 4.4) which is a three-dimensional polar plot of surface energy as a function of the crystal orientation.

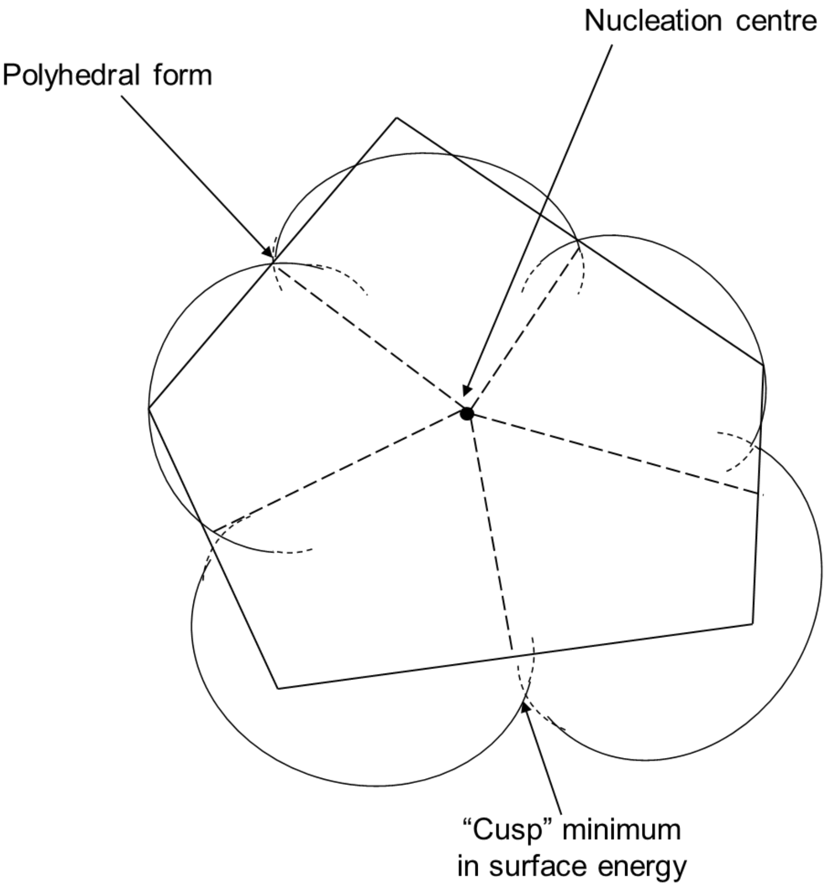

Figure 4.4 Schematic representation of the classical Wulff plot for the derivation of equilibrium form (Docherty, 1990)

The equilibrium form in the shape of a polygon (as shown in Figure 4.4), that is created from the construction of planes tangent to the cusp minimum, is based on Gibbs' theorem. Wulff plots are generally prepared using the gnomonic projection which in recent times, has been enhanced by the availability of more efficient computer programs (Roosen et al., 1998).The Wulff construction predicts the shape of crystals in equilibrium and also aids in understanding the main features of crystals. It is basically an optimization problem and requires knowledge of the interfacial free energies. The equilibrium form of a crystal aims at minimizing the total surface energy for a given volume. This suggests that the crystal will consist of faces located at distances proportional to their surface energies, with the largest faces possessing the lowest surface energies and the greatest interplanar distances, d_{hkl} (Prywer, 2004).

4.4.4.2 The Bravais- Friedel-Donnay-Harker (BFDH) approach

As aforementioned, the BFDH model is based on crystal lattice geometry (Docherty, 1990, Sunagawa, 2005). The BFDH law states that the larger the interplanar distance d_{hkl}, the larger the morphological importance (MI) of the *hkl* face and can be taken as (Prywer, 2004);

$$d_{h_1k_1l_1} > d_{h_2k_2l_2} \Longrightarrow MI_{h_1k_1l_1} > MI_{h_2k_2l_2} \tag{4.8}$$

MI of a given *hkl* face is its relative size in a given crystal morphology. The BFDH may also be taken as;

$$R_{hkl} \propto \frac{1}{d_{hkl}} \tag{4.9}$$

Where R_{hkl} is the growth rate of the *hkl* face. A theoretical BFDH morphology may be obtained from the unit cell parameters, space group, and the reciprocal of the interplanar distances $1/d_{hkl}$ which is used as the distance or growth rates from the centre of the crystal to the respective *hkl* surfaces.

4.4.4.3 The surface energy approach

Surface free energies of the crystallographic faces *(hkl)* of a material are required for predicting the equilibrium forms of crystals. Surface energy refers to the measure of the amount of energy required to split or cleave a surface from a bulk material, and is the work necessary to form a unit area of surface (Shuttleworth, 1950). It is the excess energy associated with the surface, and determines the stability of a surface (Tasker, 1979). Given a bulk energy of U_{bulk} and an energy for a surface created in the same system, $U_{surface}$, the surface energy ΔU_{SE} can be defined as (Gale and Rohl, 2003);

$$\Delta U_{SE} = \frac{(U_{surface} - U_{bulk})}{A} \tag{4.10}$$

Where *A* is the resulting surface area. Following this, surface energy for stable materials will be endothermic and a negative surface energy will mean that a material should dissociate or disperse into the surrounding medium. Two main practical approaches used to determine the surface energy by computational methods include; formation of a 2D slab of material from the bulk thereby creating two surfaces in total and formation of a single surface using a two region strategy. In the case of the former, large vacuum gaps are introduced between the images so that there will be no interaction between surfaces across the vacuum. The thickness of the slab is of great importance as it is necessary for the properties to converge to the bulk at the centre of the slab. In the case of the latter, the material is divided into region 1 and 2 (Figure 4.5). Region 1 consists of the surface and all layers of atoms below it that show a major atomic relaxation and region 2 consists of the remainder of the bulk material with the assumption that no displacements from the 3D crystal structure are induced. Basically, the second method is the most efficient and accurate for calculating surface energy for atomistic methods as only the atoms of region 2 that have an interaction with region 1 are considered (depths are controlled by the cut-offs of the force field and the Parry sum used for the electrostatics) (Gale and Rohl, 2003). In the two region model, the energy, $U_{surface}$, required to determine the surface energy is given as (Gale and Rohl, 2003);

$$U_{surface} = U_{11} + \frac{1}{2}U_{12} \tag{4.11}$$

The total energy for a surface calculation which consists of two regions is given in terms of the interaction energies within and between the different regions (Watson et al., 1996);

$$U_{tot} = U_{11} + U_{12} + U_{22} \tag{4.12}$$

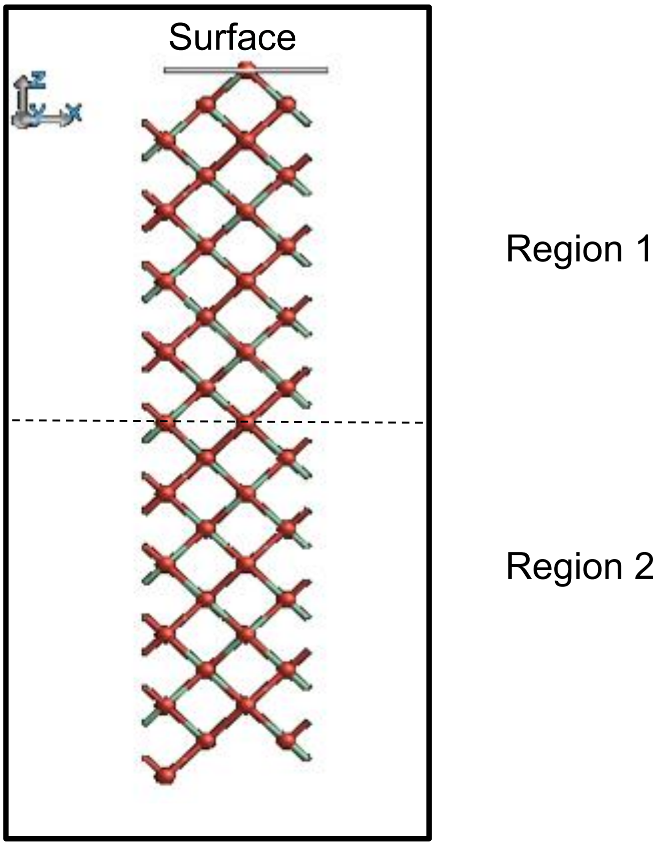

Figure 4.5 The two region surface simulation cell viewed at right angles to the surface normal, where the solid vertical lines represent the boundaries between 2D periiodic images of the cell and the dash lines represent the boundary between region 1 and the stagnant region 2.

4.4.4.4 The attachment energy approach

The attachment energy can be described as the energy associated with the addition of a stoichiometric layer of material on a surface. Crystal morphology can be quantified in terms of the interaction energy between crystallizing units (Hartman and Perdok, 1955). (Hartman and Perdok, 1955) suggested that surface energy is directly related to the chemical bond energies and strong chains of intermolecular interactions also known as periodic bond chains (PBC). PBC can be used to determine slice (U_{slice}) and attachment (U_{att}) energies. U_{slice} is the energy released when a growth slice of thickness d_{hkl} is constructed with the perfect crystal coordinates (Haussühl, 1974, Hartman and Bennema, 1980, Berkovitch-Yellin, 1985). U_{att} is the energy released when a growth slice is attached to a growing crystal surface (Gale and Rohl, 2003). It is the energy associated with the addition of a stoichiometric layer of material on to a surface cut. These definitions imply that (Docherty, 1990);

$$U_{cr} = U_{slice} + U_{att} \tag{4.13}$$

Where U_{cr} is the total lattice energy released on the growing crystal surface. The faces with the lowest attachment energies are known to have the most morphological importance as they will be the slowest growing faces (Hartman and Bennema, 1980). This has been observed even at low supersaturations where the birth-and-spread growth mechanisms dominate crystal growth (Burton et al., 1951). Calculations of attachment energy can be done by making partitions of the lattice energy between the slice and attachment energies (Berkovitch-Yellin, 1985). Interactions between a central molecule and all the molecules within and without a slice of thickness d_{hkl}, can be used in calculating the slice and attachment energies (Docherty, 1990). Slice energy is the summation of all the atom-atom interaction energies between the atoms in a central molecule in the slice, and all the atoms in all the other molecules contained within the same slice. Attachment energy is the summation of all the atom-atom interaction energies between the atoms in a central molecule in the slice, and all the atoms in all the other molecules outside the same slice. A schematic diagram showing the partitioning is shown in Figure 4.6.The BFDH analysis can be used in selecting suitable slices (*hkl*) for these calculations. The attachment energy model assumes that the surface represents a perfect termination of the bulk and that no surface reordering will take place (Docherty, 1990).

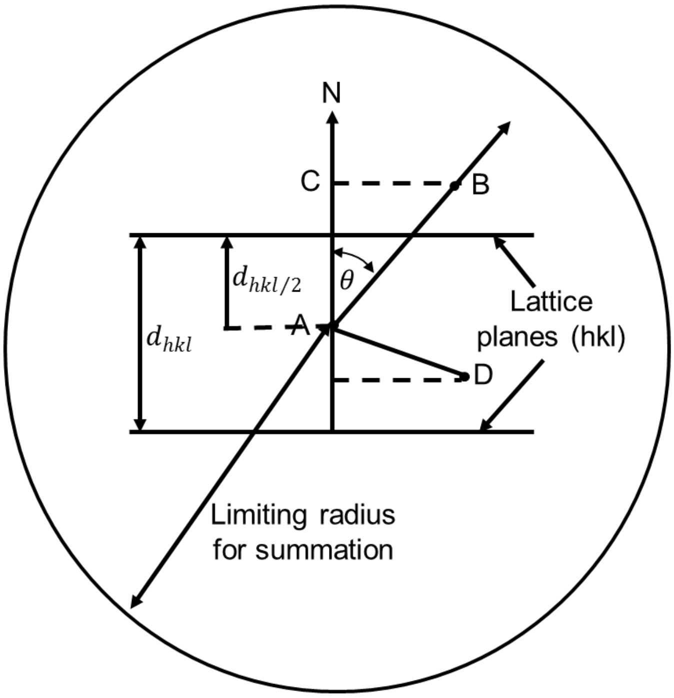

A is the central molecule

B is a molecule in the crystal out of the slice

D is a molecule in the slice

N is the growth normal to the planes (hkl)

AB and **AD** are 'bonding vectors'

$\boldsymbol{d_{hkl}}$ is the interplanar spacing

$\boldsymbol{\theta}$ is the angle between the growth normal and the bonding vector

AC is the component of the vector **AB** parallel to **N**

Figure 4.6 Schematic diagram showing the partition of slice and attachment energies. The figure was obtained from (Docherty, 1990).

4.4.4.5 The concept of surface relaxation

The concept of surface relaxation involves the geometric rearrangement of surface atoms and is associated with the energetics of the system. This involves the reduction of the surface free energy of the system as most surfaces have positive free energy of formation. This concept is similar to that which involves the formation of new surfaces by cleavage of a solid leading to the breaking of bonds between atoms on both/either side of the cleavage plane. Since this breakage of bonds requires work to be done, the surface free energy contribution to the total free energy of the system must be positive.

The process of relaxation involves slight rearrangement or adjustment to the surface layers. This adjustment usually occurs in the layer spacings perpendicular to the surface. However, the direction and magnitude of relaxation depends on the type of material and the orientation of the surface (Bréchignac et al., 2008). It provides a way of compensating for changes in the electron density in each atom layer in a way as to make it as homogenous as possible throughout the material up till the outermost surface (Bréchignac et al., 2008). Usually, when a solid material is cut, the atoms close to the resulting created surface are exposed to different forces exerted on them by the atoms in the bulk, leading to the geometric rearrangement of the surface atoms as a result of the unbalanced forces (Sun et al., 2008). Surface relaxation has an effect on surface energy and surface stress. When surface relaxation occurs, there is a distribution of energy and bulk stresses in the surface region. This distribution provides relevant understanding of surface properties. Figure 4.7 shows a schematic representation of an unrelaxed, a relaxed surface with relaxation in the normal (surface atom layer relaxing vertically) direction, and another relaxed surface in the lateral (surface atom layer relaxing horizontally) direction. Figure 4.8 shows the possible mechanism of relaxation where in case (a), a balanced symmetry of localised forces acting on a central atom can be observed in the bulk of the material. As a result of this balance, a pulling of the central atom by the neighbouring atoms or vice versa is not possible. However, in case (b) the forces are imbalanced at the surface of the material and a pulling of the central atom at the surface by the neighbouring atoms in the bulk is possible, leading to surface relaxation.

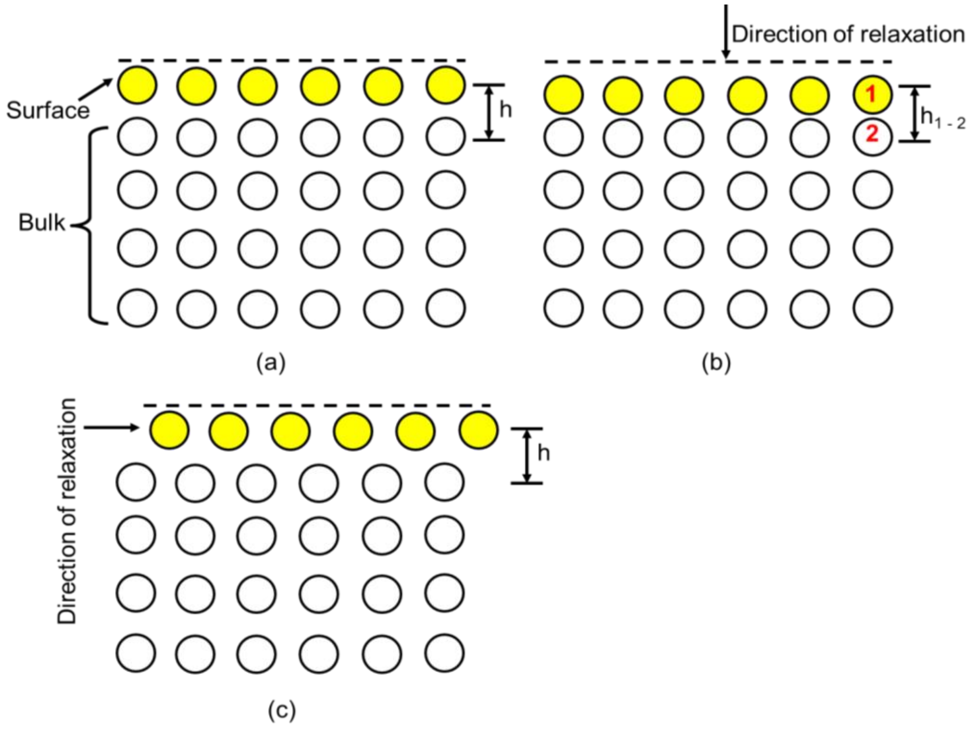

Figure 4.7 Schematic representation of (a) unrelaxed surface, including (b) normal, and (c) lateral relaxation of the upper atomic layer of a crystal (Hermann, 2011).

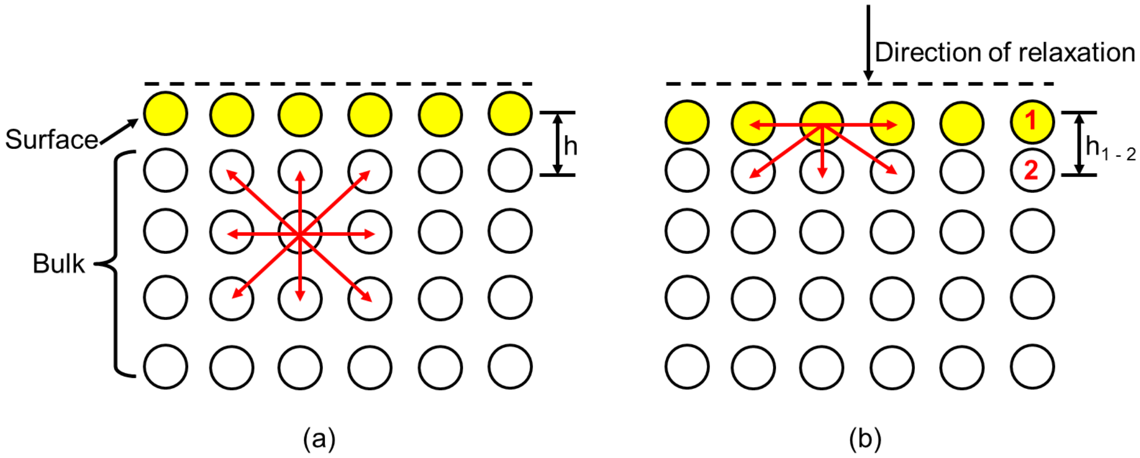

Figure 4.8 Schematic representation of relaxed surfaces showing a localised symmetry set of (a) balanced forces, and (b) unbalanced forces

4.4.4.6 The concept of surface unit cell and surface relaxation

Surface structures are usually described in terms of the original bulk crystal surface unit cell. Surface unit cells can be identified by an ordered arrangement of surface atoms to form a periodically repeating unit. Considering some simple low index surfaces of *fcc* metals such as (1 0 0), (1 1 0) and (1 1 1) surfaces with a primitive unit cell as shown below;

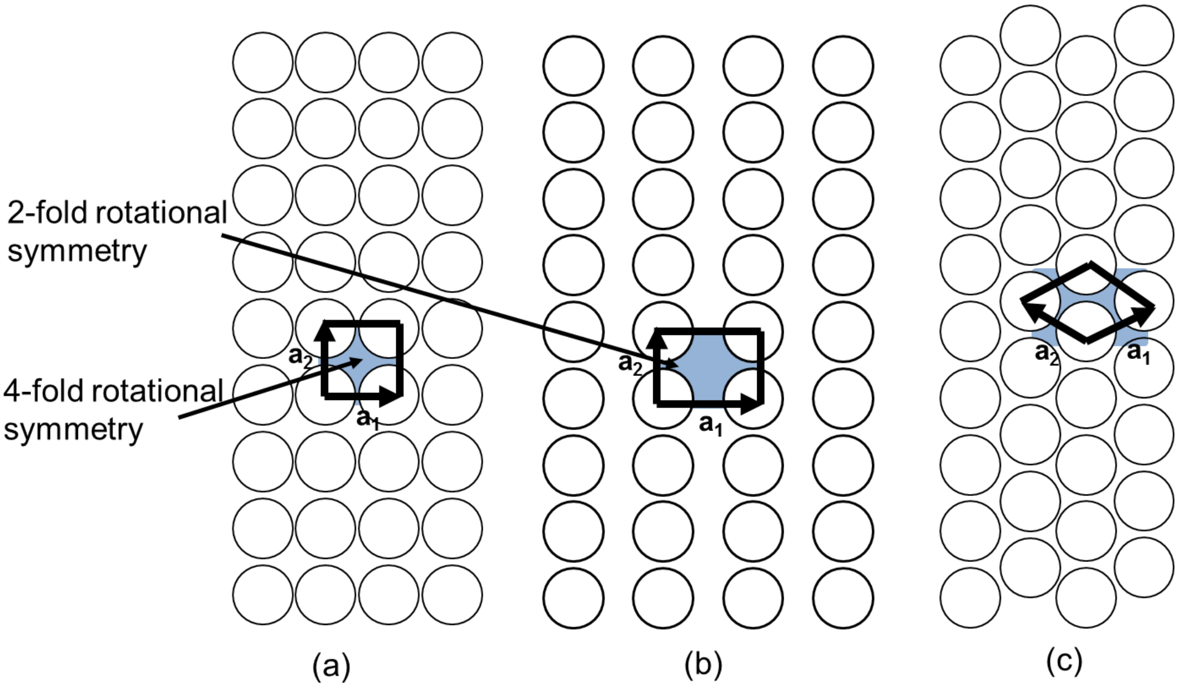

Figure 4.9 Schematic representation of *fcc* (a) (1 0 0), (b) (1 1 0) and (c) (1 1 1) bulk surfaces with square, rectangular and hexagonal Bravais unit lattices respectively.

Figure 4.9 above, shows an *fcc* (1 0 0), (1 1 0) and (1 1 1) bulk surface with a square, rectangular and hexagonal shaped Bravais lattice respectively. For all surfaces, the length of the vectors are a_1 and a_2. For the *fcc* (1 0 0) surface, the length of the vectors are same (i.e. $|a_1| = |a_2|$) and are perpendicular to each other. This surface also has a 4-fold rotational symmetry with a square shaped unit cell as shown in Figure 4.9. The *fcc* (1 1 0) surface has a 2-fold rotational symmetry with a rectangular shaped unit cell (i.e. $|a_1| > |a_2|$). In the case of the *fcc* (1 1 1) surface, the vectors a_1 and a_2 are of similar length, however there is an angle above 90^0 between them.

Furthermore, atoms and molecules can form ordered adsorbate layers on surfaces (especially low index surfaces), forming overlayer structures. There are two basic methods for specifying such structures namely; Wood's notation and the Matrix notation (Guo and Tan, 2009). Woods notation describes the ordered adsorbate layer and defines it in terms of relationship to the surface of a plane lattice (i.e. primitive or centered). Consider a case of a bulk plane *fcc* (1 0 0), with an overlayer structure (adsorbate unit cell) and a simple primitive unit cell (substrate unit cell) embedded on it as shown in Figure 4.10, then the Woods notation can be used in representing this as seen below;

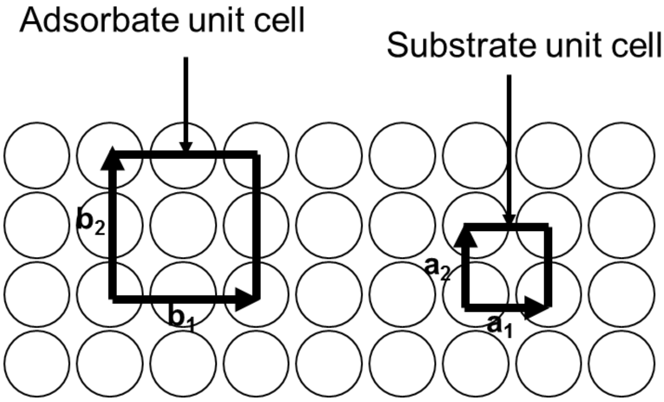

Figure 4.10 Schematic representation of an *fcc* (1 0 0) bulk surface with an adsorbate unit cell and surface unit cell embedded on it.

$$p\left(\frac{b_1}{a_1} \times \frac{b_2}{a_2}\right) R\theta - X \tag{4.14}$$

Where a_1 and a_2 are vectors of the substrate unit cell, and b_1 and b_2 are vectors of the adsorbate unit cell. "*p*" or "*c*" represent primitive or centred surfaces lattice, and *X* is the chemical symbol of the adsorbed species.

If

$$2a_1 = b_1 \qquad (4.15)$$

$$\theta = 0$$

Then the structure in Figure 4.10 can be represented as $p(2 \times 2)$. Omitting the "*p*", the structure can be taken as (2×2). The Woods notation is the most widely used, compared to the Matrix notation. Other Wood notations are shown below (Hermann, 2011) in (Figure 4.11);

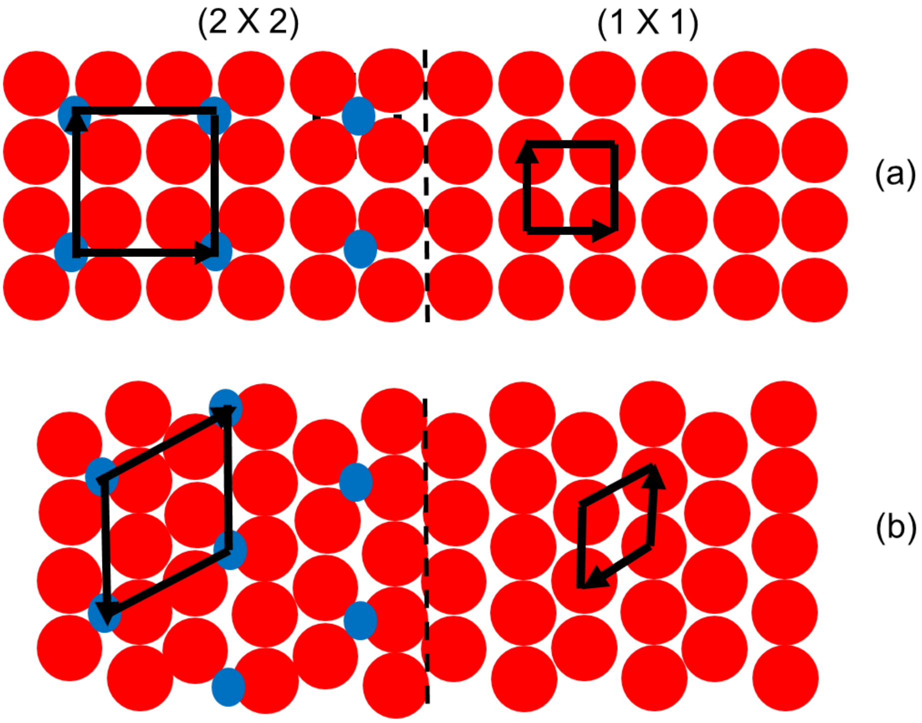

Figure 4.11 Schematic representation of *fcc* (1 0 0) and (1 1 1) bulk surfaces with unit cells represented by Woods notations

In the case of the Matrix notation, the vectors a_1, a_2, b_1, b_2 are expressed in a matrix format. b_1 and b_2 are independently defined as liner combinations of a_1 and a_2. The structure in Figure 4.10 can be represented using the Matrix notation in the form of;

$$\begin{pmatrix} b_1 \\ b_2 \end{pmatrix} = \begin{pmatrix} m_{11} & m_{12} \\ m_{21} & m_{22} \end{pmatrix} \begin{pmatrix} a_1 \\ a_2 \end{pmatrix} \qquad (4.16)$$

$$\begin{pmatrix} b_1 \\ b_2 \end{pmatrix} = \begin{pmatrix} 2 & 0 \\ 0 & 2 \end{pmatrix} \begin{pmatrix} a_1 \\ a_2 \end{pmatrix}$$

$$M = \begin{pmatrix} 2 & 0 \\ 0 & 2 \end{pmatrix}$$

The above matrix notation corresponds to the (2×2) of the Woods notation. This concept of representing unit cells on surface structures with Woods or Matrix notations can also be used in representing surface reconstruction/relaxation and corresponding terminations in crystals. After relaxation, neighboring atoms can unite to form new bonds. This means that the relaxation leading to reconstruction can change the position of surface atoms and the symmetry of the unit cell. In a situation where the vectors of the original unit cell in the bulk surface are a_1 and a_2 before relaxation, and b_1 and b_2 are the vectors of the new unit cell after relaxation, then the relationship between the vectors of both unit cells can be resolved using the Woods or Matrix notation as previously discussed (Guo and Tan, 2009).

4.5 Characteristics and properties of crystalline phases of TiO_2

To reiterate, TiO_2 naturally exists in three polymorphic forms namely; rutile, anatase and brookite. Generally, the physical and physicochemical properties including the stability criterion of TiO_2 are dependent on the shape/structure, size, surface properties, and phase composition of the particles (Koparde and Cummings, 2005, Filyukov et al., 2007, Ramamoorthy et al., 1994a). Rutile and anatase are not only known to be the more important polymorphs of titania but also the most widely researched which can be attributed to their wide range of applications (Koparde and Cummings, 2007). For the purpose of this study, the crystal structural information for the three phases of titania was taken from the Inorganic Crystal Structure Database (ICSD) (http://cds.dl.ac.uk/icsd/index.html) and the atomistic structural-models were created using Accerlys Materials Studio, which is a materials modelling and visualisation software package.

4.5.1 Rutile

Rutile titania can be prepared as an initial crystalline product from hydrolysis by direct boiling of chloride solution while the other phases (i.e. anatase and brookite) can be transformed irreversibly to rutile when heated to temperatures between 700 and 920 ^{0}C (Grant, 1959, Kiejna and et al., 2006). The opaque black nature of single crystal rutile during preparation by the Verneuil flame fusion method is as a result of a little oxygen deficiency but this can be remedied by heating the crystals in an oxygen stream thereby making them transparent with an almost yellow colour (Grant, 1959). Rutile is the most abundant and thermodynamically stable polymorph. It also possesses high refractive index and UV absorption crossover including chemical inertness even in strongly acidic and basic environments (Tao et al., 2004). This unique property makes rutile titania most suitable as a white pigment and an excellent photo-catalyst (Tao et al., 2004).

4.5.1.1 Crystal structure

In terms of its crystal structure, rutile has a tetragonal lattice type (*a* = *b* ≠ *c,* P42/*mnm*). An ionic model is more often used to describe the crystal structure of rutile based on the ions Ti^{4+} and O^{2-} (Grant, 1959). (Syrkin and Di͡atkina, 1950) suggest that rutile has a structure that may be regarded as intermediate between ionic and molecular models. However, the Ti – O separation in the O – Ti – O grouping which is slightly greater than the other four Ti – O spacings justifies the fact that rutile is described by an ionic model. The increased separation has been suggested to be a result of the repulsion between one oxygen ion and four equidistant oxygen ions in the same octahedron (Remy, 1956). The oxygen ions in the rutile crystal structure are arranged in a sort of distorted octahedral form with each octahedron sharing one edge with adjacent members of the chain. Ti^{4+} is surrounded by six O^{2-} at the corners of the octahedron which is slightly deformed and each O^{2-} as surrounded by three Ti^{4+} lying in a plane at the corners of an equilateral triangle (Oliver et al., 1997). The crystal structure manifests chains of ions – O – Ti – O – O – Ti – O with all chains in the same layer parallel and those in adjacent layers perpendicular to one another.

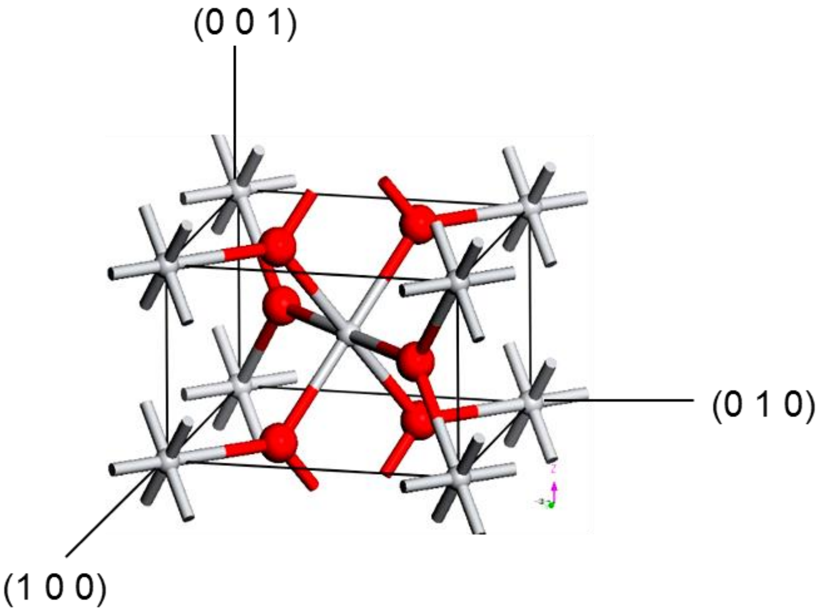

Figure 4.12 Crystal structure of rutile. The grey and red atoms represent the Ti and O atoms respectively. (sourced from the Inorganic Crystal Structure Database (ICSD) (http://cds.dl.ac.uk/icsd/index.html)). Structure generated using Materials Studio

Figure 4.12 above shows the crystalline structure of the rutile phase of TiO_2 with unit cell parameters: *a* (Å) = 4.594 ± 0.003 and *c* (Å) = 2.959 ± 0.002 (Grant, 1959, Baur, 1956). Its *c/a* ratio is 0.6441 (Parker, 1961). In terms of bond lengths, the titanium ions in rutile are at the positions (0, 0, 0) and (½, ½, ½), and the four oxygen ions are at positions ±(x, x, 0), and ±(½ + x, ½ + x, ½ + x). Table 4.3 shows the bond distances and angles of rutile. Figure 4.13 shows the atomic arrangement of a typical tetragonal rutile crystal structure.

Table 4.3 Bond distances and angles of rutile crystal structure (Grant, 1959)

Bond	**Type***	**Number of bonds**	
Ti – O	1	4	1.944 ± 0.004 Å
Ti – O	2	2	1.988 ± 0.006 Å
O – O	3	8	2.780 ± 0.002 Å
O – O	4	2	2.520 ± 0.012 Å
O – O	5	2	2.959 ± 0.002 Å
Bond	**Bond types***	**Number of bonds**	
O – Ti – O	1, 1 (smaller angle)	2	80.8^0
O – Ti – O	1, 1 (greater angle)	2	99.2^0
O – Ti – O	1, 2	8	90.0^0

*The figures refer to the bonds in Figure 4.13

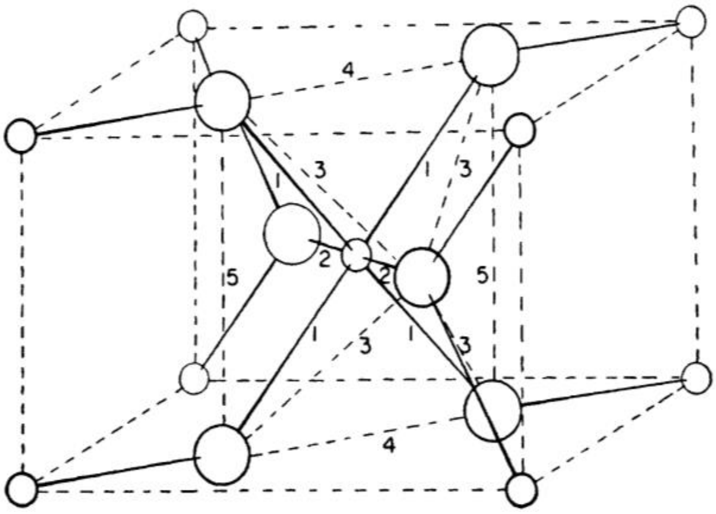

Figure 4.13 Atomic arrangement of tetragonal crystal structure of rutile. Small circles represent Ti, and large circles represent O. The figures refer to the bond types (*) listed in Table 4.3 (Grant, 1959).

Other mechanical and structural properties of rutile titania are given below.

Table 4.4 Some mechanical properties of rutile

Properties	**Value**
Stiffness constants (10^{11} dynes/cm^2) (Parker, 1961)	c_{11}: 27.143 or 26.74
	c_{12}: 17.796 or 18.08
	c_{44}: 12.443 or 12.33
	c_{33}: 48.395 or 47.90
	c_{66}: 19.477 or 18.94
	c_{13}: 14.957 or 14.66
Compressibility (10^{11} dynes/cm^2) (Parker, 1961)	0.0478
Elastic moduli (10^{11} dynes/cm^2) (Grimsditch and Ramdas, 1976)	c_{11}: 2.674 ± 0.002
	c_{33}: 4.790 ± 0.002
	c_{44}: 1.232 ± 0.008
	c_{66}: 1.886 ± 0.020
Refractive indices (Parker, 1961)	n_c = 2.903, n_a = 2.616
Static dielectric constant (at 300^0K) (Parker, 1961)	ϵ_c = 170, ϵ_a = 86
Density (g/cm^3) (sourced from www.azom.com/details.asp)	4.26

4.5.1.2 Crystal Surfaces

The TiO_2 surfaces that are mostly studied are the lowest-energy surfaces (e.g. (110)) which are known to be the thermodynamically most stable surfaces (Barteau, 1996, Idriss and Barteau, 1996). The (011) surface is among the low-energy surfaces and has been predicted by first principles DFT calculations of bulk-terminated rutile surfaces to have the third-lowest surface energy, a little higher than (110) and (100) (Ramamoorthy et al., 1994b). The (011) surface planes are quite common in nano and microcrystalline powder materials (Dulub et al., 2006). Surface relaxation is known to be vital in determining the relaxed equilibrium structures and surface energies of the low index surfaces (Kiejna and et al., 2006). (Ramamoorthy et al., 1994a) observed that the surface energies of these surfaces have an oscillatory variation with the number of layers in a slab. The crystal morphology of rutile crystals has been predicted using the BFDH method in Material Studio and is shown in Figure 4.14.

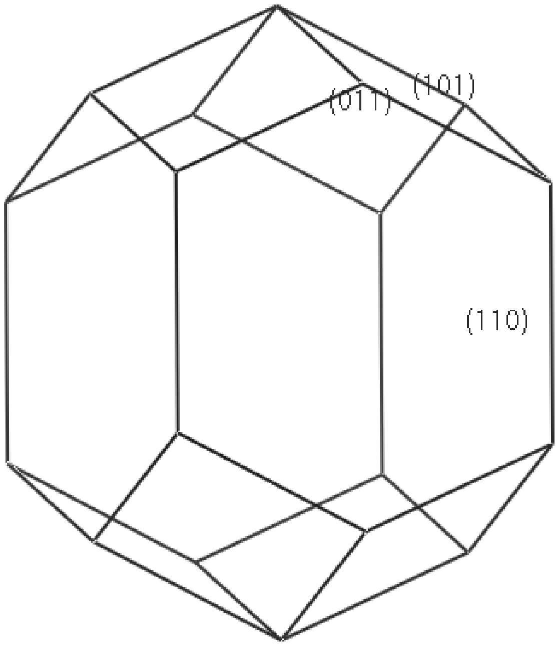

Figure 4.14 Predicted morphology for rutile obtained using the BDFH method of the morphology module in Accelrys Materials Studio 5.2 software.

The rutile (1 1 0) surface as shown in Figure 4.15 is the most studied low index metal oxide surface (Pang et al., 2013) and is very thermodynamically stable as shown using first principles calculations for TiO_2 (Henrich, 1983, Henrich and Cox, 1994, Ramamoorthy et al., 1994a, Hameeuw et al., 2006), making it the dominating facet of rutile crystals (Hameeuw et al., 2006). There are three basic terminations for the rutile (1 1 0) surface which are (1 x 1), (1 x 2) and (1 x 3), with the most studied the (1 x 1) and (1 x 2) terminations.

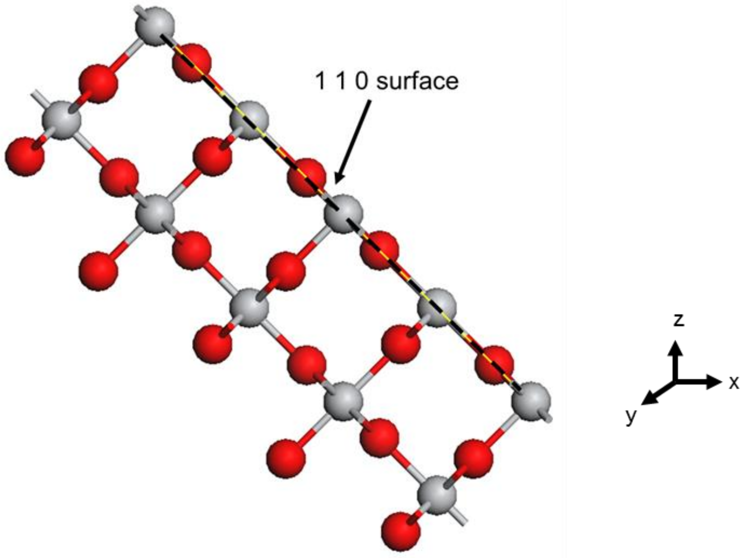

Figure 4.15 Rutile (1 1 0) surface obtained using the cleaved surface builder module in Accelrys Materials Studio 5.2 software.

(Diebold, 2003) has reviewed the structure of the (1 0 0) surface and revealed that it has a complex set of possible terminations. The (1 0 0) surface is shown in Figure 4.16. The scanning probe microscope (SPM) has been used to study this surface and its terminations which are predominantly (1 x 1), (1 x 3) and (1 x 7) (Raza et al., 1999, Klusek et al., 2006).

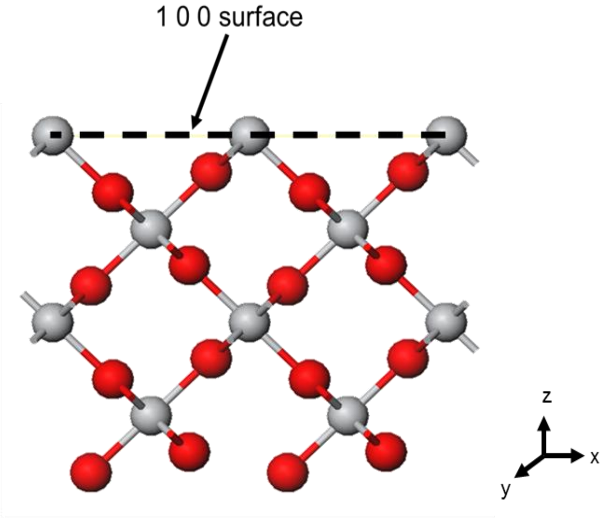

Figure 4.16 Rutile (1 0 0) surface obtained using the cleaved surface builder module in Accelrys Materials Studio 5.2 software.

The (0 0 1) surface (as shown in Figure 4.17) has all its Ti and O atoms as fourfold and twofold coordinated respectively. This has resulted in a higher number of broken bonds on the surface compared to the other low-index rutile surfaces, making the surface energy of (0 0 1) high.

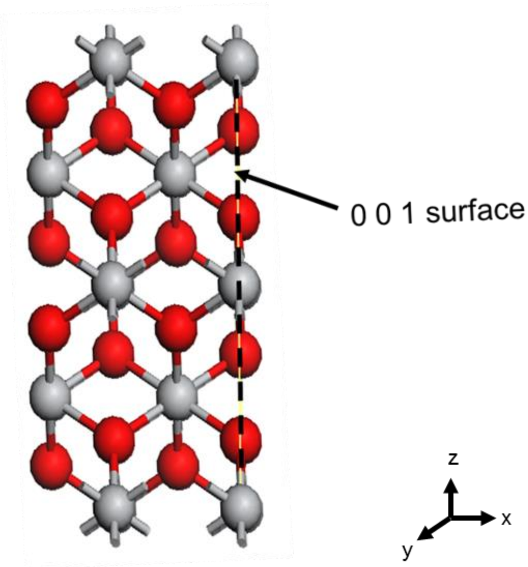

Figure 4.17 Rutile (0 0 1) surface obtained using the cleaved surface builder module in Accelrys Materials Studio 5.2 software

4.5.2 Anatase

The thermodynamic phase stability of titania is dependent on particle size. The anatase form of titania has been found to be the most stable when this form is expressed as nanocrystalline particles and is characterised by higher catalytic activity compared to other forms of titania (Koparde and Cummings, 2007, Erdin et al., 2007). Its unstable nature in the bulk form can be observed upon heating above a threshold temperature at atmospheric pressure (usually about 1000^{0}C but can vary from 400^{0}C to 1200^{0}C, depending on particle size, atmosphere and nature/amount of impurities) where it transforms irreversibly to rutile (Horn et al., 1972). Its stability in the nanocrystalline form makes it important and useful in a wide variety of applications. For example, its stability in the nano phase makes it an important component in most charge separating devices such as dye-sensitized solar cells or rocking-chair lithium batteries which are based on highly porous films with extremely large surface areas that comprise nanocrystalline anatase (Iuga et al., 2007). Furthermore, unlike rutile crystals, which are widely and readily available, anatase crystals are more difficult to obtain (Diebold, 2003).

4.5.2.1 Crystal structure

In 1916, Vegard originally determined the structure of anatase (Horn et al., 1972). It also has a tetragonal lattice type ($a = b \neq c$, *I*41/*amd*), possessing similar coordination to rutile. The difference in structure between anatase and rutile is in the mode of connection of the octahedra units. Unlike rutile, where the chains are connected linearly by the corners of the edge-sharing octahedra, the anatase structure consists of chains of edge-shared octahedral connected in a zigzag manner which are linked to produce a three-dimensional system of edge-shared octahedra (Oliver et al., 1997).

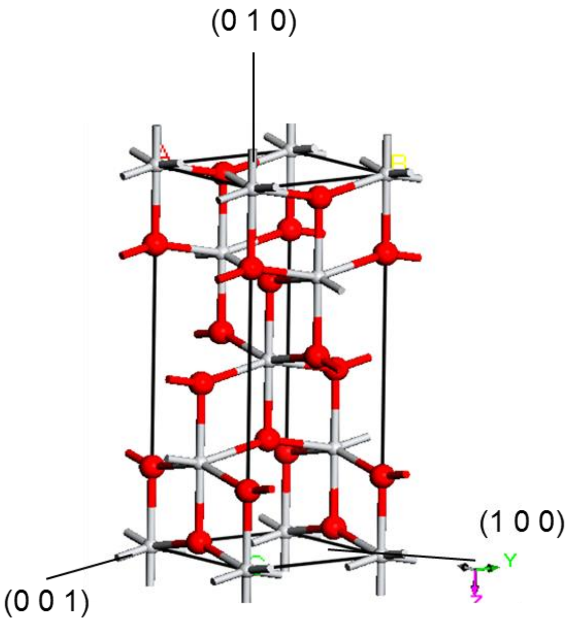

Figure 4.18 Crystal structure of anatase. The grey and red atoms represent the Ti and O atoms respectively. (sourced from the Inorganic Crystal Structure Database (ICSD) (http://cds.dl.ac.uk/icsd/index.html)). Structure generated using Materials Studio

Figure 4.18 above shows the crystalline structure of the anatase phase of TiO_2 with unit cell parameters: *a* (Å) = 3.786 and *c* (Å) = 9.514 (Naicker et al., 2005).

Some properties of anatase titania are given below in Table 4.5;

Table 4.5 Some mechanical properties of anatase

Properties	**Value**
Elastic moduli (10^{11} dynes/cm^2) (Iuga et al., 2007)	c_{11}: 3.20
	c_{33}: 1.90
	c_{44}: 0.54
	c_{66}: 0.60
Refractive indices (sourced from www.azom.com/details.asp)	2.49
Density (g/cm^3) (sourced from www.azom.com/details.asp)	3.84

4.5.2.2 Crystal Surfaces

The stability of the different low-index anatase surfaces has been predicted in several theoretical studies (Vittadini et al., 1998, Ahdjoudj and Minot, 1997, Bredow and Jug, 1995). The crystal morphology of anatase, and its surfaces, has been predicted using the BFDH approach and is shown in Figure 4.19. The (1 0 1) surface has been observed to be the most stable surface, having the lowest calculated surface-energy (Lazzeri et al., 2001, Lazzeri et al., 2002). The (1 0 1) surface has been found to be the most thermodynamically stable anatase surface compared to the more chemically reactive (0 0 1) surface. Research shows that the calculated average surface energy of an equilibrium shaped anatase crystal is smaller than a corresponding rutile crystal (Lazzeri et al., 2001, Lazzeri et al., 2002). This research was based on Perdew-Burke-Ernzergof (PBE) exchange-correlation functional. This observation can be seen in surface energy results for some surfaces for the three crystalline phases of TiO_2 (Table 6.2).

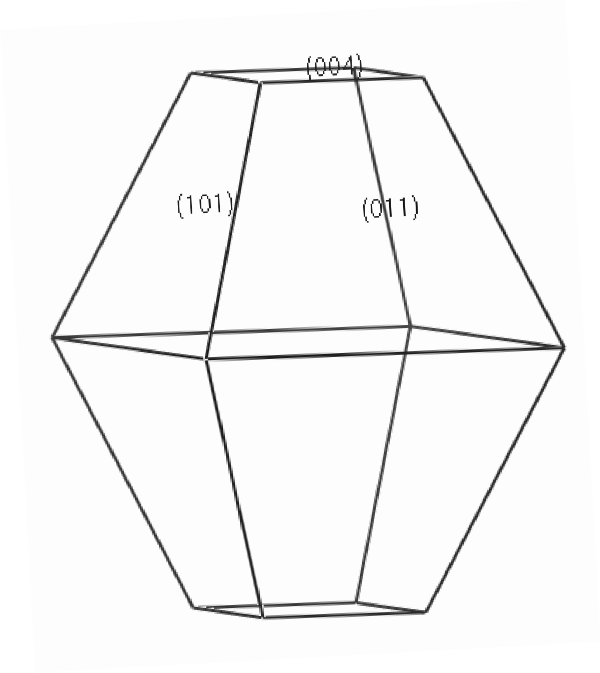

Figure 4.19 Predicted morphology structure for anatase using the BDFH method of the morphology module in Accelrys Materials Studio 5.2 software.

Ti atoms for the (1 0 1) surfaces at the terraces have five-fold and six-fold coordination while Ti atoms at the step edges have four-fold coordinations (Diebold, 2003). The (1 0 1) surface is shown in Figure 4.20.

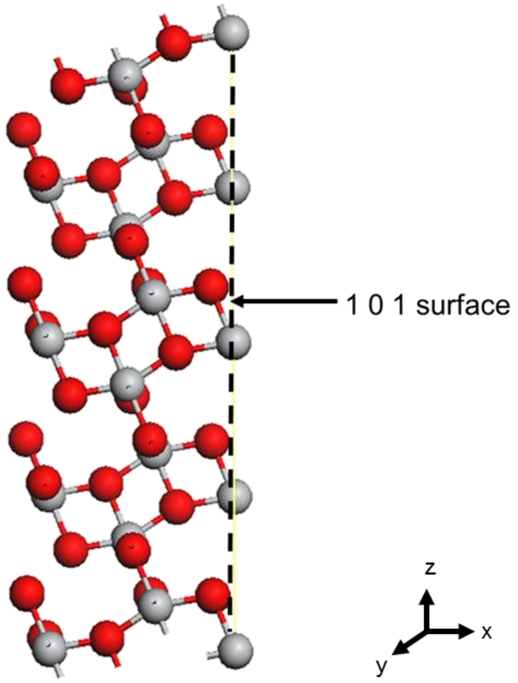

Figure 4.20 Anatase (1 0 1) surface obtained using the cleaved surface builder module in Accelrys Materials Studio 5.2 software

Anatase has a significantly lower proportion of the (0 0 1) surface due to the fact that since it is the surface with higher reactivity, it is usually easier for it to transform to other types of facets during crystal growth. The stable (0 0 1) anatase surface (as shown in Figure 4.21) exhibits a significant number of five-fold Ti coordinated atoms including two-fold and three-fold coordinated oxygen atoms (Diebold, 2003). The (1 x 1) termination is partially unstable and tends to reconstruct to a two-domain (1 x 4) termination, when heated to high temperatures (Herman et al., 2000, Hengerer et al., 2000, Liang et al., 2001, Tanner et al., 2002).

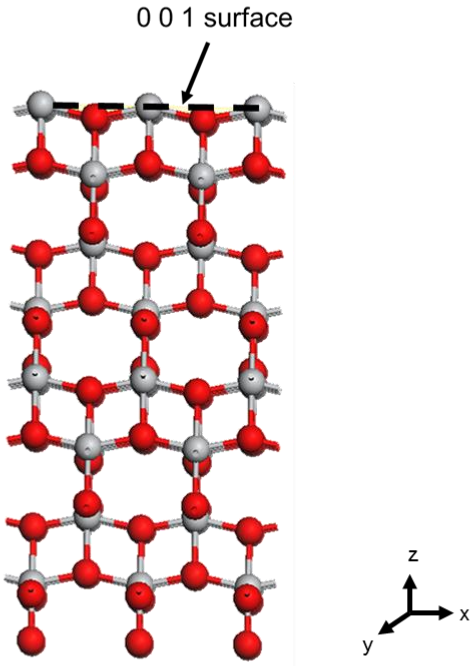

Figure 4.21 Anatase (0 0 1) surface obtained obtained using the cleaved surface builder module in Accelrys Materials Studio 5.2 software

4.5.3 Brookite

The brookite crystalline phase of titania transforms irreversibly to rutile when subjected to high temperatures (usually about 750^{0}C). The crystals of brookite are orthorhombic with space group, *Pbca* (*a* (Å) = 9.166, *b* (Å) = 5.436, *b* (Å) = 5.135) (Figure 4.22) (Naicker et al., 2005). Its Point Group is 2/*m* 2/*m* 2/*m* and its crystals are mostly tabular on, elongated and striated on (0 0 1), rarely tabular on (0 0 1), generally pyramidal on (1 1 1) (sourced from (www.handbookofmineralogy.org/pdfs/brookite.pdf). The crystal morphology of brookite predicted using the BFDH approach, indicating its different surfaces, is shown in Figure 4.23. Unfortunately there is not much detailed information in the literature on the individual surfaces of brookite and since this project is mainly focused on rutile and anatase, discussion about the individual surfaces of TiO_2 phases has been limited to rutile and anatase.

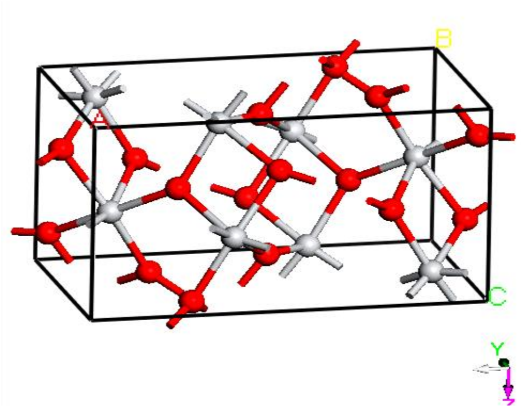

Figure 4.22 Crystal structure of brookite. The grey and red atoms represent the Ti and O atoms respectively. (sourced from the Inorganic Crystal Structure Database (ICSD) (http://cds.dl.ac.uk/icsd/index.html)**).** Structure generated using Materials Studio

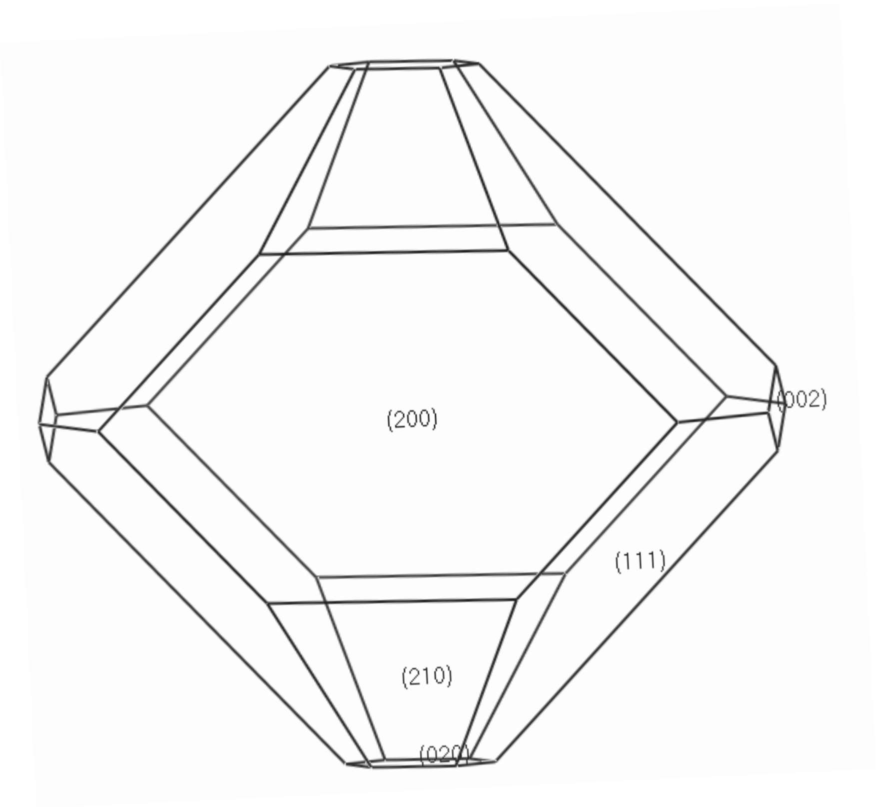

Figure 4.23 Predicted morphology for brookite using the BDFH method of the morphology module in Accelrys Materials Studio 5.2 software.

.

In summary, the basic characteristics of the three crystalline phases of titania are given below in Table 4.6;

Table 4.6 Summary of characteristics of the three crystalline phases of titania

	Rutile	**Anatase**	**Brookite**
Crystal structure	Tetragonal	Tetragonal	Orthorhombic
Lattice parameters (Å)	a = 4.594 b = 2.959	a = 3.786 b = 9.514	a = 9.166 b = 5.436 c = 5.135
Space group	P42/*mnm*	*I*41/*amd*	*Pbca*
Molecule/cell	2	4	8
Density (g/cm^3)	4.26	3.84	3.99
Volume (J. Buongiorno et al.)	62.07	136.25	257.38
Ti-O bond length (Å)	1.95(J. Buongiorno et al.) 1.98(J. Buongiorno et al.)	1.94(J. Buongiorno et al.) 1.97(J. Buongiorno et al.)	1.87 ~ 2.04
O-Ti-O bond angle	81.2^0 90.0^0	77.7^0 92.6^0	77.00 ~ 105^0
Refractive index	2.903	2.49	

More morphological information will be presented in Chapter 6 where the relaxed and unrelaxed crystal morphologies for the three titania phases are predicted using their calculated surface and attachment energies. Also, the mechanical properties (most especially the elastic constants) in Tables 4.4 and 4.5, and the information in Table 4.6 obtained from the literature will be compared to the predicted and calculated properties in Chapter 5 and 6.

4.6 Computational background of the Molecular modelling approach

Molecular modelling can be used to predict the behavioural patterns of nanoparticles including their interactions within the fluid system from a molecular point of view. As ‘molecular’ can simply be related to molecules, a model best describes a system or process by making use of mathematical terms to aid in calculations and predictions. Molecular modelling would therefore have to do with the use of models in the form of systems (usually mathematical) to predict the behaviour of molecules and molecular systems. In recent times, molecular modelling is mostly linked to computer modelling as most mathematical calculations using mathematical concepts such as vectors, matrices, differential equations etc., can be performed using computational techniques. Molecular modelling is spread across such areas as quantum mechanics, molecular mechanics, minimisations, simulations and other computer-based techniques that can aid in understanding and predicting the behaviour of molecular systems (Leach, 2001). Some relevant concepts and techniques to molecular modelling include;

4.6.1 Coordinate systems

The ability to specify the positions of atoms and /or molecules in molecular modelling is of great importance. This can be carried out in two general ways which are; by specifying the ***Cartesian (x, y, z) coordinates*** of all the atoms present (this is the simplest method) and by using ***internal coordinates*** in which case the position of each atom is illustrated relative to other atoms in the system. It is possible to convert internal coordinates to Cartesian and vice versa. However, Cartesian coordinates may be more appropriate when illustrating a set of discrete molecules while internal coordinates are useful when describing the relationship between the atoms in a single molecule (Leach, 2001). Another fact to consider is that Cartesian coordinates are mostly used for molecular mechanics calculations while internal coordinates are used as input when running quantum mechanics programs. Also, internal coordinates remove six degrees of freedom that represent three rigid body translations and three rigid body rotations when dealing with a molecular framework.

4.6.2 Potential energy surfaces

The Born-Oppenheimer approximation, which allows the electronic and nuclear motions to be separated, is usually assumed to operate in molecular modelling. This takes into account the fact that nuclei do not change their relative positions significantly on the timescale of the motion of electrons given the mass difference (~ 3 orders of magnitude). The energy of a molecule in its ground state can be taken as a function of only the nuclear coordinates. The energy will normally change as a result of movement of the nuclei (Leach, 2001). This nuclear movement leading to new positions may be as a result of simple processes such as a single bond rotation or movement of a large number of atoms. This movement and change in nuclear positions will greatly influence the system energy. In cases where there is a small change in energy, this could be due to rotation about single bonds which occurs mostly in small isolated molecules. Usually movements on a multi-dimensional surface, otherwise called an energy surface, can be associated with the energy of a system. Of more interest are stationary points on the energy surface where the first derivative of the energy is zero with respect to the internal or Cartesian coordinates and means that at a stationary point the forces on all the atoms are zero (Leach, 2001).

4.6.3 Molecular Surfaces

Almost all investigations carried out using molecular modelling involve non-covalent interaction between two or more molecules. Studying these interactions can be best undertaken by analysing the *van der Waals* (constructed from the overlapping van der Waals spheres of the atoms), *molecular* (constructed by tracing out the inward-facing part of the probe sphere as it rolls on the van der Waals surface of the molecule) or *accessible surfaces* (constructed by tracing the centre of the probe molecule as it rolls on the van der Waals surface of the of molecule) of the molecule (Leach, 2001) (Figure 4.24). The molecular surface contains two different types of surface element which include the *contact surface* (regions where the probe is really in contact with the van der Waals surface of the target sphere) and the *re-entrant surface* (regions where there are crevices that are too narrow for the probe molecule to break through) (Leach, 2001). The accessible surface is widely used.

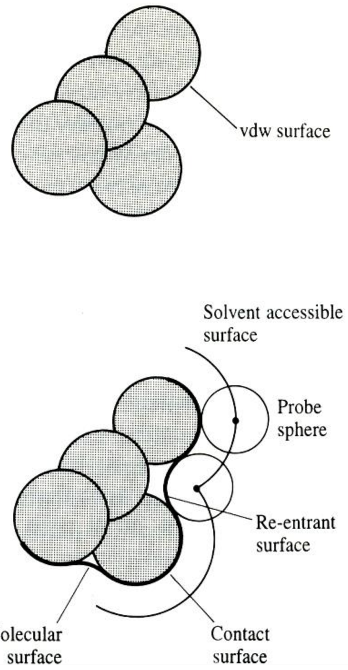

Figure 4.24 The van der Waals, molecular and accessible surfaces of a molecule. (Leach, 2001)

4.7 Molecular mechanics: Force field models

Unlike quantum mechanics, which considers the electrons in a system, molecular mechanics derives the energy of a system as a function of only the nuclear positions and so is used to carry out calculations on systems with large number of atoms. Force fields can predict more accurately than quantum mechanics for this kind of system within a short computer time. However, the latest DFT calculation methods can calculate dispersion forces, for example, but at a much greater cost in terms of computational time and effort. Molecular mechanics is based on the assumption of the Born-Oppenheimer approximation and is based on the interactions within a system being due to processes such as the stretching of bonds, the rotations about single bonds and the opening and closing of angles (Leach, 2001).

Most force fields used in molecular modelling can be described in terms of four components which capture both intra and intermolecular forces within the system. Although certain complicated force fields contain additional terms/functions, functions (which are contained in these four components) present in this force field describe: the deviation of bonds and angles away from their equilibrium position, the mode of change of the energy as rotation of bonds occur and the interaction between non-bonded component of the system (Leach, 2001). A form of this force field which can be used to model single molecules or assemblies of atoms and/or molecules is: (Leach, 2001);

$$U(r^N) = \sum_{bonds} \frac{k_i}{2}(l_i - l_{i,0})^2 + \sum_{angles} \frac{k_i}{2}(\theta_i - \theta_{i,0})^2 + \sum_{torsions} \frac{V_n}{2}(1 + \cos(n\omega - \gamma)) + \sum_{i=1}^{N} \sum_{j=i+1}^{N} \left(4\varepsilon_{ij} \left[\left(\frac{\sigma_{ij}}{r_{ij}} \right)^{12} - \left(\frac{\sigma_{ij}}{r_{ij}} \right)^{6} \right] + \frac{q_i q_j}{4\pi\varepsilon_0 r_{ij}} \right) \tag{4.17}$$

From Equation 4.17 above, $U(r^N)$ is the potential energy which is a function of the positions (r) of N particles or atoms. The first term above models the interaction between pairs of bonded atoms using the harmonic potential and reveals the increase in energy as the bond length l_i deviates from the reference value $l_{i,0}$. The second term, which is modelled using the harmonic potential as well, involves the summation of all valence angles in the molecule. The third term which is a torsional potential models the mode of energy changes with respect to the rotation of a bond. The fourth term captures the non-bonded interactions which are usually estimated for all sets of atoms (i.e. i and j) that are either in different molecules or in the same molecule but separated by at least three bonds with a 1, n relationship (where $n \geq 4$) (Leach, 2001). Non-bonded terms for simple force fields are normally modelled using a Coulomb potential term for electrostatic interactions and a Lennard-Jones potential for van der Waals interactions (Leach, 2001). These contributions are represented in Figure 4.25 below

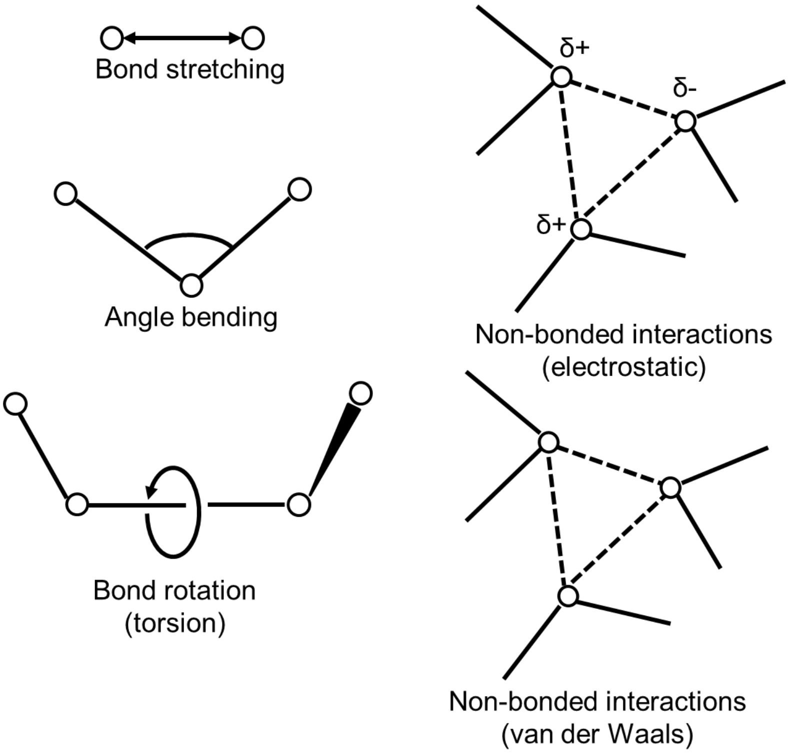

Figure 4.25 Schematic representation of the four main contributions to a molecular mechanics force field: bond stretching, angle bending, torsional terms and non-bonded interactions. (Leach, 2001)

4.7.1 Bond stretching

The Morse potential is the most useful potential that can be used to model the potential energy curve (shown in Figure 4.26) associated with bond stretching.

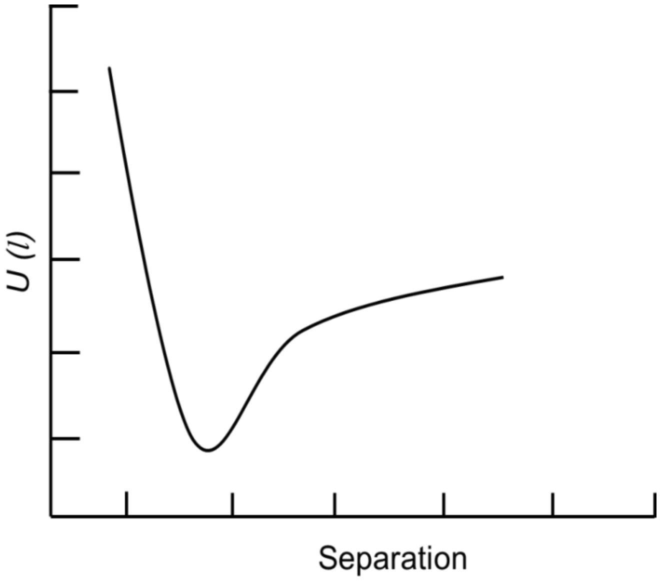

Figure 4.26 Variation in bond energy with interatomic separation. (Leach, 2001)

The Morse potential can be taken as (Leach, 2001);

$$U(l) = D_e\{1 - exp[-a(l - l_0)]\}^2 \tag{4.18}$$

D_e is the depth of the potential energy minimum and $a = \omega\sqrt{(\mu/2D_e)}$ where μ is the reduced mass and ω is associated with the stretching constant of the bond k by, $\omega = \sqrt{(k/\mu)}$. l_0 is the reference value of the bond. Apart from the fact that the Morse potential is not computationally efficient (as it requires three parameters per bond to be specified), it is rarely used in the force fields of molecular mechanics owing to the fact that in molecular mechanics calculations, bonds hardly ever deviate far from their equilibrium positions (Leach, 2001). A Harmonic potential formula influenced by Hooke's law is a simpler method in which case the energy varies with the square of the displacement from the reference bond length l_0 and is shown below;

$$U(l) = \frac{k}{2}(l - l_0)^2 \tag{4.19}$$

The parameter, l_0 can be referred to as either as the ***reference bond length*** or the ***equilibrium bond length***, although they might have specific definitions (depending on its application). While the *reference bond length* is the value which the bond assumes when all the terms in the force field are set to zero, the *equilibrium bond length* is the value assumed in a minimum energy structure when all other terms in the force field contribute (Leach, 2001). The Harmonic potential is a good fit to the shape of the potential energy curve at the bottom of the potential well, especially at distances that are associated with bonding in ground-state molecules and also is less exact away from equilibrium (Figure 4.27) (Leach, 2001).

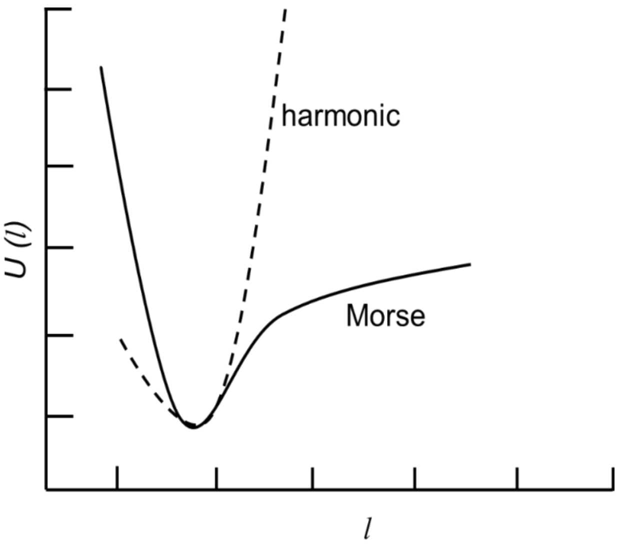

Figure 4.27 Comparison of the simple harmonic potential (Hooke's law) with the Morse curve. (Leach, 2001)

4.7.2 Angle bending

Hooke's law, also referred to as harmonic potential, can also be used to describe the deviation of angles from their reference values and is given below (Leach, 2001);

$$U(\theta) = \frac{k}{2}(\theta - \theta_0)^2 \tag{4.20}$$

Compared to bond stretching, which requires more energy to stretch or relax a bond, less energy can actually displace an angle away from its equilibrium position. A force constant and reference value takes into account the contribution of each angle as seen in Equation 4.20 above.

4.7.3 Torsional terms

Most of the deviations observed in structures and their energies can be linked to the influence of torsional and non-bonded contributions such as bond stretching and angle bending are known for their hard degrees of freedom due to the fact that large energies are required to create significant observable deviation. Torsional potentials are usually expressed as a cosine series expansion as given below (Leach, 2001);

$$U(\omega) = \sum_{n=0}^{n} \frac{V_n}{2}[1 + \cos(n\omega - \gamma)] \tag{4.21}$$

where ω is the torsion angle.

Equation 4.21 above can also be expressed as;

$$U(\omega) = \sum_{n=0}^{n} C_n\,(\cos(\omega))^n \tag{4.22}$$

Where V_n can be taken as the barrier height, although it could be misleading at times especially when more than one term such as terms for non-bonded interactions (which could also contribute to the barrier height) are present in the force field equation. V_n also shows the relative barriers to rotation (Leach, 2001). *n* which is the multiplicity, gives the number of minimum points in the function as the bond is rotated through 360^0 and γ, the phase factor, gives the position in which the torsion angle potential energy goes through its minimum value (Leach, 2001). Figure 4.28 shows the effects of varying V_n, *n* and γ for frequently used torsional potentials.

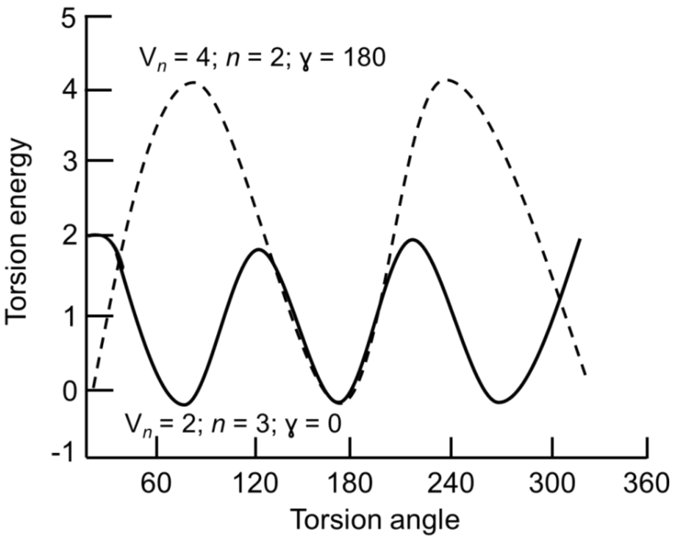

Figure 4.28 Torsional potential varies as shown for different values of V_n, *n* and *γ*. (Leach, 2001).

Although this project focuses on intermolecular non-bonded interactions, a background on intramolecular interactions and its force field (Equation 4.17) has been provided to give a general overview of molecular mechanics. Especially, the first three terms in Equation 4.17 (i.e. for bonds, angles and torsions) are not relevant to the current project. The subsequent section (i.e. Section 4.7.4) will provide more detail on intermolecular non-bonded interactions which are most relevant to this project.

4.7.4 Non-bonded interactions

As the name implies, non-bonded interactions are independent of an explicit bonding connection between atoms. These types of interactions occur in independent molecules and atoms which can greatly influence the resulting molecular structures. Modelling these interactions is dependent on the distance between the molecules/atoms and so these through-space interactions are usually modelled as a function of an inverse power of the distance (Leach, 2001). In force fields, the non-bonded terms are usually regarded as electrostatic interactions and van der Waals interactions (or dispersion forces).

4.7.4.1 Electrostatic interactions (Coulomb Interaction)

An uneven charge distribution in a molecule occurs when electrons from less electronegative elements are been attracted by more electronegative elements. The resulting charge distribution (which is intended to replicate the electrostatic properties of the molecule) can be characterised in different ways, especially by an organisation of fractional point charges all through the molecule. Charges confined at the nuclear centres, are usually known as partial atomic or net atomic charges. Subsequently, Coulomb's law can be used to estimate the electrostatic interaction between two molecules or different parts of same molecule, in terms of the summation of interactions between pairs of point charges (Leach, 2001);

$$U = \sum_{i=1}^{N_A} \sum_{j=0}^{N_B} \frac{q_i q_j}{4\pi\varepsilon_0 r_{ij}} \tag{4.23}$$

Where N_A and N_B are the numbers of point charges in the two molecules, q_i and q_j are point charges separated by a distance r_{ij} and ε_0 is the permittivity of empty space.

The *central multipole expansion* is a method for calculating electrostatic interactions and its principle is on the basis that the molecule is a single unit. This expansion is based on the electric moments or multipoles: the charge (*q)*, dipole (*μ*), quadrupole (*Θ*), octopole (*Φ*), etc. Usually, the lowest non-zero electric moments of interest are dipoles, for most uncharged molecules possess this lowest non-zero moment. Following this, multipole moments can be represented by a suitable distribution of charges. Dipoles can be represented using two charges placed at a suitable distance apart. A quadrupole can be represented using four charges and an octopole by eight charges (Leach, 2001). Now, considering the simple case of a molecule with two charges q_1 and q_2 placed at positions $-z_1$ and $-z_2$ respectively (Figure 4.29), the electrostatic potential at point P (which is a distance r_1 from charge q_1 and r_2 from charge q_2) is given by (Leach, 2001);

$$\emptyset(r) = \frac{1}{4\pi\varepsilon_0}\left(\frac{q_1}{r_1} + \frac{q_2}{r_2}\right) \tag{4.24}$$

Applying the cosine rule will give;

$$\emptyset(r) = \frac{1}{4\pi\varepsilon_0}\left(\frac{q_1}{\sqrt{r^2 + z_1^2 + 2rz_1\cos\theta}} + \frac{q_2}{\sqrt{r^2 + z_1^2 - 2rz_1\cos\theta}}\right) \tag{4.25}$$

For the case where $r \gg z_1$ and $r \gg z_2$, then this expressions can be expanded as shown below;

$$\emptyset(r) = \frac{1}{4\pi\varepsilon_0}\left(\frac{q_1 + q_2}{r} + \frac{(q_2 z_2 - q_1 z_1)\cos\theta}{r^2} + \frac{(q_1 z_1^2 + q_2 z_2^2)(3\cos^2\theta - 1)}{2r^3} + \cdots\right) \tag{4.26}$$

The suitable terms in the expansion can now be linked to the different electric moments as seen below;

$$\emptyset(r) = \frac{1}{4\pi\varepsilon_0}\left(\frac{q}{r} + \frac{\mu\cos\theta}{r^2} + \frac{\Theta(3\cos^2\theta - 1)}{2r^3} + \cdots\right) \tag{4.27}$$

From Equation 4.27 above, $(q_1 + q_2)$ is the charge, $(q_2 z_2 - q_1 z_1)$ is the dipole, $(q_1 z_1^2 + q_2 z_2^2)$ is the quadropole, and so on.

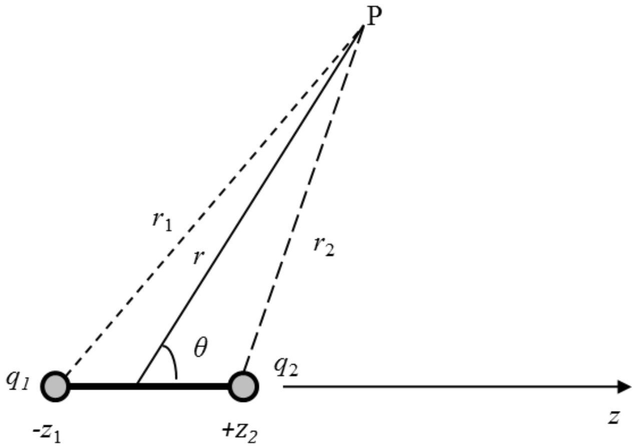

Figure 4.29 The electrostatic potential due to two point charges. (Leach, 2001)

Now taking into account the effect of placing another molecule with a linear charge distribution (i.e. charges $q_1' + q_2'$) with its centre of mass at the point P, four parameters can be used to describe the relative orientation of the two molecules (Leach, 2001). This can be seen in Figure 4.30 which reveals the distance joining the centres of mass of the molecules and three angles.

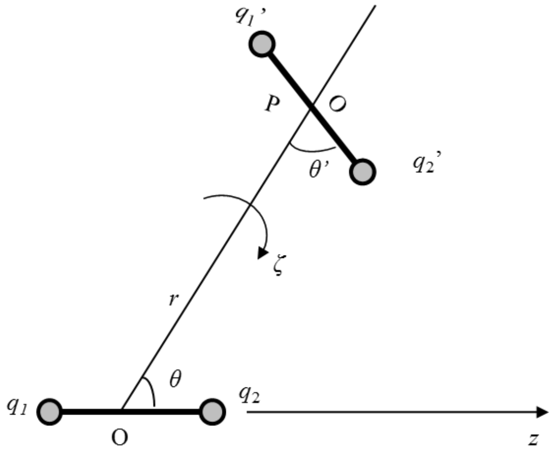

Figure 4.30 The relative orientation of two dipoles. (Leach, 2001)

It has been gathered that the energy of interaction between two charge distributions is an infinite series that includes charge-charge, charge-dipole, dipole-dipole, charge-quadrupole, dipole-quadrupole interactions, quadrupole-quadrupole terms and so on which depend on various inverse powers of the separation *r* (Leach, 2001). A notable fact is that for proper utilisation of these expressions, the separation of the two molecules *r* has to be much larger than the internal dimensions of the molecules. Figure 4.31 shows adequate arrangements for the different multipoles (Leach, 2001).

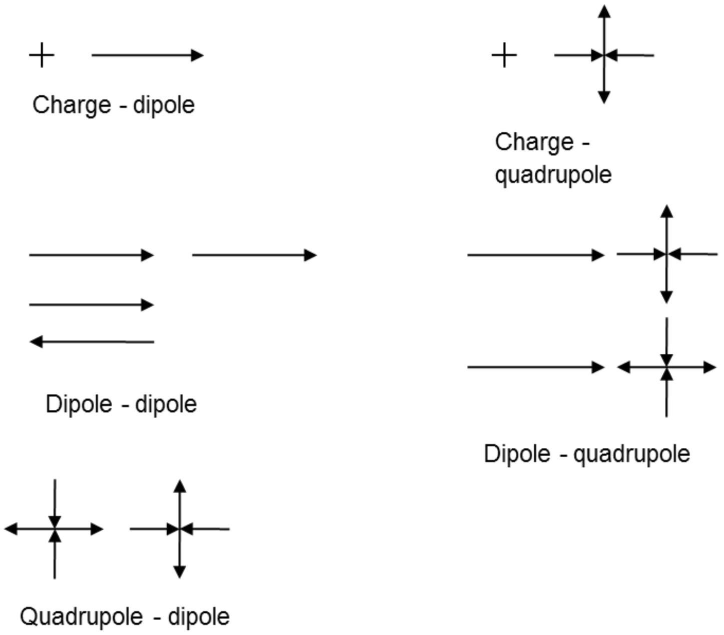

Figure 4.31 The most favourable orientations of various multipoles. (Leach, 2001)

4.7.4.1.1 The Ewald method for calculating Coulomb interactions

The Ewald method is a widely employed approach used in calculating the electrostatic potential experienced by an ion in the presence of other ions in a three-dimensional material such as a crystal. Consider a lattice made up of ions with spherically shaped positive or negative charges, the total potential at an ion can be computed as the sum of two distinct but related potentials, $\varphi = \varphi_1 + \varphi_2$ (Kittel, 1971). φ_1 is the potential of a periodic structure having a Gaussian distribution of charges positioned at each ion site, with similar signs as those of the real ions. φ_2 is the potential of a lattice of point charges having an extra Gaussian distribution of opposite sign positioned directly on the sites of the point charges. φ_1 may be calculated as the difference between two potentials, φ_a and φ_b, where φ_a is the potential of a continuous series of Gaussian distributions and φ_b is the potential of the single Gaussian distribution on the reference point. Splitting the calculation into two parts φ_1 and φ_2 provides an optimum width for each Gaussian peak for good convergence of both parts at the same time (Kittel, 1971). φ_2 can be calculated based on three contributions from each ion point. These contributions are from the point charge, from the part of the Gaussian distribution situated inside a sphere of radius r_1 about the *i*th ion point, and from the part situated outside the sphere. The Ewald method can also be applied to dipolar and quadrupolar arrays.

4.7.4.2 van der Waals interactions

The behaviour of atoms like those of the rare gas has shown that all of the multipole moments are zero and so the presence of dipole-dipole or dipole-induced dipole interactions is impossible. This obviously means that electrostatic interactions cannot possibly account for all of the non-bonded interactions (Leach, 2001). This does not mean that interactions between atoms in a system are not present. These other forces of interaction which exist are known as van der Waals forces and the interaction energy will vary with the separation distance of atoms.

a) Dispersive interactions

The van der Waals interaction between atoms or molecules is usually as a result of attractive and repulsive forces. While the attraction forces are long-range, the repulsive forces are short-range. London in 1930 used quantum mechanics to illustrate that the *dispersive forces* (which are due to instantaneous dipoles which occur during the fluctuations in the electron cloud) actually give rise to the attractive interaction and so this interaction is at times referred to as the London force (Leach, 2001). Dipoles of atoms could be induced by neighbouring instantaneous dipoles in a molecule thereby creating an attractive inductive effect. Drude proposed a simple model to illustrate the dispersive interaction and it comprises molecules with two charges, +*q* and –*q* separated by a distance *r* (Figure 4.32).

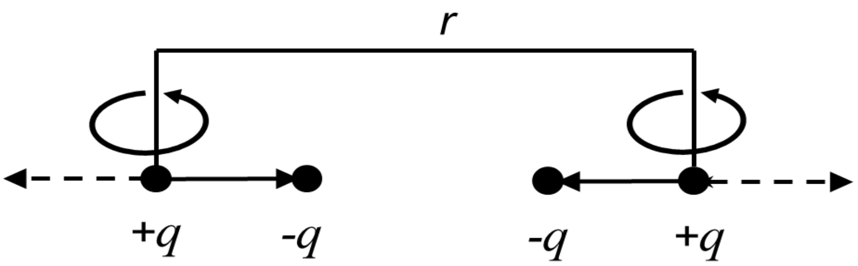

Figure 4.32 The Drude model for dispersive interactions. (Leach, 2001)

As seen in Figure 4.32, the negative charge makes a simple harmonic motion with angular frequency ω along the z axis about the stationary positive charge. The potential energy of an isolated Drude molecule is $\frac{1}{2}kz^2$ when the force constant for the oscillator is k and if the mass of the charge of the oscillator is m, where z is the separation distance of the two charges. $\omega = \sqrt{(k/m)}$ relates ω to the force constant (Leach, 2001). Now by introducing a second identical Drude molecule as seen in Figure 4.32 with an oscillating negative charge and positive charge also situated on the z axis as well, it can be observed that when the two molecules are separated infinitely there will be no interaction. The total ground state energy of the system will have the form, $\hbar\omega / 2\pi$, implying that the energy is twice the zero-point energy of a single molecule (Leach, 2001). Also as the molecules get closer along the z axis, the interactions between the two dipoles can be represented in an approximation given by (Leach, 2001);

$$U(r) = -\frac{\alpha^4 \omega}{2(4\pi\varepsilon_0)^2 r^6} \tag{4.28}$$

The Drude model show that the dispersion interaction varied as $1/r^6$. By expanding the two-dimensional Drude model to three dimensions we have (Leach, 2001);

$$U(r) = -\frac{3\alpha^4 \hbar\omega}{4(4\pi\varepsilon_0)^2 r^6} \tag{4.29}$$

Considering a more sophisticated model written as a series expansion (as the Drude model considers just the dipole-dipole interaction) where higher order due to dipole-quadrupole, quadrupole-quadrupole, etc interactions are taken into account, we have (Leach, 2001);

$$U(r) = \frac{C_6}{r^6} + \frac{C_8}{r^8} + \frac{C_{10}}{r^{10}} + \cdots \tag{4.30}$$

For this, all of the C_n coefficients are negative which depicts an attractive interaction.

b) Repulsive interaction

Most of the time, for distances below about 3 Å, further decrease in the separation between a pair of atoms could lead to a large increase in the energy which has its origin in quantum mechanics and is given in terms of the Pauli principle (Leach, 2001). This principle disallows two electrons of any kind in a system from possessing the same set of quantum numbers. The short-range repulsive forces are usually referred to as *exchange forces* or *overlap forces* as the interaction is as a result of electrons with the same spin. A reduction in the electrostatic repulsion between pairs of electrons is a resulting effect of the exchange of forces. This occurs by restricting the electron pairs from occupying similar space region (i.e. internuclear region) (Leach, 2001). Repulsion between the incompletely shielded nuclei occurs as the electron density in the internuclear region is reduced.

c) Two-body Short-range Interactions

Quantum mechanics can be used to calculate the dispersive and exchange-repulsive interactions between atoms and molecules. Terms that represent the interaction between atoms when they are bonded must be incorporated as contributions to the energy. For a force field approach, a simple empirical expression that can be more easily calculated is required to precisely model the interatomic potential curve (Figure 4.33).

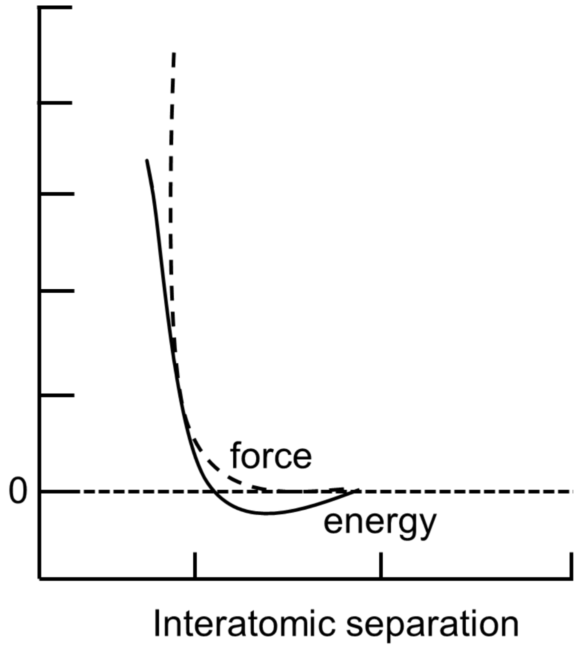

Figure 4.33 The interaction energy and the force between two argon atoms. (Leach, 2001)

A widely recognised and suitable van der Waals potential function of this kind is the *Lennard-Jones 12-6 function* which is given by (Leach, 2001);

$$U(r) = 4\varepsilon\left[\left(\frac{\sigma}{r}\right)^{12} - \left(\frac{\sigma}{r}\right)^{6}\right] \tag{4.31}$$

The above potential comprises of two adjustable parameters which are; the collision diameter σ and the well depth ε (Figure 4.34). The collision diameter is the separation distance for which the energy is zero.

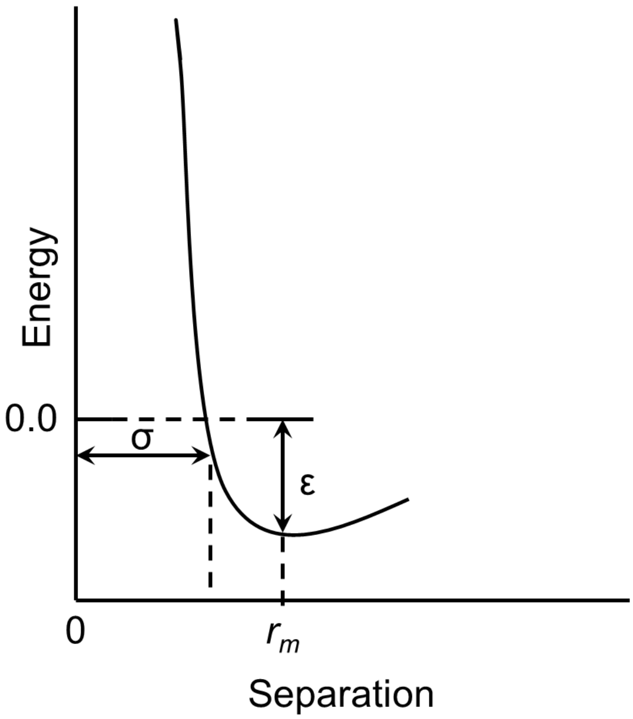

Figure 4.34 The Lennard-Jones potential. (Leach, 2001)

A case in which the Lennard-Jones equation is expressed in terms of the separation where the energy passes through a minimum, r_m is possible. The first derivative of the energy with respect to the internuclear distance is zero at this separation (i.e.$\partial U/\partial r = 0$). From this derivative it can be shown that $r_m = 2^{1/6}\sigma$ and so the Lennard-Jones potential can be written as a function of *r* (Leach, 2001);

$$U(r) = \varepsilon\{(r_m/r)^{12} - 2(r_m/r)^6\} \tag{4.32}$$

Or

$$U(r) = A/r^{12} - C/r^6 \tag{4.33}$$

Where $A = \varepsilon r_m^{12}$ or $(4\varepsilon\sigma^{12})$ and $C = 2\varepsilon r_m^6$ or $(4\varepsilon\sigma^6)$.

The Lennard-Jones potential is composed of an attractive part that varies as r^6 and a repulsive part that varies as r^{12} (Equation 4.33) (Leach, 2001).

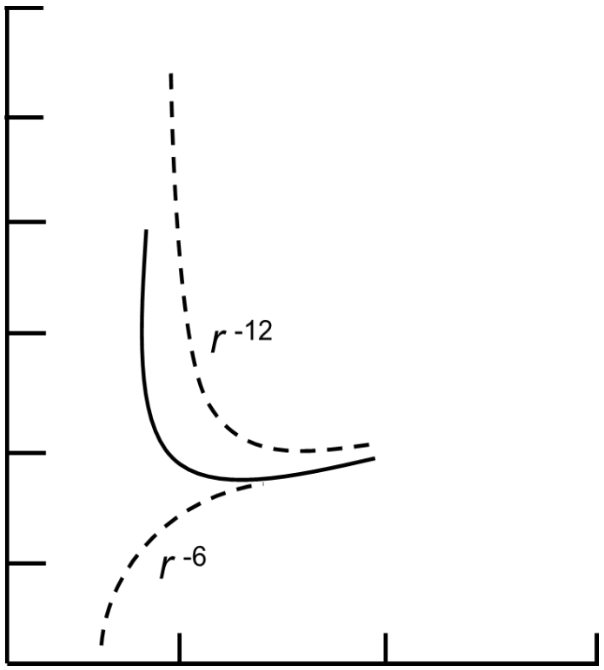

Figure 4.35 Diagram showing the Lennard-Jones potential constructed from a repulsive component $\boldsymbol{\alpha r^{-12}}$and an attractive component $\boldsymbol{\alpha r^{-6}}$. (Leach, 2001)

A *Buckingham potential* is a proposed potential for the case where r^{12} is replaced by a more realistic exponential expression and is given by;

$$U(r) = \varepsilon\left[\frac{6}{\alpha - 6}e^{-\alpha\left(\frac{r}{r_m}-1\right)} - \frac{6}{\alpha - 6}\left(\frac{r_m}{r}\right)^6\right] \tag{4.34}$$

There are basically three parameters which can be adjusted in the Buckingham potential and they are; ε, r_m and α. During calculations, the Buckingham potential becomes strongly attractive at extremely short distances as can be seen in Figure 4.36.

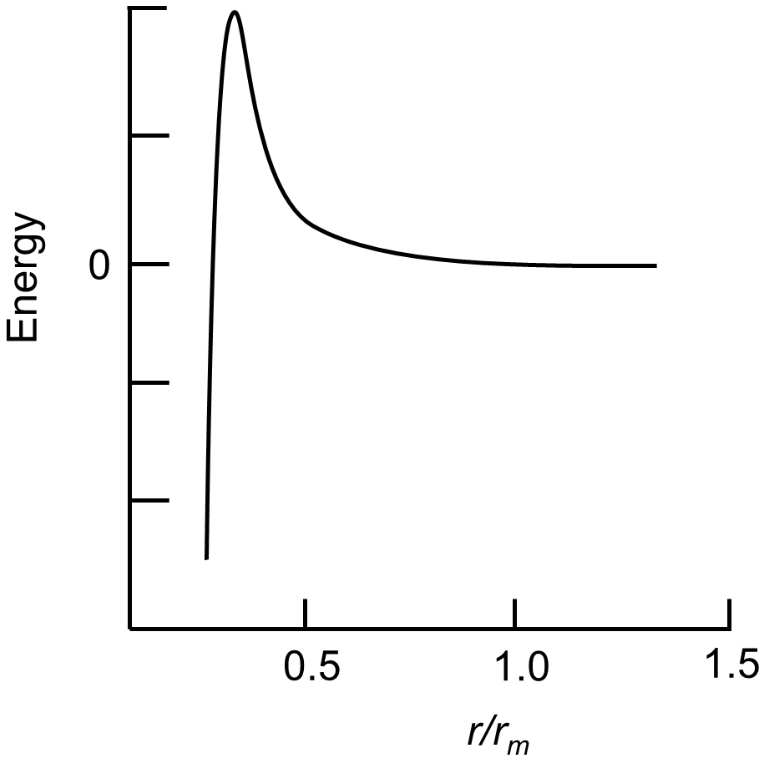

Figure 4.36 A setback of the Buckingham potential is that it becomes steeply attractive at short distances. (Leach, 2001)

Although the Lennard-Jones potential with an exponent form between 9 and12 is more robust, as the repulsion increases faster with decreasing distance than the attractive dispersion term, theoretically, the Buckingham potential is easier to validate as the repulsion between overlapping electron densities due to the Pauli principle take an exponential form at reasonable distances (Leach, 2001, Gale and Rohl, 2003).

d) Three-body Interactions

We can consider three-body terms from either a covalent or ionic perspective. In the former it represents the repulsion between bond pairs or lone pairs and so the expression used is usually harmonic in nature, which accounts for deviation from the expected angle for the coordination environment (Leach, 2001, Gale and Rohl, 2003);

$$U_{ijk} = \frac{1}{2}k_2(\theta_{ijk} - \theta_0)^2 \tag{4.35}$$

For the latter (referring to ionic materials), the three-body potential represents the contribution of the three-centre dispersion especially between the more polarisable anions and is usually modelled by the Axilrod-Teller potential (Gale and Rohl, 2003);

$$U_{ijk} = k\frac{(1 + 3\cos(\theta_{ijk})\cos(\theta_{jki})\cos(\theta_{kij}))}{r_{ij}^3 r_{jk}^3 r_{ik}^3} \tag{4.36}$$

e) Four-body Interactions

Four-body interactions are usually included only where they describe torsional angles and so the functional form involves the cosine of the torsional angle with factors which take into account the equilibrium torsional angle, $\emptyset_0$, and the periodicity in terms of rotation about the central bond, and is of the form (Gale and Rohl, 2003);

$$U_{ijkl} = k_4(1 + m\cos(n\,\emptyset - \emptyset_0)) \tag{4.37}$$

Another form of torsional potential is the one that uses a harmonic potential to describe the mode of the bending in the outer plane of a central atom with planar coordination geometry. This can be used when describing aromatic systems and can also be used in modelling carbonate anions.

As important as the bulk properties of the material are, so are the properties of the materials surfaces. This is because these surface properties play a major role in determining the interaction between the material and the external environment. It is evident that, apart from the fact that reactions and catalysis of the material mainly occurs at the surface, the shape of the particles or crystals formed is determined by the properties of the surface relative to the bulk (Gale and Rohl, 2003). The surface structure and its properties is a key determining factor for the bulk polarization and net dipole of a material. Surface calculations are mainly performed in two stages which are; the formation of the surface from the bulk material and then the calculation of its optimized structure and properties. Basically, the surfaces are each specified by at least two pieces of information which are; the Miller indices (*hkl*) of the plane which defines the orientation of the bulk cleavage, and also the shift (which is the displacement of the plane relative to the unit cell origin). There are three types of surface which are key factors in determining the mode of surface cleaving (Figure 4.37).

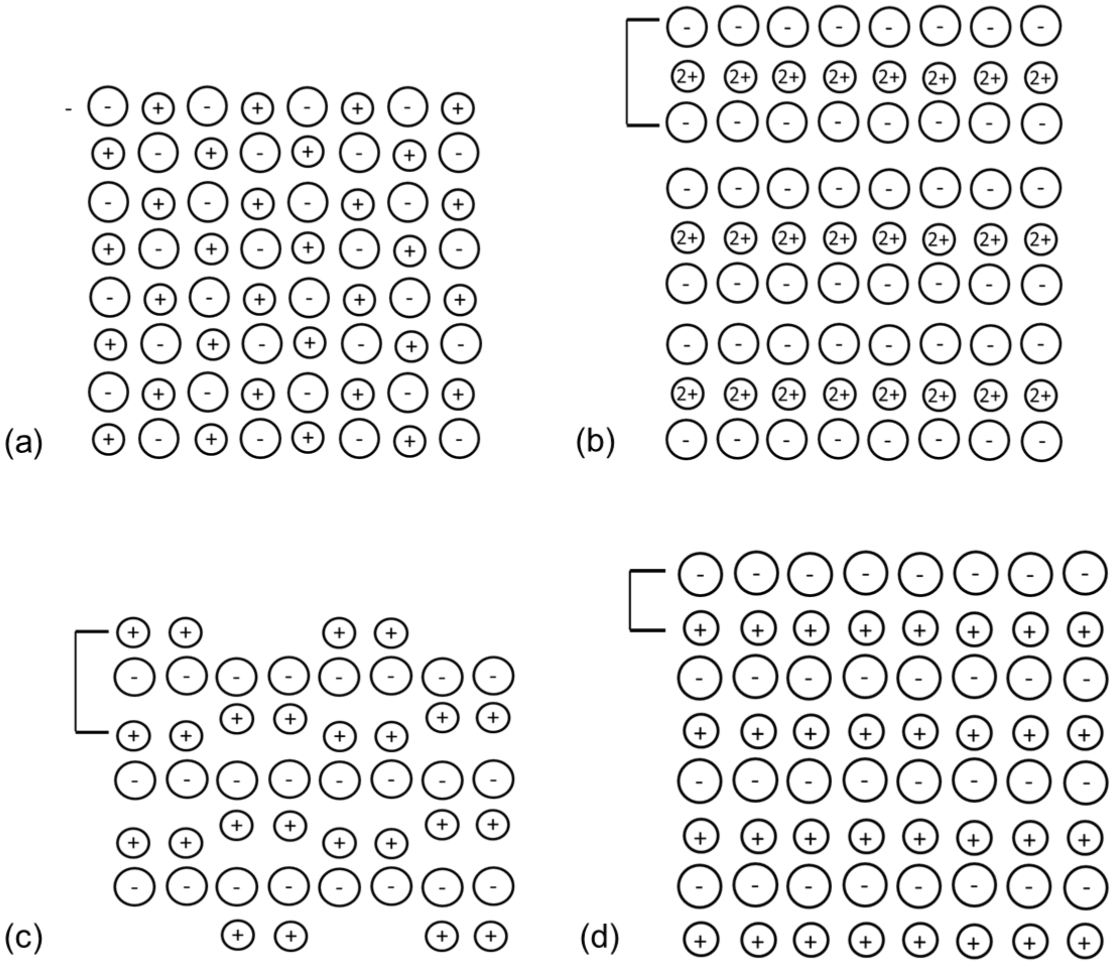

Figure 4.37 The three types of surface as grouped by Tasker (a) type I, where each layer consists of coplanar anions and cations and all planar cuts lead to a non-polar surface; (b) type IIa, where the anions and cations containing the layers are not coplanar but permits the cuts of some surface to split the layers in a way as to produce no dipole; (c) type IIb, which is almost similar to type IIa, except that some ions are moved from the surface to the bottom of region 2 in order to derive zero dipole; (d) type III, where there are alternating layers of cations and anions, and all possible planar cuts result in a surface with a dipole moment (Tasker, 1979).

For the first type, the atomic structure comprises charge neutral ionic sheets which are parallel to the surface plane and so all shifts generate a surface with no dipole moment in the direction of the normal surface (Gale and Rohl, 2003). The second type of surface consists of a combination of cations and anions with zero net dipole in the proper direction and so a non-dipolar surface can be derived if the right shift values are selected. For the third type of surface, a dipolar surface, which is probably to be less stable, exists due to cleavage planes. For this situation, the dipole as a result of the presence of dipolar surfaces can be removed either as a result of twining of crystals (or strong solvation) or by reconstruction of the surfaces.

This reconstruction involves the formation of cation or anion vacancies at the surface or chemical modification (Gale and Rohl, 2003).

4.7.5 The concept of force field fitting/parameterisation

There are two general approaches used in carrying out fitting which excludes rule based extrapolations. The first involves fitting to a potential energy surface obtained from a non-empirical theoretical method. By doing this, the potential energy surface can be fitted either as a sequence of geometries with their corresponding energies or the inclusion of energy derivatives to maximise the amount of information from each calculation (Gale and Rohl, 2003). The second involves empirical fitting of a range of experimental data such as the crystal structure, elastic constants, bulk moduli (Swamy and Dubrovinsky, 2001), piezoelectric constants, dielectric constants, or phonon frequencies (Gale and Rohl, 2003).

The first step in performing a fit is to define a quantity that measures the quality of the fitting, the objective function, which often takes the form of a sum of squares and is described by;

$$F = \sum_{i=1}^{N_{obs}} w_i \left(f_i^{obs} - f_i^{calc} \right)^2 \tag{4.38}$$

Where N_{obs} is the number of observables, f_i^{obs} and f_i^{calc} are the fitted and calculated values of the observable respectively, and w_i is the weighting factor for the given observable. Since with the weighting factor an infinite number of possible solutions exist, a major challenge is choosing the most appropriate weighting factors. Ways of achieving this are either by making the weighting factor inversely proportional to the uncertainty in the measured value (i.e. if fitting experimental data) or by making the weight factor inversely proportional to the magnitude of the observable squared.

The fitting process involves minimizing the function *F*, using an approach similar to that of optimization. The experimental, structural data are fitted by varying the potential parameters so as to minimize the forces at this configuration. Subsequently, other observables such as elastic constant etc. are calculated at the same experimental structure. The quality of a fit is usually judged by the percentage error in the structural variables. After a successful fit, it is essential to check the quality of the results since convergence during minimization does not necessarily mean that a good quality solution has been reached. This can be done by testing the potential model for all reasonable properties and not just those used during the fit. Properties such as the bulk modulus, elastic constant tensor, dielectric properties and phonons can be used in testing, rather than just testing to see if the symmetry structure is reproduced. Furthermore, testing can also be carried out by transferring the derived force field to a different material which was not used in the original fit. The point of doing this is to see whether the results obtained are reasonable. Testing can also be conducted by visibly assessing whether the potential parameters are physically reasonable.

In fitting, the key quantity which measures how good the fit is the ‘sum of squares’ which is usually zero at the end of a fit. The main aim of a fit is to minimize the sum of squares by varying the potential parameters.

4.7.6 The concept of energy minimization

The concept of energy minimization involves locating the minimum energy structure for a material. The minimum energy structure is the local minimum on the global potential energy surface, which is where the starting coordinates of the structure lie closest to. This provides the means for locating an optimum structural geometry. Atoms in molecules possess three independent Cartesian variables with respect to which all non-zero potential energy terms in the potential energy summation are minimised. The conditions for minimum energy of a molecular system with U as the potential energy and r_{ij} as the distance between two atoms, can be expressed as;

$$\left(\frac{\partial U}{\partial r_{ij}}\right) = 0 \qquad (4.39)$$

$$\left(\frac{\partial^2 U}{\partial r_{ij}^2}\right) > 0$$

Characterizing a stationary point as a minimum involves the generation of the Hessian matrix of second order derivatives of the energy with respect to pairs of the independent Cartesian coordinates. A form of the Hessian matrix for a diatomic molecule can be expressed as;

$$\begin{pmatrix} \left(\frac{\partial^2 U}{\partial x_1^2}\right)\left(\frac{\partial^2 U}{\partial x_1 \partial y_1}\right) & \cdots & \left(\frac{\partial^2 U}{\partial x_1 \partial z_2}\right) \\ \left(\frac{\partial^2 U}{\partial y_1 \partial x_1}\right)\left(\frac{\partial^2 U}{\partial y_1^2}\right) & \cdots & \vdots \\ \vdots \qquad \vdots & \ddots & \vdots \\ \left(\frac{\partial^2 U}{\partial z_2 \partial x_1}\right) \quad \cdots & \cdots & \left(\frac{\partial^2 U}{\partial z_2^2}\right) \end{pmatrix} \qquad (4.40)$$

where x_1, y_1, z_1, x_2, y_2, z_2 are Cartesian coordinates of first and second atoms. When diagonalized, the Hessian matrix gives a set of eigenvalues and eigenvectors. The resulting eigenvectors are referred to as the normal coordinates of the molecule. When diagonalized at its equilibrium geometry, the Hessian matrix gives zero and positive eigenvalues which are characterized as the minimum in the potential energy.

4.8 Conclusion

As discussed in this chapter, titania possesses a wide range of applications owing to its unique thermophysical and photocatalytic properties especially at the nanoscale. It also possesses enhanced chemical and electrical properties at the nanoscale compared to bulk scale. Titania exists in three main crystalline forms (i.e. rutile, anatase and brookite) of which rutile and anatase are the most important. Anatase is known to be the most thermodynamically stable form in the nanocrystalline phase, while rutile is known to be stable only at room temperature. Brookite is seen to transform irreversibly to rutile at high temperature. Investigating these phases of titania beginning from their atomic scale is of great importance as atomic scale properties of materials are known to influence their bulk properties. Knowledge of these properties is important in understanding the interaction mechanism of nanoparticles. Investigating the atomic and bulk properties of these phases can be carried out using the concept of molecular modelling as discussed in sections 4.6 and 4.7. These concepts involve the use of models to predict the behaviour of molecules and molecular systems. Theoretical analysis of this concept has been made and discussed in this chapter. Chapter 5 will focus on the computational methods of molecular modelling which involves the molecular modelling packages used and the selection of an appropriate force field.

Chapter 5

Molecular Modelling: Computational Methods of Molecular Modelling

5 Computational Methods of Molecular Modelling

5.1 Introduction

As particle aggregation has been observed to be significant in controlling thermal enhancement of nanofluids, surface properties of nanoparticles are known to play an important role in influencing the interaction of particles and the mechanisms that underpin aggregation. Molecular modelling helps to study particle scale properties from an atomic/molecular level, which will eventually give a clearer and better understanding of particle aggregation. This chapter introduces the concept of molecular modelling which incorporates force fields, molecular mechanics and molecular dynamics simulations. Molecular modelling has been used to predict the mechanical, structural and surface properties of both bulk and nanocrystalline TiO_2. The knowledge of these properties will help us to understand the mechanism of interparticle interactions. In this section, the force field used in modelling TiO_2 nanoparticles and water molecules is presented, as well as the molecular dynamics simulation packages.

5.2 Why Molecular modelling?

The computational background to the numerical modelling discussed in Chapter 2, has provided information about the aggregation model which captures particle aggregation and also takes into account various key parameters such as particle volume fraction, interfacial thermal resistance, and how they influence thermal conductivity enhancement of nanofluids. Investigating particle interactions is vital in understanding the mode and mechanism of particle aggregation. Molecular modelling provides a clearer view of atomic scale (from a microscopic point) properties and interactions. These surface properties are known to influence the surface behaviour of the particles (from a macroscopic point) as atomic/molecular scale properties can greatly influence bulk scale properties. Hence, the next section of this chapter will focus on molecular modelling methods and how they were applied in this project, to predict particle scale properties including atomic scale and particle scale interactions.

5.3 Molecular modelling packages used

Initially, the *General Utility Lattice Program (GULP)* was used to test the performance of the proposed force field, obtained from the literature, on the different crystalline phases of titania. The force field or interatomic potentials from the literature was re-fitted to an extended data set in the form of elastic constant values, derived from a first principles calculation involving CASTEP, with the aim of assessing its performance by reproducing the structural and material properties of TiO_2. Properties such as lattice energy and other mechanical properties of the titania structure were calculated during this investigation. Surface energy of the crystal structure was also calculated using GULP. Subsequently, the classical molecular dynamics code DL_POLY was used to predict structural and surface properties of titania nanoparticles for different particle sizes, temperature and simulation time step. DL_POLY was also used to predict interparticle interactions with relation to separation distance.

5.3.1 The General Utility Lattice Program (GULP) Package

GULP, which began development in the early 1990s, performs force field simulations using static lattice/lattice dynamical methods. GULP puts together many of the facilities required for solid state simulation such as static lattice, quasi-harmonic approaches, etc. Its starting point is the calculation of the system energy. For most methods, the internal energy is first obtained followed by the treatment of the nuclear degrees of freedom so as to determine the appropriate free energy. The internal energy is dependent on the positions and momenta of all electrons and nuclei (Gale and Rohl, 2003). As solving this problem could be complicated, performing an approximation will simplify the condition. To perform this, the effect of the electrons is assumed to be incorporated into a forcefield the energy can be disintegrated into an expansion in terms of interactions between different subsets of the total number of atoms, as seen in Equation 4.17. The computational task can also be simplified by introducing cut-off distances since interactions will get weaker as atoms move farther apart from each other. The interactions between atoms can be chosen based on the nature of forces between the particles. For example when considering a covalent diatomic molecule, the potential energy surface would be represented by a Morse potential since it is harmonic at the minimum and results in separation at large bond lengths. Some potential terms which are also relevant and available in GULP have been described in chapter four. Below are some potentials available in GULP (Table 5.1).

Table 5.1 Potentials available in GULP

Potential name	**Formula**	**Units for input**
Buckingham	$A\,exp(-r/\rho) - Cr^{-6}$	A in eV, ρ in Å, C in eV Å^{6}
Lennard-Jones (combination rules permitted)	$Ar^{-m} - Br^{-m}$ or $\varepsilon\left[c_1(\sigma/r)^m - c_2(\sigma/r)^n\right]$ $c_1 = [n/(m-n)]^*(m/n)^{**}[m/(m-n)]$ $c_2 = [m/(m-n)]^*(m/n)^{**}[n/(m-n)]$	A in eV Å^{m}, B in eV Å^{n} ε in eV, σ in Å
Harmonic (k^3/k^4 optional)	$1/2\,k_2(r-r_0)^2 +$ $1/6\,k_3(r-r_0)^3 +$ $1/12\,k_4(r-r_0)^4$	k_2 in eV Å^{-2},r_0 in Å k_3 in eV Å^{-3} k_4 in eV Å^{-4}
Morse Spring (core-shell) general	$D(\{1 - exp[-a(r-r_0)^2]\}^2 - 1)$ $1/2\;k_2r^2 + 1/24\,k_4\,r^4$ $A\,exp(-r/\rho)r^{-m} - Cr^{-n}$	D in eV, a in Å^{-2}, r_0 in Å k_2 in eV Å^{-2}, k_4 in eV Å^{-4} A in eV Å^{m}, ρ in Å, C in eV Å^{n}
Stillinger-Weber (2-body) Stillinger-Weber (3-body)	$A\,exp[\rho/(r - r_{max})]\,(Br^{-4} - 1)$ $k\,exp[\rho/(r_{12} - r_{max}) + \rho/(r_{13} - r_{max})]$ $[\cos(\theta_{213}) - \cos(\theta_0)]^2$	A in eV, ρ in Å, B in Å^{4} K in eV, ρ in Å
Three-body harmonic	$1/2\;k_2(\theta-\theta_0)^2 +$ $1/6\,k_4(\theta-\theta_0)^3 +$ $1/12\;k_4(\theta-\theta_0)^4$	k_2 in eV rad^{-2}, θ_0 in degrees k_3 in eV rad^{-3} k_4 in eV rad^{-4}

With the internal energy of the system defined, the minimum energy structure for the material can be determined as well. In GULP, this will probably be a local minimum on the global potential energy surface that the coordinates at the starting structure lie close to. Methods available for finding the global minimum include; simulated annealing, Monte Carlo or molecular dynamics, and genetic algorithms, as it may be difficult and unsuccessful using GULP. GULP mainly focuses on searching for the local minimum.

When the minimum energy structure (optimised structure) has been defined, a wide range of physical bulk properties can be calculated based on the curvature of the energy surface about the minimum (Gale and Rohl, 2003). These properties include both mechanical and dielectric properties such as bulk modulus and elastic constants, Young's moduli, Poisson's ratio, acoustic velocities, static and high frequency dielectric constants, refractive indices, piezoelectric constants, born effective charges, phonons, amongst others.

In GULP, all surface constructions and structural manipulation can be carried out independently by graphical means through a freely available interface program *GDIS* developed by Dr Sean Fleming (http://gdis.seul.org/). In this interface, surfaces can be specified in terms of their Miller indices, shifts to be searched for and the geometries to be manipulated. Subsequently, GULP calculations can be performed on the generated surface structure. Surface properties that can be determined include; surface energy, attachment energy, morphology and surface phonons.

5.3.1.1 Format of Input files

A typical GULP input file will contain information on different lines. The first line is usually the keyword line and then subsequent lines will contain information on the unit cells, the fractional coordinates and types of the atoms, the space group symmetry, the species charge, and the potential. The keyword line contains control words which specify the tasks to be performed by the program. For the unit cells, the cell parameter form is a preferable way of specifying the unit cells instead of the cell vector form. The atomic coordinates can be specified as either fractional or Cartesian with the former preferred. The space group symmetry can be given either through the space group number or through the standard Hermann-Mauguin symbol. There are various types of potential in GULP, some have been listed previously in this chapter. A typical GULP input file will be of the form;

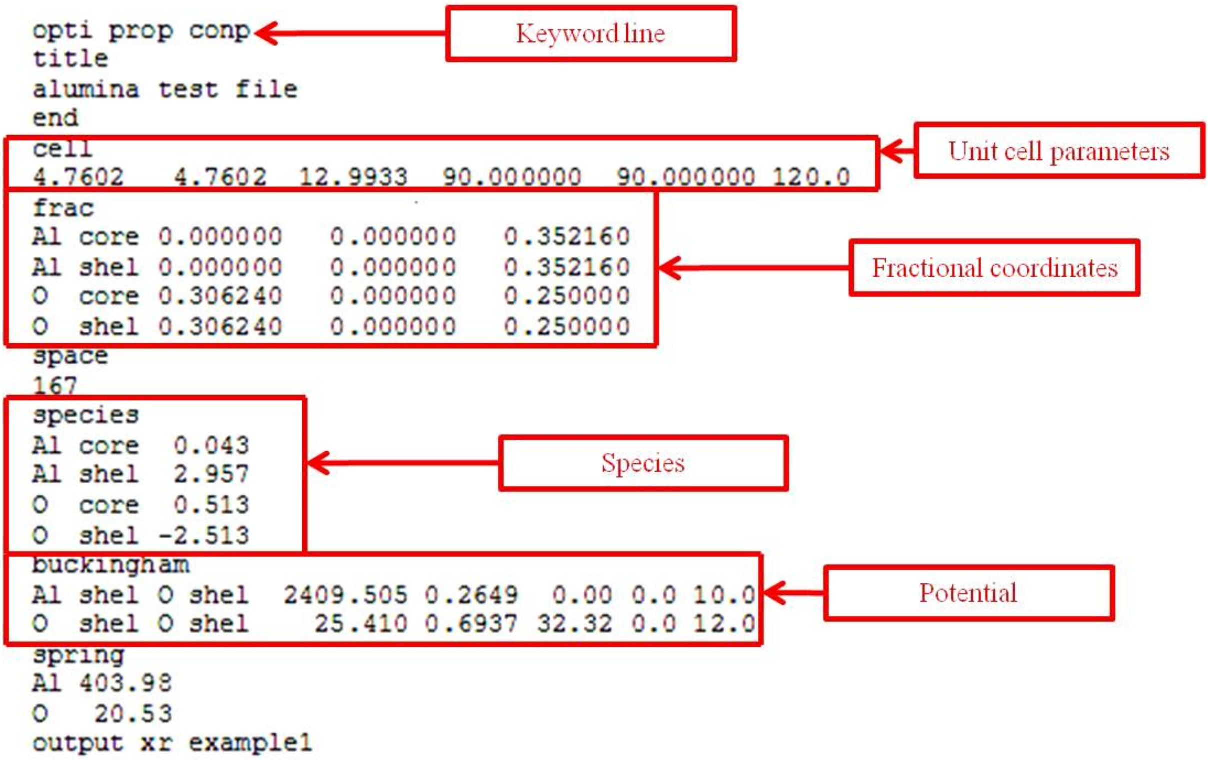

```
opti prop conp
title
alumina test file
end
cell
4.7602   4.7602  12.9933  90.000000  90.000000 120.0
frac
Al core 0.000000   0.000000   0.352160
Al shel 0.000000   0.000000   0.352160
O  core 0.306240   0.000000   0.250000
O  shel 0.306240   0.000000   0.250000
space
167
species
Al core  0.043
Al shel  2.957
O  core  0.513
O  shel -2.513
buckingham
Al shel O shel  2409.505 0.2649  0.00 0.0 10.0
O  shel O shel    25.410 0.6937 32.32 0.0 12.0
spring
Al 403.98
O   20.53
output xr example1
```

Some keywords in GULP are shown in Table 5.2;

Table 5.2 Keywords in GULP

Keywords	Meaning
conp	Perform constant pressure calculation – cell to vary
conv	Perform constant volume calculation – hold cell fixed
compare	Produce a table comparing the initial and final geometries
distance	Calculate interatomic distances
fit	Perform a fitting run
predict	Perform structure prediction calculation
optimise	Minimise the energy with respect to geometrical variables
property	Calculate the bulk lattice properties
relax	Use relax fitting
simultaneous	Simultaneously optimise shells while fitting

More keywords and general information about GULP can be found in the manual (Gale and Rohl, 2003)

5.3.2 Structural information and input data

The structural information for the three crystalline phases of titania are required to perform the GULP simulation and were obtained from the Inorganic Crystal Structure Database (ICSD) (http://cds.dl.ac.uk/icsd/index.html). The crystal structures for the three crystalline phases are presented in Figures 4.12, 4.18 and 4.22, and were obtained from ICSD. The unit cell parameters for these phases are given in Table 5.3 below;

Table 5.3 Experimental unit cell parameters and fractional coordinates for rutile, anatase and brookite. (Naicker et al., 2005)

Phase	Crystal System	Space group	*a*, Å	*b*, Å	*c*, Å
Rutile	Tetragonal	*P42/mnm*	4.3644	4.3644	2.9919
Anatase	Tetragonal	*I41/amd*	3.784	3.784	9.514
Brookite	Orthorhombic	*Pcab*	9.166	5.411	5.149

Based on structural information obtained from the ICSD, input files were created for the three crystalline phases of titania.

5.3.3 TiO_2 Nanoparticle Simulation Technique: The DL_POLY Package

The classical molecular dynamics code, DL_POLY version 2, was used (Smith and Forester, 1996) to carry out simulations and Newton's equations of motion were integrated using the Verlet leapfrog algorithm. Temperature was maintained using the Berendsen thermostat and the simulations were carried out in the canonical ensemble (NVT). The cuboidal periodic simulation box used here had an edge length more than four times the diameter of the nanoparticle contained therein

(Figure 5.1). This was the case for all the simulations (different particle sizes) and cell dimensions were large enough to avoid interactions between a given particle and its periodic images in the adjoining cells. Simulations were carried out for 1 ns which was sufficiently long to achieve steady state of the molecular structure of the particles and water molecules in this study. A time step of 1 fs was used.

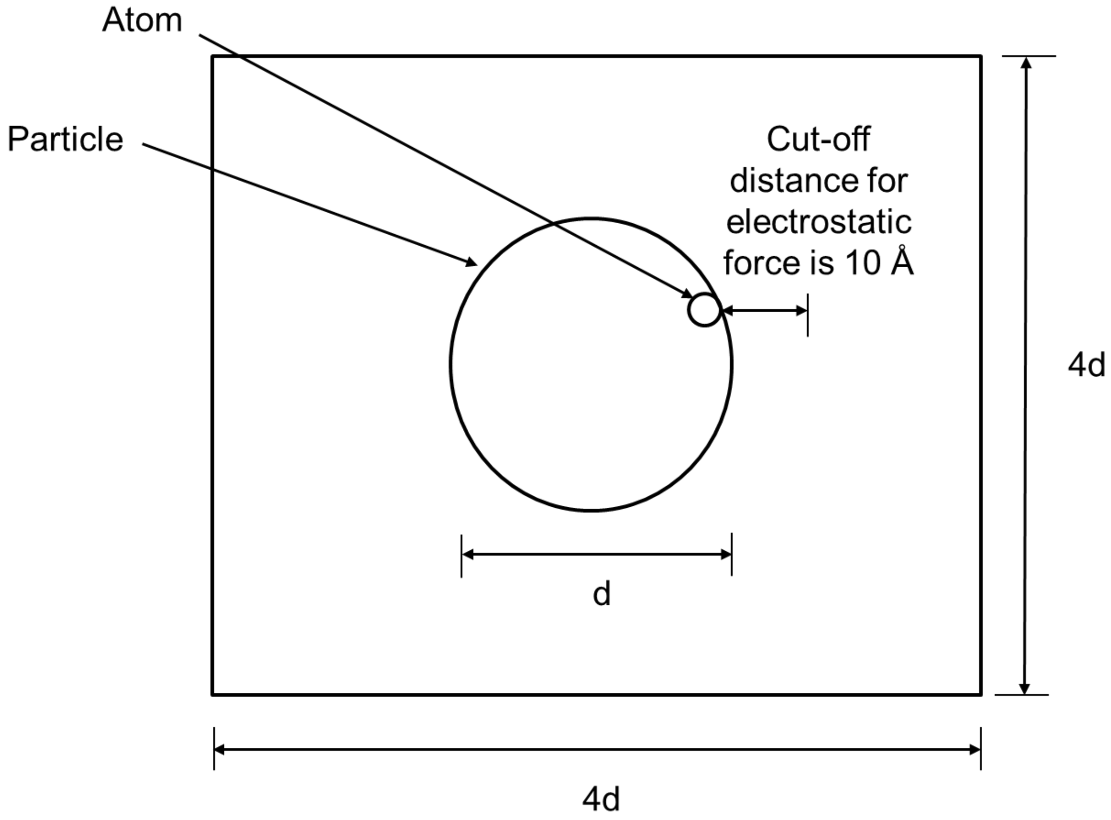

Figure 5.1 Schematic diagram of a mid-sectional view of a 3-dimensional cuboidal simulation cell with size *4d* containing a nanoparticle of size *d (periodic conditions apply to all boundaries of the box)*

DL_POLY is a molecular dynamics simulation package of subroutines, programs and data files. It can be used in carrying out simulations on molecular systems such as simple atomic systems, rigid and flexible molecules with bonds, simple metals and alloys, covalent systems, biological systems polymers, ionic systems, macromolecules, solutions, etc (Smith et al., 2010). DL_POLY can use periodic boundary conditions such as; none, cubic, orthorhombic, slab (x, y periodic, z non-periodic) etc. The conventional MD integration algorithms (i.e. Verlet Leapfrog and the Velocity Verlet) are optionally available in DL_POLY. Properties that depend on position and velocity at time *t* are usually required to carry out molecular dynamics simulation. The Verlet scheme in DL_POLY is both time reversible and simple (Smith, 1987). It conserves the total energy (i.e. kinetic plus potential energy) by generating trajectories in the microcanonical (NVE) ensemble. With the velocities usually half a timestep behind, the Leapfrog algorithm requires values of position ($\underline{r}$) and force ($\underline{f}$) at time t. Initially, the velocities are advanced to $t + (1/2)\Delta t$ by integration of the force (Gale and Rohl, 2003);

$$\underline{v}(t + \frac{1}{2}\,\Delta t) \leftarrow \underline{v}(t - \frac{1}{2}\,\Delta t) + \Delta t\,\frac{\underline{f}(t)}{m} \tag{5.1}$$

Where m is the mass of a site and Δt is the timestep. Following this, the positions are advanced using the new velocities (Gale and Rohl, 2003);

$$\underline{r}(t + \,\Delta t) \leftarrow \underline{\mathrm{r}}(t) + \Delta t\,\underline{v}(t + \frac{1}{2}\,\Delta t) \tag{5.2}$$

In the Leapfrog algorithm, the velocity at time t is derived from the average of the velocities half a timestep either side of time t;

$$\underline{v}(t) = \frac{1}{2}\left[\underline{v}(t - \frac{1}{2}\,\Delta t) + \underline{v}(t + \frac{1}{2}\,\Delta t)\right] \tag{5.3}$$

Rigid body rotational motion is also available within DL_POLY and is handled under the leapfrog scheme with Fincham's implicit quartenion algorithm (FIQA). Various ensembles such as NVE (i.e. constant mass, volume and energy), NVT (i.e. constant mass, volume and temperature) and NPT (i.e. constant mass, volume and pressure) are available with a selection of thermostats (such as Berendsen, Evans and Hoover), and barostats. Structural relaxation methods available are; 'Zero' temperature molecular dynamic, conjugate gradients minimization, and 'programmed' energy minimization. In this study, the Zero temperature molecular dynamics method was used and is similar to a dynamical simulation at low temperature. In 'Zero' dynamics, the molecules move in the direction of the computed forces at each time step whilst still retaining a velocity within the limits of a corresponding temperature of 1 Kelvin. The Conjugate Gradients minimization method involves minimizing the system configuration energy using the conjugate gradients method (Smith et al., 2010). The 'Programmed' energy minimization method involves both molecular dynamics and conjugate gradients. DL_POLY contains a wide range of methods to sum the long ranged electrostatic (coulombic) potentials. The Ewald sum which has been used in this study was suggested by the authors of DL_POLY as the preferred method used for calculating electrostatics interactions in periodic systems. This method is known to be accurate for summing long ranged Coulomb potentials in periodic systems.

5.3.4 Creation of nanoparticles

The Accelrys Materials Studio 5.2 visualization package was used to create the TiO_2 nanoparticles of the rutile and anatase phases. Materials Studio is a molecular modelling package used to study and analyze models of molecular structures and provides the ability to build and represent molecular structures with enhanced graphics. The ***Build Nanostructure*** utility of the ***Build*** utility within Materials Studio was used to create nanoparticles used in present study. This was carried out by initially creating the bulk crystal with a perfect lattice, using the unit lattice of rutile and anatase TiO_2 in Table 5.3 (Naicker et al., 2005, Ahmad and Bhattacharya, 2009, Jagtap et al., 2005). These lattices were used to create the bulk crystal with a perfect lattice. Subsequently, spheres of anatase and rutile with diameters ranging from 2 to 6 nm were cut from the bulk lattice and some of the surface oxygen and titanium atoms were removed to ensure electroneutrality (Figure 5.2).

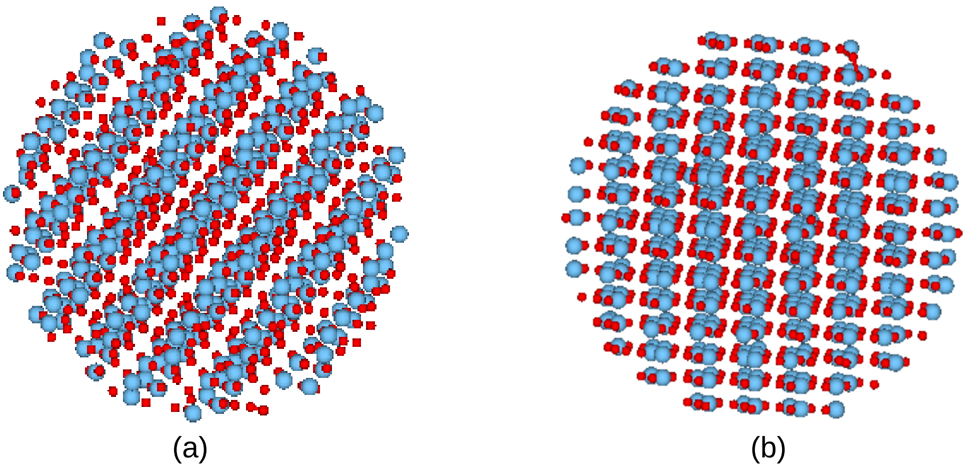
(a) (b)

Figure 5.2 Image of typical structure generated for 3 nm (a) rutile and (b) anatase TiO_2 nanoparticle created using Materials Studio. Ti and O atoms in red and blue colours respectively

The size of the particles for anatase and rutile, and their corresponding number of TiO_2 units is shown in Table 5.4.

Table 5.4 Size of nanoparticles and the corresponding number of TiO_2 units for anatase and rutile

Particle size (nm)	Anatase	Rutile
2	122	126
3	415	420
4	992	980
5	1941	1918
6	3335	3304

5.3.5 Creation of water molecules

For simulations in water, the wateradd utility of the DL_POLY Java GUI (Figure 5.3) was used to add SPC/E water molecules to the simulation box. To achieve the target water density of 0.9882 g/cm^3, adding the right and optimum number of water molecules for the corresponding box and particle sizes was necessary. Figure 5.4 shows an image of a TiO_2 nanoparticle in water.

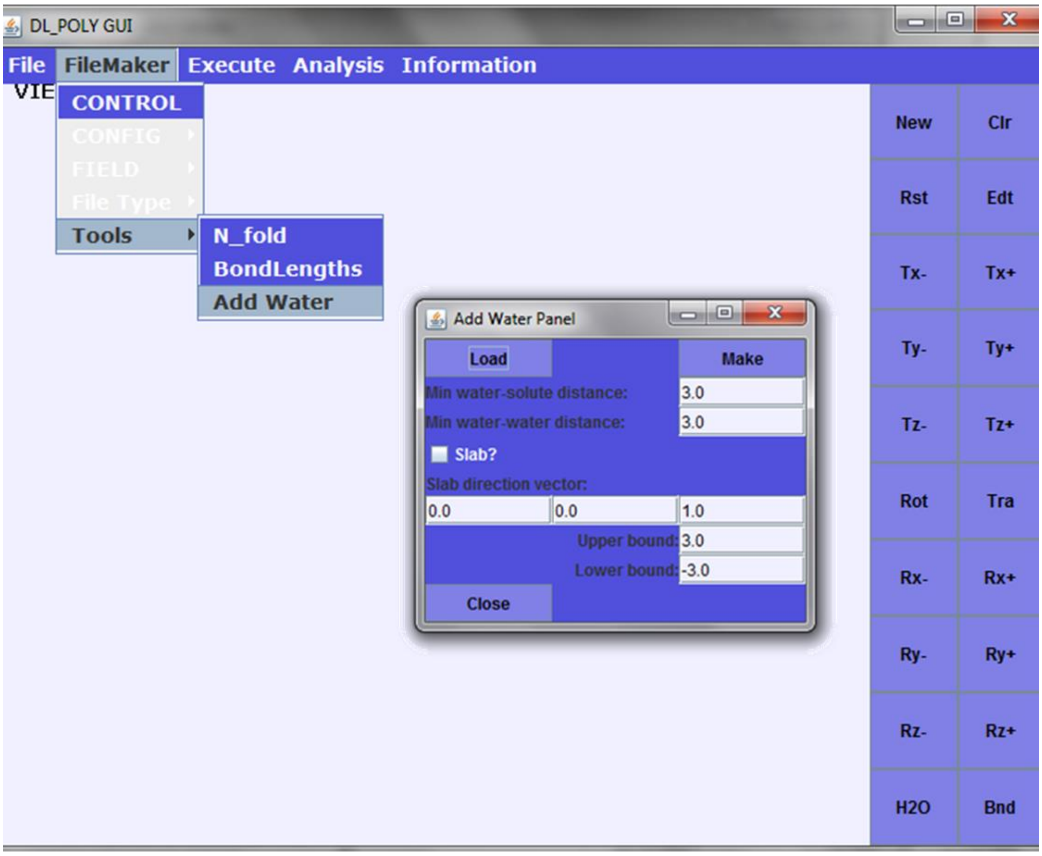

Min water-solute distance: 3.0
Min water-water distance: 3.0
☐ Slab?
Slab direction vector: 0.0 0.0 1.0
Upper bound: 3.0
Lower bound: -3.0

Figure 5.3 Wateradd utility of the DL_POLY Java GUI

The different sizes of anatase nanoparticles and their corresponding water molecules and water densities in the simulation box are shown in Table 5.5.

Table 5.5 Size of anatase nanoparticles and corresponding water molecules and water density in each simulation box

Particle size (nm)	No. of H_2O molecules	H_2O Density (g/cm^3)
Water only	901	0.9983
2	1583	0.9983
3	2756	0.9983
4	6672	0.9980
5	12730	0.9981
6	24537	0.9896

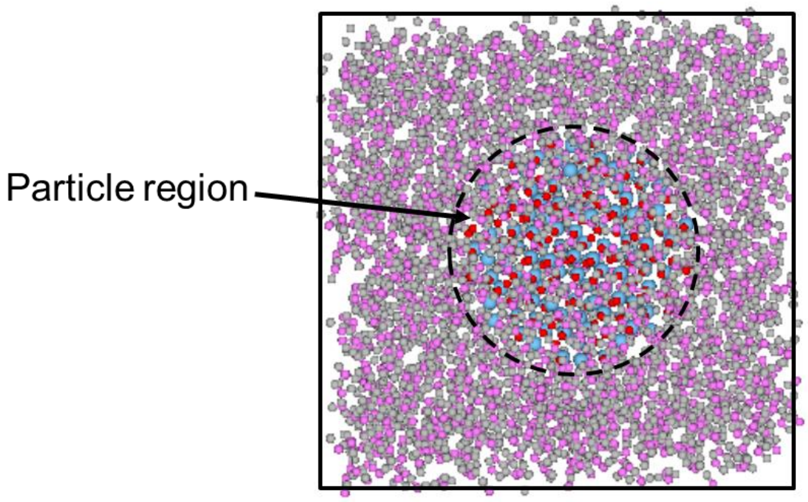

Figure 5.4 Image of a 3 nm TiO_2 anatase nanoparticle in water (Ti, red; O, blue; HW, grey; OW, pink)

5.3.6 The Force Field Selection

For this study, which is focused on TiO_2 nanoparticles, the force field selected is one reported widely in the literature for modelling TiO_2 polymorphs. Various reports from the literature have concluded that the Matsui – Akaogi force field (Koparde and Cummings, 2005, Filyukov et al., 2007, Koparde and Cummings, 2007, Matsui and Akaogi, 1991) is the most suitable for molecular modelling simulations of bulk titania polymorphs for a wide range of temperatures and, when compared, out-performs the more complicated variable charge force field (Filyukov et al., 2007, Koparde and Cummings, 2007). Whilst being a two-body rigid-ion potential with an easier and less computationally demanding form, when compared to experimental data the Matsui – Akaogi force field reproduces the structures of the three main titania polymorphs and their order of relative stabilities (Koparde and Cummings, 2007). Its reliability over a range of TiO_2 configurations makes it suitable for carrying out molecular dynamics simulations at high temperatures (Collins et al., 1996). This force field is given as;

$$U(r_{ij}) = \underbrace{\boxed{A_{ij}\, exp\left(-\frac{r_{ij}}{\rho_{ij}}\right)}}_{\text{Repulsive term (short-range interaction)}} - \underbrace{\boxed{\frac{C_{ij}}{r_{ij}^{6}}}}_{\text{Dispersion term}} + \underbrace{\boxed{\frac{q_i q_j}{4\pi\varepsilon_0 r_{ij}}}}_{\text{Electrostatic term}} \tag{5.4}$$

With $U(r_{ij})$ as the interaction energy, r_{ij} is the distance between sites *i* and *j*. The Ti and O ions possess partial charges (*q*) of +2.196 and -1.098 respectively. The parameters A_{ij}, ρ_{ij} and C_{ij} are given in Table 5.6 below (Oliver et al., 1997);

Table 5.6 Potential parameters for TiO_2. (Oliver et al., 1997, Matsui and Akaogi, 1991)

Interaction	A_{ij} / eV	ρ_{ij} / Å	C_{ij} / eV Å^6
$Ti^{2.196+}$ -$O^{1.098-}$	16957.53	0.194	12.59
$Ti^{2.196+}$ -$Ti^{2.196+}$	31120.2	0.154	5.25
-$O^{1.098-}$ -$O^{1.098-}$	11782.76	0.234	30.22

Simulations of water molecules around TiO_2 nanoparticles were carried out using the three-site SPC/E (extended simple point charge) water potential (Berendsen et al., 1987, Mark and Nilsson, 2001). The potential has one negatively (q_{OW} = -0.8476) and two positively (q_{HW} = +0.4238) charged sites representing the O and H atoms in the water molecules, respectively (Koparde and Cummings, 2008). It can be represented in the form of Lennard Jones (LJ) potential as;

$$U(r_{ij}) = \varepsilon_{ij}\left[\left(\frac{\sigma_{ij}}{r_{ij}}\right)^{12} - 2\left(\frac{\sigma_{ij}}{r_{ij}}\right)^{6}\right] + \frac{q_i q_j}{r_{ij}} \tag{5.5}$$

In this form of LJ potential, σ_{ij} is the distance at which the potential has its minimum value of $-\varepsilon_{ij}$ (Koparde and Cummings, 2008). The values of the parameters in Equation 5.5 are shown in Table 5.7. Interactions between the water molecules and the nanoparticles were modeled using the interaction parameters (Table 5.8) of Bandura and Kubicki derived from ab initio calculations (Bandura and Kubicki, 2003).

Table 5.7 SPC/E water potential parameters (Bandura and Kubicki, 2003, Předota et al., 2004)

Interaction	ε_{ij} / eV	σ_{ij} / Å
OW - OW	0.006738	3.166
OW - HW	0.000	0.000
HW - HW	0.000	0.000

Table 5.8 Parameters for interaction between water molecules and TiO_2 nanoparticles (Bandura and Kubicki, 2003)

Interaction	A_{ij} / eV	ρ_{ij} / Å	C_{ij} / eV Å^6
Ti – OW	1239.911	0.265	6.4178

5.3.6.1 Force field fitting

Before performing simulations for this research, the force field parameters of Matsui – Akaogi were re-fitted by including additional structural data, in the form of elastic constant values, derived from *ab initio* calculations which were high level calculations using density functional theory carried out using CASTEP. CASTEP is a materials modelling code which calculates the properties of materials including energetics, structure at the atomic level, vibrational properties, etc. from first-principles (Segall et al., 2002). Its concept is based on a first-principles quantum mechanical description of electrons and nuclei. Calculations performed using CASTEP were carried out as part of a separate PhD programme through a collaboration with members of a research group (Professor Rick Brydson, Dr Andrew Scott and Trevor Hardcastle) from the Institute of Materials Science and Research (IMR), at the University of Leeds. Hence there will be no detailed illustration on the method of calculation of the elastic constants using CASTEP in this thesis. The aim of this was to compare the original and the updated version of the force field and see how well both versions reproduce (at least approximately) experimentally determined structural properties. GULP was used to carry out this fitting, which provides a method of deriving interatomic potential parameters.

GULP uses a Newton-Raphson functional minimisation approach in solving the least square problems. The choice of which potential parameters to fit is at the users discretion and is controlled by a series of flags on the potential line in the input file (0 ⇒ fix, 1 ⇒ vary). Constraints on fitting variables may also be imposed using a ‘constrain fit’ option with GULP. A quality check on the program’s performance is to identify if the total number of variables being fitted is sufficiently smaller than the total number of observables. Relax fitting in GULP has been used in this study. Relax fitting involves fitting according to the criteria by which the structures are judged which means that the structure is optimised and the displacement of the structural parameters calculated at every point in the fit. An important benefit of using the relax fit is that the properties are calculated for the optimised structure where they are valid.

A typical GULP input file for carrying out fitting and which includes the keywords, observables, species and force field is shown below;

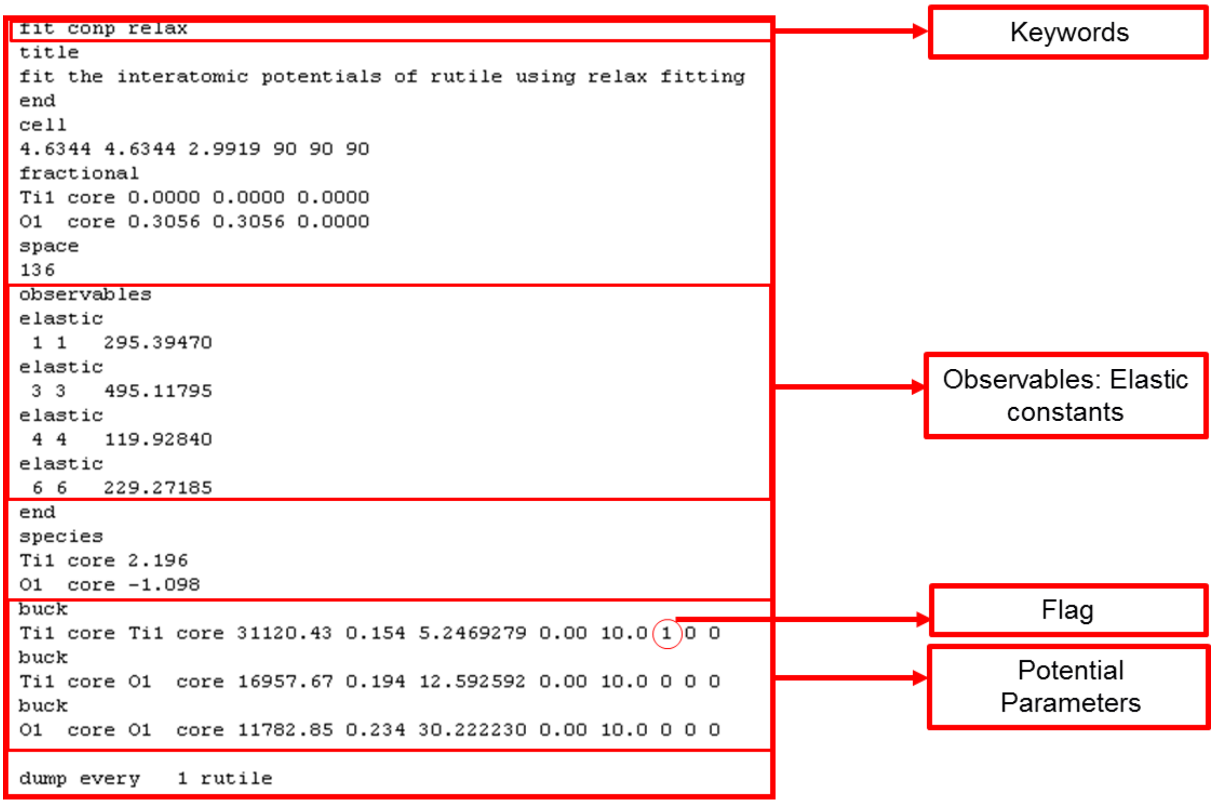

```
fit conp relax
title
fit the interatomic potentials of rutile using relax fitting
end
cell
4.6344 4.6344 2.9919 90 90 90
fractional
Ti1 core 0.0000 0.0000 0.0000
O1  core 0.3056 0.3056 0.0000
space
136
observables
elastic
 1 1   295.39470
elastic
 3 3   495.11795
elastic
 4 4   119.92840
elastic
 6 6   229.27185
end
species
Ti1 core 2.196
O1  core -1.098
buck
Ti1 core Ti1 core 31120.43 0.154 5.2469279 0.00 10.0 1 0 0
buck
Ti1 core O1  core 16957.67 0.194 12.592592 0.00 10.0 0 0 0
buck
O1  core O1  core 11782.85 0.234 30.222230 0.00 10.0 0 0 0

dump every   1 rutile
```

The properties used as the observables in this study are the elastic constants.

Elastic constants from *ab initio* calculations have been fed into the program. Elastic constants derived from different methods including from GULP in the present study using the Matsui – Akaogi force field, and from experiments (Isaak et al., 1998) are shown in Table 5.9.

Table 5.9 Observables: Elastic constants (Units in GPa)

Indices	**GULP (Present – Matsui - Akaogi)**	**GULP (Swamy et al., 2001)**	***Ab initio* (IMR group)**	**Experiment (Isaak et al., 1998)**
C_{11}	332.1	322.0	295.4	268.0
C_{33}	444.3	444.1	495.1	484.0
C_{44}	122.6	122.6	119.9	124.0
C_{66}	226.2	226.1	229.3	190.0

Elastic constants for four indices (i.e. C_{11}, C_{33}, C_{44}, C_{66}) derived from GULP, from present study using the original Matsui – Akaogi force field (Matsui and Akaogi, 1991), are presented in Table 5.9. Also presented in this Table, are elastic constants derived from GULP studies from literature (Swamy et al., 2001), those from *ab initio* calculations (IMR group), and those from experiments (Isaak et al., 1998). Comparing the elastic constants across the four methods in which they were derived from, it can be seen that they are within reasonable limits. Since the elastic constants derived from GULP using the original Matsui – Akaogi force field are within reasonable limits with those derived from the other sources, it suggests that the Matsui – Akaogi force field is suitable enough to carry out simulations on TiO_2 nanoparticles. Going further, force field parameters of the original Matsui - Akaogi (Matsui and Akaogi, 1991), and those derived from the fitting of elastic constants from *ab initio* calculations (IMR group) and experiments (Isaak et al., 1998), are presented in Table 5.11. In this study, these force fields will be identified as presented in Table 5.10.

Table 5.10 Sources of elastic constants used in force field fitting and their corresponding refined force field identity

Original Source	Force field fitting using elastic constants (Yes/No)	Refined identity
Matsui - Akaogi force field	No	Not applicable
Elastic constants from *ab initio* calculations (IMR group)	Yes	Refined force field 1
Elastic constants from experiment (Isaak et al., 1998)	Yes	Refined force field 2

Table 5.11 Force field parameters derived using elastic constants in Table 5.9. Refined force field 1 derived from *ab initio* (IMR group). Refined force field 2 derived from experiments (Isaak et al., 1998)

Ti - Ti	**Original Matsui - Akaogi**	**Refined force field 1**	**Refined force field 2**
A	31120.4	31089.6	31089.3
ρ	0.154	0.155	0.155
C	5.25	5.51	5.51
Ti - O	**Original Matsui - Akaogi**	**Refined force field 1**	**Refined force field 2**
A	16957.7	16891.7	16696.9
ρ	0.194	0.194	0.194
C	12.60	12.60	12.7
O - O	**Original Matsui - Akaogi**	**Refined force field 1**	**Refined force field 2**
A	11782.85	10669.77	10669.85
ρ	0.234	0.234	0.221
C	30.22	36.50	37.08

Based on method-wise comparison and for each TiO_2 pair, it can be observed from Table 5.10 that the force field parameters are within reasonable limits. This further suggests the suitability of the Matsui – Akaogi force field. Results of the cell parameters and lattice energies, for rutile, anatase, and brookite predicted from the force fields in Table 5.11 and derived using the elastic constants in Table 5.9 have been reported in Table 5.12.

The predicted relaxed lattice energies in Table 5.12 are those derived after energy minimisation (see details on concept of energy minimisation in section 4.7.6). This is the point where the energy has been relaxed to equilibrium and the optimum structural geometry has been located. Results in Table 5.12 for the three TiO_2 phases are within reasonable limits and further confirms the suitability of the Matsui – Akaogi force field to be used in carrying out molecular dynamics simulations of TiO_2. However, it can be seen in Table 5.12, that for the three TiO_2 phases, the relaxed lattice energies predicted using the refined force field 2, are slightly lower than those predicted using the refined force field 1, and the Matsui – Akaogi force field. In the case of rutile, it is lower by an average of 2.1 %, for anatase, 1.59 %, and for brookite, 5.6 %. Also, in the case of rutile, the final cell parameters predicted using the refined force field 2, are within the closest limits with the corresponding initial cell parameters by an average of 0.2 %. For anatase, the final cell parameters predicted using the refined force field 1, are within the closest limit with the corresponding initial cell parameters by an average of 0.1 %. For brookite, the final cell parameters predicted using the force field of Matsui-Akaogi are within the closest limit with the corresponding initial cell parameters by an average of 0.2 %.

Table 5.12 Properties of bulk TiO_2 phases predicted using the Matsui – Akaogi force field, the refined force field 1 derived from *ab initio* (IMR group), and the refined force field 2 derived from experiments (Isaak et al., 1998)

Rutile					
Parameter			**Original Matsui - Akaogi**	**Refined force field 1**	**Refined force field 2**
Lattice Energy (eV)	Unrelaxed		-79.42	-79.98	-80.93
	Relaxed		-79.60	-80.27	-81.66
Cell	**Coordinates**	**Initial**	**Final**		
	a = b	4.3644	4.4929	4.4561	4.3460
	c	2.9919	3.0085	2.9993	2.9915
Anatase					
Parameter			**Original Matsui - Akaogi**	**Refined force field 1**	**Refined force field 2**
Lattice Energy (eV)	Unrelaxed		-78.987	-79.573	-80.658
	Relaxed		-78.991	-79.595	-80.885
Cell	**Coordinates**	**Initial**	**Final**		
	a = b	3.7840	3.7705	3.7468	3.6745
	c	9.5140	9.5681	9.5361	9.5575
Brookite					
Parameter			**Original Matsui - Akaogi**	**Refined force field 1**	**Refined force field 2**
Lattice Energy (eV)	Unrelaxed		-316.548	-318.958	-323.229
	Relaxed		-316.972	-319.438	-327.452
Cell	**Coordinates**	**Initial**	**Final**		
	a	9.1660	9.1464	9.1133	9.3667
	b	5.4110	5.3896	5.3501	4.7281
	c	5.1490	5.1447	5.1056	4.6568

The refined force fields 1 and 2, and that of Matsui – Akaogi, have been used to predict individual elastic constants for the three TiO_2 phases. These predicted elastic constants have been compared with those from other literature sources (Grimsditch and Ramdas, 1976; Iuga et al., 2007) and presented in Table 5.13. Elastic constants predicted from the Matsui – Akaogi force field and the refined force field 1, are very close to those of Table 4.4 and Table 4.5, for both rutile and anatase (taking unit conversion into account). Careful observation shows that both methods predict elastic constants closer to experiment depending on the indices being considered. For example in the case of rutile, the Matsui – Akaogi force field, predicts very close C_{44} indices (122.602 GPa) to that of rutile in Table 4.4 (1.232 10^{11} dynes/cm^2 ≈ 123.2 GPa) with a difference of 0.6 GPa as seen in Figure 5.13. There are no experimental elastic constants available with which to use in comparing the predicted elastic constants for brookite.

Table 5.13 Comparison of predicted elastic constants for the three TiO_2 phases with elastic constants in Table 4.4 and 4.5 from literature. The elastic constants were predicted using the Matsui – Akaogi force field, the refined force field 1 derived from ab initio (IMR group), and the refined force field 2 derived from experiments (Isaak et al., 1998).

Rutile					
Elastic Constant (Units in GPa)	**Indices**	**Original Matsui - Akaogi**	**Refined force field 1**	**Refined force field 2**	**Table 4.4 (Grimsditch and Ramdas, 1976)**
	C_{11}	332.074	321.859	302.133	267.4
	C_{33}	444.256	455.265	484.851	479
	➡ C_{44}	122.602	119.357	100.047	123.2
	C_{66}	226.239	237.871	264.551	188.6
Anatase					
Elastic Constant (Units in GPa)	**Indices**	**Original Matsui - Akaogi**	**Refined force field 1**	**Refined force field 2**	**Table 4.5 (Iuga et al., 2007)**
	C_{11}	450.876	471.195	506.431	320
	C_{33}	207.265	211.938	230.230	190
	C_{44}	25.299	20.027	4.357	54
	C_{66}	49.466	44.005	24.307	60
Brookite					
Elastic Constant (Units in GPa)	**Indices**	**Original Matsui - Akaogi**	**Refined force field 1**	**Refined force field 2**	
	C_{11}	262.6227	265.1391	375.6844	-
	C_{33}	273.7096	265.7700	180.2052	-
	C_{44}	99.0853	94.9264	163.2839	-
	C_{66}	158.1317	164.2711	194.9229	-

Also, the relaxed unit cell parameters predicted using both the Matsui – Akaogi force field and the refined force field 1, are very close to those in Table 4.6 as can be seen in Table 5.14.

Table 5.14 Comparison of cell parameters predicted from Matsui – Akaogi and the refined force fields, to Table 4.6 from literature

Rutile						
Cell	**Coordinates**	**Initial**	**Final**			**Table 4.6**
			Original Matsui - Akaogi	**Refined force field 1**	**Refined force field 2**	
	a = b	4.36440	4.49293	4.45613	4.34599	4.594
	c	2.99190	3.00851	2.99934	2.99146	2.959
Anatase						
Cell	**Coordinates**	**Initial**	**Final**			**Table 4.6**
			Original Matsui - Akaogi	**Refined force field 1**	**Refined force field 2**	
	a = b	3.7840	3.7705	3.7468	3.6745	3.786
	c	9.5140	9.5681	9.5361	9.5575	9.514

Comparisons above in Table 5.13 and 5.14 further goes to confirm the suitability of the Matsui Akaogi force field for carrying out subsequent simulations in this research.

Unfortunately it is not possible at this point, to determine the experimental data originally used by Matsui and Akaogi (Matsui and Akaogi, 1991) to derive their force field parameters. However, they confirmed the transferability of the force field across the three polymorphs of titania by stating that the crystal structures of the polymorphs were reproduced. Elastic constants have been used in this research to perform force field fitting as they were readily available from *ab initio* calculations and experiments from literature. As part of future recommendations after this research, further performance testing of the force fields derived from elastic constants of *ab initio* calculations and those from experiments, should be conducted. This would aim at investigating to see how well they can reproduce the crystal structures and other properties (such as mechanical, surface, thermodynamics etc) of the three polymorphs compared to those of the originally derived force field of Matsui - Akaogi.

5.4 Conclusion

The molecular modelling packages to be used are the *General Utility Lattice Program* (GULP) and DL_POLY which is a classical molecular dynamics code. GULP is mainly used in carrying out static lattice simulations and calculates properties of bulk crystalline materials such as lattice and surface energies, including mechanical properties. DL_POLY is mostly used for carrying out molecular dynamics simulations where atoms and molecules are made to interact and their trajectories are determined using Newton's equations motions. These trajectories are used to predict the forces and potential energy between the atoms. GULP will be used in this research to investigate the bulk crystalline properties of the three TiO_2 phases, while DL_POLY will be used to carry out molecular dynamics simulations of TiO_2 nanoparticles. The force field to be used for the modelling of TiO_2 nanoparticles is that of Matsui – Akaogi which is similar to the conventional Buckingham potential. This force field has been widely used to model TiO_2 nanoparticles and is known to reproduce the structures of titania polymorphs and their order of relative stabilities. The force field has however been fitted and tested in this chapter to determine its suitability for conducting molecular modelling. The force field fitting was carried out using GULP and showed that the force field reproduced properties (such as elastic constants, cell parameters, lattice energies) for the titania phases similar to those from experiments. Hence, no modification was made to the Matsui – Akaogi force field parameters used in this research. Furthermore, as molecular dynamics simulations will be carried out in both vacuum and water environments, the Matsui – Akaogi force field only takes into account, simulations of TiO_2 nanoparticles in vacuum. The SPC/E water potential which is in the form of Lennard Jones will be used to carry out simulations of the particles in water.

Chapter 6 presents the results of properties of TiO_2 crystals and nanoparticles based on predictions of molecular modelling.

Chapter 6

Properties of TiO_2 Crystals and Nanoparticles Predicted by Molecular Modelling

6 Properties of TiO_2 Crystals and Nanoparticles Predicted by Molecular Modelling

6.1 Introduction

In this chapter, macro-scale properties such as lattice and surface energies, and mechanical properties, are predicted for the bulk crystal structures of the three TiO_2 phases. Following this, molecular dynamics simulations are described for anatase and rutile nanoparticles with sizes ranging between 2 and 6nm at different temperatures in both vacuum and liquid environments. Thermodynamic, structural and surface properties such as total system energies, radial distribution functions and surface energies are reported for the different nanoparticle sizes and their dependence on temperature and simulation time revealed. Comparison has been made between the properties of rutile and anatase, and results are reported here. Consideration is taken of the degree of structural change in nanoparticles during Molecular Dynamics simulations as a function of particle size. Assessment of the sphericity of the nanoparticles showed that the particles became less spherical with increasing temperature. The simulation results provide a platform for, potentially, accounting for effects of internal, atomic-scale phase characteristics of TiO_2 nanoparticles on their bulk properties using multi-scale modelling approaches in future.

6.2 Properties of TiO_2 crystal structure

The force-field fitting which was performed on the Matsui and Akaogi force field (in section 5.3.4) confirmed the suitability of that force field for carrying out simulations in this research, as it produced results for bulk properties of titania that were within reasonable agreement with those from experiments and literature as shown in Figure 5.10 – 5.13. As a result of this, this force field was not modified. The Matsui and Akaogi force field was used in this study to calculate the lattice energy and obtain some mechanical properties for the different phases of TiO_2 using the GULP software. The surface energy for different surfaces of the three titania phases was also calculated using the GULP interface, GDIS. GDIS is chemical-visualization software designed to display molecular and periodic systems such as surface slabs and crystal unit cells (Gale and Rohl, 2003). It also performs energy minimization. The input parameters required include structural information obtained from the crystal structure database (ICSD) and the force field parameters presented in Table 5.3 and 5.6 respectively. Some input files for the GULP simulation are attached in Appendix A. A typical output file includes mechanical properties such as elastic constants, bulk and Young's moduli, static dielectric constant tensor and refractive indices. In this research, all GULP simulations were conducted at room temperature (i.e. 300 K). Lattice energy and structural results for both the relaxed and unrelaxed structure of the three phases are presented in Table 6.1;

Table 6.1 Results for the three phases of TiO_2 calculated using GULP

Phase	Parameters	Unrelaxed	Relaxed	Difference	% Difference
Rutile	**Lattice Energy**	-79.42 eV or -7662.90 KJ/(mole unit cells)	-79.60 eV or -7680.06 KJ/(mole unit cells)	0.18	0.20
	Cell Volume	64.26 Å^3	60.73 Å^3	3.53	5.49
	a	4.6344 Å	4.4929 Å	0.1415	3.05
	b	4.6344 Å	4.4929 Å	0.1415	3.05
	c	2.9919 Å	3.0085 Å	-0.0166	0.55
	Cell density	4.13 g/cm^3	4.37 g/cm^3	-0.24	5.81
Anatase	**Lattice Energy (Primitive unit cell)**	-78.987 eV or -7621.08 KJ/(mole unit cells)	-78.991 eV or -7621.43 KJ/(mole unit cells)	0.004	-0.0051
	Lattice Energy (Non-Primitive unit cell)	-157.975 eV or -15242.16 KJ/(mole unit cells)	-157.982 eV or -15242.87 KJ/(mole unit cells)	0.007	0.0044
	Cell Volume (Primitive unit cell)	68.11 Å^3	68.01 Å^3	0.10	0.15
	Cell Volume (Non-Primitive unit cell)	136.23 Å^3	136.02 Å^3	0.21	0.15
	a	3.7840 Å	3.7705 Å	0.0135	0.36
	b	3.7840 Å	3.7705 Å	0.0135	0.36
	c	9.5140 Å	9.5681 Å	-0.0541	0.57
	Cell density	3.896 g/cm^3	3.901 g/cm^3	-0.005	0.13
Brookite	**Lattice Energy**	-316.5 eV or -30542.09 KJ/(mole unit cells)	-316.9 eV or -30582.94 KJ/(mole unit cells)	0.40	0.13
	Cell Volume	255.38 Å^3	253.61 Å^3	1.77	0.69
	a	9.1660 Å	9.1464 Å	0.0196	0.21
	b	5.4110 Å	5.3896 Å	0.0214	0.40
	c	5.1490 Å	5.1447 Å	0.0043	0.08
	Cell density	4.15 g/cm^3	4.18 g/cm^3	-0.026	0.63

Clearly, it can be observed that there is no significant change in the lattice energy, cell volume and the unit cell parameters (i.e. between the unrelaxed and relaxed structure) for anatase. For both rutile and brookite significant changes in the lattice energy and unit cell parameters were manifested as can be observed in the individual percentage differences for the respective phases following structural relaxation. The percentage difference is lowest for anatase followed by brookite and then rutile. Further results on the relaxation of some important surfaces for the three phases after energy minimization, are subsequently presented. Observations made will be discussed and compared to present observation of anatase as the most thermodynamically stable phase.

6.2.1 Surface and attachment energy calculation of TiO_2 bulk crystalline phases

For the purpose of surface energy calculations, GDIS was used to construct, visualize and calculate the surface and attachment energies of crystal surfaces. The theoretical method of surface construction and calculation has been discussed in section 4.4.4. In GDIS, the Miller (*hkl*) indices and a shift value can be used to define a planar, cleaved surface. The thicknesses of the regions 1 and 2 (as discussed in section 4.4.4.3) were taken into consideration with the size of region 2 selected to be as thick as possible to allow the atoms to represent the effect of the bulk structure on the atoms in region 1. GDIS, automatically determines the optimum growth-slice thickness, d_{hkl} (d_{hkl} as discussed in section 4.4.4.4) for both regions to allow for sufficient and optimum convergence of the energy block. The criteria for this convergence is based on the gradient norm which is determined as the root mean square gradient per number of gradients. Based on the settings made, surfaces can be created from the unit cells of the three TiO_2 polymorphs, viewed and analyzed. The unit cell considered in this study was the simple (1 X 1) structure, and the area of the cleaved surfaces was the reticular area. For the three crystalline phases of titania, surfaces have been created, and surface and attachment energy calculations made and represented subsequently.

Before the surfaces were cleaved, the bulk crystal structure was minimized to get an optimum energy structure and geometry. The surface energy of surfaces was calculated using Equation 4.9 and is based on the difference between the energy of the surface block and the bulk energy per unit area. For this calculation, the lower index planes were chosen as they are known for their stability and are more likely to be expressed in the crystal morphology. Surface energy calculations in GDIS were carried out at constant volume, and no space group symmetry was applied during the optimization/relaxation of the surfaces. While cleaving surfaces, it might be possible to cut surfaces with dipoles. A dipole represents a high energy configuration which is not favorable especially for energy calculations such as surface and attachment energies. Surface dipoles can be removed from crystal surfaces by reconstruction, involving displacement of atoms. In this study, it was observed that the minimization of the crystal structure provided an optimum geometry which had fewer surfaces with dipoles after cleavage. To achieve a crystal structure in which a wide range of surfaces without dipoles can be cleaved, symmetry operations can be performed on atomic positions. This involves defining a 3 X 3 transformation matrix, and 3 X 1 translational offset. Here, by defining a 3 X 1 translational offset, the atom coordinates were translated as seen in Figure 6.1. This is possible for rutile and anatase as these TiO_2 phases possess space groups with a center of inversion (Oliver et al., 1997). The resulting crystal structure allowed the cleavage of a wide range of surfaces without dipoles as seen in Figure 6.2. Note that the atom coordinates of the brookite phase were not translated as most of its surfaces upon cleavage, were observed to be without dipoles.

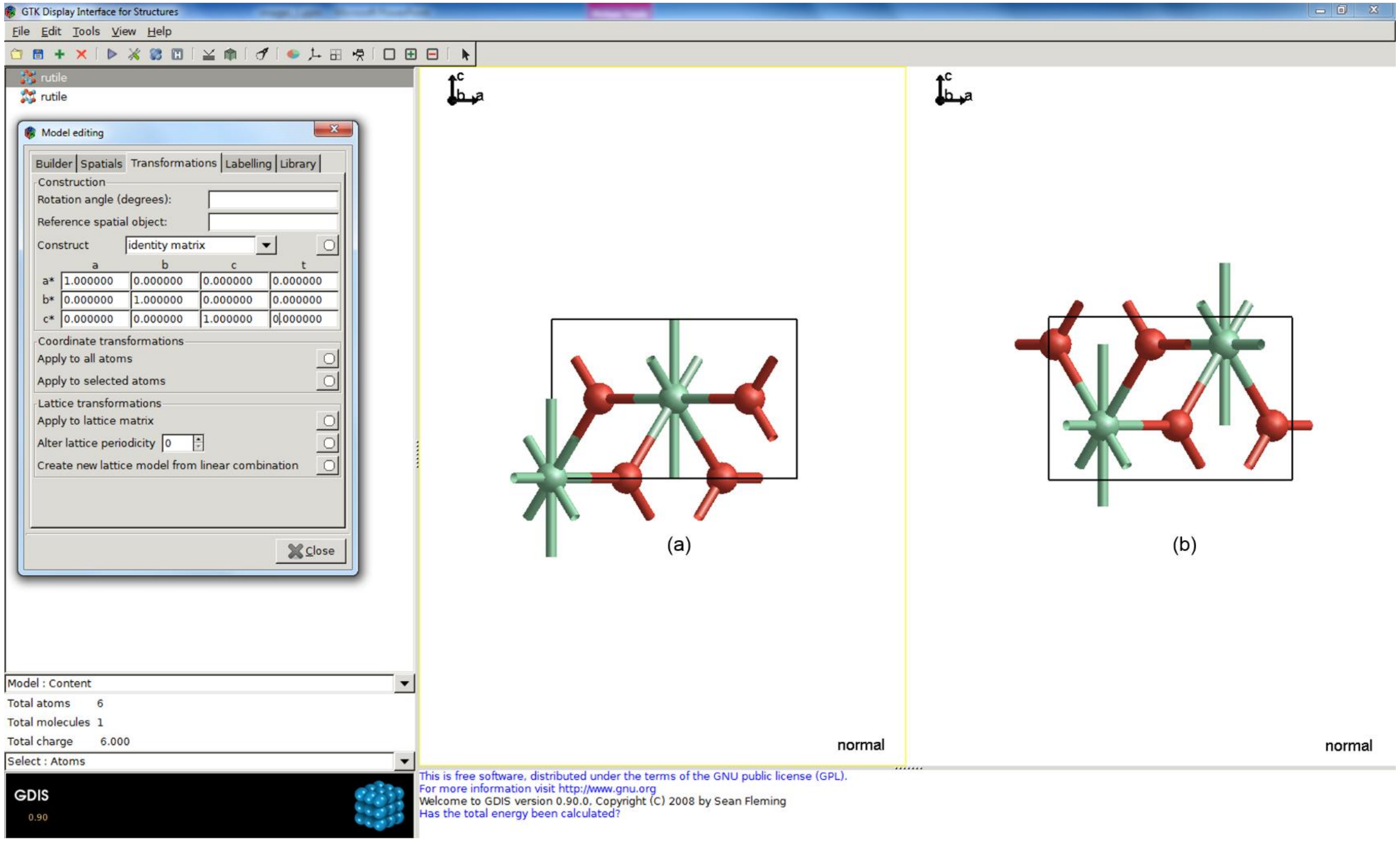

Rotation angle (degrees):

Reference spatial object:

Construct: identity matrix

	a	b	c	t
a*	1.000000	0.000000	0.000000	0.000000
b*	0.000000	1.000000	0.000000	0.000000
c*	0.000000	0.000000	1.000000	0.000000

Apply to all atoms ○

Apply to selected atoms ○

Apply to lattice matrix ○

Alter lattice periodicity 0 ○

Create new lattice model from linear combination ○

Model : Content

Total atoms	6
Total molecules	1
Total charge	6.000

Select : Atoms

```
This is free software, distributed under the terms of the GNU public license (GPL).
For more information visit http://www.gnu.org
Welcome to GDIS version 0.90.0, Copyright (C) 2008 by Sean Fleming
Has the total energy been calculated?
```

Figure 6.1 Screenshot of a the GDIS software containing a Model Editing window (left) for defining 3 X 3 transformation matrix and 3 X 1 translational offset, and rutile crystal structures (right). (a) normal structure, and (b) structure with translated/inverted atom coordinates.

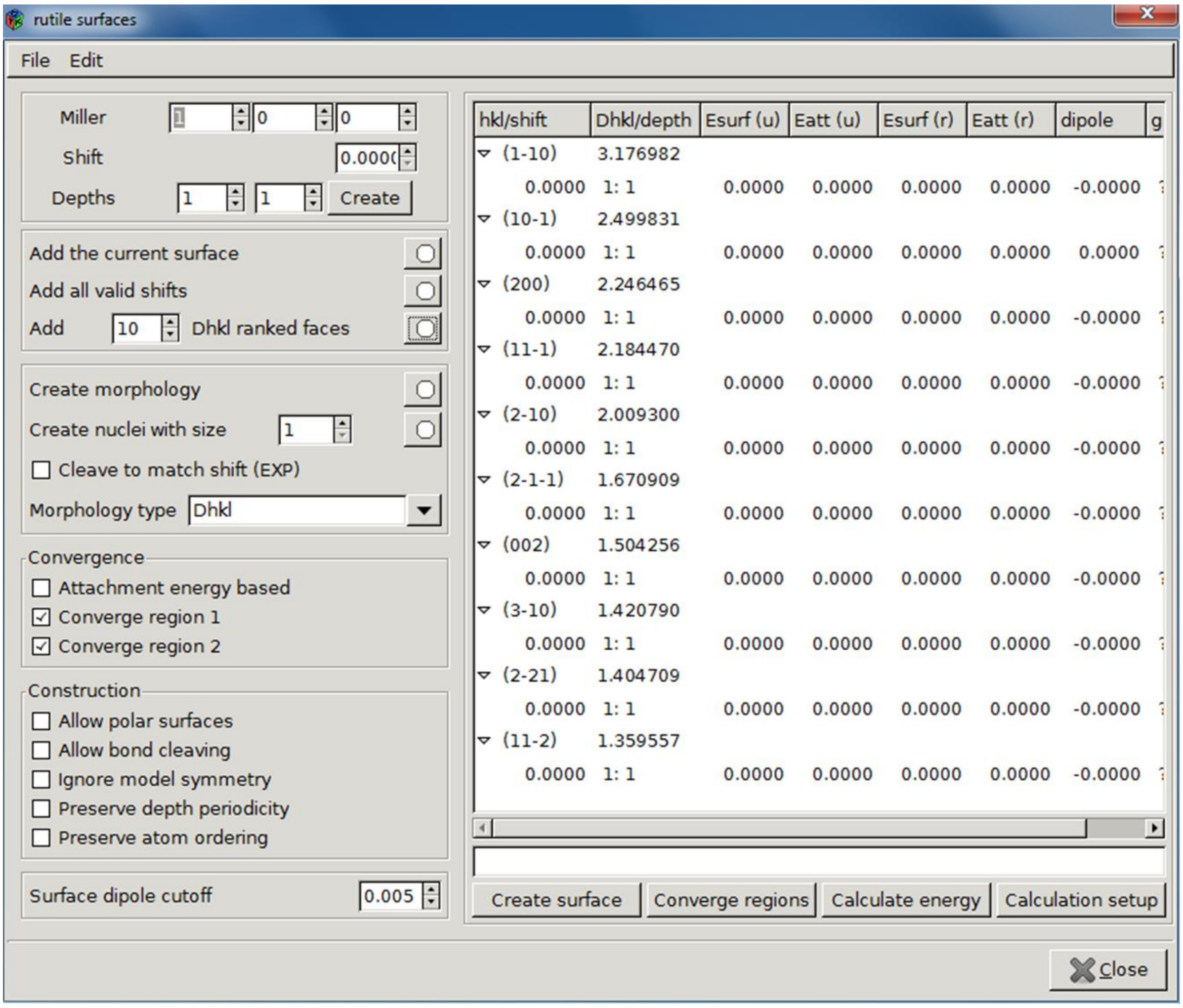

Miller 1 0 0
Shift 0.000
Depths 1 1

Add the current surface ○
Add all valid shifts ○
Add 10 Dhkl ranked faces ○

Create morphology ○
Create nuclei with size 1 ○
☐ Cleave to match shift (EXP)
Morphology type Dhkl

Convergence
☐ Attachment energy based
☑ Converge region 1
☑ Converge region 2

Construction
☐ Allow polar surfaces
☐ Allow bond cleaving
☐ Ignore model symmetry
☐ Preserve depth periodicity
☐ Preserve atom ordering

Surface dipole cutoff 0.005

hkl/shift	Dhkl/depth	Esurf (u)	Eatt (u)	Esurf (r)	Eatt (r)	dipole	g
▿ (1-10)	3.176982						
0.0000	1: 1	0.0000	0.0000	0.0000	0.0000	-0.0000	
▿ (10-1)	2.499831						
0.0000	1: 1	0.0000	0.0000	0.0000	0.0000	0.0000	
▿ (200)	2.246465						
0.0000	1: 1	0.0000	0.0000	0.0000	0.0000	-0.0000	
▿ (11-1)	2.184470						
0.0000	1: 1	0.0000	0.0000	0.0000	0.0000	-0.0000	
▿ (2-10)	2.009300						
0.0000	1: 1	0.0000	0.0000	0.0000	0.0000	-0.0000	
▿ (2-1-1)	1.670909						
0.0000	1: 1	0.0000	0.0000	0.0000	0.0000	-0.0000	
▿ (002)	1.504256						
0.0000	1: 1	0.0000	0.0000	0.0000	0.0000	-0.0000	
▿ (3-10)	1.420790						
0.0000	1: 1	0.0000	0.0000	0.0000	0.0000	-0.0000	
▿ (2-21)	1.404709						
0.0000	1: 1	0.0000	0.0000	0.0000	0.0000	-0.0000	
▿ (11-2)	1.359557						
0.0000	1: 1	0.0000	0.0000	0.0000	0.0000	-0.0000	

Figure 6.2 Screenshot of the surface builder of GDIS showing a list of rutile cleaved surfaces without dipoles.

Surface and attachment energies for the three phases have been reported in Table 6.2 – 6.5. Table 6.2 and 6.4 show surface and attachment energy values respectively. Table 6.3 and 6.5 show the differences (also in terms of percentage) between the unrelaxed and relaxed surface and attachment energies, respectively. Results have also been compared with those taken from the literature (Oliver et al., 1997).

Table 6.2 Surface energies for the three phases of TiO_2 calculated using GULP. Simulation data obtained from (Oliver et al., 1997).

Rutile						
Surface (*hkl*)	**Surface area (Å^{2})**		**ΔU_{SE} Unrelaxed (Jm^{-2})**		**ΔU_{SE} Relaxed (Jm^{-2})**	
	Present	**Simulation**	**Present**	**Simulation**	**Present**	**Simulation**
(1 1 0)	19.12	19.12	2.07	2.05	1.79	1.78
(0 1 1)	24.29	24.30	2.08	2.06	1.86	1.85
(1 0 0)	13.52	13.52	2.43	2.40	2.10	2.08
(1 2 1)	36.34	36.35	4.57	2.67	2.16	2.16
(0 0 1)	20.19	20.19	2.83	2.81	2.42	2.40
(2 2 1)	43.23	43.24	3.77	3.83	2.12	2.02
Anatase						
Surface (*hkl*)	**Surface area (Å^{2})**		**ΔU_{SE} Unrelaxed (Jm^{-2})**		**ΔU_{SE} Relaxed (Jm^{-2})**	
	Present	**Simulation**	**Present**	**Simulation**	**Present**	**Simulation**
(0 1 1)	38.78	38.79	1.67	1.60	1.41	1.40
(0 0 1)	14.22	14.22	1.30	1.28	1.30	1.28
(1 0 0)	36.08	36.09	2.28	2.26	1.69	1.68
(1 1 0)	51.01	51.03	2.91	2.65	2.26	2.19
(1 2 0)	80.67	80.69	2.83	2.54	2.12	1.98
Brookite						
Surface (*hkl*)	**Surface area (Å^{2})**		**ΔU_{SE} Unrelaxed (Jm^{-2})**		**ΔU_{SE} Relaxed (Jm^{-2})**	
(1 0 0)	27.86		2.46		2.07	
(2 1 0)	73.02		2.85		2.40	
(1 1 1)	73.92		3.32		2.78	
(0 1 0)	47.20		3.23		2.50	
(0 0 1)	49.60		4.43		2.17	

Table 6.3 Differences between the surface energies of the unrelaxed and relaxed surfaces for the three phases of TiO_2. Simulation data obtained from (Oliver et al., 1997)

Rutile				
Surface (*hkl*)	**Difference (eV)**		**%**	
	Present	**Simulation**	**Present**	**Simulation**
(1 1 0)	0.28	0.27	13.53	13.17
(0 1 1)	0.22	0.21	10.58	10.19
(1 0 0)	0.33	0.32	13.58	13.33
(1 2 1)	2.41	0.51	52.74	19.10
(0 0 1)	0.41	0.41	14.49	14.59
(2 2 1)	1.65	1.81	43.77	47.26
Anatase				
Surface (*hkl*)	**Difference (eV)**		**%**	
	Present	**Simulation**	**Present**	**Simulation**
(0 1 1)	0.26	0.20	15.57	12.50
(0 0 1)	0	0	0	0
(1 0 0)	0.59	0.58	25.88	25.66
(1 1 0)	0.65	0.46	22.34	17.36
(1 2 0)	0.71	0.56	25.09	22.05
Brookite				
Surface (*hkl*)	**Difference (eV)**		**%**	
	Present			
(1 0 0)	0.39		15.85	
(2 1 0)	0.45		15.79	
(1 1 1)	0.54		16.27	
(0 1 0)	0.73		22.60	
(0 0 1)	2.26		51.02	

From Table 6.2, rutile and brookite from present study showed the highest surface energies for their unrelaxed surfaces. For example, surface energies for the (0 0 1) and (1 0 0) surfaces of anatase are 1.30 Jm^{-2} and 2.28 Jm^{-2} respectively. However, the surface energies of these surfaces for rutile and brookite, are 2.83 Jm^{-2} and 2.43 Jm^{-2} respectively (higher than anatase by an average of 31.93 %), for rutile, and 4.43 Jm^{-2} and 2.46 Jm^{-2} respectively, for brookite (higher than anatase by an average of 48.04 %). Overall, the surface and attachment energies for most of the surfaces from the present study are very close to those from simulations carried out by (Oliver et al., 1997). (Naicker et al., 2005) reported that the surface energies for the low-index surfaces of larger or microscopic rutile are higher than the surface energies for the corresponding low-index surfaces of larger or microscopic anatase. This can be seen when comparing the surface energies of the unrelaxed surfaces of the (0 1 1), (1 0 0) and (0 0 1) surfaces of rutile to those of anatase, from the present study. The (0 0 1) surface energy of rutile is higher than its corresponding anatase surface by 46.28 %. (Diebold, 2003) stated that the (0 0 1) rutile surface has a high surface energy as a result of a higher number of broken bonds. Also, the (0 1 1) surface energy of rutile is higher than its corresponding anatase surface by 24.19 %. On average, anatase showed the least surface energy (≈ 1.76 Jm^{-2}) compared to rutile (≈ 2.05 Jm^{-2}) and brookite (≈ 2.38 Jm^{-2}).

Table 6.4 Attachment energies for the three phases of TiO_2 calculated using GULP. Simulation data obtained from (Oliver et al., 1997). (Note: ΔU_{att} per atom)

Rutile						
Surface (*hkl*)	**Surface area (Å^2)**		**ΔU_{att} Unrelaxed (eV)**		**ΔU_{att} Relaxed (eV)**	
	Present	**Simulation**	**Present**	**Simulation**	**Present**	**Simulation**
(1 1 0)	19.12	19.12	-0.42	-	-0.45	-0.42
(0 1 1)	24.29	24.30	-0.53	-	-0.50	-0.50
(1 0 0)	13.52	13.52	-0.64	-	-0.67	-0.64
(1 2 1)	36.34	36.35	-0.81	-	-1.15	-1.11
(0 0 1)	20.19	20.19	-1.40	-	-1.42	-1.40
(2 2 1)	43.23	43.24	-1.64	-	-1.80	-1.78
Anatase						
Surface (*hkl*)	**Surface area (Å^2)**		**ΔU_{att} Unrelaxed (eV)**		**ΔU_{att} Relaxed (eV)**	
	Present	**Simulation**	**Present**	**Simulation**	**Present**	**Simulation**
(0 1 1)	38.78	38.79	-0.32	-	-0.33	-0.32
(0 0 1)	14.22	14.22	-0.37	-	-0.38	-0.37
(1 0 0)	36.08	36.09	-1.02	-	-1.13	-1.02
(1 1 0)	51.01	51.03	-1.57	-	-1.77	-1.57
(1 2 0)	80.67	80.69	-1.46	-	-1.72	-1.61
Brookite						
Surface (*hkl*)	**Surface area (Å^2)**		**ΔU_{att} Unrelaxed (eV)**		**ΔU_{att} Relaxed (eV)**	
	Present					
(1 0 0)	27.86		-0.35		-0.36	
(2 1 0)	73.02		-1.41		-1.58	
(1 1 1)	73.92		-0.76		-0.74	
(0 1 0)	47.20		-0.48		-0.42	
(0 0 1)	49.60		-0.34		-0.35	

Table 6.5 Differences between the attachment energies of the unrelaxed and relaxed for the three phases of TiO_2.

Rutile		
Surface (*hkl*)	**Difference (eV)**	**%**
	Present	
(1 1 0)	0.03	-7.14
(0 1 1)	-0.03	5.66
(1 0 0)	0.03	-4.69
(1 2 1)	0.34	-41.98
(0 0 1)	0.02	-1.43
(2 2 1)	0.16	-9.76
Anatase		
Surface (*hkl*)	**Difference (eV)**	**%**
	Present	
(0 1 1)	0.01	-3.13
(0 0 1)	0.01	-2.70
(1 0 0)	0.11	-10.78
(1 1 0)	0.2	-12.74
(1 2 0)	0.26	-17.81
Brookite		
Surface (*hkl*)	**Difference (eV)**	**%**
	Present	
(1 0 0)	0.01	-2.86
(2 1 0)	0.17	-12.06
(1 1 1)	-0.02	2.63
(0 1 0)	-0.06	12.50
(0 0 1)	0.01	-2.94

6.2.2 Prediction of morphology structures and surfaces of TiO_2 crystalline phases

Models of the equilibrium crystal morphology for the three phases of TiO_2 are presented in Figures 6.3 – 6.17. The structures were predicted using the BFDH model (see section 4.4.4.2 for details), and the calculated surface and attachment energies from the present study presented in section 6.2.1. Three morphological models were produced, one using the BFDH model, the second using the attachment and surface energies calculated for the unrelaxed crystal lattice, and the third model using those quantities calculated for the relaxed crystal lattice. These morphological models were compared with that predicted from experimental data from (Kostov, 1968). The surfaces that make up these structures correspond to those whose surface and attachment energies were calculated. As earlier discussed in section 6.2.1, these surfaces are non-dipolar (i.e. no dipoles). In Figure 6.3, the morphology predicted using the BFDH model expresses the (1 1 0) and (0 1 1) surfaces of rutile. In the unrelaxed morphology predicted using the calculated surface energies, the (1 1 0), (0 1 1) and (1 0 0) surfaces are expressed. The (2 2 1) surface is expressed in the relaxed morphology predicted using the surface energies and is mainly due to the reduction in its surface energy upon relaxation from 3.77 Jm^{-2} to 2.12 Jm^{-2}. Furthermore, the both the unrelaxed and relaxed morphologies predicted using the attachment energies, expressed the (1 1 0) and (0 1 1) surfaces similar to the morphology prediction using the BFDH model. Upon relaxation, the relaxed structure obtained using the attachment energies had a slightly squashed habit (compared to the unrelaxed morphology) in the z direction. The relaxed morphologies predicted using the surface energies are similar to that predicted using (Kostov, 1968), as both morphologies express similar surfaces. Overall, the morphologies are similar to those predicted in (Oliver et al., 1997). Surface relaxation can be observed by visualising the rutile surfaces shown in Figures 6.4 – 6.8 as atom relaxations and relocations are observed. Visualisation of the (1 1 0) rutile surface as seen in Figure 6.5 shows two relaxed O atoms at (2) and a relocated O atom from (3) to pair with the Ti atoms at (4). The (0 1 1) surface in Figure 6.6 shows relaxation of the O atoms at (4) in the y direction forming an angle of about 120^0, (5) in the z direction, and (6) in the x direction. The (1 0 0) surface in Figure 6.7 also shows similar surface relaxation with O atoms at (3) and (4) relaxing in the y and x directions, respectively. The expression of surfaces upon relaxation as a result of reduction in surface energy or increase in attachment energy, shows the relevance of surface relaxation in the prediction of a morphology structure. Surface relaxation can be linked to the relationship between attachment energy and the kinetics of crystal growth. Since attachment energy can be regarded as a thermodynamic quantity, it means that surfaces with attachment energy that become more exothermic (since energy is released during the addition or growth of a layer) upon surface relaxation will grow more rapidly compared to those that become less exothermic.

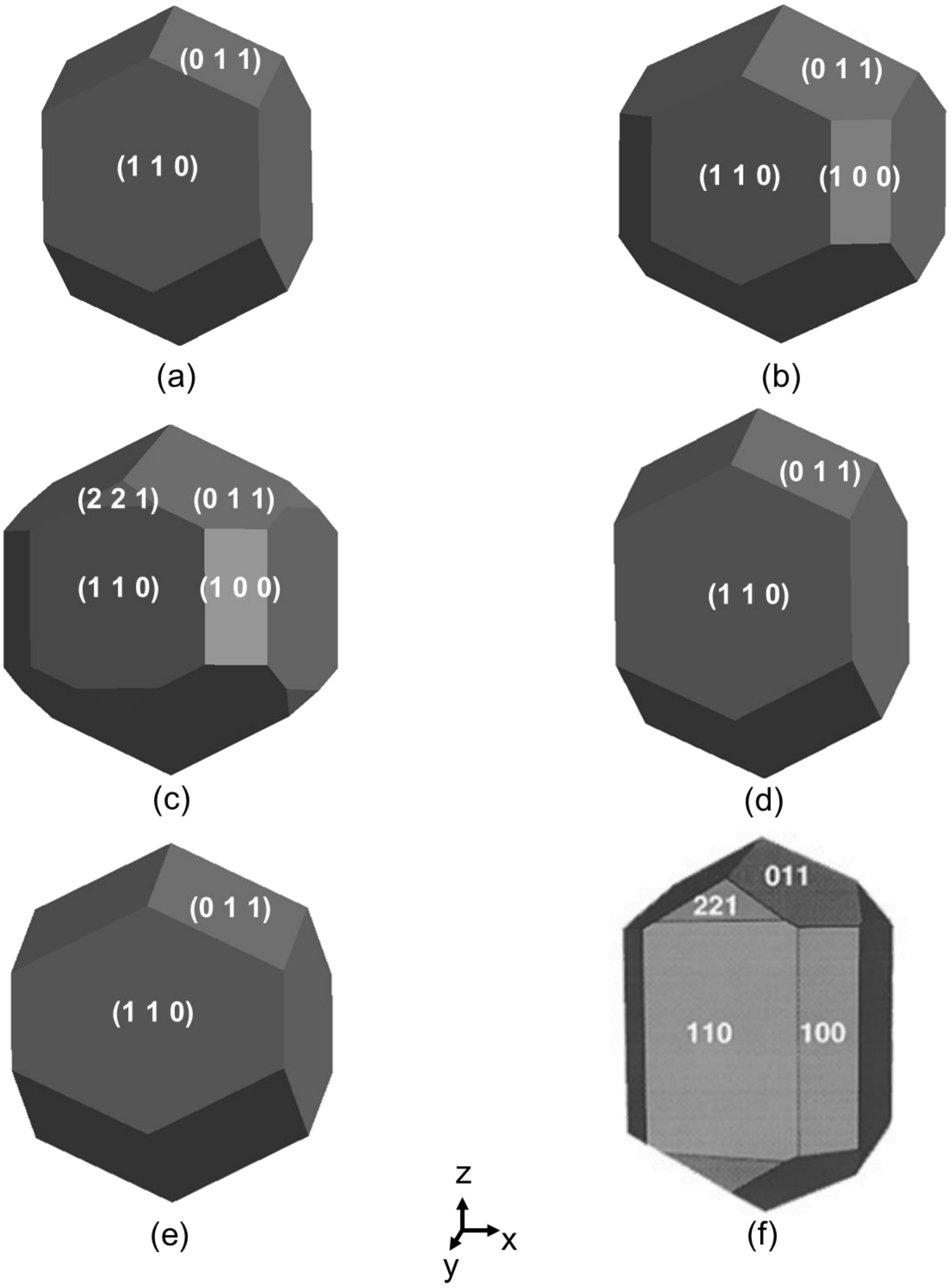

Figure 6.3 Prediction of the calculated and experimental equilibrium morphology rutile structure (a) BFDH model, (b) unrelaxed morphology using surface energies, (c) relaxed morphology using surface energies, (d) unrelaxed morphology attachment energies, (e) relaxed morphology attachment energies and (f) experimental data (Kostov, 1968). Structures predicted using the surface builder module in GDIS.

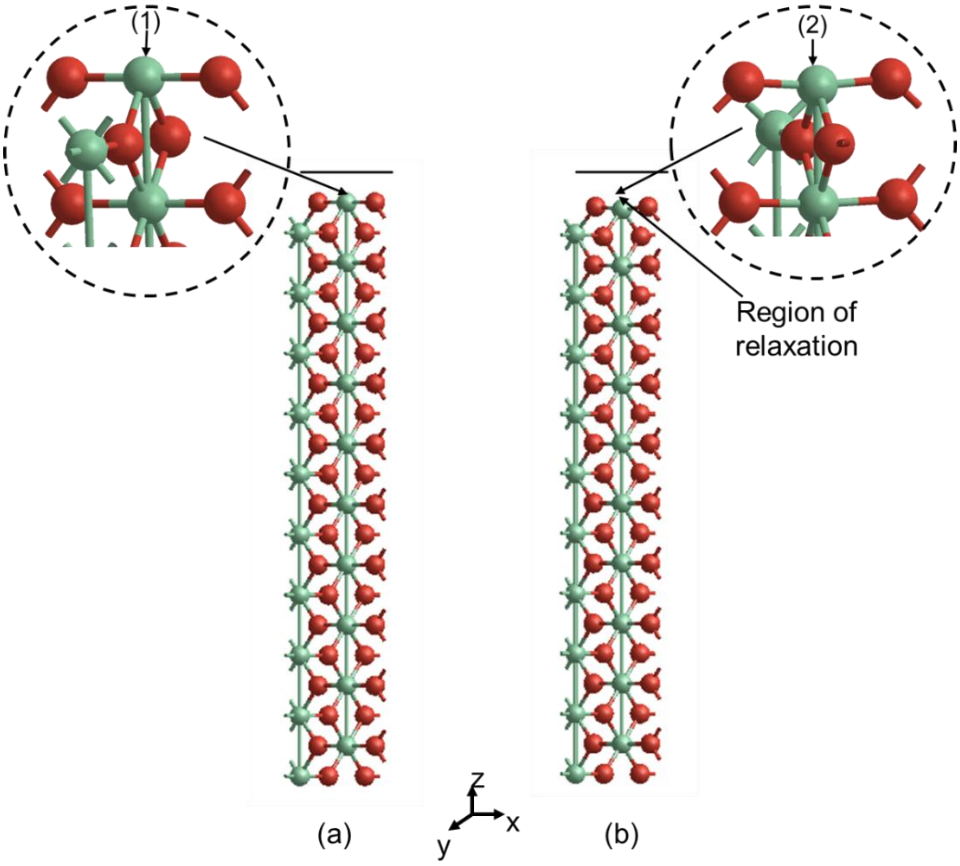

Figure 6.4 Cleaved (a) unrelaxed and (b) relaxed (0 0 1) surface of rutile. Surfaces were obtained using the surface builder module in GDIS. Ti and O atoms are in green and red respectively

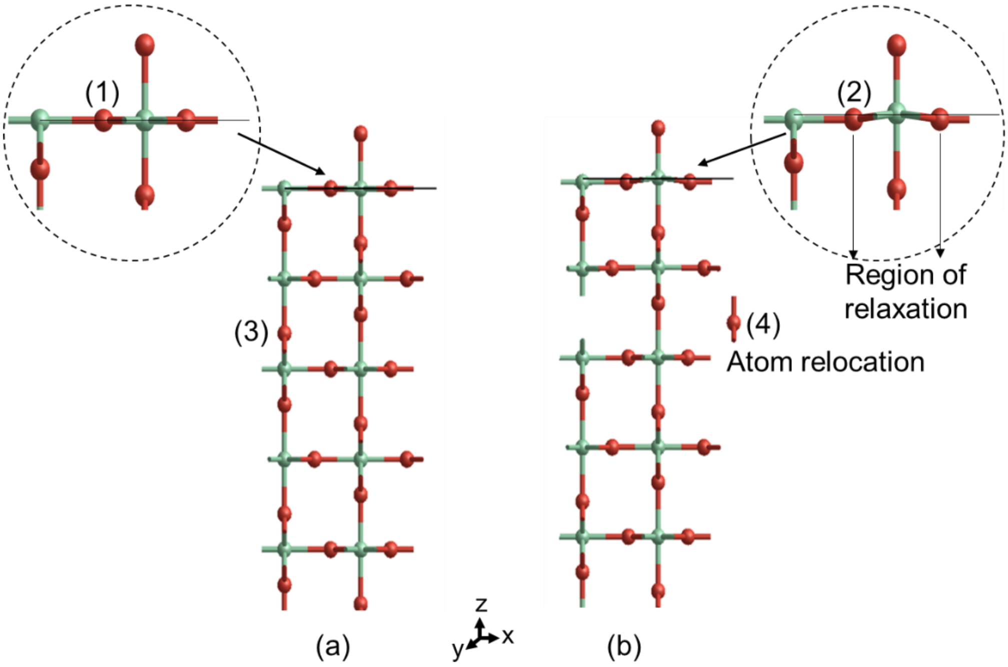

Figure 6.5 Cleaved (a) unrelaxed and (b) relaxed (1 1 0) surface of rutile. Surfaces were obtained using the surface builder module in GDIS. Ti and O atoms are in green and red respectively

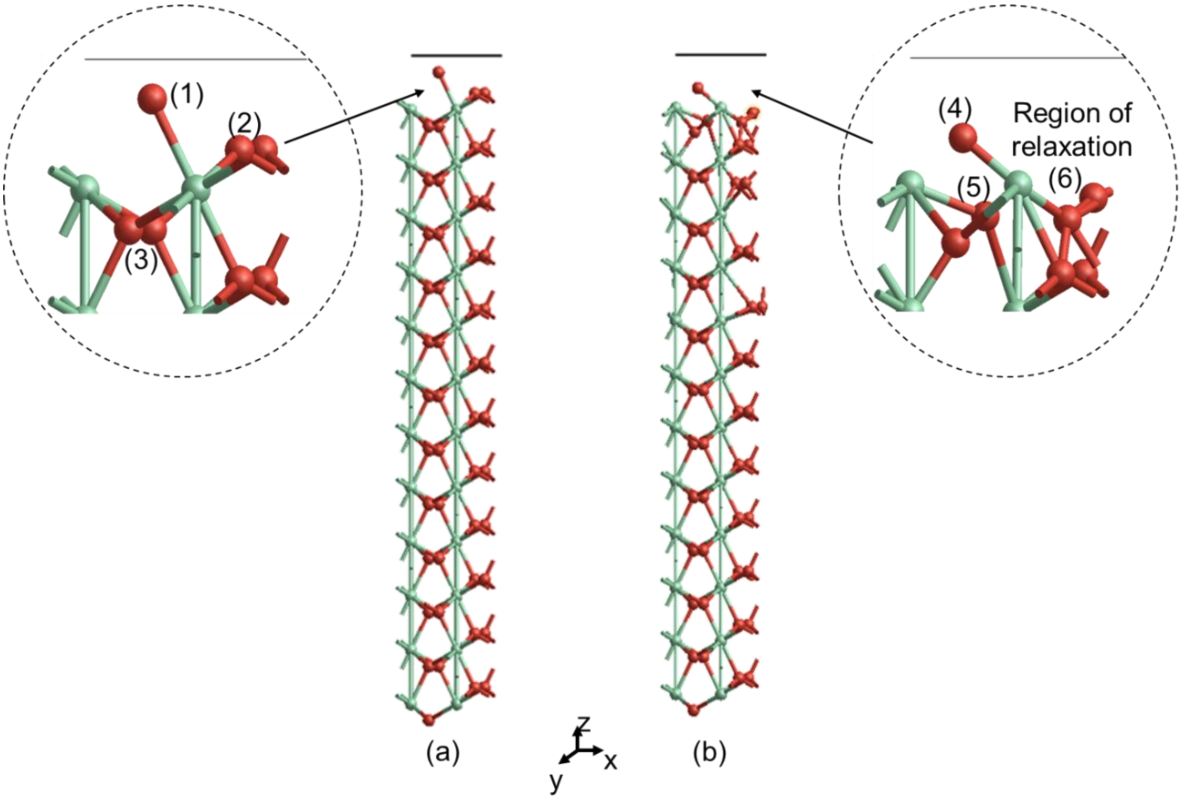

Figure 6.6 Cleaved (a) unrelaxed and (b) relaxed (0 1 1) surface of rutile. Surfaces were obtained using the surface builder module in GDIS. Ti and O atoms are in green and red respectively

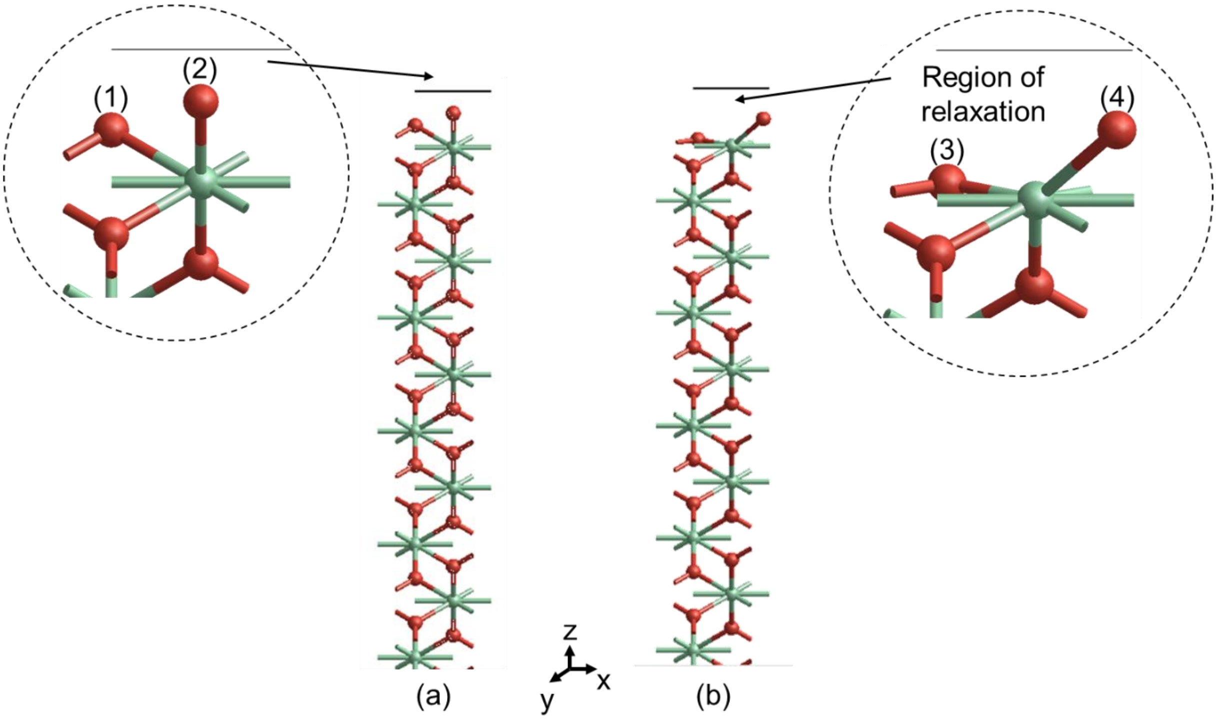

Figure 6.7 Cleaved (a) unrelaxed and (b) relaxed (1 0 0) surface of rutile. Surfaces were obtained using the surface builder module in GDIS. Ti and O atoms are in green and red respectively

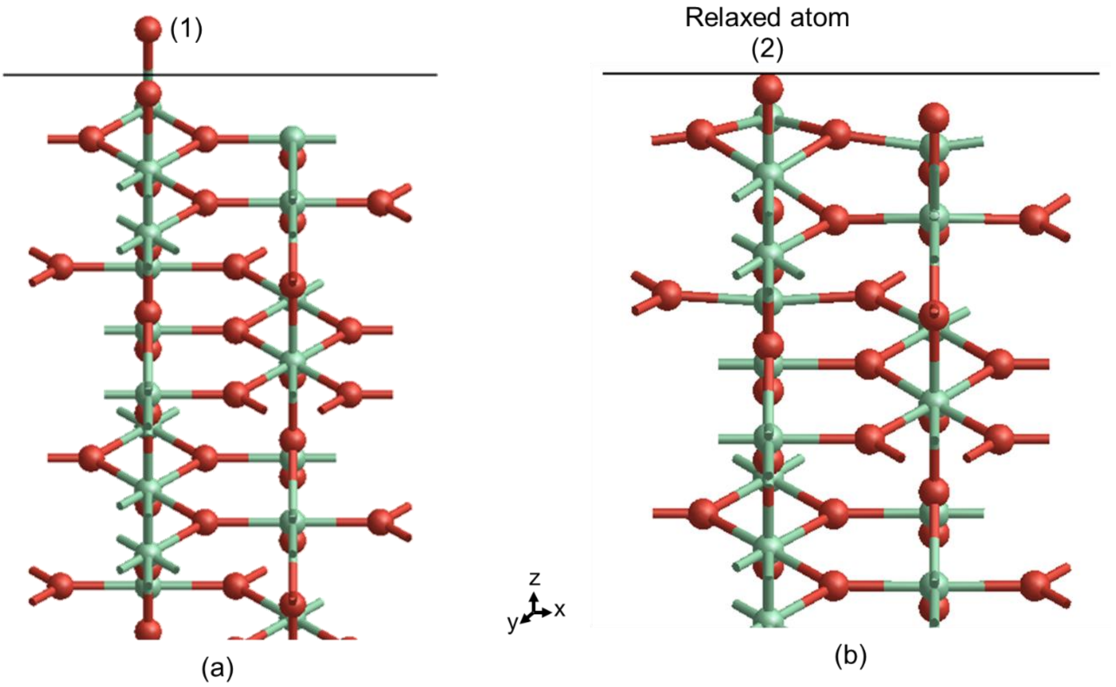

Figure 6.8 Cleaved (a) unrelaxed and (b) relaxed (2 2 1) surface of rutile. Surfaces were obtained using the surface builder module in GDIS. Ti and O atoms are in green and red respectively

Models of the equilibrium crystal morphology for anatase shown in Figure 6.9 - 6.11 were predicted using the calculated surface and attachment energies from the present study. Morphologies (a – e) in Figure 6.9 are seen to express the (0 0 1) and (0 1 1) surfaces and are similar to that predicted using the BFDH model in (a) of Figure 6.9. Overall, the capped octahedral shape observed in the morphologies is as a result of the (0 1 1) octahedral which is capped with the (0 0 1) surface. The (0 1 1) surface expressed on morphology from present study in (f) can be compared to that from experiment (Kostov, 1968) in (g). (Oliver et al., 1997) stated that the (0 0 1) surface is a major cleavage plane for anatase confirming it is a stable surface reflected in its low surface energy. Furthermore, the anatase phase showed the least change in surface energy when comparing the unrelaxed to the relaxed surfaces. The (0 0 1) surface showed no change in surface energy between its unrelaxed and relaxed surfaces, as seen in Table 6.2 and 6.3. This is further evident in Figure 6.10, as no significant change in terms of atom relocation or relaxation can be observed. This observation can be linked to the prediction of the morphology structure as there was also no change between the unrelaxed and relaxed morphology. The (0 1 1) however, showed Ti and O atom relocation from (1) to (2) as seen in Figure 6.11.

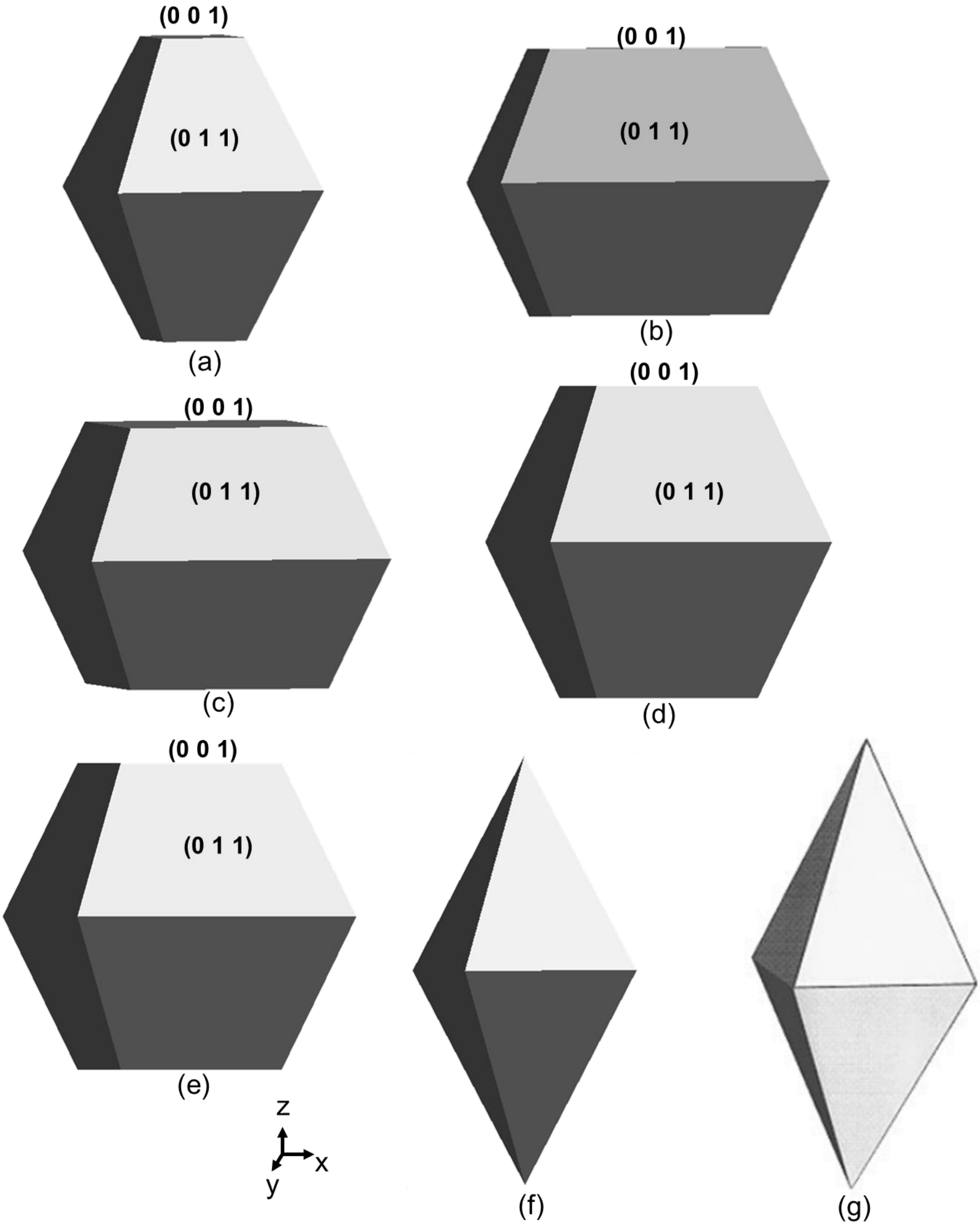

Figure 6.9 Prediction of the calculated and experimental equilibrium morphology anatase structure (a) BFDH model, (b) unrelaxed morphology using surface energies, (c) relaxed morphology using surface energies, (d) unrelaxed morphology attachment energies, (e) relaxed morphology attachment energies and (f) experimental data (Kostov, 1968). Structures predicted using the surface builder module in GDIS.

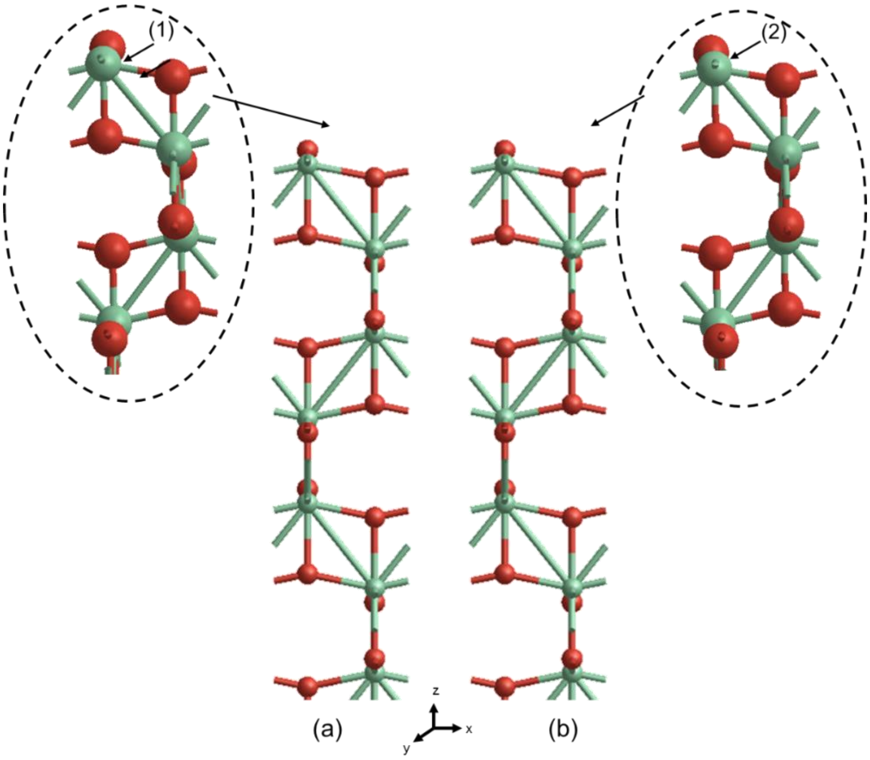

Figure 6.10 Cleaved (a) unrelaxed and (b) relaxed (0 0 1) surface of anatase. Surfaces were obtained using the surface builder module in GDIS. Ti and O atoms are in green and red respectively

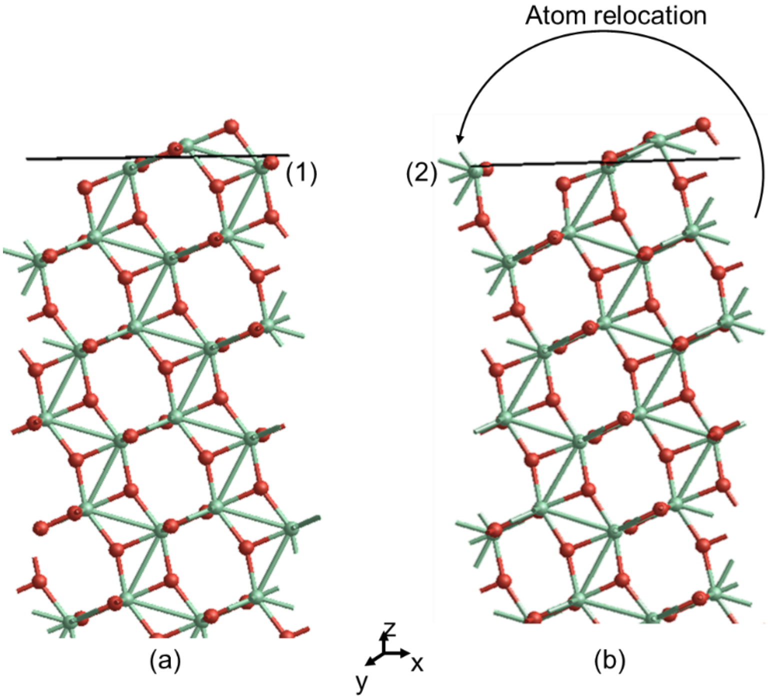

Figure 6.11 Cleaved (a) unrelaxed and (b) relaxed (0 1 1) surface of anatase. Surfaces were obtained using the surface builder module in GDIS. Ti and O atoms are in green and red respectively

Models of the equilibrium crystal morphology for brookite are presented in Figure 6.12 - 6.17, and were predicted using the calculated surface and attachment energies from the present study. As shown in Figure 6.12, the (0 0 1), (0 1 0), (1 0 0), (1 1 1) and (2 1 0) surfaces are expressed in all morphologies predicted using the BFDH model, surface and attachment energies. As in the case of rutile and anatase, the (0 0 1) surface formed at a cap on the orthorhombic brookite structure. The (0 1 0) formed a hexagonal protrusion on all the morphologies. The relaxed morphologies predicted using the surface and attachment energies showed a relaxing of the (0 1 0) surface in the x direction when compared to the unrelaxed morphologies. The (1 0 0) surface has the lowest surface and highest attachment energies before and after relaxation, and is seen to grow mostly in the z direction. It can be seen in Figure 6.15 and 6.17 that the (1 0 0) and (2 1 0) surfaces showed no significant change upon relaxation. This observation is also represented in their surface energy values in Table 6.2 – Table 6.5 which shows the (2 1 0) has the lowest change in surface energy (15.79 %), followed by (1 0 0) which is 15.85 %, upon relaxation. Visualisation of the other brookite surfaces showed that they experienced more significant atom relaxation (for the (0 0 1), (1 1 1) and (2 1 0) surfaces) and atom relocation (for the (0 1 0) surface).

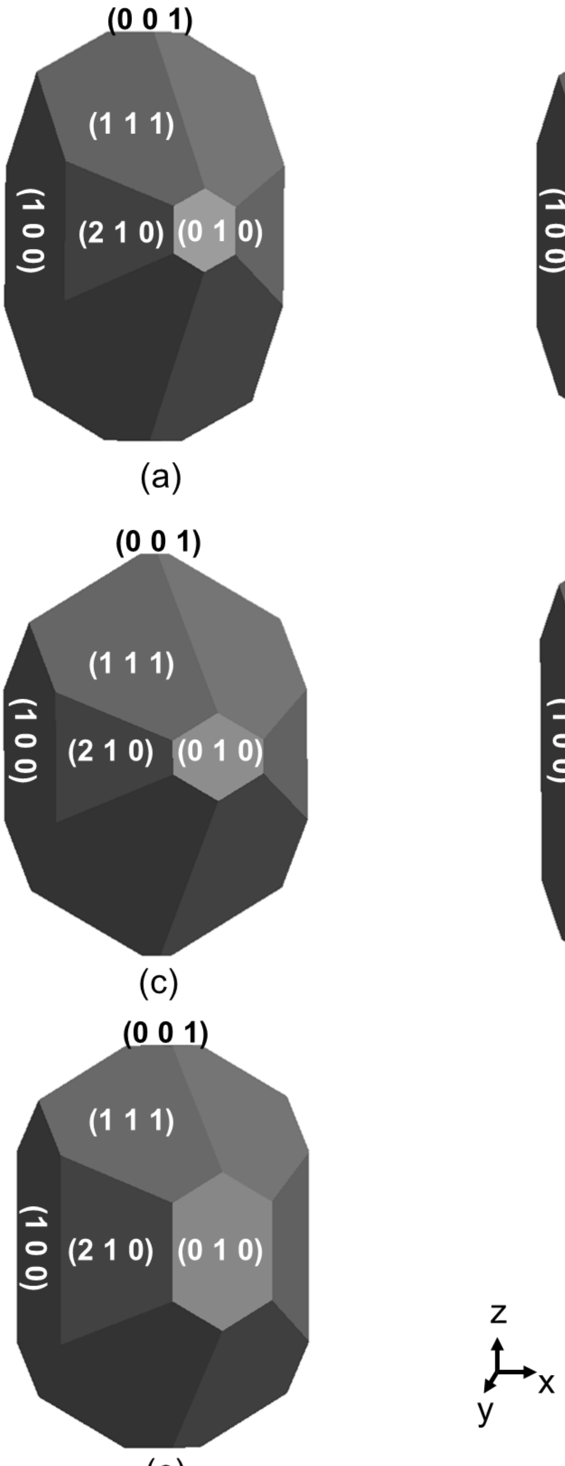

Figure 6.12 Prediction of the calculated and experimental equilibrium morphology brookite structure (a) BFDH model, (b) unrelaxed morphology using surface energies, (c) relaxed morphology using surface energies, (d) unrelaxed morphology attachment energies, (e) relaxed morphology attachment energies and (f) experimental data (Kostov, 1968). Structures predicted using the surface builder module in GDIS.

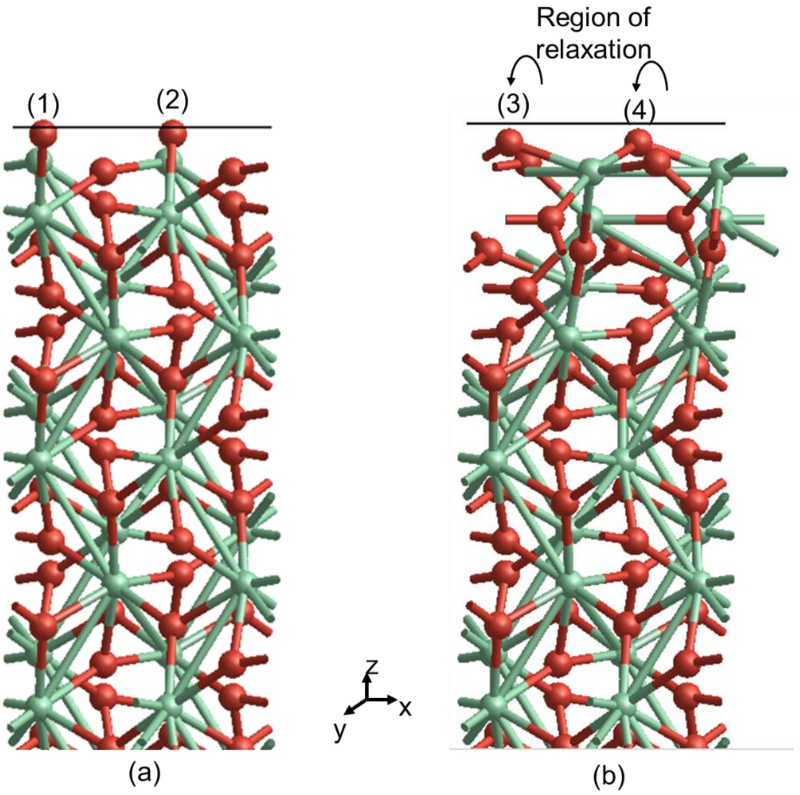

Figure 6.13 Cleaved (a) unrelaxed and (b) relaxed (0 0 1) surface of brookite. Surfaces were obtained using the surface builder module in GDIS. Ti and O atoms are in green and red respectively

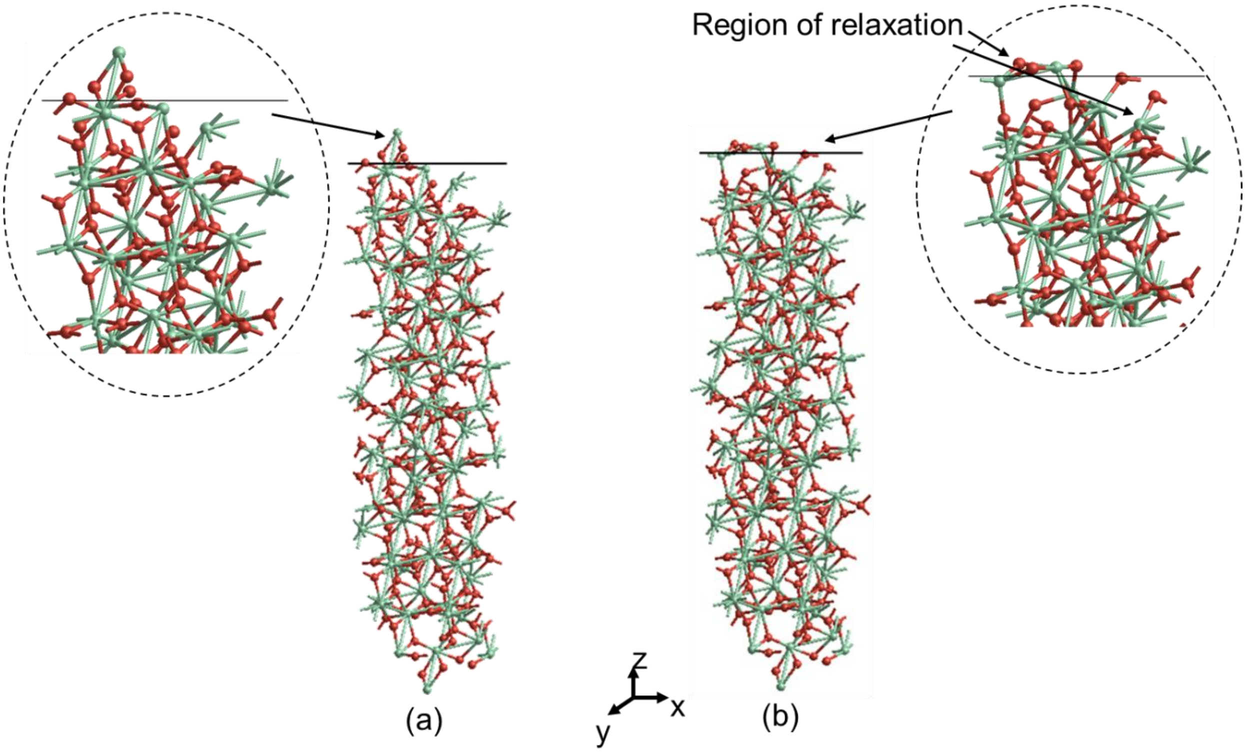

Figure 6.14 Cleaved (a) unrelaxed and (b) relaxed (1 1 1) surface of brookite. Surfaces were obtained using the surface builder module in GDIS. Ti and O atoms are in green and red respectively

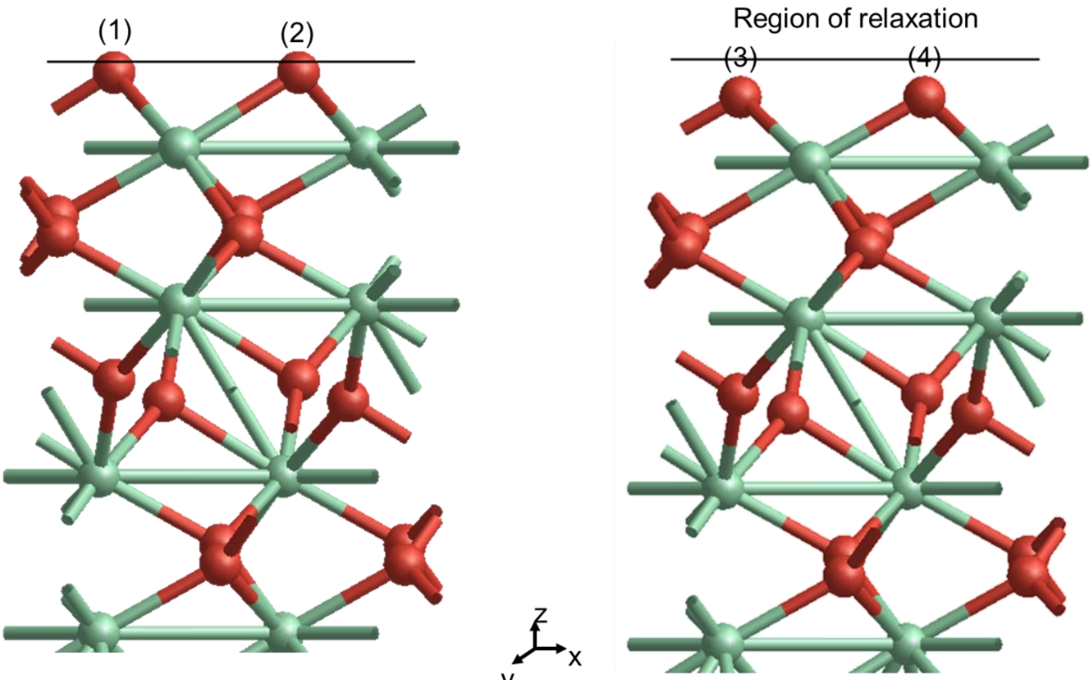

(a) (b)

Figure 6.15 Cleaved (a) unrelaxed and (b) relaxed (1 0 0) surface of brookite. Surfaces were obtained using the surface builder module in GDIS. Ti and O atoms are in green and red respectively

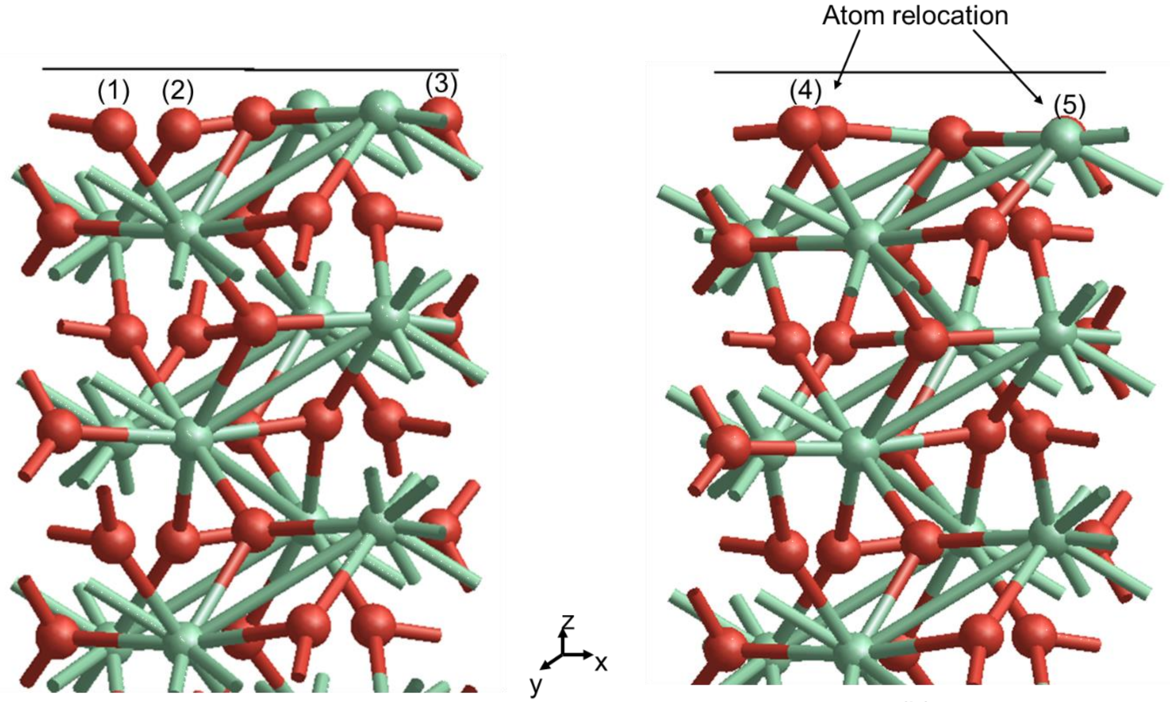

(a) (b)

Figure 6.16 Cleaved (a) unrelaxed and (b) relaxed (0 1 0) surface of brookite. Surfaces were obtained using the surface builder module in GDIS. Ti and O atoms are in green and red respectively

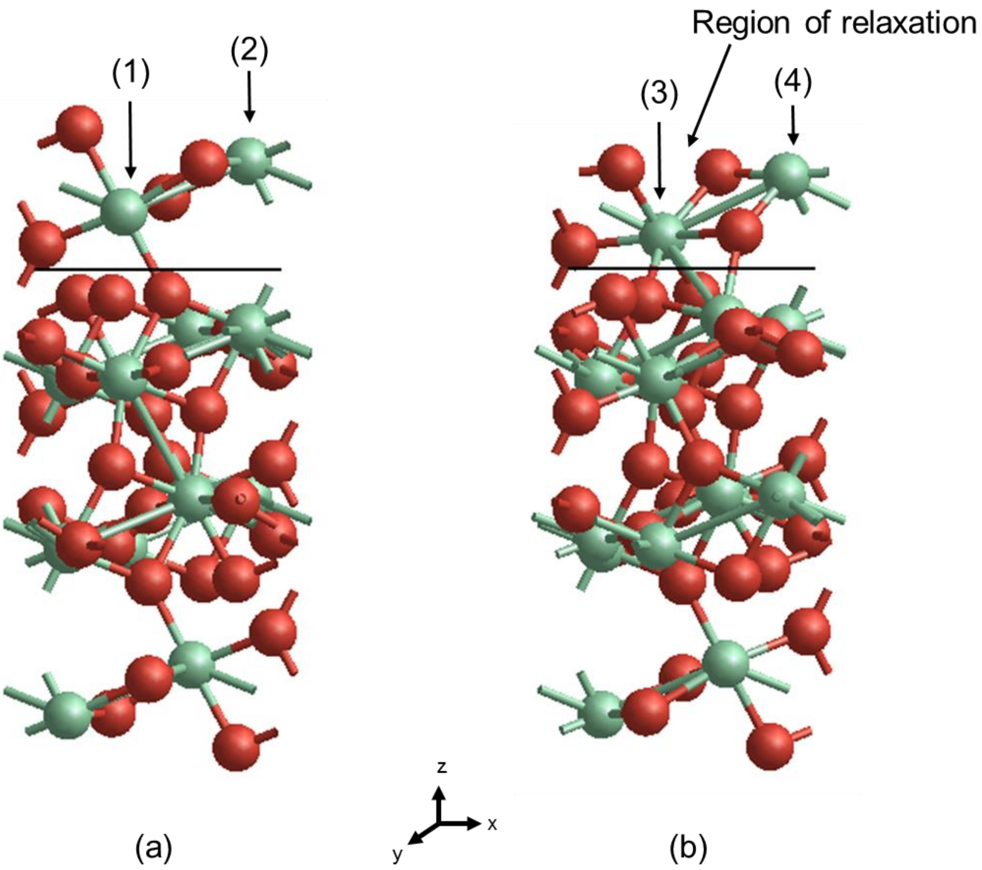

Figure 6.17 Cleaved (a) unrelaxed and (b) relaxed (2 1 0) surface of brookite. Surfaces were obtained using the surface builder module in GDIS. Ti and O atoms are in green and red respectively

6.3 Conclusion of results on properties of TiO_2 crystalline phases

Overall, anatase has shown the most stability as very little change between the unrelaxed and relaxed surface and attachment energies from the present study occurred. As discussed in section 4.2 and from literature findings, rutile and anatase are known to be most thermodynamically important phases as rutile is known to be the stable phase at room temperature in the bulk form and anatase, the most stable phase in the nanocrystalline form. Moving on, further simulations have been carried out to investigate the properties of rutile and anatase TiO_2 nanoparticles and results are presented in the subsequent in sections.

6.4 Properties of TiO_2 nanoparticles

Molecular dynamics simulations have been performed using DL_POLY on anatase and rutile TiO_2 nanoparticles with sizes ranging between 2 and 6 nm as a function of temperature. As discussed in section 5.3.1, simulations were carried out using the NVT ensemble and Berendsen thermostat, in a cuboidal periodic simulation box. The edge length of the simulation box was more than four times the diameter of the nanoparticle (Figure 5.1), large enough to avoid interactions between a given particle and its periodic images in the adjoining cells. The size of the simulation cells and their corresponding containing nanoparticle sizes, is given below.

Table 6.6 Size of cuboidal simulation box and their corresponding containing nanoparticle sizes.

Particle size (nm)	Cuboidal simulation box size (nm^3)
2	51,200
3	172,800
4	409,600
5	800,000
6	1,382,400

Simulations were carried out with time step of 1 fs and for a simulation or production time of 1 ns, sufficiently long enough to achieve steady state of the molecular structure of the particles. The equilibration time was for a period of 100 ps and was at the start of each simulation. Test runs were carried out initially, to investigate the influence of the choice of the thermostat, extended equilibration and production times, as well as time step, on the simulation output. Production times were extended to 3 ns during testing, for a typical case of 2 nm anatase, and analysis conducted did not reveal any significant difference in results between simulations ran for 1 and 3 ns. (Naicker et al., 2005) suggested that extended simulation times could possibly lead to phase change from rutile to anatase for smaller particles, and from anatase to rutile for larger particles, hence the choice of production time of 1 ns, in this research. Upon testing, the Berendsen thermostat evolved as the preferred choice for thermostat, as it adequately conserved the system energy throughout the simulations. Thermodynamic and structural properties such as total energies and radial distribution functions for the particles in both vacuum and water environments are reported for the different nanoparticle sizes and their dependence on temperature revealed. Studies have also been conducted on the change of anatase nanoparticles (as model nanoparticles) from their initial (before simulation) to final (after simulation) structures (Bates et al., 1997). Surface energies for the different particle sizes have also been reported for both vacuum and liquid environments.

6.4.1.1 Thermodynamic properties

The variation of the Total Energy (ETOT) as a function of temperature, particle size and simulation time is revealed in the plots of Figures 6.18 – 6.21 and Figures A.1 – A.6 for anatase and rutile. The temperature and total energy (i.e. ETOT) profile in the plots reveal that the average system temperature and energy for both anatase and rutile were successfully maintained and conserved using the Berendsen thermostat in the NVT ensemble during the simulations.

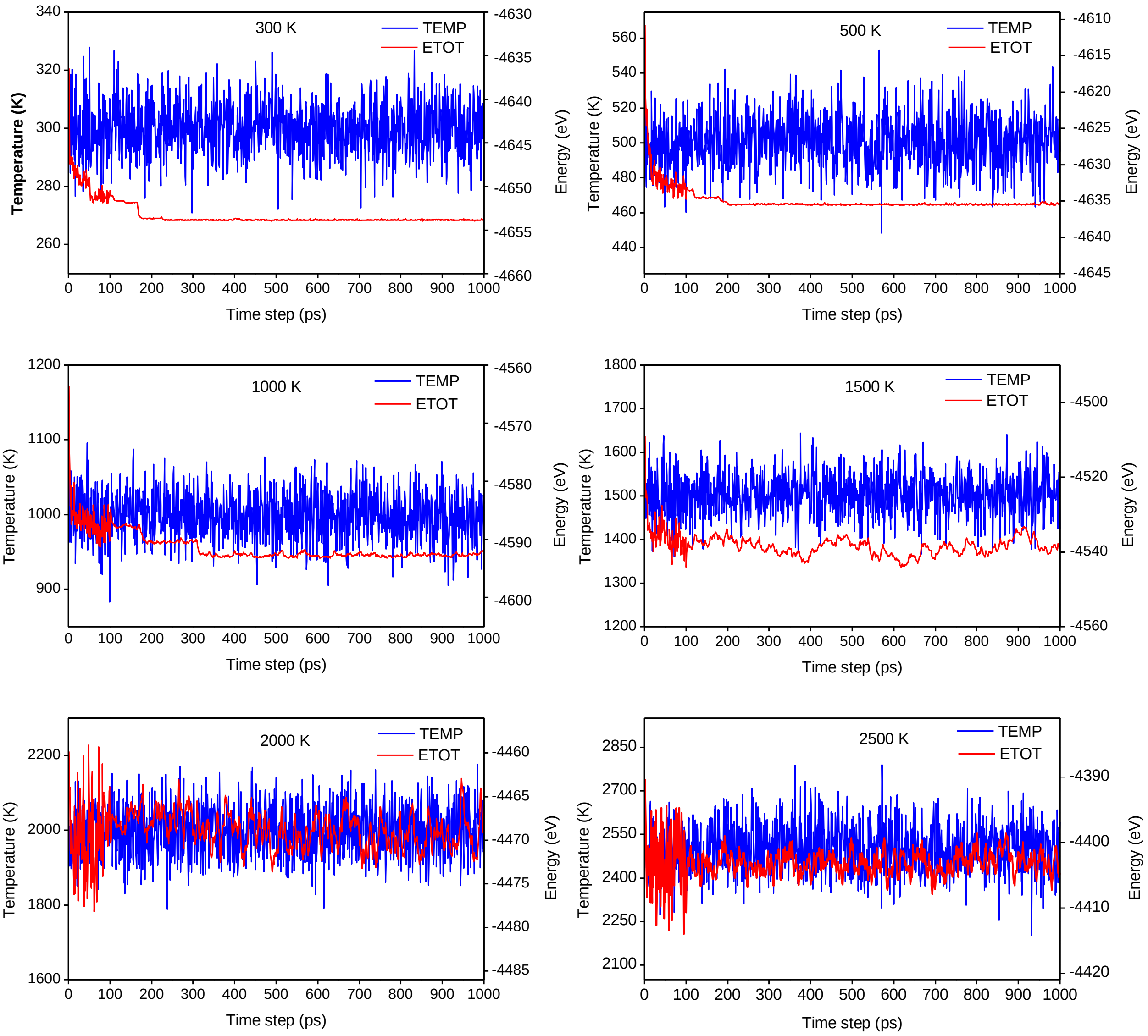

Figure 6.18 Temperature and Total Energy (ETOT) plotted against time for 2nm anatase TiO_2 nanoparticles

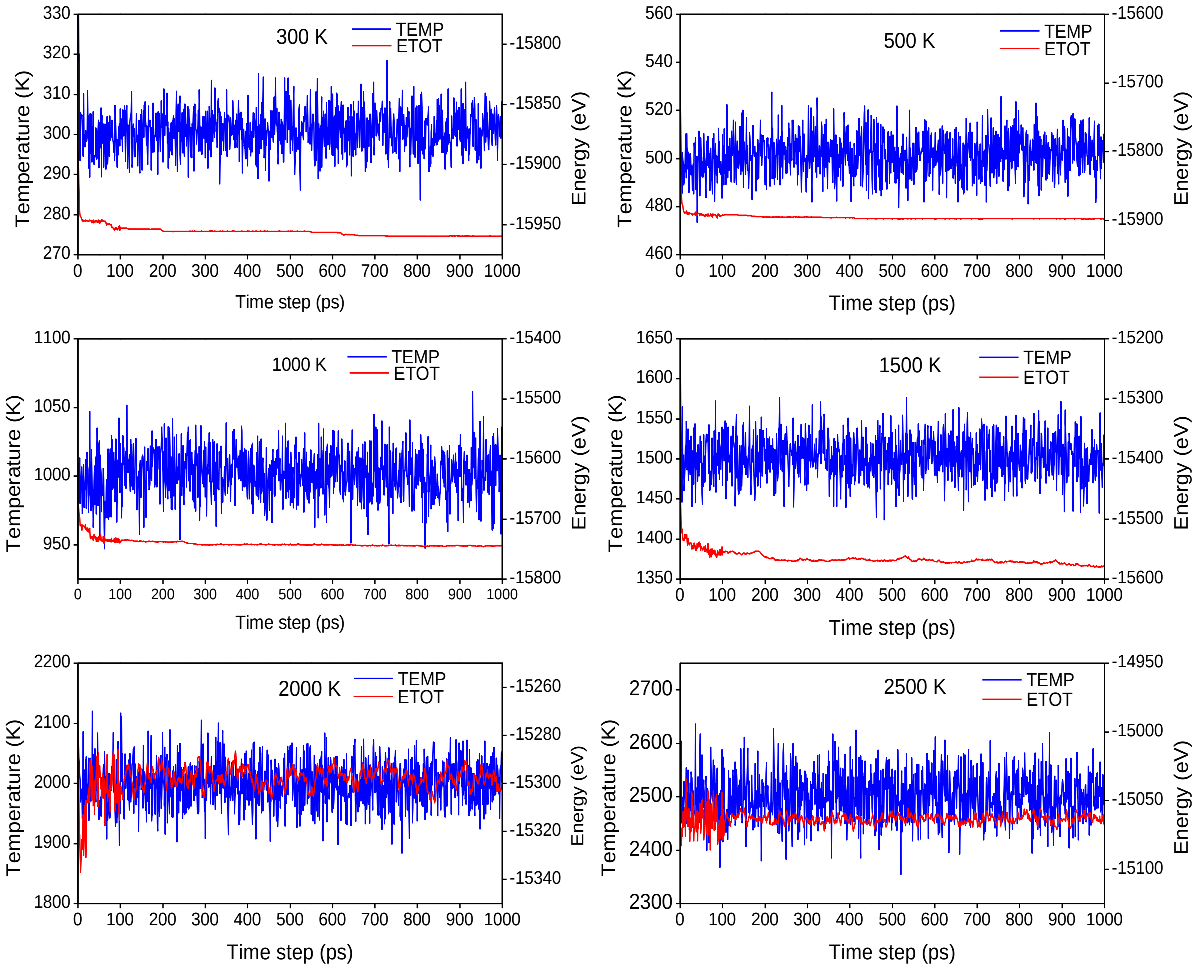

Figure 6.19 Temperature and Total Energy (ETOT) plotted against time for 3nm anatase TiO_2 nanoparticles

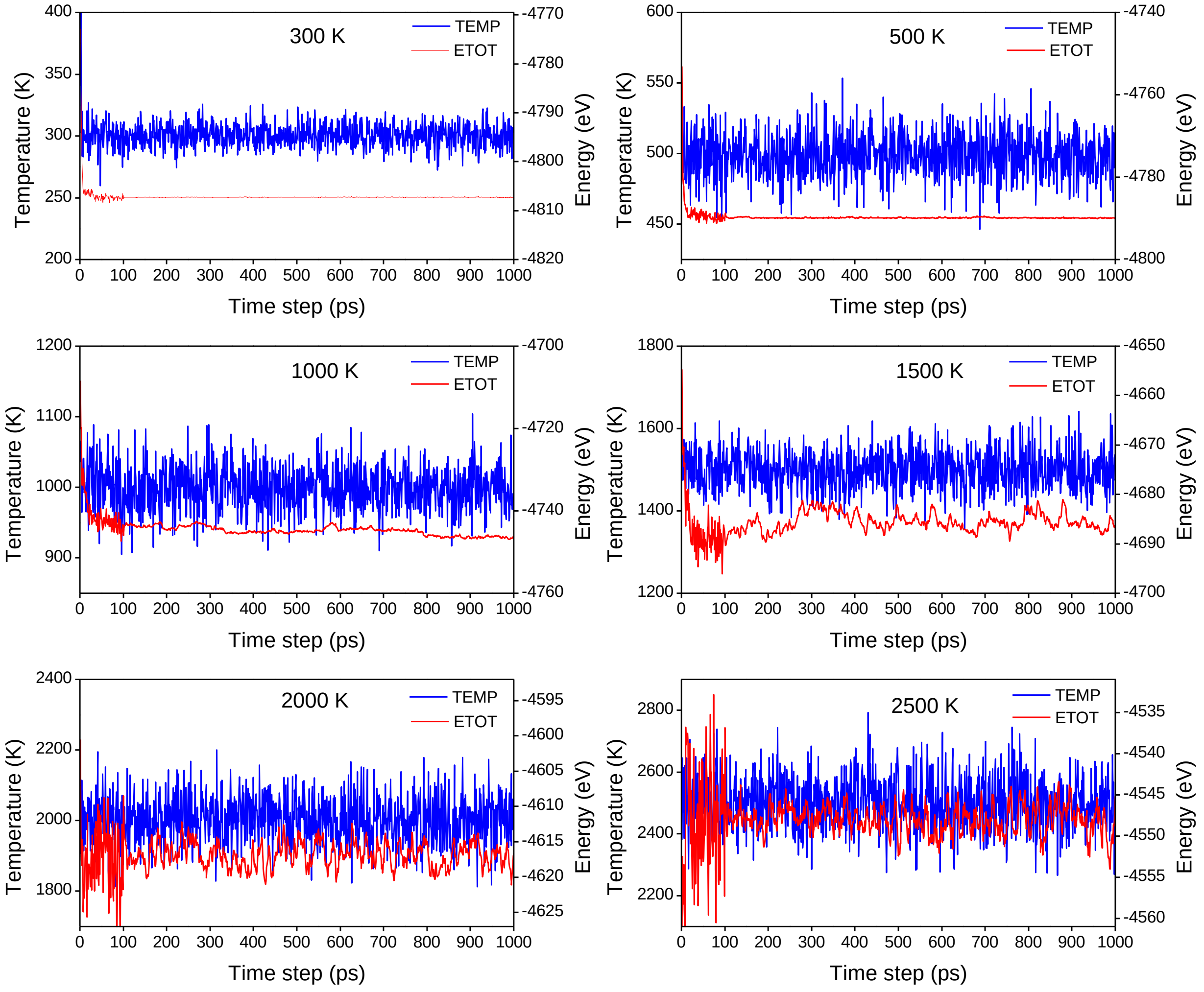

Figure 6.20 Temperature and Total Energy (ETOT) plotted against time for 2nm rutile TiO_2 nanoparticles

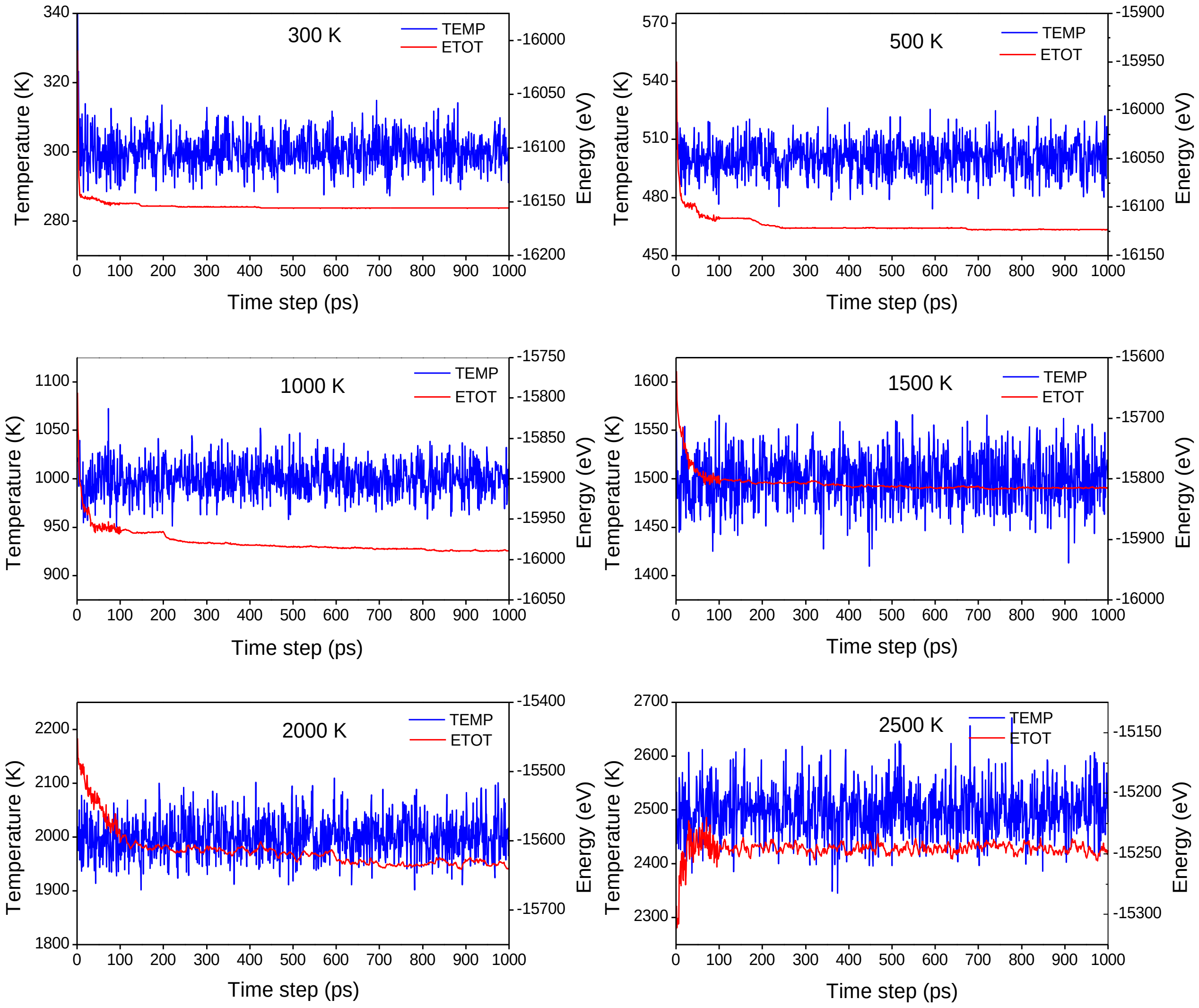

Figure 6.21 Temperature and Total Energy (ETOT) plotted against time for 3nm rutile TiO_2 nanoparticles

The plot of ETOT as a function of simulation time in Figure 6.18 - 6.21 and A.1 – A.6, shows an increase in ETOT with increase in temperature, for all particle sizes. Figure 6.22, shows the variation of ETOT with temperature for different nanoparticle sizes. An increase in ETOT with temperature can be observed across all particles sizes. This temperature dependence on energy, can also be used to estimate the melting point of the TiO_2 rutile and anatase phases. This is similar to the work of (Collins et al., 1996, Filyukov et al., 2007) who have used ETOT profile to estimate the melting point and phase transition of titanium dioxide microclusters of 1011 and 1245 atoms. The number of atoms used in their work correspond to a particle size of diameter of about 3nm. (Filyukov et al., 2007) confirmed that the melting point for anatase is 2250 K while (Collins et al., 1996) confirmed that the melting point for rutile clusters was in the range of 2150 to 2300 K. In Figure 6.22, apart from the case of 2 nm, the total energy is seen to increase linearly with temperature up to

2000 K, after which a sudden increase is observed between 2000 and 2500 K. 2000 K can be considered as a transition regime, in which melting begins of to occur. The energy is seen to further increase linearly, from 2500 K to 3000 K. Although it is difficult to establish the exact melting point in this case, the region of melting point in Figure 6.22 is similar to the observations and reported melting points for (Collins et al., 1996, Filyukov et al., 2007). However, this observation does not apply to the 2 nm particle size as the total energy is seen to increase linearly from 300 K to 3000 K. This suggests that apart from the fact that melting point and phase transition are temperature dependent, they may also be dependent on particle size. Note that in smaller particles, there are fewer atoms at the surface than at the core of the particles, compared to larger particles. The surface to volume ratio for smaller particles is large and changes with particle size.

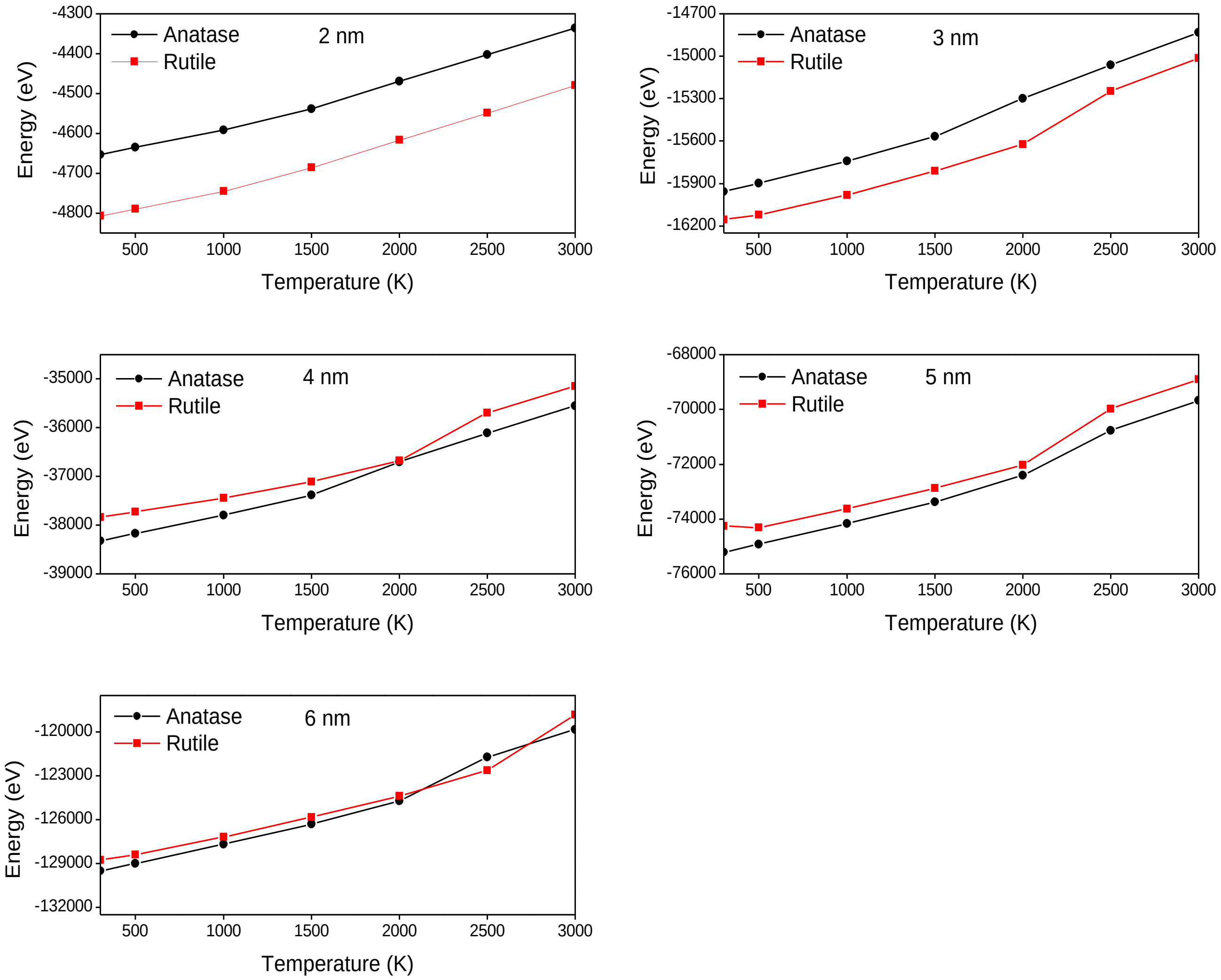

Figure 6.22 Total Energy (ETOT) as a function temperature for 2 – 6 nm nanoparticles

6.4.1.2 Structural properties

Radial distribution functions (RDFs) for anatase and rutile are shown for Ti – Ti, Ti – O and O – O pairs at temperatures between 300 and 3000 K in Figures 6.23 and 6.24, and Figures B.1 – B.8. The radial distribution function best describes the variation of atomic density as a function of the distance from a reference atom (Brostow, 1977). They are useful in describing the structure of a system. The radial distribution function $G(r)$ (which is dimensionless), represents the probability of locating an atom at a distance *r* from a reference atom, compared to an ideal gas distribution of same density. For example, a system of atoms with a $G(r)$ value of 2 at a separation distance, *r*, will mean that it is two times more likely that two atoms would have this separation than in the ideal gas. This is because an ideal gas is isotropic and homogenous, and therefore atoms or particles will be non-interacting. At long distances of r, $G(r)$ tends to the ideal gas value, which means that there is no long range order (Leach, 2001). In crystals, the radial distribution function has an infinite number of sharp peaks, with separations and heights which are characteristic of their lattice structure. In liquids, the radial distribution function is in between the solid and the gas, and is associated with a small number of peaks as short distances, and eventually decays to a constant value at longer distances (Leach, 2001).

The function $G(r)$ can be used to estimate the coordination number $n_{ij}(r)$. The coordination number of a central/reference atom represents the number of its nearest neighbours, which as a structural parameter is used in structural analysis. As this number captures the number of nearest neighbour atoms bonded to a central atom (either by single or multiple bonds), it is also associated to the bond length. The coordination number, $n_{ij}(r)$ is given by the following equation (Brostow, 1977);

$$n_{ij}(r) = 4\pi\rho \int_{r_{min}}^{r_{max}} r^2 G(r) dr \tag{6.1}$$

Where ρ is the number density and is given as; $\rho = N/V$ in which case N is the number of atoms/molecules in a system of volume V (Brostow, 1977).

It is important to note that all simulations were conducted at equivalent amounts of simulation time (i.e. 0 to 1000 ps) and all results presented correspond to the results at the end of the simulation. For the purpose of determining the coordination number of Ti atoms, a cut-off radius which describes the number of oxygen atoms in the cut-off region was used and was set at 2.3 Å. In the context of the RDF plot, the cut-off region represents the position of the first minimum after the first peak (r_{min} is the lower limit before the first peak and r_{max} is the upper limit after the first peak). Based on this, the coordination numbers of Ti for the different particle sizes and temperatures are reported in Table 6.7.

Table 6.7 Coordination number for corresponding particle size, bond length/position of the first peak, r_{ij}, and temperature for anatase and rutile TiO_2 nanoparticles (Okeke et al., 2013)

Anatase								
Particle size (nm)	r_{ij} **(Å)**	$n_{ij}(r)$						
		High ordered				**Metastable/High temperature**		**Liquid TiO_2**
	Ti - O	**300 K**	**500 K**	**1000 K**	**1500 K**	**2000 K**	**2500 K**	**3000 K**
2	1.89	5.33	5.31	5.22	5.01	4.78	4.58	4.38
3	1.91	5.48	5.48	5.41	5.27	4.96	4.72	4.50
4	1.91	5.62	5.60	5.53	5.42	5.06	4.79	4.56
5	1.91	5.68	5.68	5.61	5.52	5.32	4.83	4.60
6	1.91	5.72	5.72	5.67	5.58	5.40	4.85	4.61
Rutile								
Particle size (nm)	r_{ij} **(Å)**	$n_{ij}(r)$						
		High ordered				**Metastable/High temperature**		**Liquid TiO_2**
	Ti - O	**300 K**	**500 K**	**1000 K**	**1500 K**	**2000 K**	**2500 K**	**3000 K**
2	1.89	5.31	5.38	5.24	5.11	4.88	4.69	4.50
3	1.91	5.61	5.54	5.43	5.37	5.17	4.72	4.50
4	1.91	5.91	5.62	5.56	5.50	5.36	4.82	4.59
5	1.91	5.69	5.68	5.64	5.60	5.48	5.24	4.70
6	1.91	5.74	5.72	5.69	5.62	5.49	5.26	4.79

Table 6.7 above reveals a bond length for both anatase and rutile nanoparticles of 1.89 Å for 2 nm particle size while a bond length of 1.91 Å is seen for particle sizes between 3 and 6 nm. (Naicker et al., 2005), suggested that based on molecular dynamics simulation results, 5-coordinated titanium had bond lengths of 1.92 Å which corresponds well with the current results presented in Table 6.7. The RDF at 3000 K best describes a molten TiO_2 system. The bond length for Ti – O in anatase was also revealed by (Tang et al., 1993, Zhang et al., 2008, Banfield et al., 1993) who observed a coordination number of 5.3. (Tang et al., 1993) confirmed a bond length of 1.91 Å and 1.94 Å for anatase and rutile respectively, while (Zhang et al., 2008) confirmed a bond length of 1.94 Å for anatase and rutile nanoparticles. This suggests a combining of Ti – O octahedra and pentahedra with, respectively, coordination numbers of 6 and 5. It can be observed from Table 6.7 that both anatase and rutile nanoparticles become tetrahedrally coordinated (i.e. 4-coordinated titanium) as temperature increases in fact, the coordination number

increases with increasing particle size but decreases with increasing temperature. The reason for the increase in coordination number with particle size is as a result of the large surface-to-volume ratio which small particles possess, and which changes substantially with increasing particle size. This has an effect on the calculation of coordination number. The tetrahedrally coordinated titanium in Table 6.6 represents under-coordinated TiO_4 units such as observed in Ba_2TiO_4 where the Ti – O bond length was 1.82 Å (Hoang, 2008). This tetrahedral, under-coordinated titanium is thought to represent molten TiO_2 systems (Hoang, 2008). It can be observed that the 4-coordinated titanium is manifested at temperatures between 2000 and 3000 K for all particle sizes. These observations correspond to the thermodynamic properties of the particles where it is seen that the melting point is approached at temperatures between 2000 and 2500 K after which the system is observed to become more liquid-like.

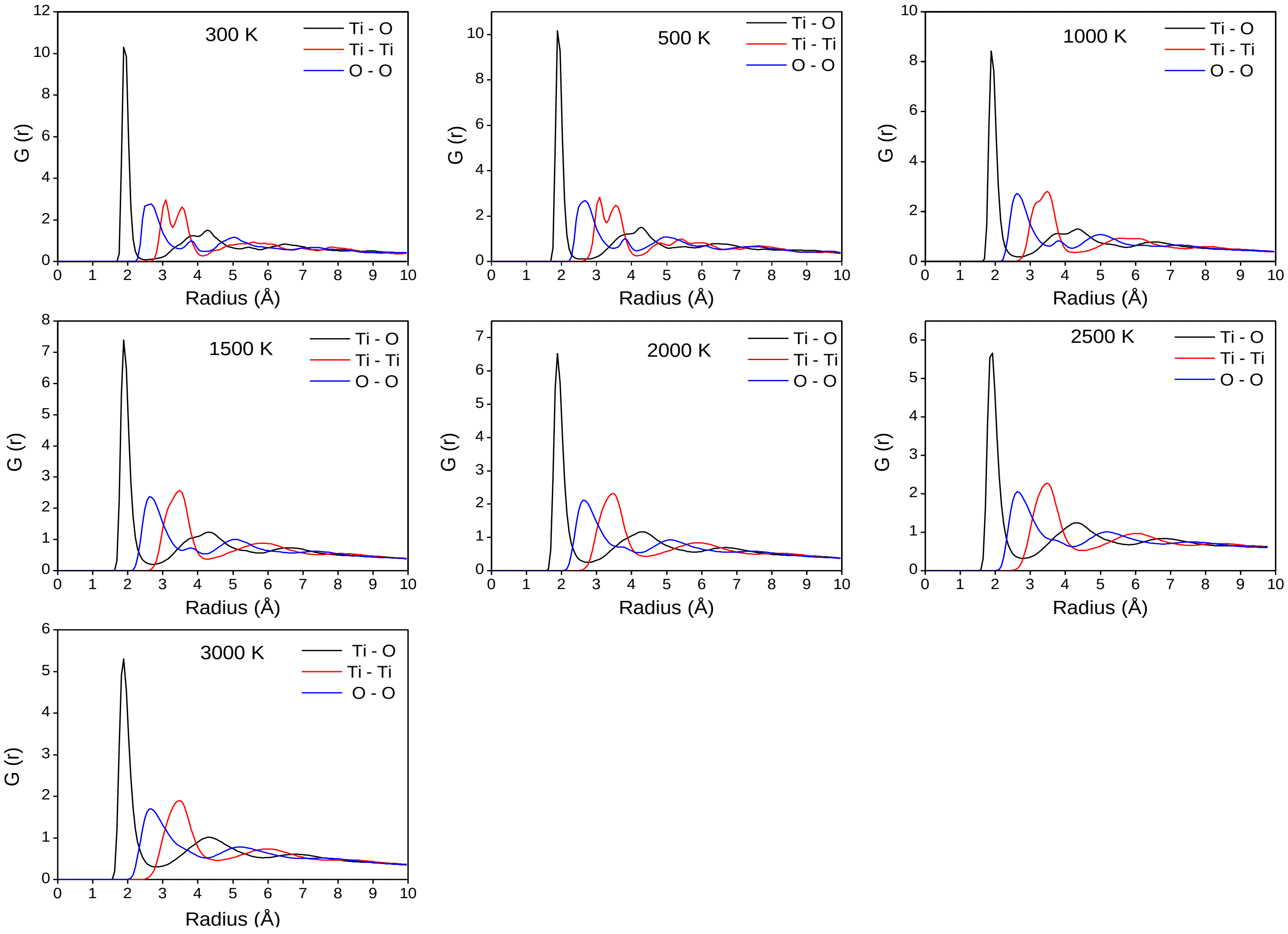

Figure 6.23 RDF's for anatase Ti – Ti, Ti – O and O – O pairs for 2 nm

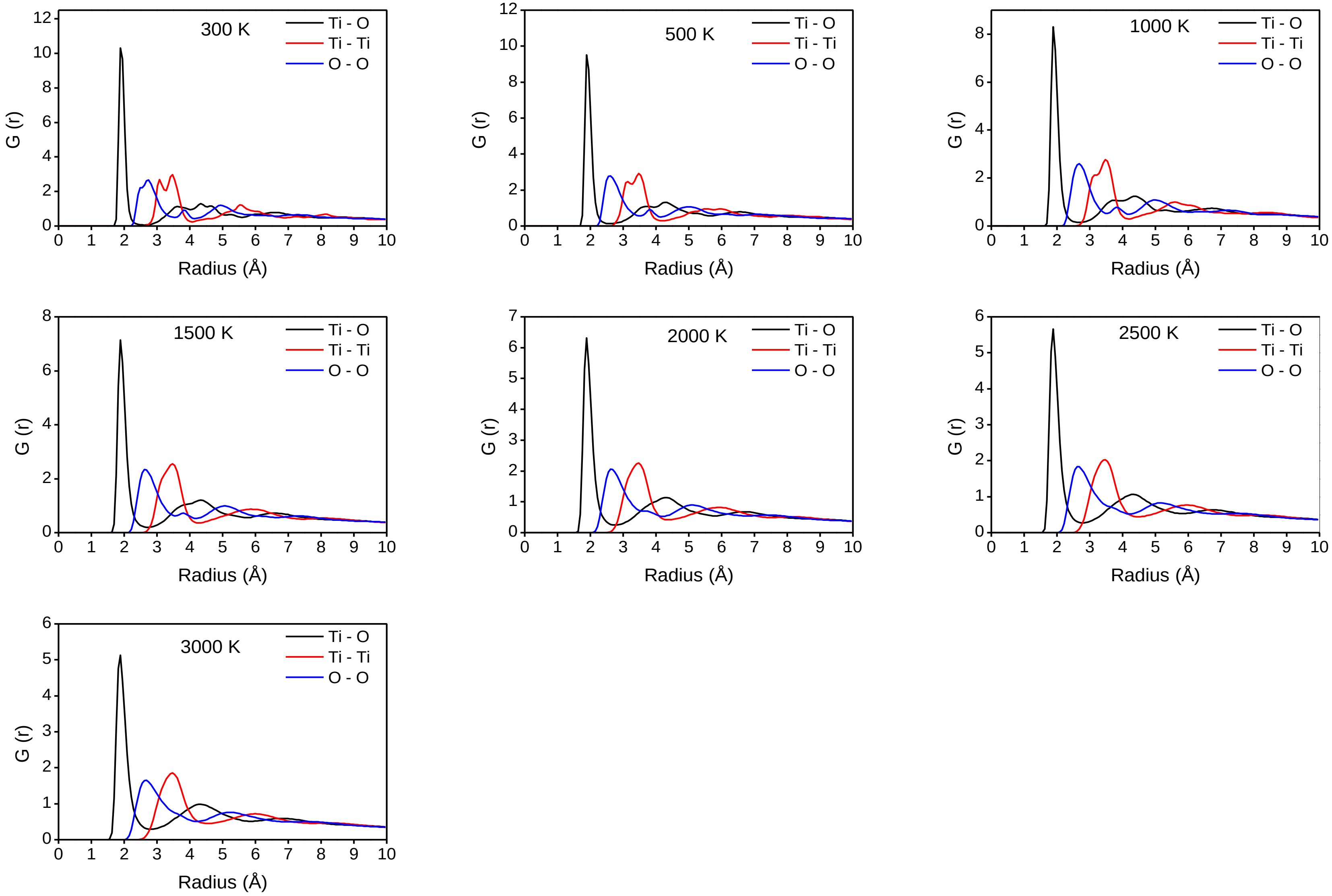

Figure 6.24 RDF's for rutile Ti – Ti, Ti – O and O – O pairs for 2 nm

The RDFs in Figures 6.23 – 6.24, and Figures B.1 – B.8 represent a well ordered (represented by the turning points in the RDF plot), high temperature and liquid anatase and rutile TiO_2 nanoparticles for temperatures between 300 and 3000 K and for all particle sizes. The high orderliness in the case of low temperature (300 K) can be attributed to the high coordination number of titanium which is seen to decrease to a point of under-coordination as the temperature increases, as seen in Table 6.7. It is observed that the peak that corresponds to the first coordination sphere, for each pairing of atoms broadens as the temperature increases. This is more evident for the Ti – O pairs as they possess the highest peaks. For example, the peaks of Ti – O pairs for 2 nm anatase and rutile in Figure 6.23 and 6.24 respectively, both have a G(r) of 10 at 300 K. However, at the same temperature, the peaks of O – O and Ti – Ti both have a G(r) of 2.5. The initial double peak observed in the Ti – Ti and O – O RDF's is seen to broaden as the temperature is increases. At 300 K, the structure is highly crystalline and well ordered. The peaks reduce as temperature increases, and the structure is observed to be more liquid-like. For example, the Ti – O peak for rutile in Figure 6.24 has a G(r) of 9 at 500 K, 8 at 10 K, 7 at 1500 K, and 5 at 3000 K. Furthermore, an increased number of turning points in the RDF plots is observed as the particle size increases. This however, is seen to straighten and broaden out as the temperature increases. This can be observed for anatase particles of 3 - 6nm in Figure B.1 – B.4, where the plots are seen to have 4 turning points of Ti – O at 3 nm, 5 turning points of Ti - O at 4 nm, 6 turning points of Ti – O at 5 nm and 7 turning points of Ti – O at 6 nm. The stretching and broadening of the RDF pairs is also observed to be associated with a rising of the initial minimums after the first peaks, mostly at temperatures, 2500 and 3000 K. These minimums, especially in the case of the Ti – O pairs and which are seen to be at a radius of about 2.63 Å, rise as they stretch and broaden. It is important to note that the first peaks observed in the RDFs is caused by the attractive part of the potential. At distances where the potential has its minimum, there are more atoms than average. At distances further away, there are less atoms than average. Hence, the reason for the increased number of turnings with increasing particle size is that there are more atoms at the core and surface of large particles (with more interactions), compared to smaller particles.

Figure 6.25 shows an increase in surface disordering of anatase nanoparticles as temperature increases, which is also represented in the RDF plots above.

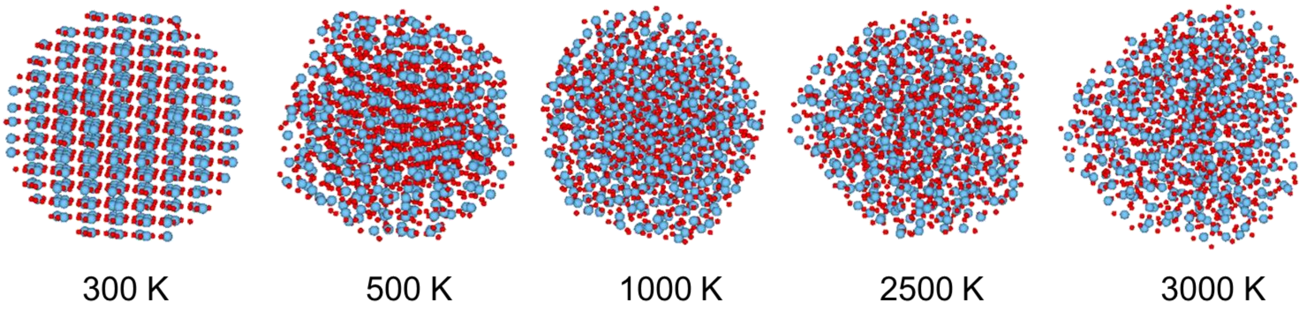

Figure 6.25 Surface disordering of anatase nanoparticles with increase in temperature

6.4.1.3 Surface energy of TiO_2 nanoparticles

In the case of the nanoparticles, the average surface energy was calculated by using the following expression (Naicker et al., 2005, Song et al., 2009);

$$U_{Surface} = \frac{(U_{cluster} - nU_{bulk})}{4\pi r^2} \tag{6.2}$$

Where $U_{cluster}$ is the potential energy of the nanoparticle, U_{bulk} is the potential energy per TiO_2 unit in the bulk material, n is the number of TiO_2 units in the nanoparticle and r is the radius of the nanoparticle. The surface energy of nanoparticles is estimated by including any differences between the energy of atoms in the interior of the nanoparticle and those in the truly bulk material within the surface energy. Therefore, it is necessary to calculate the energy of the bulk material in such as a way to minimise any effects as a result of these energy differences. In this research, surface energy of the nanoparticles was calculated at different temperature ranging from 300 K - 2500 K. The energy of the bulk material U_{bulk} was calculated corresponding to the temperature of the simulation of the nanoparticle.

Also, since the particles become less spherical as the temperature increases, the assumption that the particle is spherical and hence the use of the formula for surface area (i.e. $4\pi r^2$) in Equation 6.2 becomes a poor approximation. For this reason, true surface area values for the particles were obtained from Materials Studio. Materials Studio estimates surface area by creating a Connolly, van der Waal or solvent surface around the material (treated at the atomic scale), depending on the choice of surface. In this case, surface-area calculations were made using the Connolly surface (Connolly, 1983).

The dependence of surface energy for anatase nanoparticles on particle size, its evolution with simulation time and temperature has been investigated and the results are shown in Figure 6.26. On the basis of standard deviations in the potential energies, the surface energies were accurate to within 0.02 Jm^{-2}. At a temperature of 300 K, it can be seen that for all time steps, the surface energy increases with particle size until a maximum is reached above which no further increase is observed. At temperature of 1000 K, an increase in surface energy with particle size is observed until a maximum, at 4 nm, is reached. Beyond this, at 5 nm, a slight decrease in surface energy of 0.7 % is observed. However, the surface energy is seen to rise again to the maximum as 6 nm is approached. At 1500 K and for most of the time steps, an observed fluctuation is associated with the increase in surface energy for increasing particle size. However, an average of this fluctuation shows that the trend of the surface energy is similar to that at 300 and 1000 K. This fluctuation through time may also be indicative of an annealing process occurring in the particle. The observation shows a high dependence of surface energy on not only particle size but also especially temperature. The observed linear increase of surface energy with particle size for 2500 K (which is not the case for 300, 1000 and 1500 K), could suggest that the nanoparticles have reached their melting point (which is between 2250 and 2280 K (Filyukov et al., 2007, R. Collins et al., 1997, Schneider and Ciacchi, 2010) and have become more liquid-like. This also confirms the observation made, regarding the melting point region in Figure 6.22, which was between 2000 and 2500 K. The effect of time evolution (i.e. simulation time) on surface energy for a given particle size and at different temperatures is also observed in Figure 6.26. Overall (i.e. for all cases of temperature), surface energy is seen to reduce with increase in simulation time step for all particle sizes. For example, in the case of 300 K, surface energy of 4 nm is 1.98 Jm^{-2} at 100 ps and 1.93 Jm^{-2} at 1000 ps. Similarly at 1500 K, surface energy of 4 nm is 1.88 Jm^{-2} at 100 ps and 1.81 Jm^{-2} at 1000 ps.

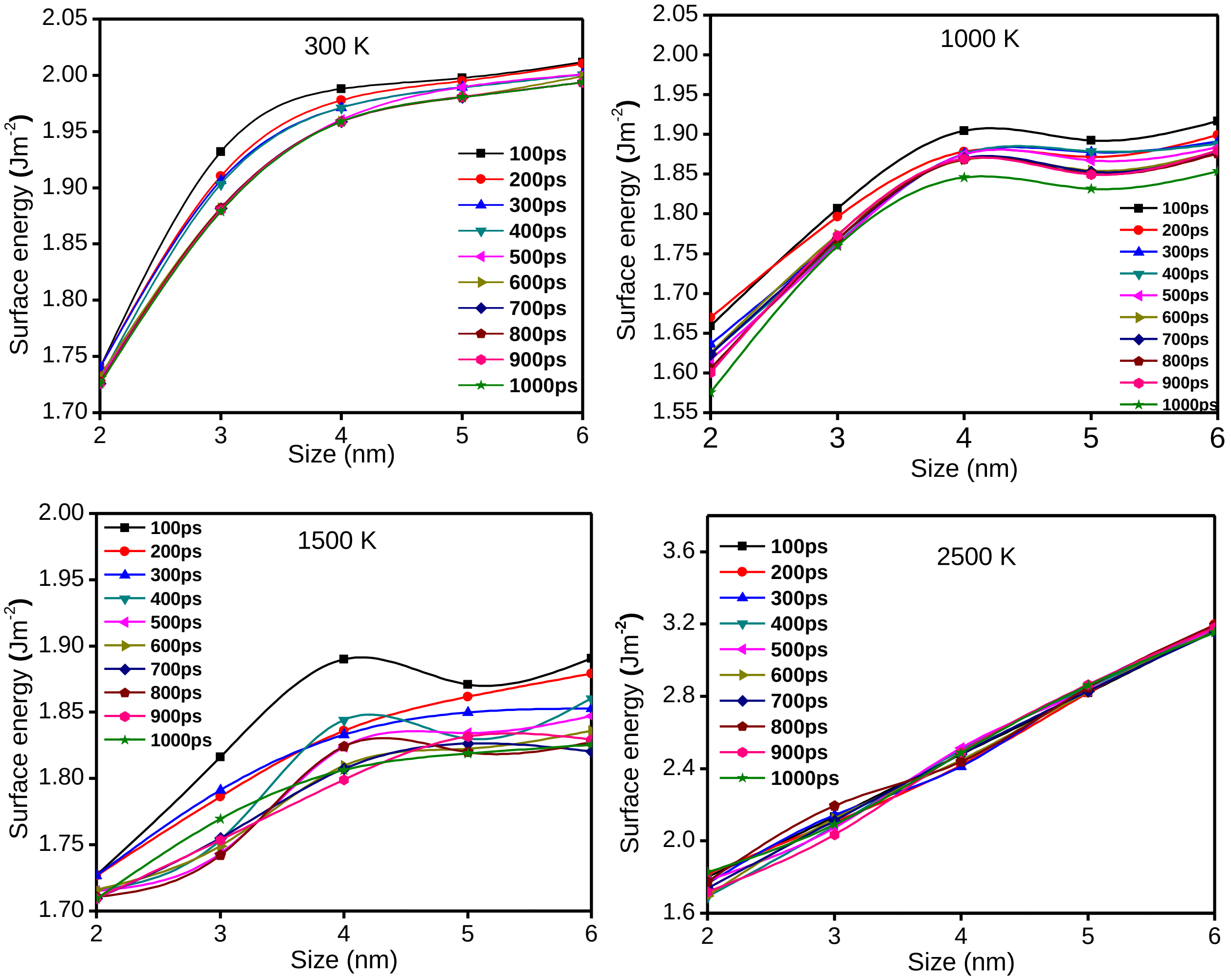

Figure 6.26 Surface energy of anatase nanoparticles as a function of particle size and time step at different temperatures

Surface energy of anatase and rutile for different particle sizes at 300 K has been reported in Figure 6.27. This has been further validated with MD simulation surface-energy data from (Naicker et al., 2005). The plots show that the surface energy of anatase from Naicker et al., 2005 is higher than that calculated in this work by about 5 % which is almost negligible and within reasonable limits. Both surface energy results also show a rise in energy for increasing particle size until a maximum is reached, and then no further increase is observed. For rutile, surface energy from the literature is higher by about 7 – 16 %. The surface energy (for rutile) reported in the literature (Naicker et al., 2005) and that from the present study is seen to rise to a maximum, around the region of 4 and 5 nm. Beyond this, no significant increase in surface energy with particle size is observed. This can be further observed in the difference in structural changes between anatase and rutile nanoparticles at 300 K in Figures 6.28 and 6.29. Additionally, the observed difference between the data set of (Naicker et al., 2005) and the present study could be due to the fact that their surface energy calculations were based on the assumption that the nanoparticles remained spherical after simulations and therefore they used the expression for surface energy in Equation 6.2 which takes into account the surface area of a spherical shaped particle. However, in the present study, the true surface area of the particles after simulation were obtained using the Materials Studio software, and were used in carrying out the surface energy calculations. This method, takes into account any effect of change in shape of the particles, including faceting.

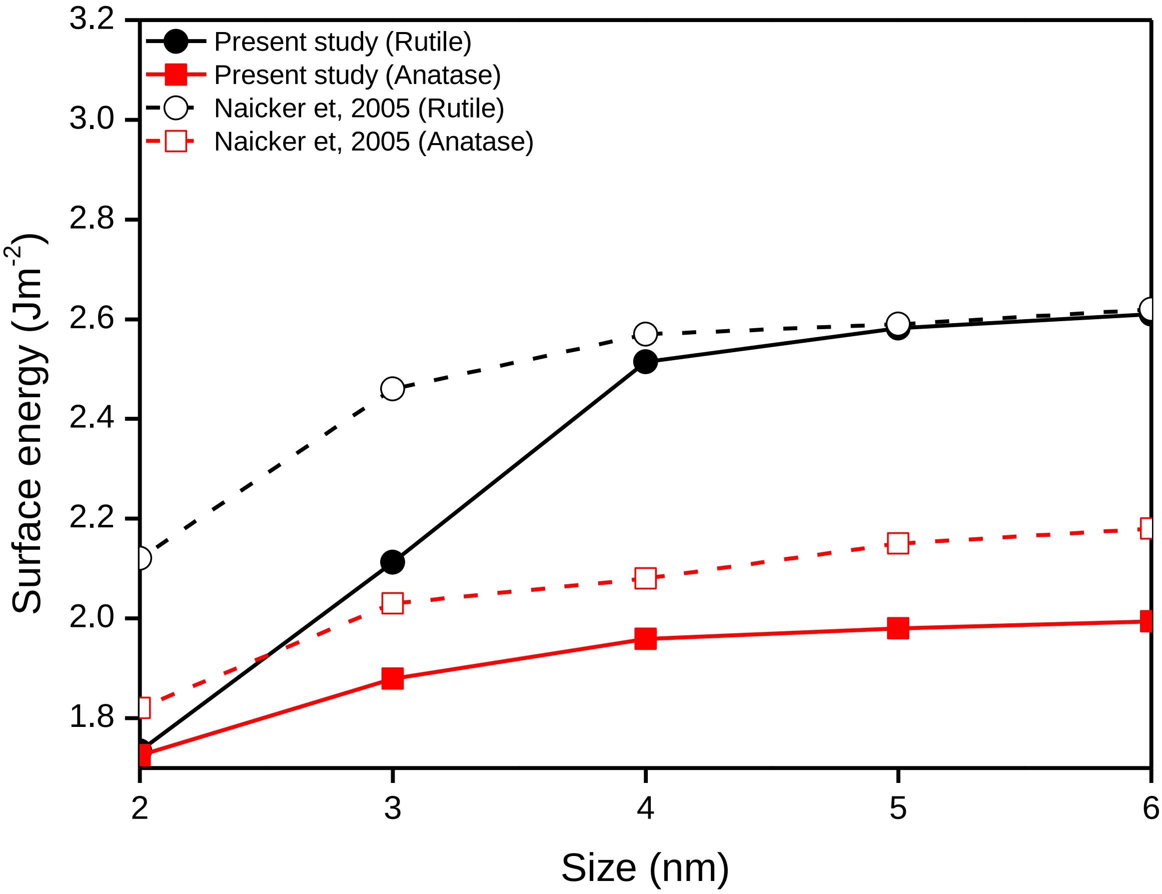

Figure 6.27 Surface energy of anatase and rutile nanoparticles from present study and literature at 300 K

Figures 6.28 and 6.29 show that the structural changes in anatase particles after MD simulation at 300 K is more evident for 2 nm particles, and reduces to a minimum as a particle size of 6 nm is approached. The particles are seen to retain their sphericity as particle size increases. However this is not the case with rutile as the particles become non-spherical and more oval shaped (as a nanorod) as the particle size increases. Notice that 2 and 3 nm rutile nanoparticles in Figure 6.29 are still a little spherical after simulation at 300 K. However, there is a sudden change at 4 to 6 nm as particles become oval shaped. This may be related to the trend in the surface energy plot for rutile in Figure 6.27. A change in the plot is observed from 4 nm as surface energy trend moves away from a simple, monotonic increase. (Reyes-Coronado et al., 2008) have observed anatase and rutile nanoparticles using TEM, following the hydrothermal treatment of these particles at 200^{0}C for a period of 48 hours. They confirmed that upon treatment, the anatase nanoparticles showed a well-faceted crystal habit. In the case of rutile nanoparticles, they observed that after treatment for a period of 5 hours at 200^{0}C, the particles were seen to organise as nanorods, and oriented to form larger aggregates in the form of nanorods. They stated that the nanorods, showed the (0 1 1) and (1 0 0) planes. (Ribeiro et al., 2007) also carried out characterisation of anatase and rutile nanoparticles following hydrothermal treatment at 95^{0}C for a period of 48 hours. Using TEM, They observed that while anatase nanoparticles were bipyramidal in shape, the rutile nanoparticles were rod-like. They also confirm that the (1 1 0) planes are predominant in the rutile morphology, and is as a result of their low energy. Figure 6.30 shows TEM images of the rutile nanorods. These observations are in line with the shape of rutile in Figure 6.29, which takes a rod-like form.

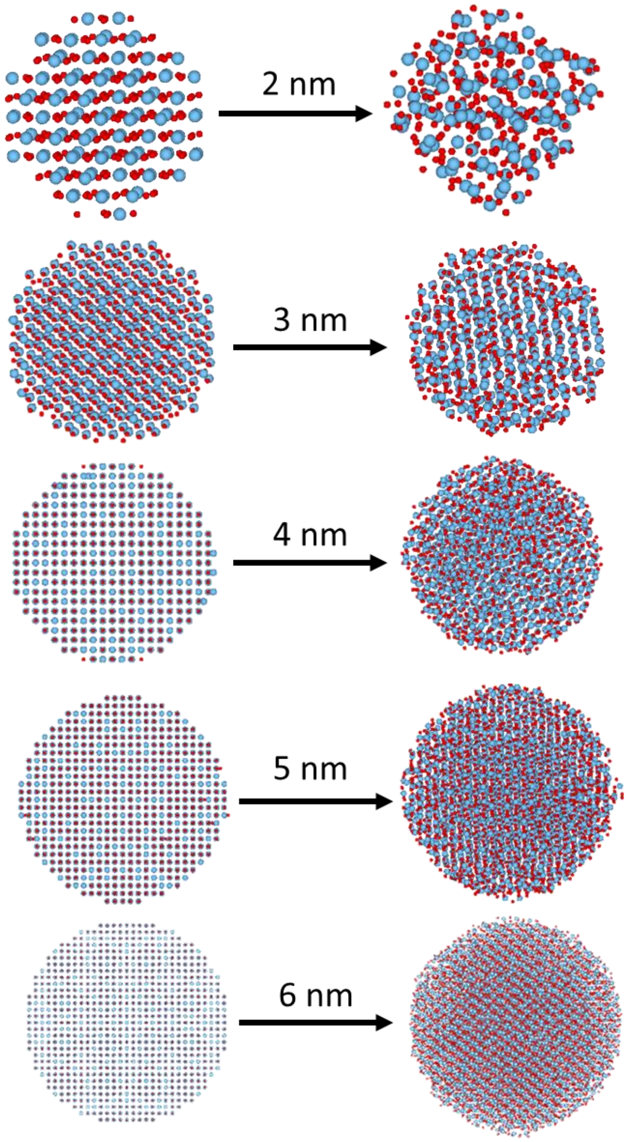

Figure 6.28 Structural change of anatase nanoparticles before and after MD simulation at 300 K

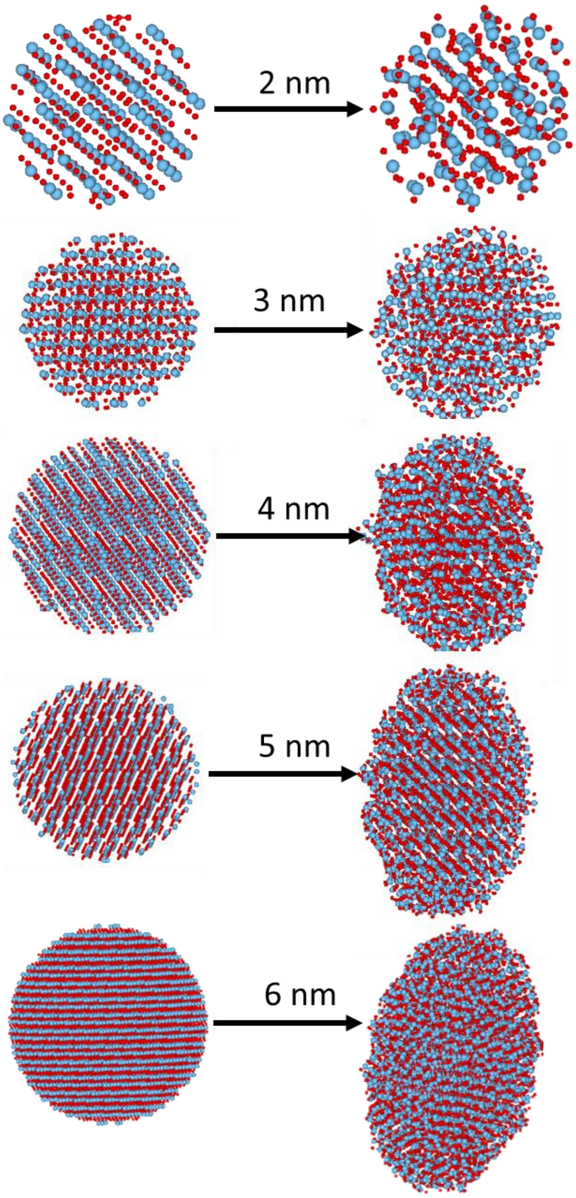

Figure 6.29 Structural change of rutile nanoparticles before and after MD simulation at 300 K

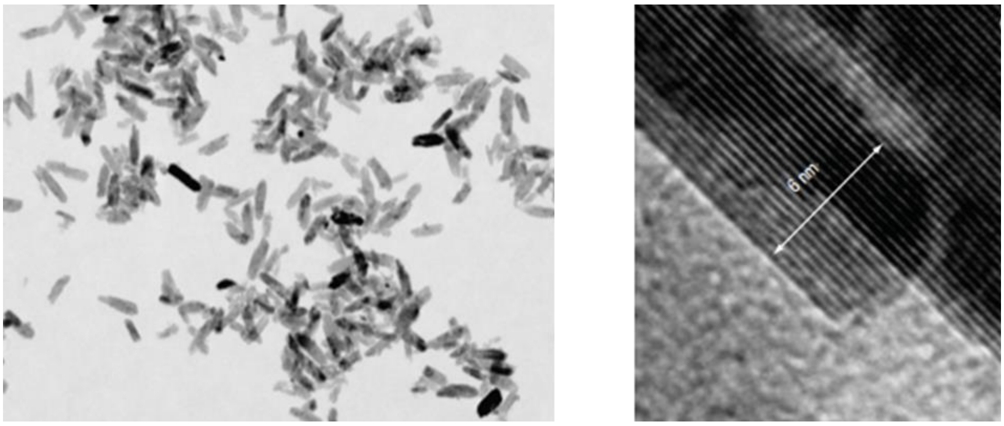

Figure 6.30 TEM images showing rutile TiO_2 nanorods (Ribeiro et al., 2007).

The (1 1 0) rutile surface in this research, has the lowest surface (2.313 Jm^{-2}) and highest attachment (-2.01 eV) energies amongst the other rutile surfaces, as seen in Table 6.2 and 6.4. Upon visual inspection of the simulated rutile nanoparticles, as seen in Figure 6.31, it can be observed that the (0 1 1), (1 1 0) and (1 0 0) surfaces are the most visible due to faceting. The (1 1 0) is the most predominant and therefore stable rutile surface, as it has the lowest surface energy amongst the other rutile surfaces.

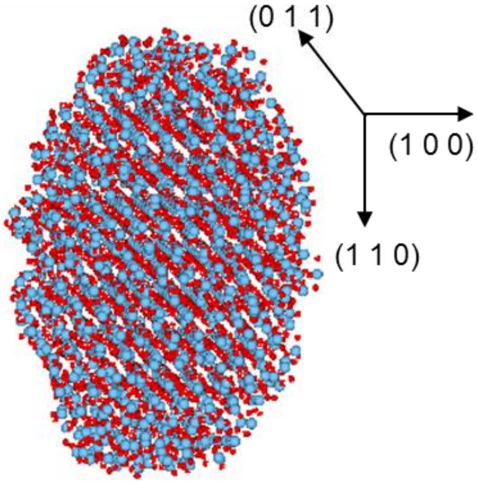

Figure 6.31 Rutile nanorod from simulation, showing the crystal surfaces upon visual inspection.

The change in rutile particle shape in Figure 6.29 at 300 K for 2 – 6 nm can also be compared to the change across temperatures 300 – 2500 K for a typical 2 nm particle size in Figure 6.32. It can be observed that the particle shape after simulation at 300 K for 4 to 6 nm (in Figure 6.29) is most similar to the shape at 2500 K for 2 nm (in Figure 6.32). In both cases, the particles become more oval/rod shaped. However, it can be observed from Figure 6.25 for anatase particles that they become a little less spherical as temperature increases up to 2500 K. This further shows that anatase is more thermodynamically stable at the nanoscale compared to rutile. For example, in the case of 6 nm particles at 300 K, the change in sphericity of the anatase particles is about 6 % while that of rutile is about 10 %.

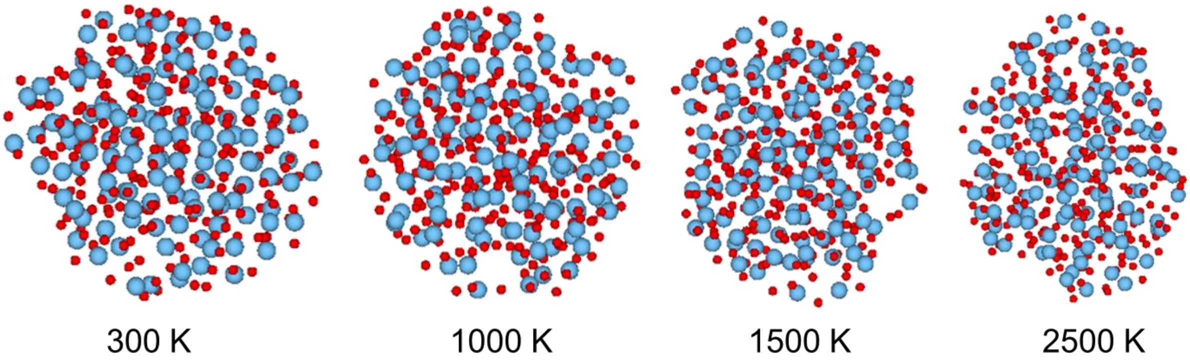

Figure 6.32 Structural change of 2 nm rutile nanoparticle after MD simulation at different temperatures

Surface energies for anatase and rutile at different temperatures and as a function of particle size, have been reported and compared in Table 6.8 and Figure 6.33. Apart from surface energy at 2500 K, surface energies for anatase nanoparticles are seen to approach the bulk surface energy values as the nanoparticle sizes increase. Surface energies for anatase particles at 300, 1000 and 1500 K are seen to increase to a maximum (optimum value) as the particle size increases after which no further significant increase is observed. The case of surface energy increasing with temperature especially for relatively small anatase particle sizes is due to the fact that the nanoparticles start to show signs of faceting with a highly non-spherical shape and become molten as the temperature increases (especially towards 2500 K) as seen in Figure 6.25. This may further mean that the anatase nanoparticles approach the melting point and become liquid-like. Furthermore, Figure 6.33 shows an increase in surface energy of rutile nanoparticles for increasing particle sizes, for temperatures 300 K, 1000 and 1500 K. At 2500 K, surface energy of rutile particles is seen to increase monotonically up to a particle size of 6 nm. This trend can be linked to the thermodynamic instability of the nano-rutile phase previously discussed and the change in particle structure with increasing particle size from spherical to the shape of a nanorod.

Table 6.8 Surface energy (in Jm^{-2}) of rutile and anatase nanoparticles for different temperatures

Diameter (nm)	**300 K**		**1000 K**		**1500 K**		**2500 K**	
	Rutile	**Anatase**	**Rutile**	**Anatase**	**Rutile**	**Anatase**	**Rutile**	**Anatase**
2	1.7340	1.7258	1.6200	1.5751	1.6648	1.7093	1.7560	1.8276
3	2.1124	1.8788	1.7650	1.7598	1.7386	1.7695	2.2718	2.0901
4	2.5145	1.9588	1.9902	1.8460	1.6970	1.8063	2.4267	2.4869
5	2.5824	1.9804	1.8386	1.8317	1.7390	1.8189	2.9578	2.8618
6	2.6115	1.9937	1.8826	1.8537	1.7712	1.8256	3.2360	3.1533

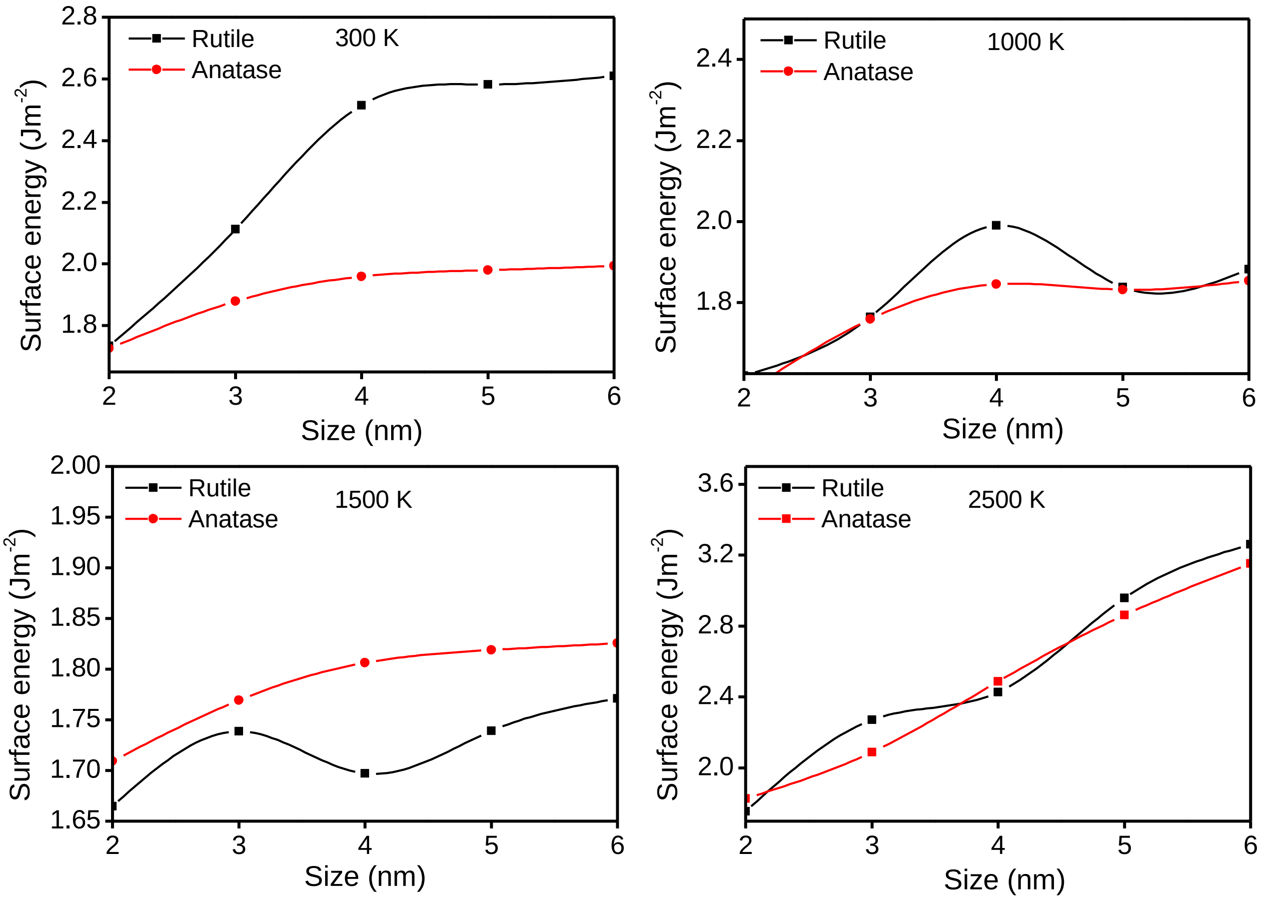

Figure 6.33 Comparison of surface energy for anatase and rutile nanoparticles at different temperatures as a function of particle size

The effect of temperature on surface energy pertaining to the final stage of the simulations for anatase and rutile has also been analysed in Figure 6.34. Remember that the final stage of simulation refers to the end of the simulation or production time (i.e. at 1000 ps) and this is the case for all simulations. Results show that surface energy tends to decrease linearly with increase in temperature until 1500 K after which a sharp and rapid increase occurs for both anatase and rutile nanoparticles. This is mostly observed for particle sizes 3 – 6 nm especially in the case of anatase. In the case of 2 nm anatase, the surface energy decreases linearly as the temperature increases to 1000 K after which an increase in surface energy is observed. For 2 nm rutile, the surface energy decrease at 1500 K and increase afterwards to 2500 K is less significant. This shows that the surface energy contribution to thermal properties such as total energy and melting point of nanoparticles is very significant especially at very small particle sizes (Naicker et al., 2005).

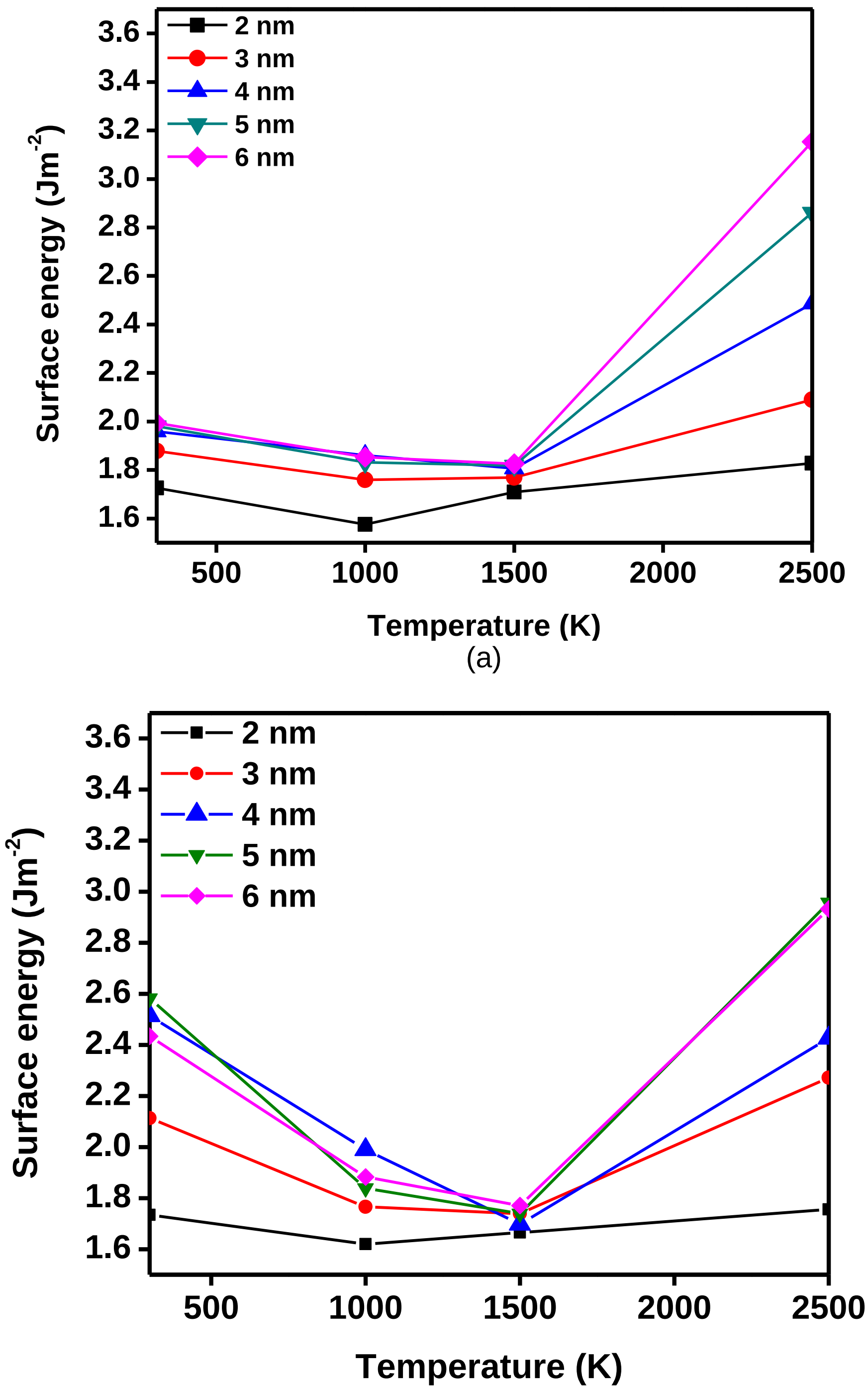

(a)

(b)

Figure 6.34 Surface energy of (a) anatase and (b) rutile nanoparticles at the final stages of simulation time, as a function of temperature

6.4.1.4 Relating the surface energies of TiO_2 crystals and nanoparticles

The variation in the surface energy of the rutile nanoparticles with an increase in particle size can be related to the surface energies of the rutile crystalline surfaces shown in Table 6.2 and 6.3. The center-face distances between the center of the crystal and its individual surfaces, were scaled to be proportional to the surface energies of the surfaces. Hence, crystal surfaces with low surface energies will experience more growth compared to surfaces with high surface energies. It was observed that compared to anatase, rutile showed more change in surface energy between the unrelaxed and relaxed cleaved crystal surfaces. This also confirms the relative instability of rutile as seen in the surface energy plots of rutile nanoparticles presented for all the temperatures in Figure 6.33. Remember (from section 5.3.4) that (Matsui and Akaogi, 1991) confirmed the transferability of their force field across the three titania polymorphs by stating that it reproduced the crystal structures of the polymorphs. Their force field was further tested in this research by fitting their parameters to elastic constants from experiments and literature. The mechanical, thermodynamics, structural, and surface properties of the three polymorphs calculated using the fitted force fields (i.e. those fitted with elastic constants from experiments and literature) were in reasonable agreement with those calculated using the original Matsui-Akaogi force field. Hence the original force field of Matsui-Akaogi was used to carry out simulations in this research.

Also, apart from the 4 nm particles, the surface energy of rutile nanoparticles is seen to be higher than for the corresponding anatase nanoparticles. This is similar to observations of surface energy of rutile and anatase crystal surfaces as the surface energy of the rutile surfaces was seen to be higher than the corresponding anatase surfaces. It can also be noticed that the surface energy values of both nanoparticles are in reasonable agreement with those of the crystal surfaces presented in Table 6.2. For example at 300 K, the mean surface energy of anatase nanoparticles between 2 and 6 nm is 1.90 Jm^{-2} while that for the relaxed crystal surfaces from the present study is 1.76 Jm^{-2}. Similarly, the mean surface energy of rutile nanoparticles between 2 and 6 nm is 2.28 Jm^{-2} while that for the crystal surfaces from the present study is 2.08 Jm^{-2}. Overall, the surface energies of rutile and anatase surfaces in Table 6.2 are within the range of 1.30 and 2.42 Jm^{-2} with the (1 1 0) and (0 0 1) surfaces having the lowest surface energy for the rutile and anatase phases, respectively. These surface energy values compare very well with those for the rutile and anatase nanoparticles. Considering the fact that the crystal surfaces investigated in this research are the low index surfaces (especially for rutile and anatase), this suggests that nanoparticles of both rutile and anatase phases are mostly dominated by low index crystal surfaces. These low index surfaces are known to be the most stable surfaces (Oliver et al., 1997).

6.4.1.5 Structural analysis

The degree of shift of the titanium and oxygen atoms in the nanoparticles on moving in a radial direction from the centre of the particle (or bulk) to the surface was investigated. The atom positions in the initial nanoparticle structure (before simulation) were compared with the positions of the same atoms in the final structure (after simulation) and on this basis, calculations were made to evaluate the degree of shift. The estimation of the shift or change, of the final structure with respect to the initial structure was calculated using the following equation (Hammond et al., 2007);

$$R_{shift} = \sum_{i=1}^{N} \frac{1}{N} \sqrt{(x_i - {x_i}^{opt})^2 + (y_i - {y_i}^{opt})^2 + (z_i - {z_i}^{opt})^2} \tag{6.3}$$

Where R_{shift} is the degree of shift, (x_i, y_i, z_i) are the coordinates of an atom (with respect to symmetry positions within the particle structure) and N is the number of atoms in the system. The coordinates of the atoms in the optimised structure (after simulation) are marked with an 'opt' superscript, while those without any superscript represent the original structure (before simulation). Figure 6.35 shows the surface and bulk of a spherical nanoparticle after simulation using spherical shells to represent the cut-off distances from the centre. It can be observed from Figures 6.36 that the degree of shift of the atoms from their original positions increases as the surface of the nanoparticle is approached and is minimal at the centre (bulk) of the nanoparticle.

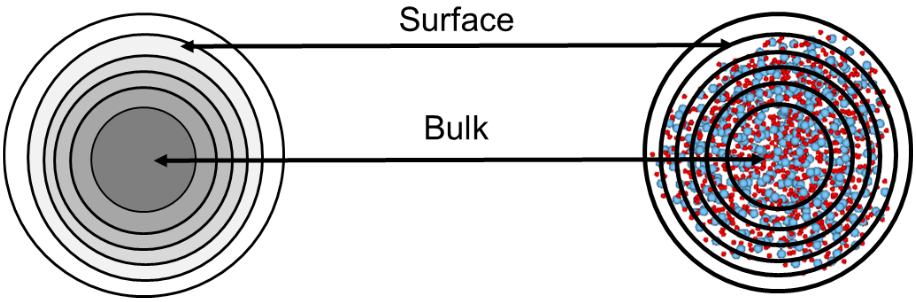

Figure 6.35 Schematic representation of a spherical shaped nanoparticle with different layers representing cut-off distances from the centre. Oxygen and titanium atoms are red and grey colours, respectively.

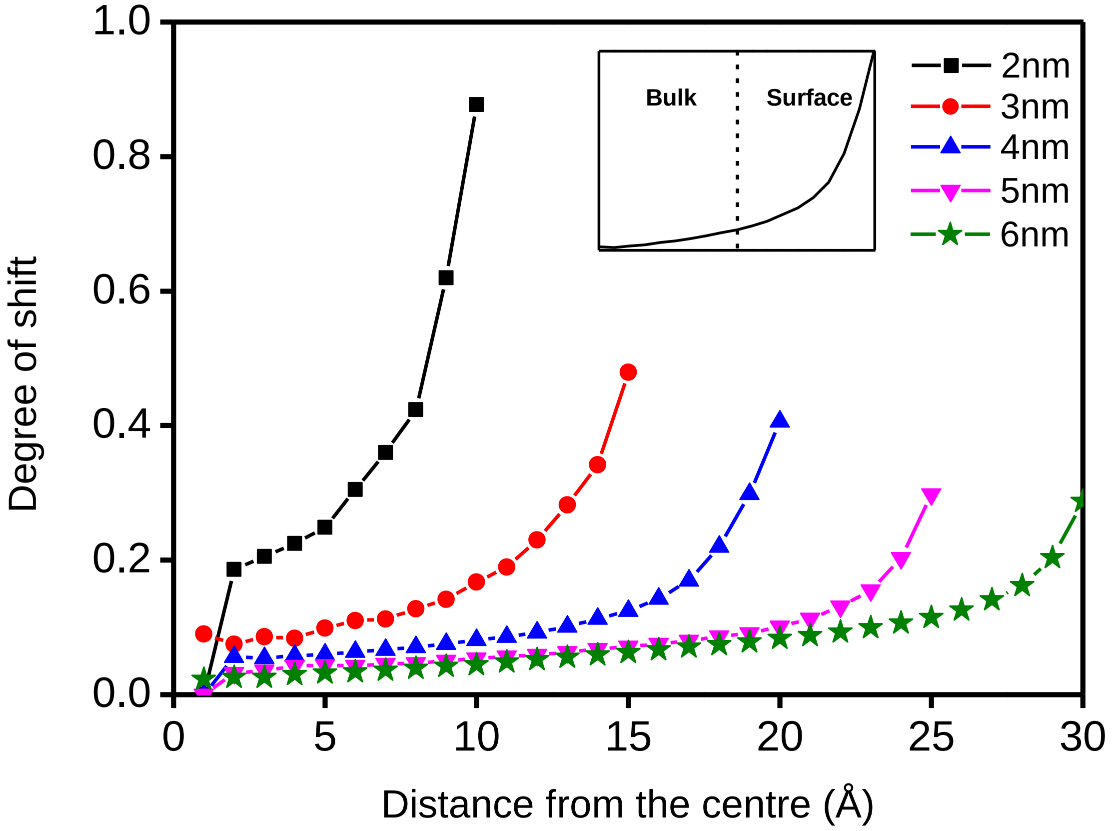

Figure 6.36 Degree of shift or change in structure for different anatase TiO_2 nanoparticle sizes with respect to its optimised structure. Optimisation simulation was conducted at 0 K

In this study, optimisation simulations were conducted at 0 K to enable the particles to relax properly with little influence of temperature scaling. It can be observed from Figure 6.36 that for all cases of nanoparticle sizes, the degree of shift of atom positions increases exponentially from the bulk to the surface of the nanoparticle. The extent of the shifting of atoms is seen to decrease with increasing particle size. A visual inspection of the 2 and 6 nm nanoparticles in Figure 6.37 shows that the shift of atoms from their original positions after optimisation is more significant for 2 nm compared to 6 nm.

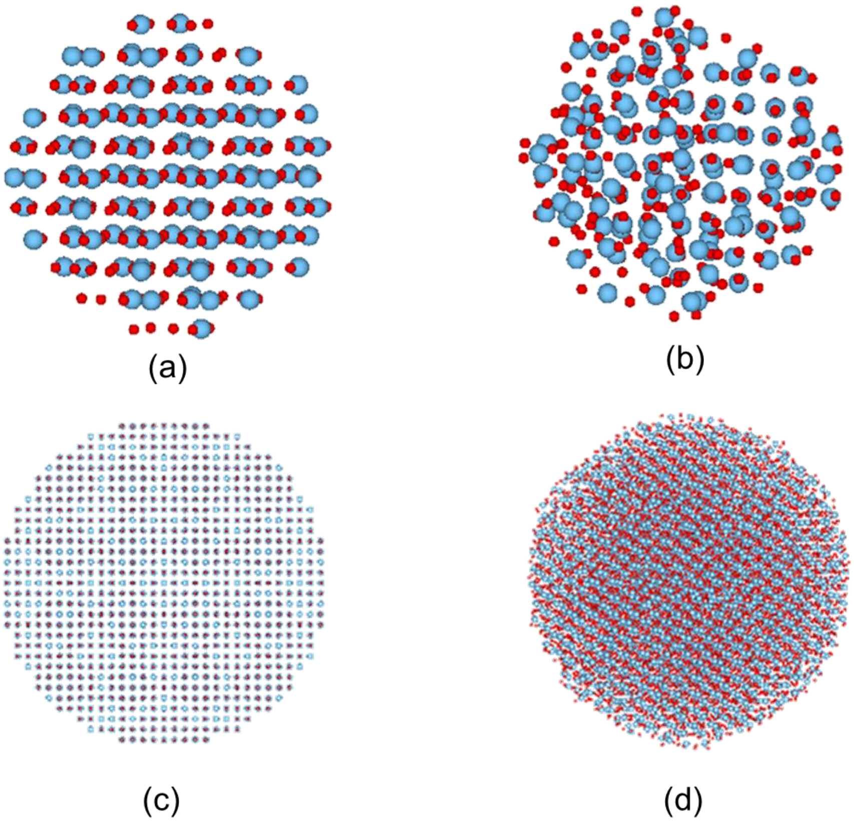
(a) (b)

(c) (d)

Figure 6.37 Degree of shift of atoms of anatase from their original positions. (a) 2 nm particle before optimisation, (b) 2 nm particle after optimisation, (c) 6 nm particle before optimisation, (d) 6 nm particle after optimization. Oxygen and titanium atoms are in red and blue colours, respectively. Optimisation simulation was conducted at 0 K.

In Figure 6.38, the bulk, intermediate and surface for a typical case of 5 nm anatase nanoparticles after optimisation, are shown. It can be seen that there is more atom shift and disorderliness at the surface (c) compared to the bulk or centre (a) of the nanoparticle, where the atoms are seen to be more orderly. This observation is similar to that seen in Figure 6.36, which revealed that there was less degree of shift at the bulk or centre of the nanoparticle than at the surface.

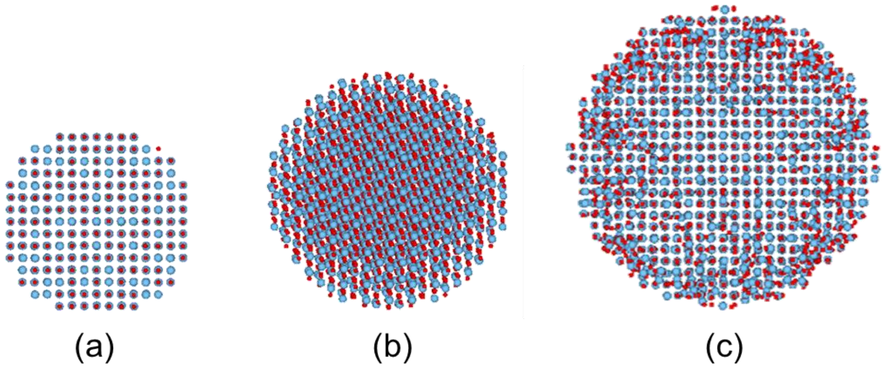
(a) (b) (c)

Figure 6.38 Atom shifts at the (a) bulk or core (b) intermediate and (c) surface, of 5 nm anatase nanoparticle. Oxygen and titanium atoms are in red and blue colours, respectively

Figure 6.39 and 6.40 show the degree of sphericity for anatase and rutile nanoparticles respectively, as a function of temperature and nanoparticle size. The sphericity calculation was carried out based on the following expression (Wadell, 1935);

$$\psi = \frac{\pi^{\frac{1}{3}}(6V)^{\frac{2}{3}}}{A} \tag{6.4}$$

Where V is the true volume of the nanoparticle and A is the true surface area of the nanoparticle. It can be seen that, for a given particle size, the particle becomes less spherical as the temperature increases. This can also be observed in Figure 6.25, where nanoparticles are seen to become less spherical and more faceted as the temperature increases. This occurs for all particles sizes as seen in Figure 6.39 (a). A steep drop in sphericity is observed at 2000 K for the different nanoparticle sizes (apart from 2 nm where an earlier steep drop in sphericity is observed at 1500 K). This could also be linked to the melting point of the nanoparticles which is being approached.

It can also be observed from Figure 6.39 (b) that for temperatures between 300 and 2000 K, the effect of particle size on the degree of sphericity is less significant compared to its effect at 2500 K. For temperatures between 300 and 2000 K, the degree of sphericity is seen to fluctuate about a mean position and only a slight drop in sphericity is observed as particle size increases. In the case of temperature at 2500 K, the degree of sphericity is seen to decrease non-linearly with increased nanoparticle size.

Similarly, in the case of the rutile nanoparticles in Figure 6.40 (a), it can be seen that for a given particle size, the particle becomes less spherical as the temperature increases. A steep drop in sphericity is observed for particles sizes 3 - 6 nm at 2000 K which is similar to observations for anatase nanoparticles. However, the steep drop in sphericity for the 2 nm rutile particle is seen to occur at 500 K which is not in line with observations for the 2 nm anatase particle (which dropped at 1500 K).

In Figure 6.40 (b), the degree of sphericity is seen to decrease for temperatures at 300 – 1000 K, as the particle size increases. For temperatures at 1500 and 2000 K, the degree of sphericity is seen to increase up to 3 nm after which a drop in sphericity occurs as the particle size increases. At 2500 K, the degree of sphericity is seen to decrease up to 3 nm after which a sharp increase in sphericity is observed from 4 nm as the particle size increases. Also, at 2500 K, a slight increase in sphericity is observed between 3 and 4 nm, however this is not as significant as the increase which occurs between 4 and 6 nm.

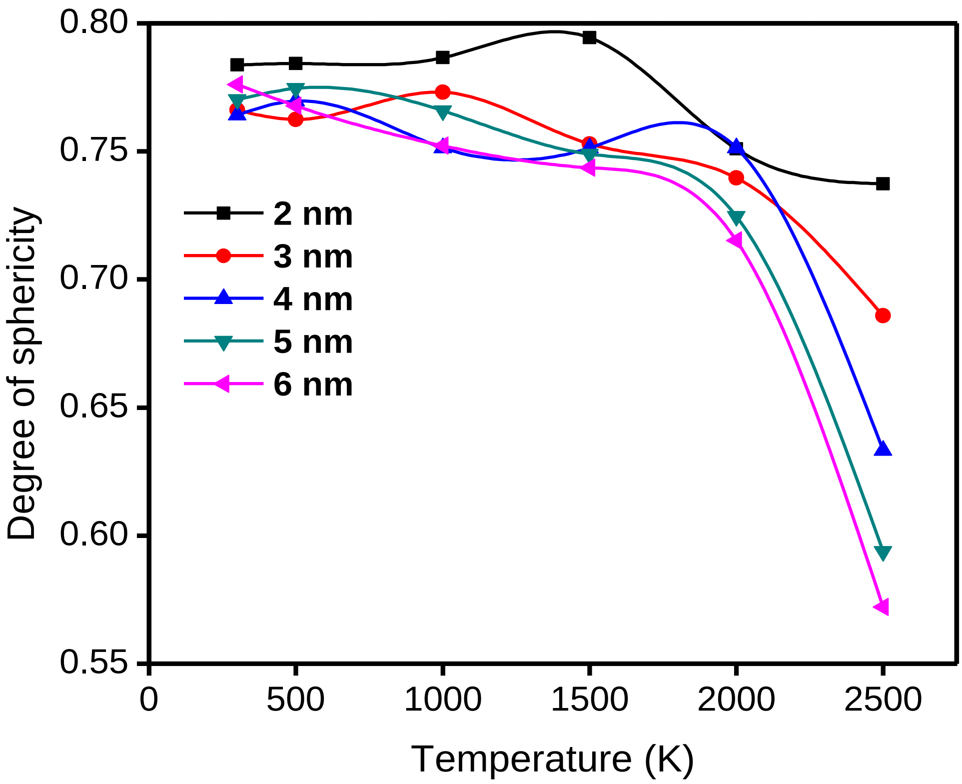

(a)

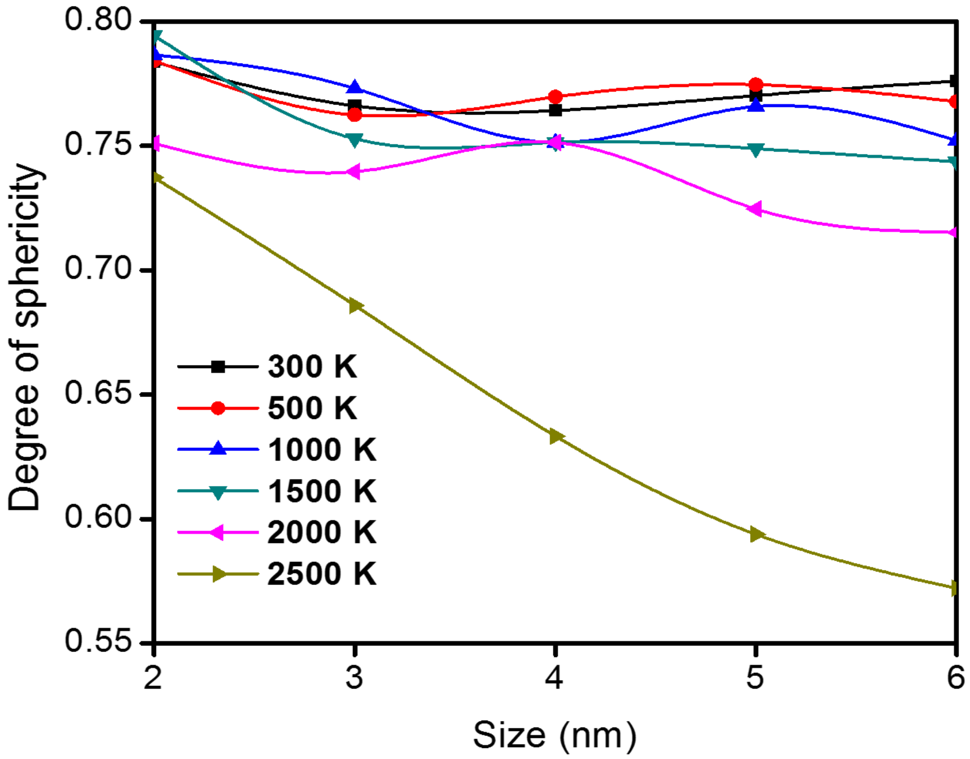

(b)

Figure 6.39 Degree of sphericity of anatase as a function of (a) temperature for different nanoparticle sizes and (b) nanoparticle size for different temperatures

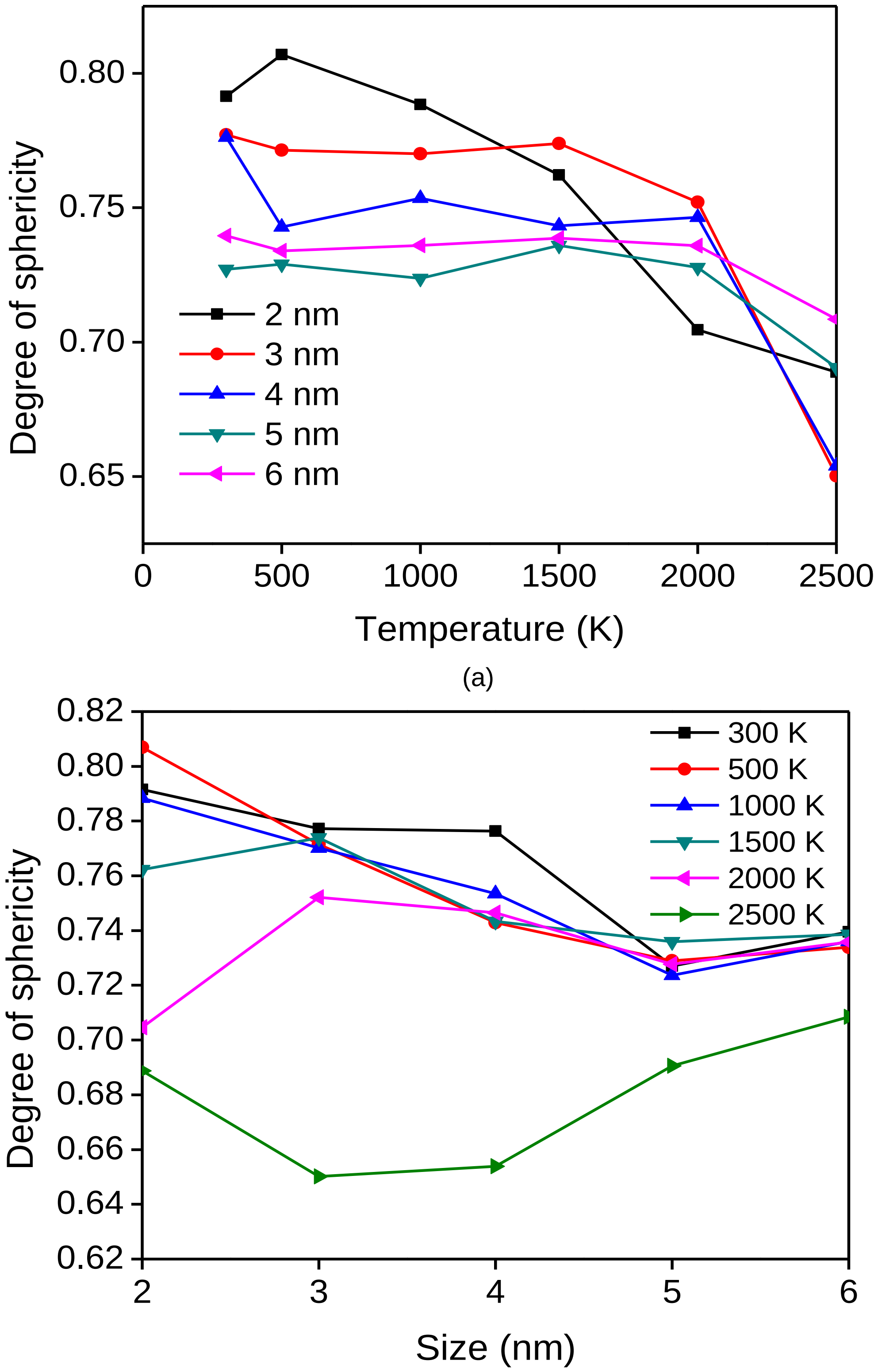

(a)

(b)

Figure 6.40 Degree of sphericity of rutile as a function of (a) temperature for different nanoparticle sizes and (b) nanoparticle size for different temperatures

Furthermore, for anatase and rutile, it is also important to note that the particles become less spherical with increase in simulation time. This can be confirmed in Figure 6.28 and 6.29, as visual inspection shows that the particles are seen to be less spherical at the end of the simulation compared to their shape at the start of simulation. However, a plot of the degree of sphericity as a function of simulation time for 2 nm anatase and rutile nanoparticles, is shown in Figure 6.41. A mean of the lines in the plot, for both anatase and rutile show that the particles were stabilized and attained their equilibrium shape after 300 ps. This further shows that the simulation time was long enough for the shape of the particles to stabilize to their equilibrium shape.

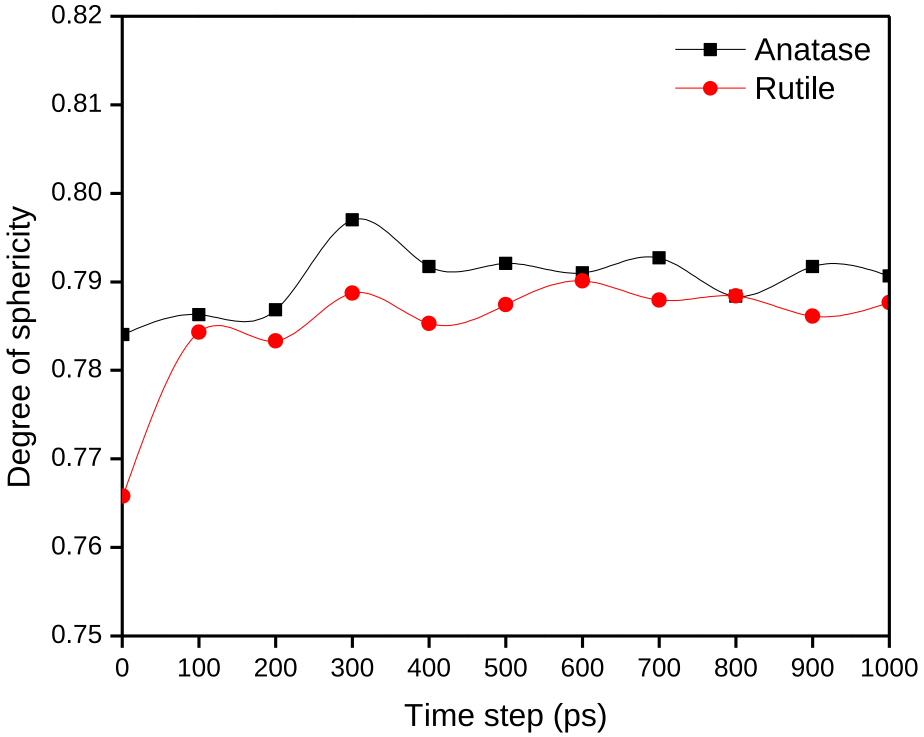

Figure 6.41 Degree of sphericity as a function of simulation time for 2 nm anatase and rutile nanoparticle at 300 K.

6.4.2 Particles in Water

6.4.2.1 Validation of radial distribution function results of SPC/E water with experimental data

The potential parameters for SPC/E water were verified by validating results of the radial distribution function for water (OW – OW, OW – HW, HW - HW pairs) from the present study with experimental results from existing literature (Mark and Nilsson, 2001, Předota et al., 2004) as shown in Figure 6.39. Radial distribution functions are often used when investigating the structure of water and when comparing different theoretical water models with experimental data (Předota et al., 2004, Mark and Nilsson, 2001, Jorgensen and Jenson, 1998). They can be calculated from molecular dynamics data. Pure water simulations were carried out at 300 K which is similar to experimental temperature used in literature.

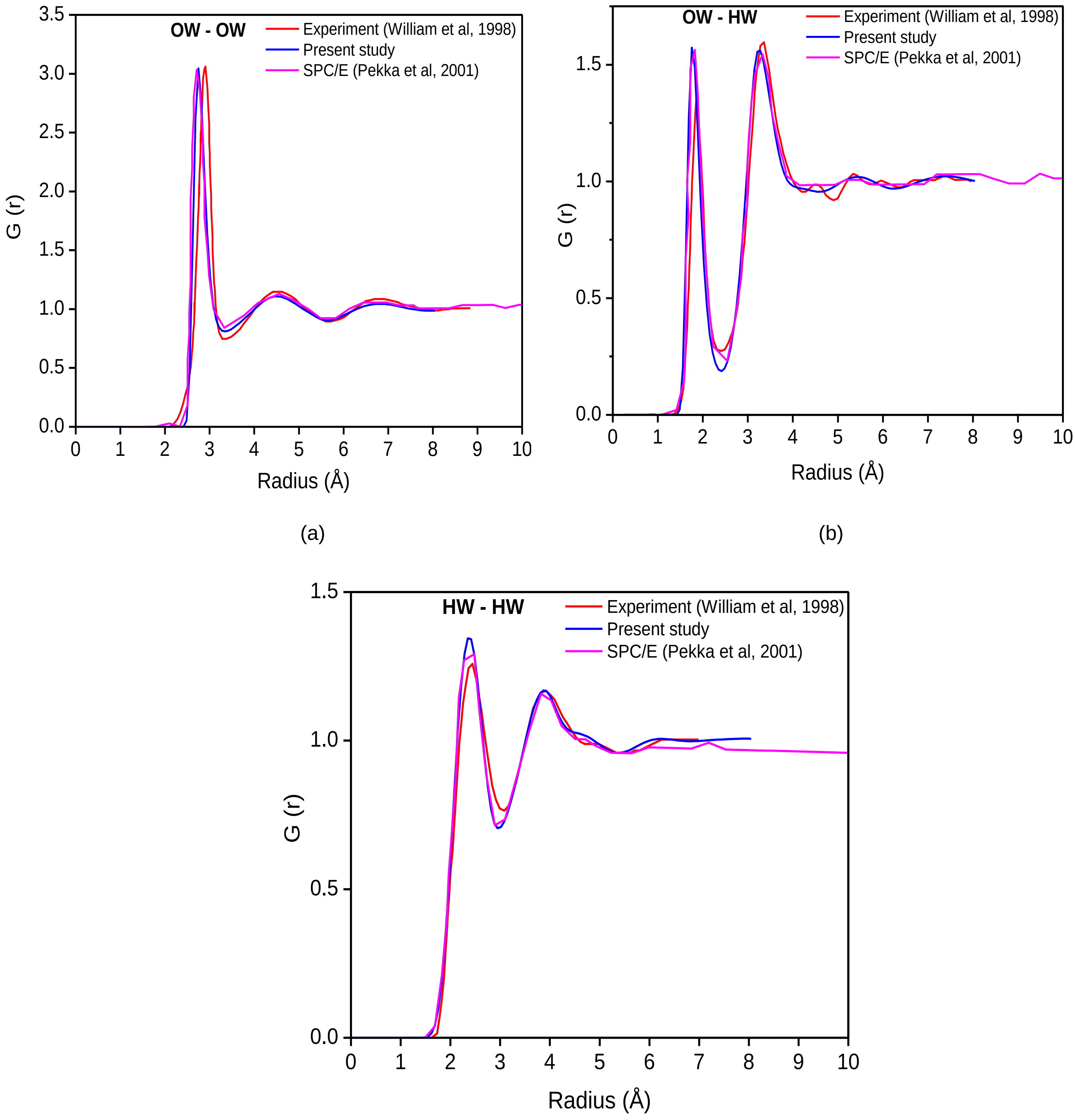

(a)

(b)

(c)

Figure 6.42 Validation of SPC/E water RDF plots (i.e. H and O atom pairs) with literature at 300 K. OW and HW represents water oxygen and hydrogen respectively (Okeke et al., 2012)

From Figure 6.42, it is clear that radial distribution function for the water OW and HW pairs are seen to be in very good agreement with experimental data taken from the literature. It can be observed that the trend of the peaks and minima, for all three pairs are quite similar.

6.4.2.2 Calculation of surface tension of water

Surface tension is an important liquid property that provides information about the behaviour of liquids. It is the property of a liquid that allows it to resist an external force and is caused by cohesion of neighbouring similar molecules within the liquid. In this work, the surface tension of water has been predicted by creating a tetragonal box with a water slab (with two surfaces) in the middle of the box using DL_POLY Java GUI (Figure 6.43). A reported experimental surface tension value from literature is given as 0.0725 J/m^2 (Pallas and Pethica, 1983).

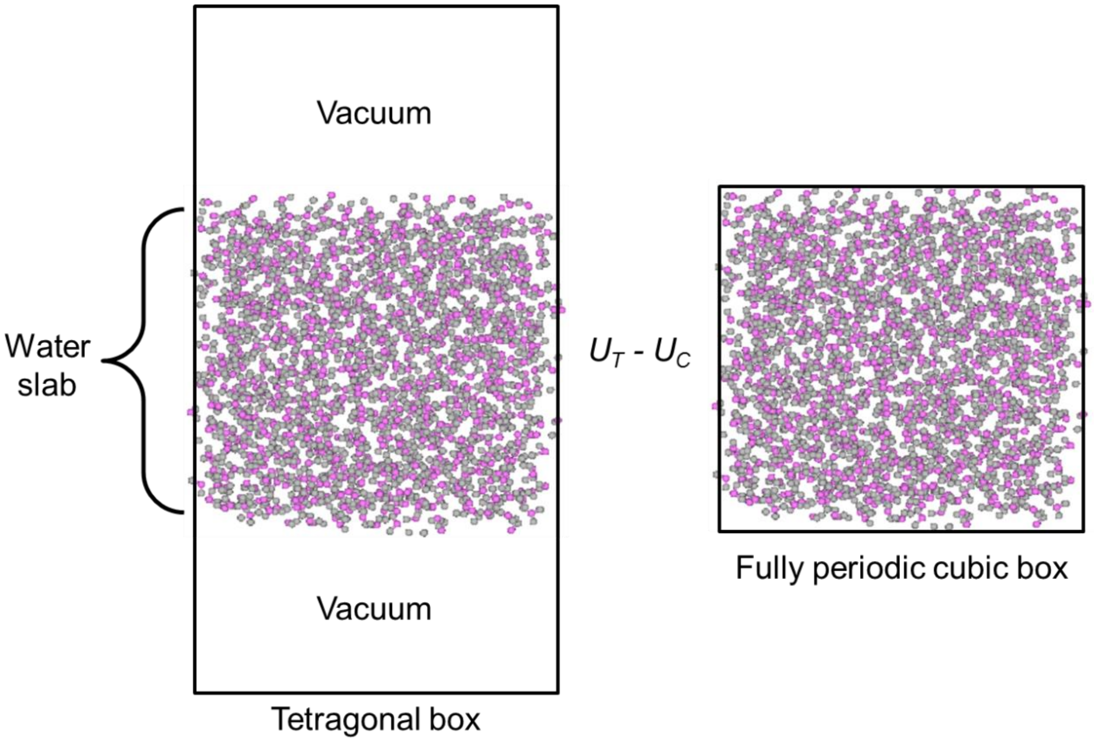

Figure 6.43 Comparison of energies of water slab in the tetragonal box (U_T) to the energies of water molecules in fully period cubic box (U_C) (HW, grey and OW, pink). Simulation was carried out at 300 K (Okeke et al., 2012)

Surface tension was calculated by comparing the energies of the water slab in the tetragonal box to the energies of the fully periodic cubic box of water molecules in the absence of any interface. Both boxes contained the same number of water molecules. Calculations were made based on the following expression;

$$\gamma = \frac{U_T - U_C}{A} \tag{6.5}$$

Where γ is surface tension, U_T and U_C are the energies of the tetragonal box and cubic boxes, and A is the surface area of the water slab which is similar to that in the periodic cubic box. The calculated surface tension from molecular dynamics data was 0.067 J/m^2 (Okeke et al., 2012) which is quite close to the reported surface tension from experiments, in literature (Pallas and Pethica, 1983).

6.4.2.3 Radial distribution function of particle in vacuum and water environments

In this study, simulations of the particles in water were carried out at the same simulation time (i.e. 1000 ps) as simulations of the particles in vacuum. It was observed that there was not much change in the structure of the radial distribution function plots at 300 K with increasing simulation time. Therefore, this shows that the particles were fully equilibrated. Typical plots of radial distribution function for 2 and 3 nm anatase particles in vacuum and water environments are shown in Figure 6.44 for Ti – Ti, Ti – O and O – O pairs at 300 K. It can be observed that the shapes and peaks of the curves for both particle sizes in vacuum are more ordered than in water. The high degree of orderliness is more evident in 3 nm particles, where sharper peaks and a higher coordination are observed for all three atom pairings. Also the magnitude of the peaks is much greater in vacuum by almost an order of magnitude for both particle sizes. This significant reduction in the magnitude of the peaks in water is associated with the interaction of the water and TiO_2 atoms. The structure of water around the particles, including the diffusion of water molecules into the particles, will affect the surface and structural properties of the particles. Radial distribution function plots of Ti and O atom pairs with water HW and OW are shown for both 2 and 3 nm anatase nanoparticles in Figure 6.45.

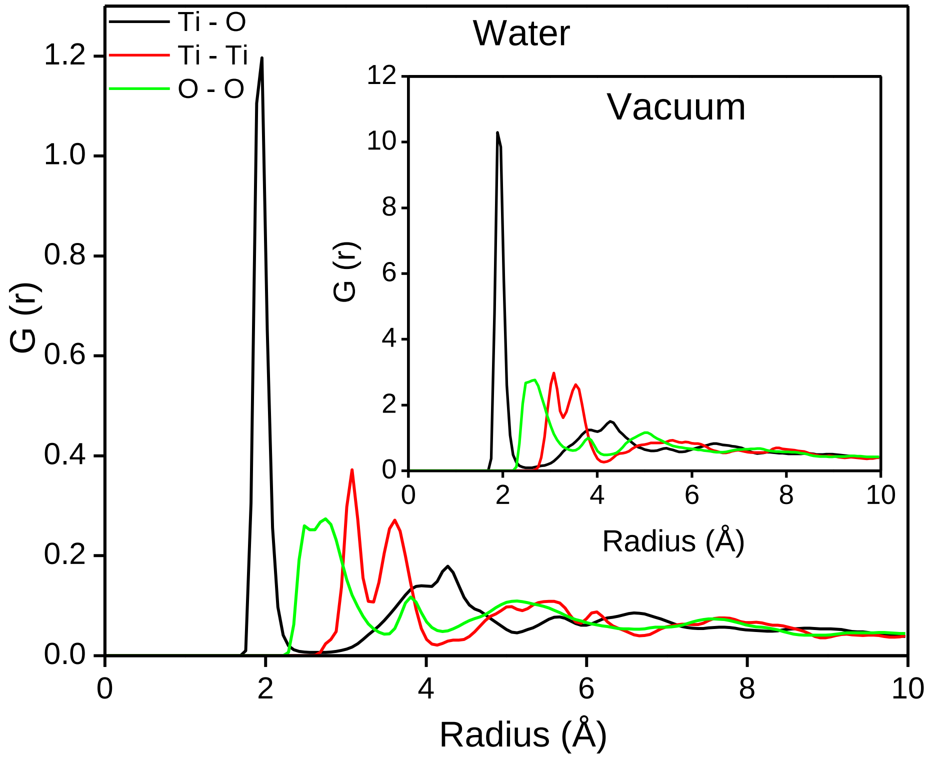

(a)

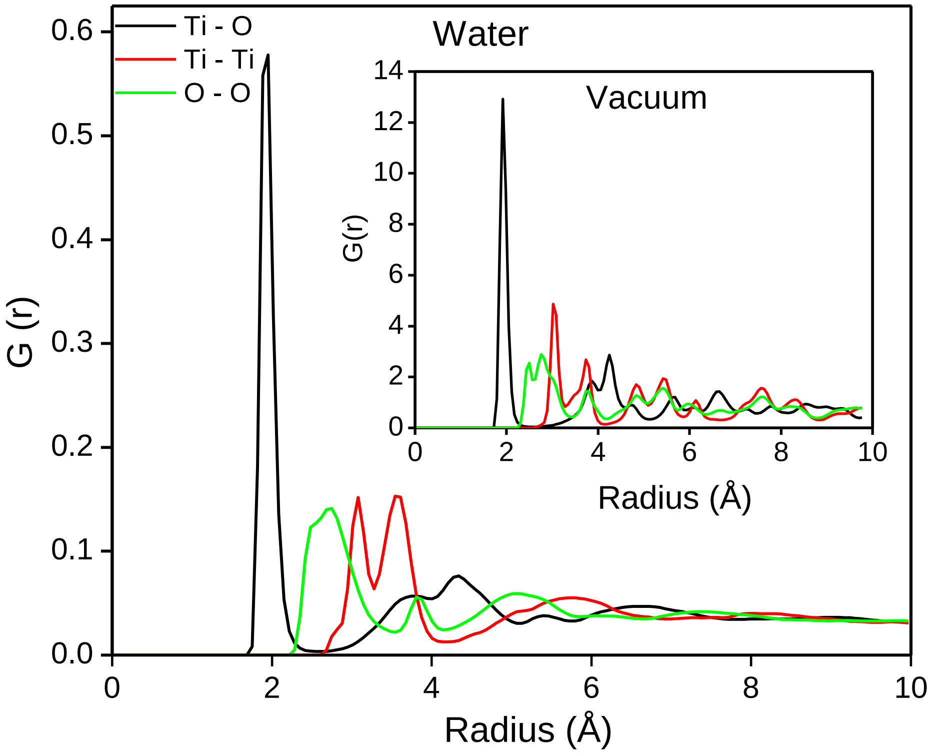

(b)

Figure 6.44 Radial distribution function for Ti – O, Ti – Ti and O – O pairs of the particle in water and vacuum at 300 K for anatase (a) 2nm and (b) 3nm nanoparticles (Okeke et al., 2012).

Figure 6.45 shows the structuring effect of water around anatase. It can be observed that the Ti atoms in the outer shell of the particle are leading to structuring in the water where the O atoms in the first shell around the particle are very strongly coordinated, and the water oxygen (OW) atoms in the second shell around the particle are also strongly coordinated. Also, the upward sloping in the RDF in Figure 6.45, is as a result of the number of Ti atoms that are within a given distance of a water molecule which increases with the Ti – OW distance, and is an effect of the geometry of the system. This leads to increased interaction between the Ti and O atoms, and water molecules as the core of the particle is approached.

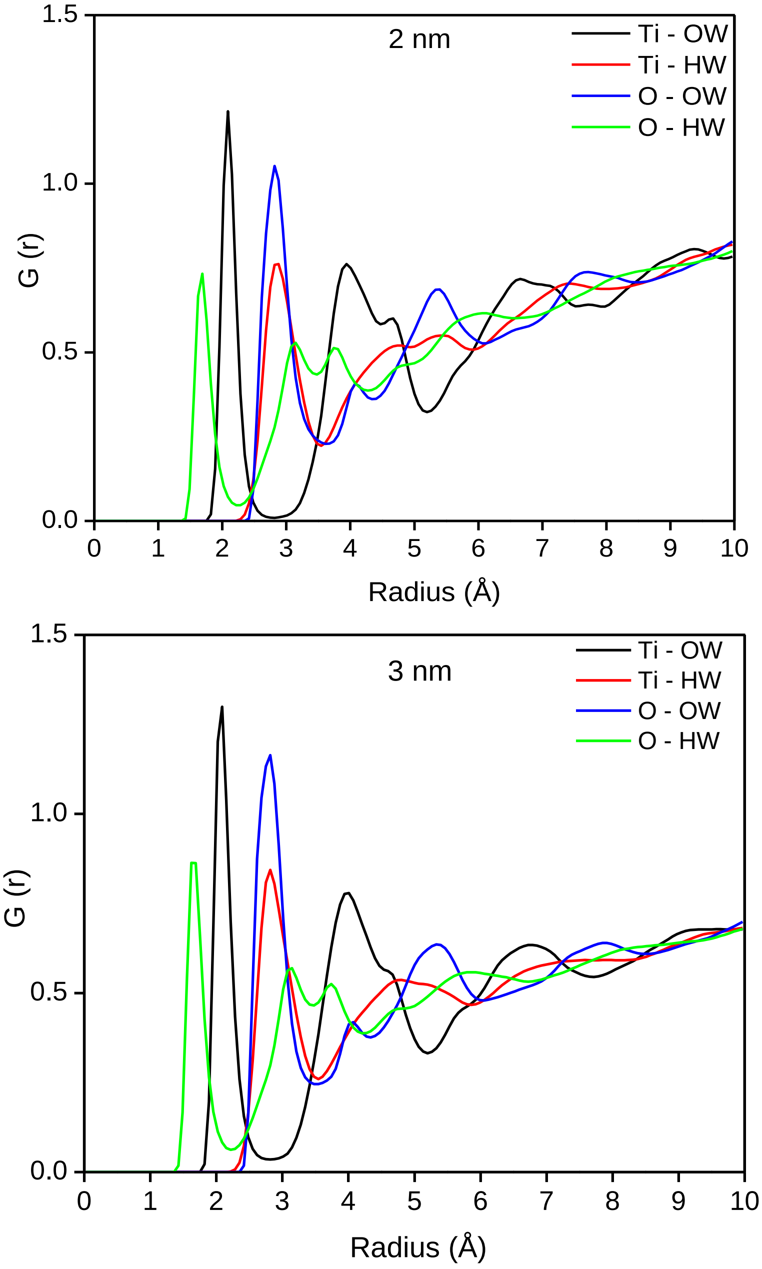

Figure 6.45 Radial distribution function for anatase Ti – OW, Ti – HW, O - OW and O – HW pairs at 300 K (Okeke et al., 2012).

6.4.2.4 Calculation of surface energy of the particles in water

The surface energy of anatase nanoparticles in water was calculated for different particle sizes ranging from 2 – 6 nm, using the following expression;

$$U_{surface} = \frac{U_{TiO_2+H_2O} - \left(nU_{bulk} + U_{bulk\,H_2O}\right)}{A} \tag{6.6}$$

Where $U_{TiO_2+H_2O}$ is the total energy of the nanoparticle and water together, *n* is the number of TiO_2 molecules, $U_{bulk\,H_2O}$ is the energy of pure bulk water, and *A* is the surface area of the nanoparticle. Figure 6.46 describes the simulation set up, for the purpose of calculating surface energy of the particles in water.

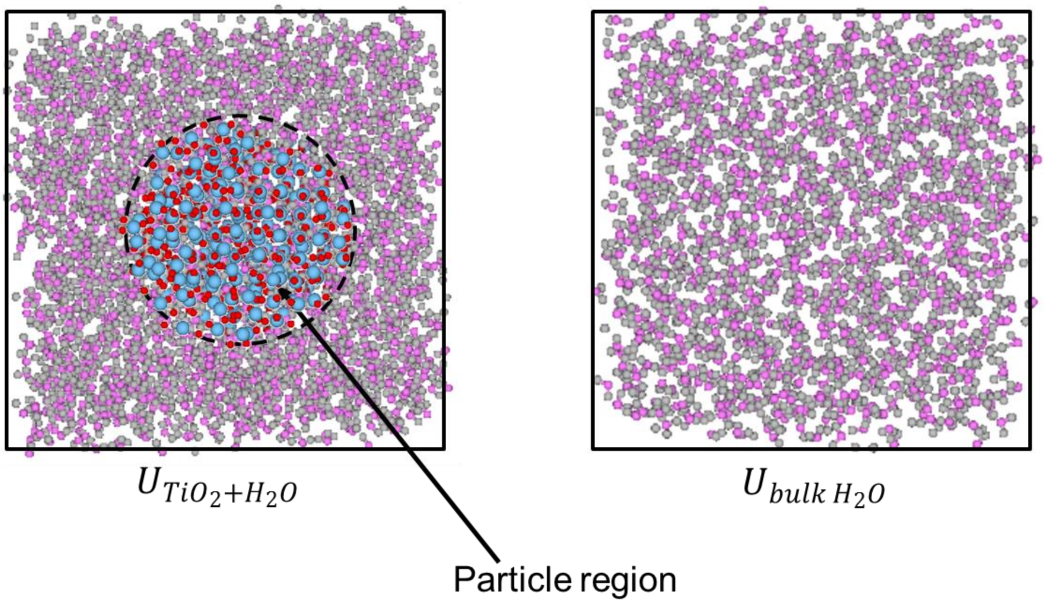

Figure 6.46 Simulation environments with TiO_2 and water in one box, and bulk water alone in the other.

Results of surface energy for anatase nanoparticles in water and vacuum are shown in Figure 6.47. It can be seen that surface energy of the particles in both environments increases with an increase in particle size until a maximum (at about 4 nm) is reached above which no further increase is observed. Surface energy of the particles in water is lower than that of the particles in vacuum by about 50%. Surface energy of the particles in vacuum is seen to be higher than that of the particles in water by about 100% for the smaller particles (i.e. 2 and 3nm) and about 60% for the larger particles (i.e. 4 to 6 nm) (Okeke et al., 2012).

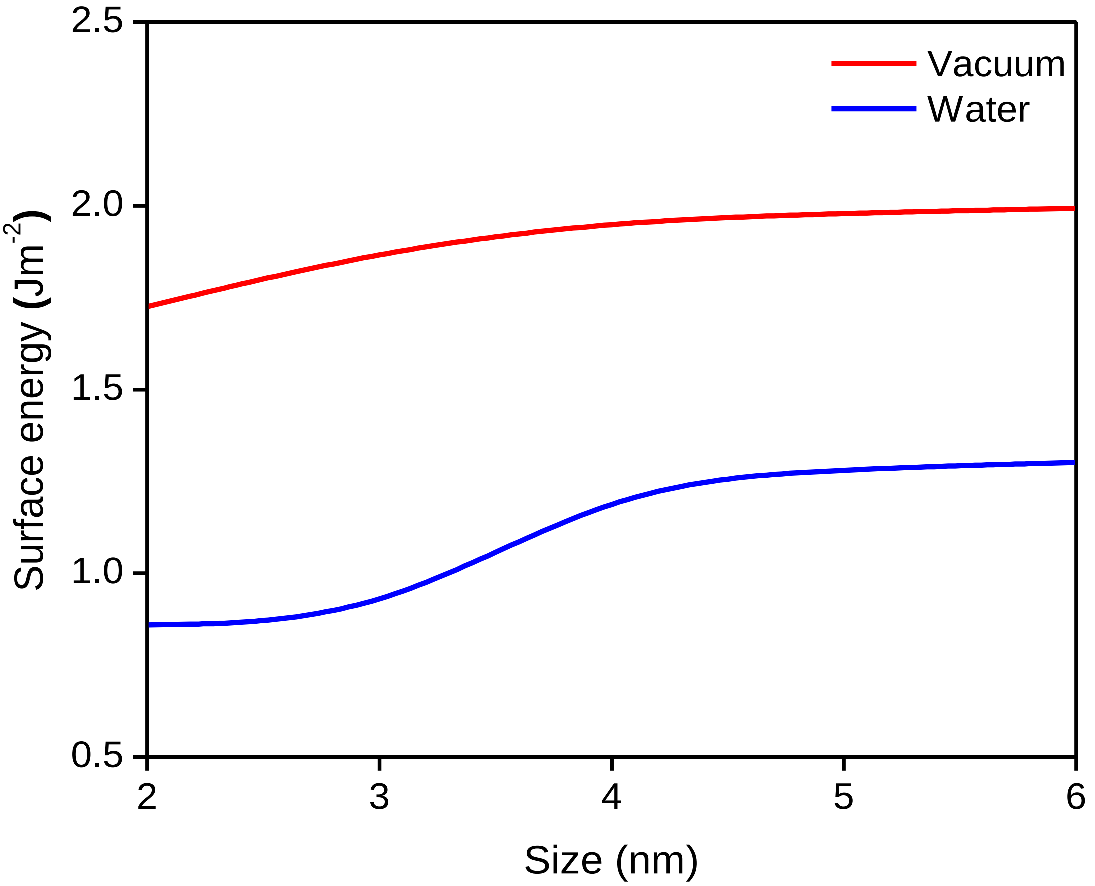

Figure 6.47 Surface energy of anatase TiO_2 nanoparticles in water and vacuum environments at 300 K (Okeke et al., 2012)

The surface areas of the anatase nanoparticles in vacuum and water environments, are presented in Table 6.9. It can be observed that the surface areas of the particles in water is higher than that in vacuum by an average of 2.9 %. This increase in surface area is as a result of the presence of water molecules which interact with the TiO_2 atoms.

Table 6.9 Surface area (in Å^2) of anatase nanoparticles in vacuum and water environments.

Particle size (nm)	Vacuum	Water
2	1541.89	1586.71
3	3646.14	3842.46
4	6617.46	6820.28
5	10286.43	10554.59
6	14697.11	14865.63

6.5 Conclusion

The energy calculations for the bulk crystalline structures showed that the extent of surface relaxation of the cleaved surfaces in most cases corresponds with the degree of change between the unrelaxed and relaxed surface and attachment energies. Anatase cleaved crystal surfaces showed the least change between the unrelaxed and relaxed surface and attachment energies. Similarly, when compared to rutile nanoparticles, anatase nanoparticles showed the least variation of surface energy with increase in particle size. This confirms the thermodynamic stability of the anatase especially in the nanocrystalline form as suggested in the literature. Further observation showed that the surface energies of the rutile and anatase nanoparticles are in reasonable agreement with those of the cleaved crystal surfaces. At 300 K, the average surface energy of anatase nanoparticles between 2 and 6 nm is observed to be 1.90 Jm^{-2} while the average relaxed surface energy of the crystal surfaces from the present study is 1.76 Jm^{-2}. Similarly, the average surface energy of rutile nanoparticles between 2 and 6 nm is 2.28 Jm^{-2} while the average relaxed surface energy of the crystal surfaces from the present study is 2.08 Jm^{-2}. Since the cleaved crystal surfaces investigated in this research are the low index surfaces, the relatively similar surface energies of the crystalline and nanoparticle structures of TiO_2 shows that both rutile and anatase nanoparticles are dominated by mostly the low index surfaces which are known for their stability.

Furthermore, investigations carried out on anatase and rutile nanoparticles showed a relationship between thermodynamic and structural properties as seen in the behaviour of parameters such as total energy, surface energy, radial distribution function and sphericity of the nanoparticles also as a function of temperature. Results show a dependence of surface energy on particle size and temperature. The surface energy of anatase in water is seen to be lower than that in vacuum by about 50 %. In both environments, surface energy is seen to increase to a maximum (optimal value) of about 4 nm, after which no further significant increase is observed. The observed difference in the surface energy of anatase and rutile is attributed to the fact that anatase is more thermodynamically stable as a nanocrystalline phase compared to rutile. Also, TiO_2 nanoparticles at temperatures between 300 and 3000 K (as shown in the radial distribution function plots) reveal that the high orderliness and coordination of titanium decreases to a point of undercoordination as the temperature increases. Plots of radial distribution function for particles in vacuum show a much higher crystallinity and coordination, with peaks of about 95% higher than that of the particles in water. Further investigation into radial distribution function plots of TiO_2 – water atom pairs show more interactions between the atoms of water and the particles at the surface than at the inner core of the particle. The estimated surface tension of water is seen to agree well with that of experiments.

Further investigations are to be carried out in the subsequent chapter, to study the interparticle forces of interacting particles relative to their separation distances apart. This will give more insight into the aggregation process of particles in vacuum and water environments with the overall aim of linking these to the thermal enhancement of nanofluids.

Chapter 7

Prediction of Particle Interaction Forces using Molecular Modelling

7 Prediction of Particle Interactions Forces using Molecular Modelling

7.1 Introduction

This chapter presents information and results on the interaction forces in relation to separation distance for different particle sizes at 300 K. Information about the interaction forces is vital in this research as it is these forces that instigate particle aggregation and also determine the mode of aggregation. They also give information about the strength and structure of the aggregate formed (i.e. loosely or densely packed aggregates). Molecular dynamics simulations have been used to predict these forces, using an approach similar to that of Atomic Force Microscopy (AFM). The observed interaction forces shown in the force-displacement curves presented here, are related to effective thermal conductivity of nanofluids.

7.2 The AFM Concept

The interaction between similar or dissimilar particles is a very important phenomenon as it influences unit operations such as fluidization (Salameh et al., 2012, Larson et al., 1993), coating (Jono et al., 2000), and agglomeration. For small particles (< 10 nm), the effects of molecular structure of the particles (in both vacuum and liquid environments) or the distribution of terminal groups on the surface of the particles (especially in liquid environments), may influence these interactions (Salameh et al., 2012, Ramirez-Garcia et al., 2011). Interparticle/atomic forces between micro and nanoparticles are usually obtained using experimental force spectroscopy measurements, for example, using an Atomic Force Microscope (AFM) (Binnig et al., 1986).

The concept of AFM is simply measuring the force or potential energy between a small tip and a sample (e.g. particle) (Figure 7.1) (Ong and Sokolov, 2007, Albers et al., 2009, Boer-Duchemin et al., 2010, Lee et al., 2009, Giessibl, 2003). To achieve this, a tiny probe called a cantilever which provides a force sensor and force actuator is used (Seo and Jhe, 2008). When the cantilever is moved close to the sample, its topographic height and the interaction force between the tip and the substrate can be measured. The tip experiences an attractive force which later becomes repulsive at a certain point (i.e. switching point), when the tip is moved close to the sample. The force in AFM is estimated by measuring the deflection of the cantilever knowing its stiffness. This basic principle can be related to Hooke's law (Salameh et al., 2012);

$$F = -kz \tag{7.1}$$

Where F is the force, k is the stiffness constant of the cantilever and z is the distance of the probe from the sample.

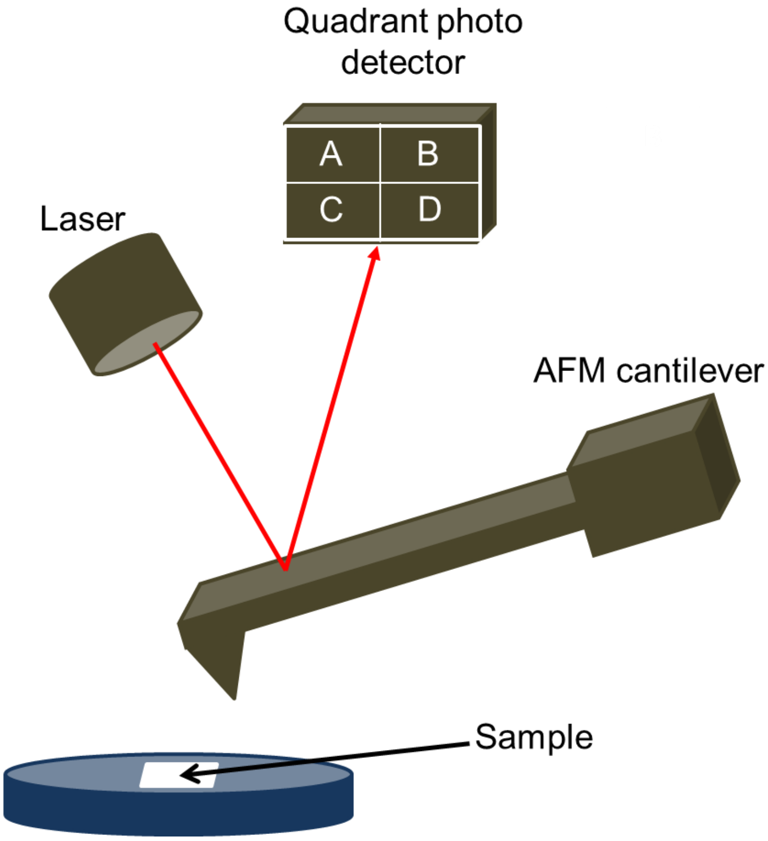

Figure 7.1 A typical AFM set up using an optical deflection technique (Leung et al., 2012).

Figure 7.2 shows a force-displacement curve showing the non-contact, attractive and repulsive regions. The curve consists of a region in which a long-range attractive force (i.e. van der Waals force) is experienced and a region at smaller separation distances in which a short-range repulsive force (i.e. Lennard-Jones, Morse force etc) is experienced. Details of these attractive and repulsive forces are discussed in detail in section 4.7.4 of Chapter 4.

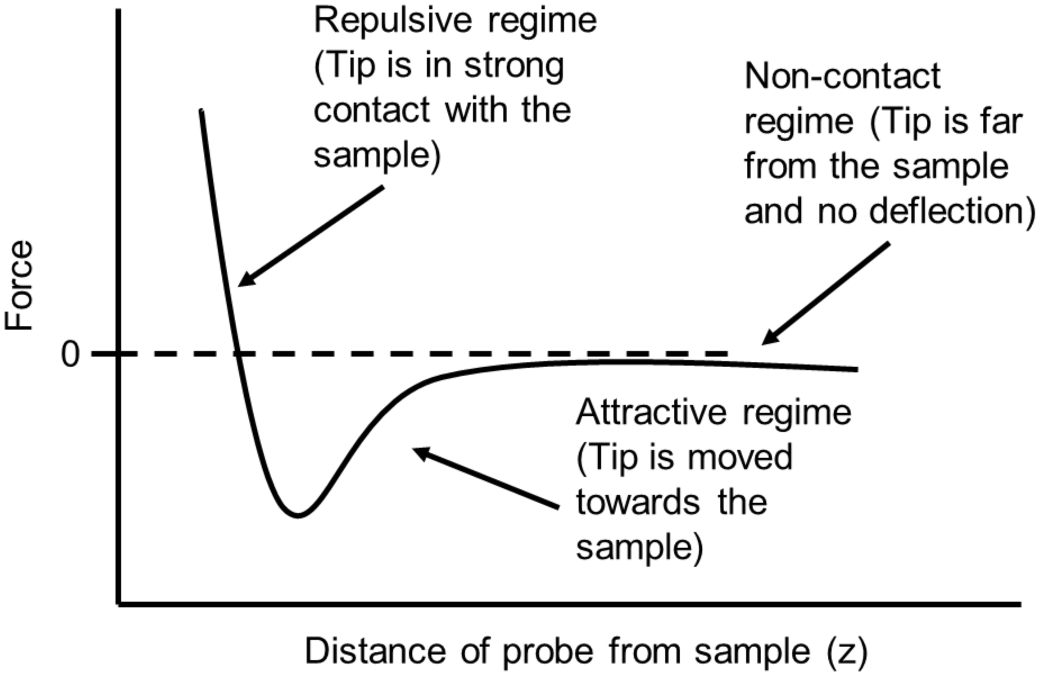

Figure 7.2 A typical force-displacement curve showing the non-contact, attractive and repulsive regimes (Giessibl, 2003).

7.3 Molecular Dynamics Simulation Concept

Force-displacement curves for separation distances between two TiO_2 nanoparticles have been obtained using a molecular dynamics simulation approach, within the DL_POLY package. This has provided the opportunity of measuring interparticle interaction forces from an atomistic perspective, visualizing the process and behaviour of particles when they aggregate, and relating the results to those derived from AFM experiments. Previous simulation studies have been conducted to elucidate the phase transformation of TiO_2 bulk and spherical shaped nanoparticles during sintering/interparticle interaction (Koparde and Cummings, 2008, Yong et al., 2002) and aggregation of TiO_2 nanocrystals (Alimohammadi and Fichthorn, 2009, Diebold, 2003). However, the force-displacement curves obtained from molecular dynamics simulations have not been reported for TiO_2 nanoparticle interactions in both vacuum and water environments. (Salameh et al., 2012) have studied the adhesion mechanisms of TiO_2 nanoparticles aggregates using AFM and LAMMPS (an MD package) and seem to be the only group to have reported force-displacement curves of TiO_2 nanoparticles coated with surface bound water layers.

In this study, molecular dynamics simulations were conducted in both vacuum and water environments at 300 K, for different sizes of nanoparticles. Two approaches were employed to study the interparticle interaction forces of TiO_2 nanoparticles. In both approaches, two particles of the same size, were separated by their centre-to-centre distances (i.e. centre of mass separation). In the first approach, the TiO_2 molecules in the particles were treated as rigid bodies, during the simulations. This reduced the effect of atomic vibration and movements within the particles, and made the particles act as cohesive solids. The particles were then allowed to advance towards each other during a single simulation. Upon advancing, the particles were observed to rotate as they approached each other. For a given separation distance, at each simulation time step, the interaction force was calculated as the sum of all individual forces acting on the atoms of one particle. The separation distance at each simulation time step, and the calculated interparticle forces for a simulation, were used to produce a force-displacement curve. Hence, the forces and distances were monitored during a single simulation, for a given nanoparticle size. In the second approach, a formula unit of TiO_2 in each particle was fixed at the centre of mass of the particles, so that the particles were constrained to their centre of mass separation distances. This allowed the particles and their atoms to freely rotate and distort, as the particles rotated around their centre of masses. The particles were constrained to their centre of mass distance for a series of simulations, and were only advanced towards each other, prior to each simulation. Each simulation formed a separation distance, and the interparticle force was averaged over each simulation. The separation distance and calculated interparticle forces obtained from the series of simulations, were used to produce a force-displacement curve.

For both approaches, simulations were carried out with time step of 1 fs and for a simulation of 1 ns. The equilibration time was for a period of 100 ps. The NVT ensemble and Berendsen thermostat were used, and simulations were conducted in a cuboidal periodic simulation box.

In molecular dynamics simulations, a rigid body is a collection of point atoms whose local geometry is time invariant (Smith et al., 2010). In DL_POLY, rigid body units are defined by describing the terms of the translational motion and rotation about the centre of mass. This is done by describing the position, orientation and inertia of a rigid body, and the rigid body equations of motion (Tersoff, 1989) using the appropriate variables. The mass of a rigid unit *M* is the sum of the atomic masses in that unit and is given by (Smith et al., 2010);

$$M = \sum_{j=1}^{N_{sites}} m_j \tag{7.2}$$

Where m_j is the mass of an atom. The position of the rigid unit is defined as the location of its centre of mass $\underline{R}$ (Smith et al., 2010);

$$\underline{R} = \frac{1}{M} \sum_{j=1}^{N_{sites}} m_j \underline{r_j} \tag{7.3}$$

Where $\underline{r_j}$ is the position vector of atom *j*. The rigid body translational velocity $\underline{V}$ is defined by (Smith et al., 2010);

$$\underline{V} = \frac{1}{M} \sum_{j=1}^{N_{sites}} m_j \underline{v_j} \tag{7.4}$$

Where $\underline{v_j}$ is the velocity of atom *j*. The vector sum of the resulting forces acting on the atoms of the body is the net translational force acting on the rigid body, and is given by;

$$\underline{F} = \sum_{j=1}^{N_{sites}} \underline{f_j} \tag{7.5}$$

Where $\underline{f_j}$ is the force on a rigid unit site. The rotational inertia matrix $\underline{\mathbf{I}}$ has components given by;

$$\boldsymbol{I}_{\alpha\beta} = \sum_{j=1}^{N_{sites}} m_j \left(d_j^2 \delta_{\alpha\beta} - d_j^{\alpha} r_j^{\beta}\right) \tag{7.6}$$

Where $\underline{d_j}$ is the displacement vector of the atoms *j* from the centre of mass given by;

$$\underline{d_j} = \underline{r_j} - \underline{R} \tag{7.7}$$

The introduction of the rigid bodies during the simulation reduced the effect of atomic vibration and movements within the particles and made the particles act as cohesive solids. This means that only the resulting particles were allowed to move and approach each other. This reduced fluctuations in the force-displacement curves. The separation distance used in this study, was the centre-to-centre distance (i.e. centre of mass separation) between the particles. The interparticle force was estimated as the sum of all individual forces acting on the atoms of a particle. The resulting interparticle force values were averaged over a simulation of

1 ns in length. The particles were allowed to move and approach each other without applying any external forces.

7.3.1 Particle interaction in vacuum

In both approaches, simulations were carried out in vacuum, for different particle sizes at 300 K. Figure 7.3 shows a schematic representation of a typical force-displacement curve for the purpose of illustrating the simulation set up, with (i) two particles separated from each other by centre-to-centre distances, (ii) two particles in contact.

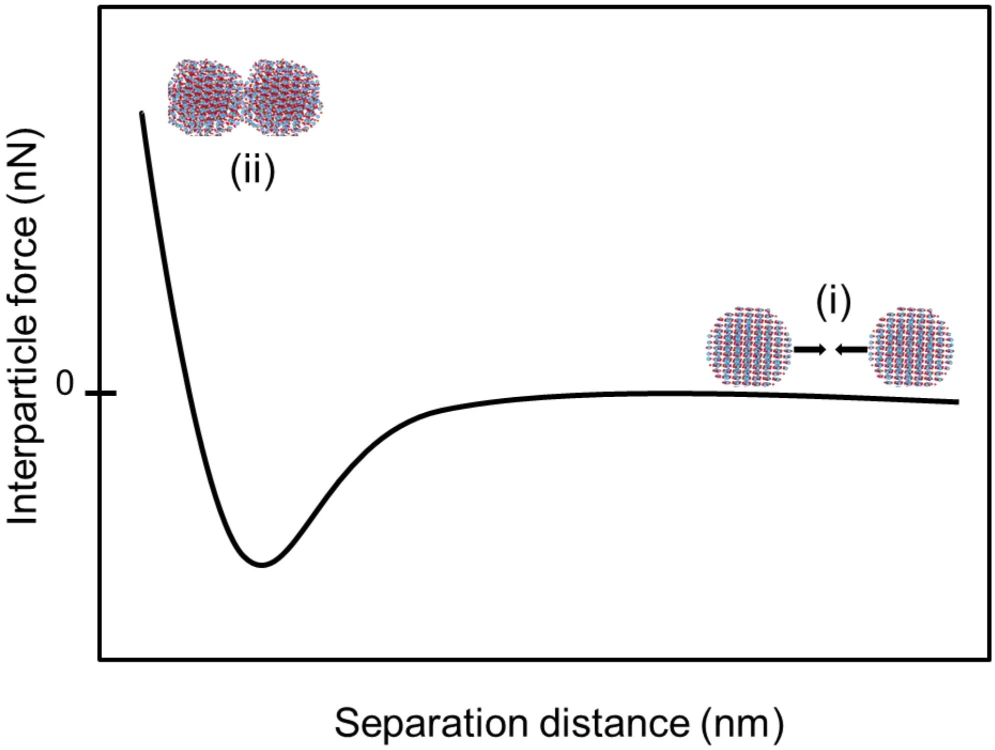

Figure 7.3 Schematic representation of a typical force-displacement curve showing (i) two particles separated from each other by centre-centre distance, (ii) two particles in contact.

7.3.1.1 Approach 1 – Particles containing rigid body molecules

Results from present study presented in Figures 7.4 – 7.7, show force-displacement curves for different particle sizes (ranging from 2 – 5 nm) of anatase and rutile nanoparticles, simulated in vacuum, using the first approach. It can be seen that for both anatase and rutile at 2 nm, the particles start becoming attracted to each other at their original centre-to-centre separation (i.e. at their original positions at start of the simulations). This can be seen in the gradual drop of the curve beginning from the original positions of the particles at the start of the simulations. This means the particles are already in the attractive regime at their centre-to-centre distance positions. However, as the particle size increases (i.e. 3 – 5nm) this attraction is observed mostly when the particles come closer. This means that unlike 2 nm, the particles are not exactly in their respective attractive regimes at their centre-to-centre distance positions. This is very evident with the 5 nm particles, as particles are seen to begin to get into the attractive regime at a centre-to-centre distance of about 7 nm. This shows that particles are more attractive at the nanoscale, with a wider attractive regime. However, this regime is seen to reduce with an increase in particle size as the particles will have to come closer to each other to fall within this regime. Visualisation of the process of particle interaction shows that the particles become repulsive when they initially touch each other, hence the steep increase in interaction force in the repulsive regime. Furthermore, it can be observed that the particles are more attractive at smaller particle sizes as can be seen in the case of 2 and 3 nm. This can be observed in the order of the magnitude of their forces (i.e. highly negative until they start becoming repulsive).

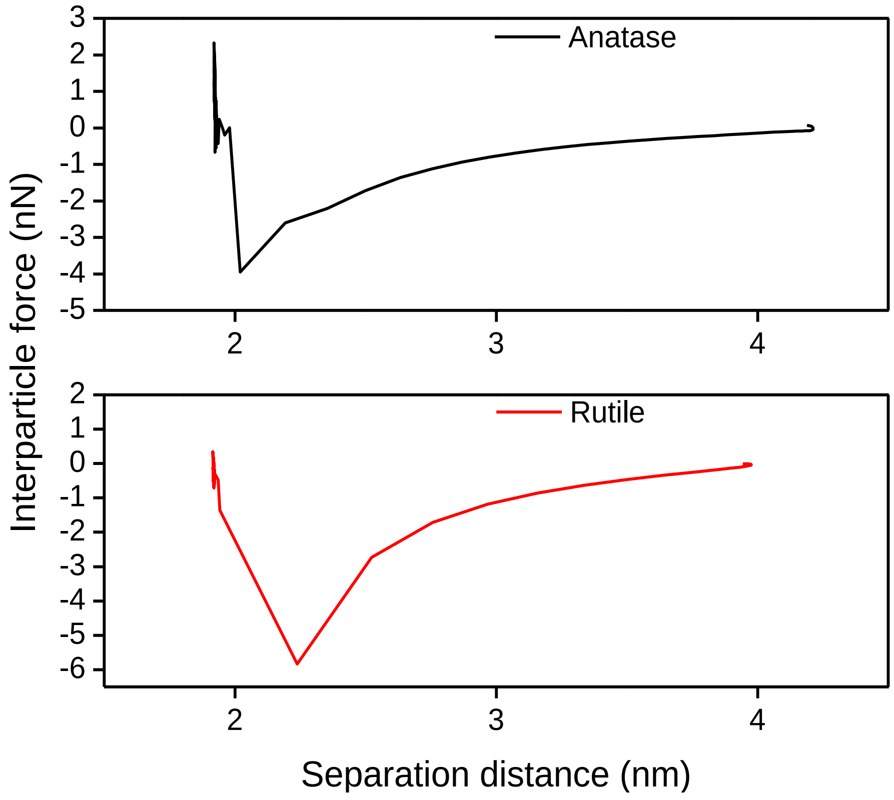

Figure 7.4 Force-displacement curves for 2nm anatase and rutile nanoparticles simulated in vacuum. Molecules in the particles were treated as rigid body units.

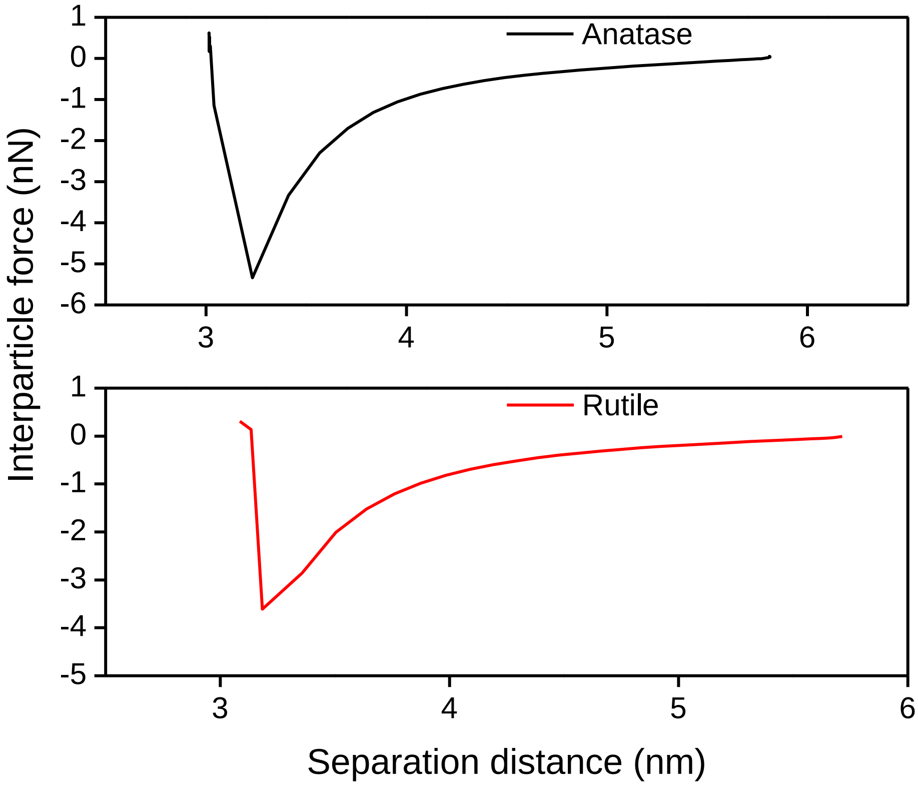

Figure 7.5 Force-displacement curves for 3nm anatase and rutile nanoparticles simulated in vacuum. Molecules in the particles were treated as rigid body units.

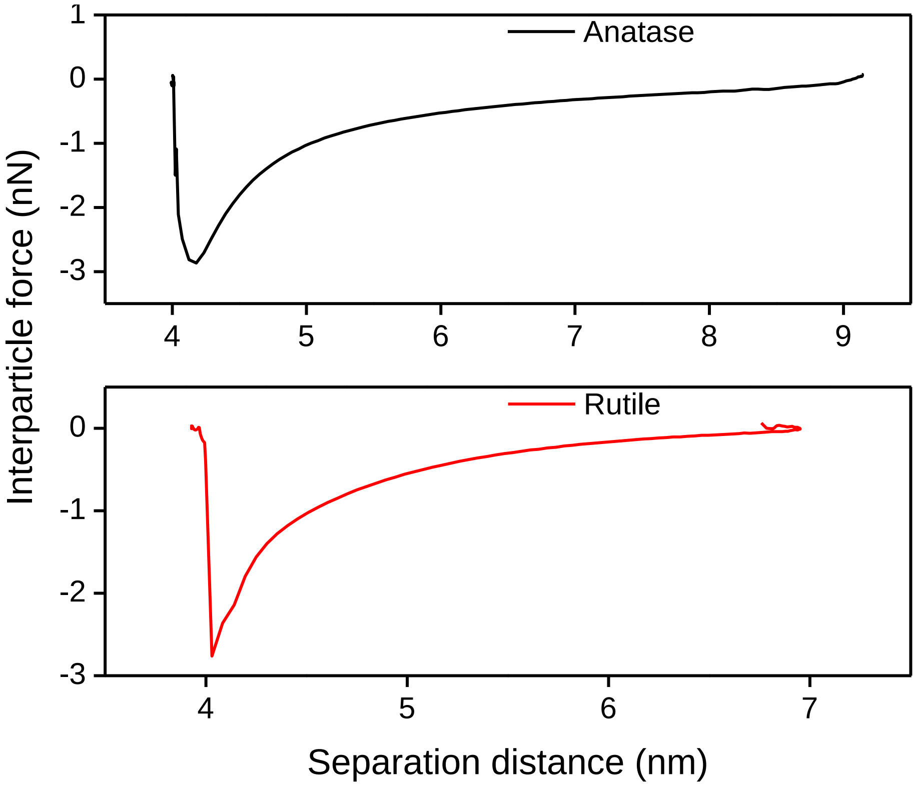

Figure 7.6 Force-displacement curves for 4nm anatase and rutile nanoparticles simulated in vacuum. Molecules in the particles were treated as rigid body units.

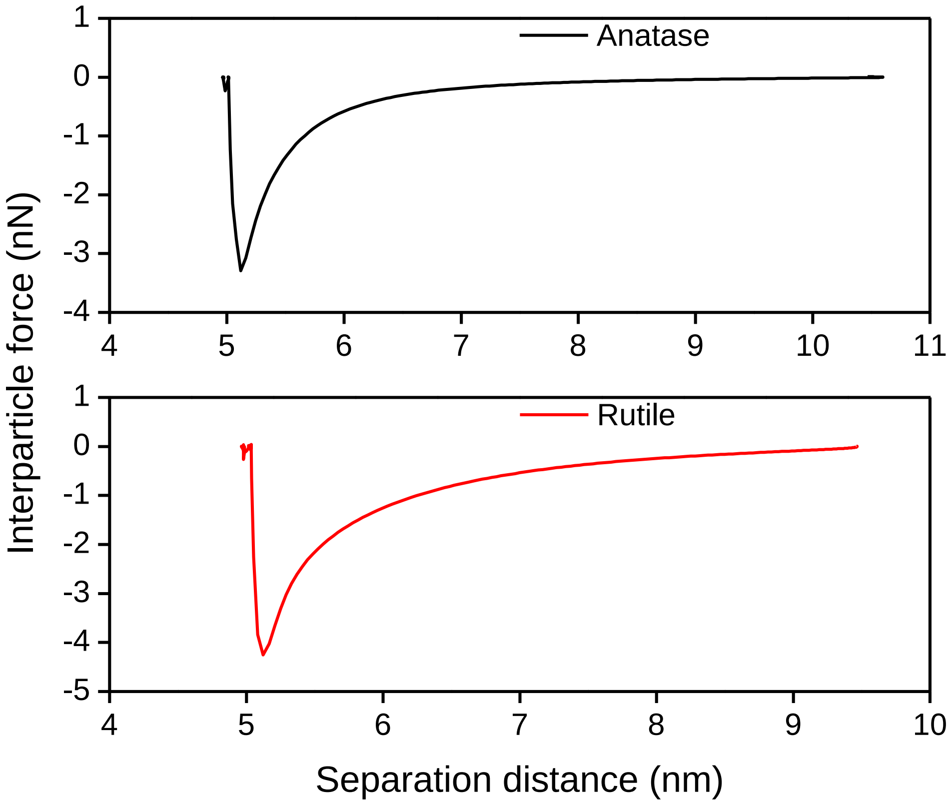

Figure 7.7 Force-displacement curves for 5nm anatase and rutile nanoparticles simulated in vacuum. Molecules in the particles were treated as rigid body units.

7.3.1.2 Approach 2 – Constrained particles at their centre of masses (non-rigid bodies)

Using the second approach, inteparticle interaction forces as a function of separation distance have been obtained and presented in the form of force-displacement curves for 2 nm anatase nanoparticles, in Figure 7.9. Remember that unlike the previous approach, the particles in this approach were constrained to their centre of masses for a series of simulations. The interparticle force was averaged for each simulation, and the particles advanced prior to subsequent simulations. In this case, 10 sets of simulations were carried out, and the averaged interparticle forces from each simulation were used to produce a force-displacement curve (Figure 7.8).

It can be observed that the interparticle forces of both approaches, are within reasonable order of magnitude. Furthermore, it can be seen from Figure 7.8, that the two particles approached each other at a centre-to-centre distance of about 3.7 nm, where an attraction force is seen to increase linearly (i.e. steep drop in the force curve) up to a distance of about 2.2 nm. Beyond this distance, a strong repulsive force (associated with a sharp rise in the force curve), is observed.

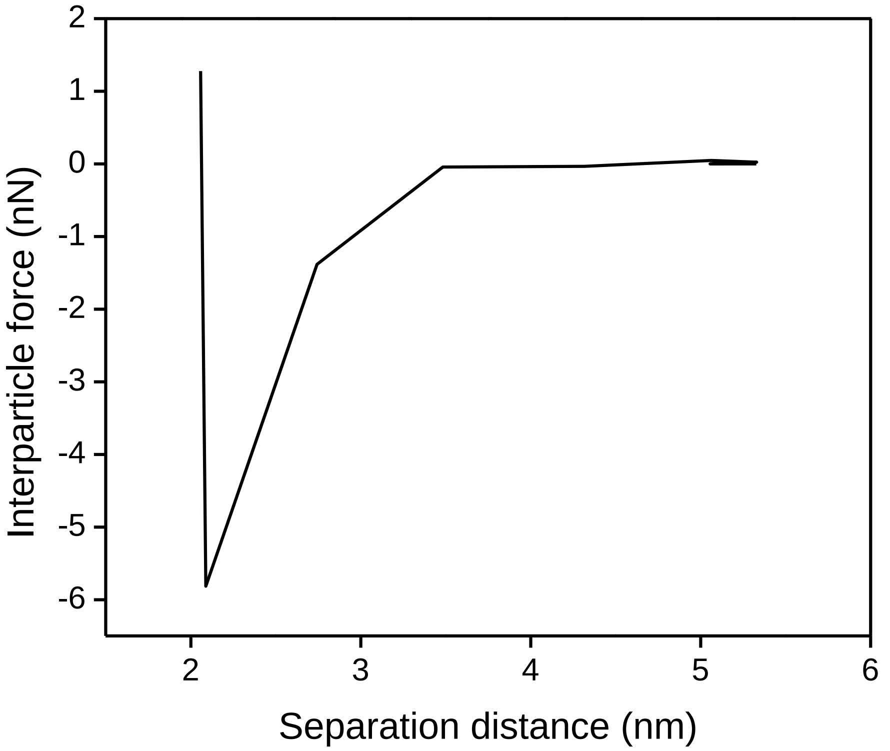

Figure 7.8 Force-displacement curve for 2nm anatase nanoparticles simulated in vacuum. Particles were constrained at their centre of masses and their atoms were allowed to rotate and distort.

7.3.2 Particle interaction in water

Similar to simulation of particles in vacuum, in this case particles were kept apart at their centre-centre distances using both approaches. Figure 7.9 shows a schematic representation of a typical force-displacement curve with two particles and water molecules around them.

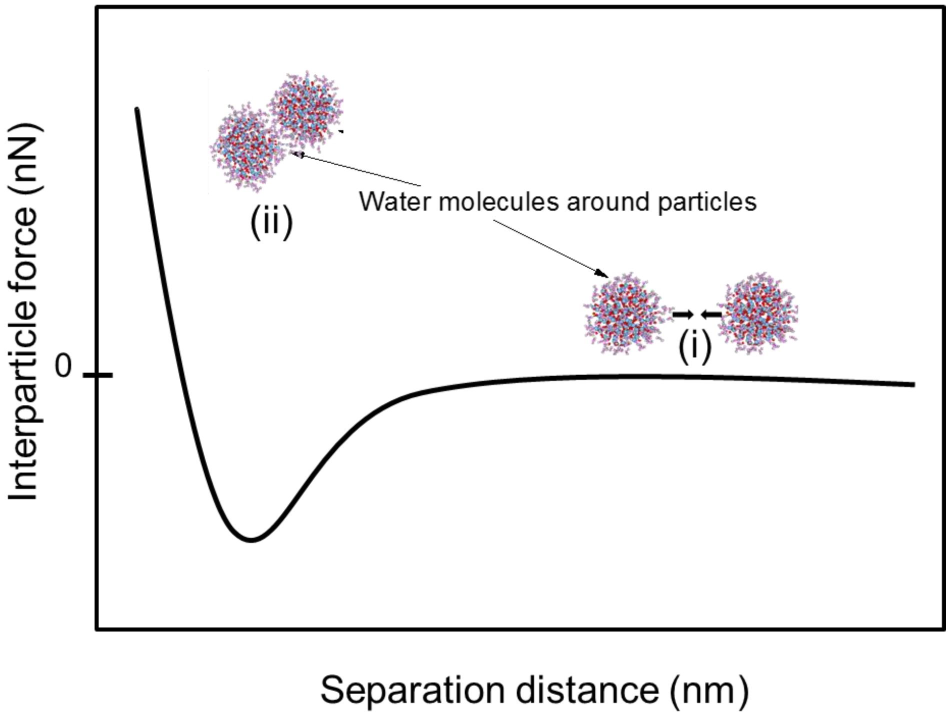

Figure 7.9 Schematic representation of a typical force-displacement curve showing two particles with water molecules around them and (i) separated from each other by centre-centre distance, (ii) two particles in strong contact.

7.3.2.1 Approach 1 – Particles containing rigid body molecules

In the first approach, the particles were coated with water molecules, in order to study their behaviour in water environment. The TiO_2 molecules were also treated as rigid bodies, similar to the first approach of simulations in vacuum. As in the case of simulations of the particles in vacuum using the first approach, here, the interparticle force was calculated as the sum of all individual forces acting on the atoms of one particle, at each simulation time step, for a given separation distance.

Force-displacement curves for 2 and 3 nm anatase and rutile have been plotted and shown in Figure 7.10 and 7.11. Due to the high computational cost of running such large simulations (i.e. about 80,000 atoms and above) simulations of interparticle interaction in water have been restricted just to 2 and 3 nm particles. Figure 7.10 reveals that anatase particles tend to have a slightly early attractive regime (at a centre-centre distance of 3 nm) compared to rutile (at a centre-to-centre distance of 2.7 nm), both at 2 nm. However in the case of 3 nm in Figure 7.11, both anatase and rutile particles are seen to have to similar attractive regime periods. Unlike the particles in vacuum where the repulsive regime begins just when the particles are in contact initially, in this case the repulsive regime begins at a centre-to-centre distance of about 2.6 nm. This is due to the water layer thickness around the particles which forms a neck when these particles come in contact with each other. Furthermore, anatase is observed to be more attractive in water compared to rutile. This can be seen in the magnitude of their forces as anatase has more negative interparticle forces (i.e. -0.65 nN for 2nm, and -0.8 nN for 3nm). Overall, both figures for 2 and 3 nm show smaller magnitude of interparticle force values (with an average between -0.8 nN and 1.6 nN) for particles in water, compared to particles in vacuum. This is because of the liquid medium forming a barrier for optimal interaction between the particles.

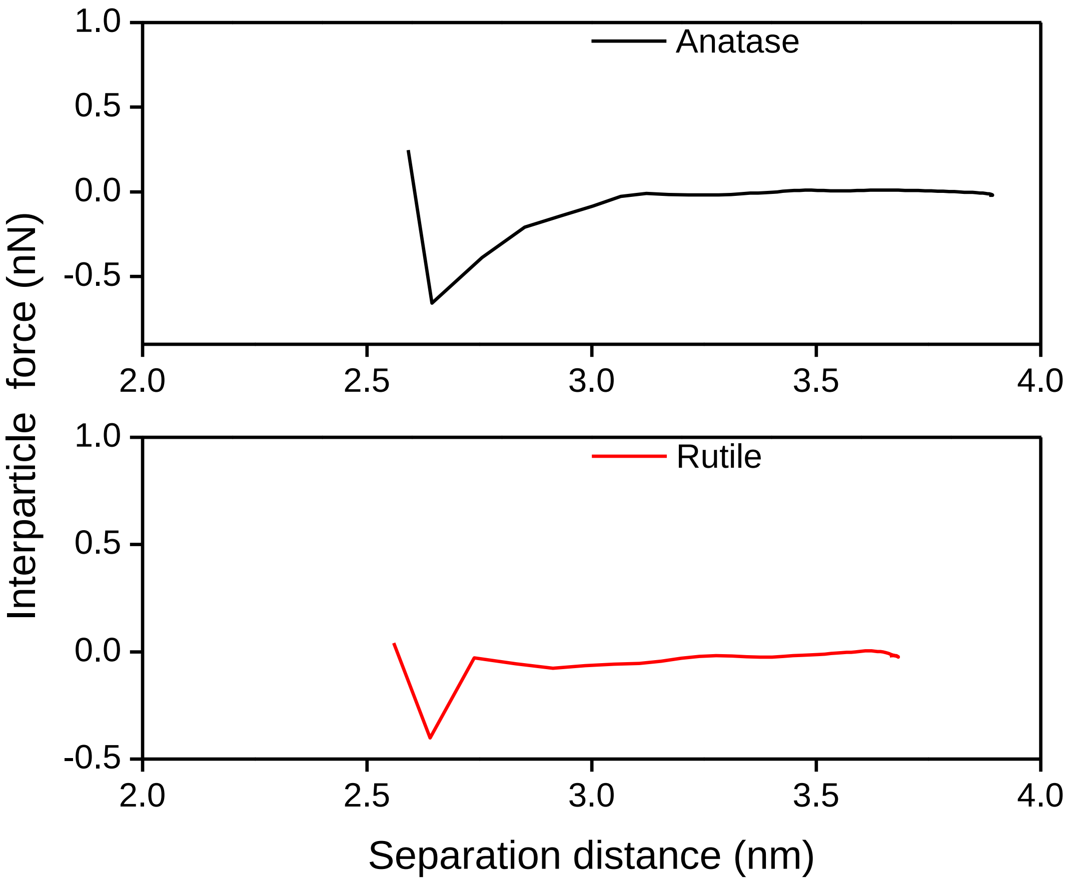

Figure 7.10 Force-displacement curves for 2nm anatase and rutile nanoparticles simulated in water. Molecules in the particles were treated as rigid body units.

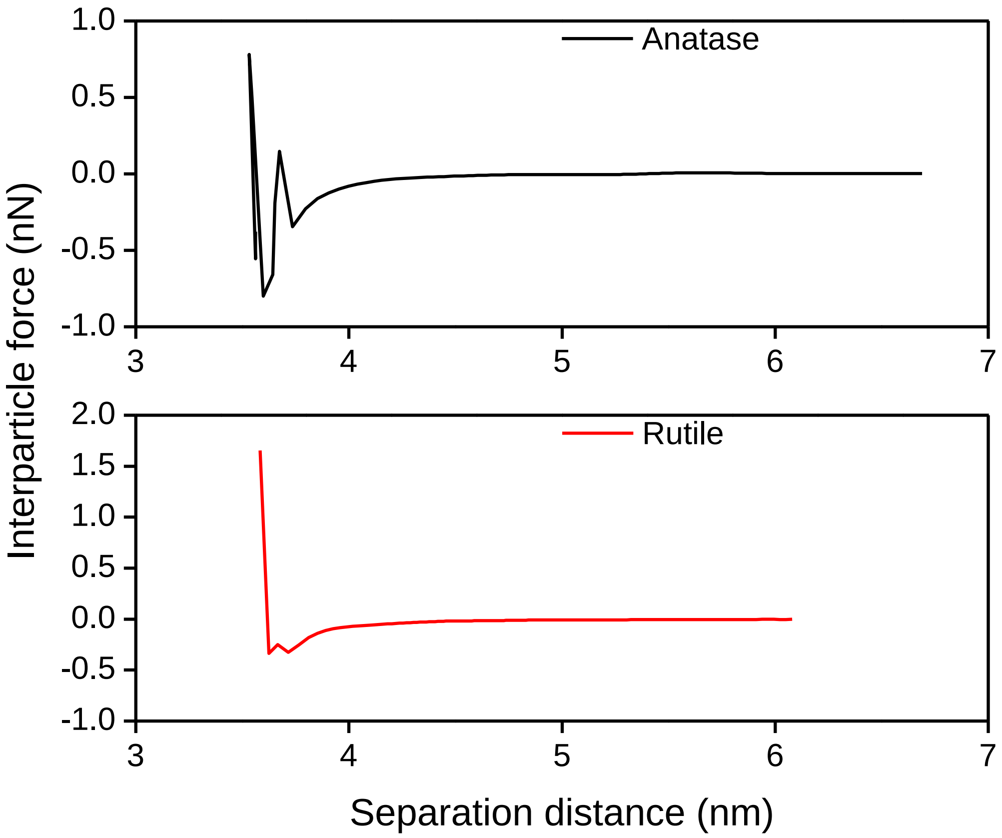

Figure 7.11 Force-displacement curves for 3nm anatase and rutile nanoparticles simulated in water. Molecules in the particles were treated as rigid body units.

7.3.2.2 Approach 2 – Constrained particles at their centre of masses (non-rigid bodies)

Similar to the simulations using this approach in vacuum, here particles were constrained at their centre-to-centre distance and the simulation box in which they were placed, was filled with water molecules. In this approach, the TiO_2 molecules were not treated as rigid bodies. Prior to each simulation, the particles were advanced to each other and then constrained. A set of 10 simulations were carried out, and the averaged interparticle forces from each simulation were used to produce a force-displacement curve as shown in Figure 7.12. Here, a strong attraction (represented by the steep drop in the force curve) can be observed beginning from a centre-to-centre distance of about 2.4 nm up to a distance of about 2.05 nm. Beyond this, a strong repulsive force (represented by a sharp rise in the force curve) is observed. This is unlike in the case of the particle in vacuum (with simulations using the second approach), where an attraction was observed at a distance of 3.7 nm. The observation of an initial attraction force at a shorter separation distance in the case of simulations in water, is as a result of the interaction between the water molecules and the particles. Here, the water molecules tend to restrict interactions between both particles, leading to a late attraction. Also, comparing simulations of both approaches in water, in relation to their separation distances, an early repulsion is observed in the first approach. This is as a result of the water molecules coated around the particles and forming a neck when the particles approach each other. As a result of the neck formation, the particles were not in contact. In the second approach, it can be considered, that the particles were in contact with each other, and water molecules were around them, but not forming a neck as in the case of the first approach. Also, it can be seen that the magnitude of the interaction force in the second approach is higher than that in the first approach. This is as a result of more interactions between both particles, leading to a stronger attraction when the particles were close to each other, and repulsion, when the particles were in contact.

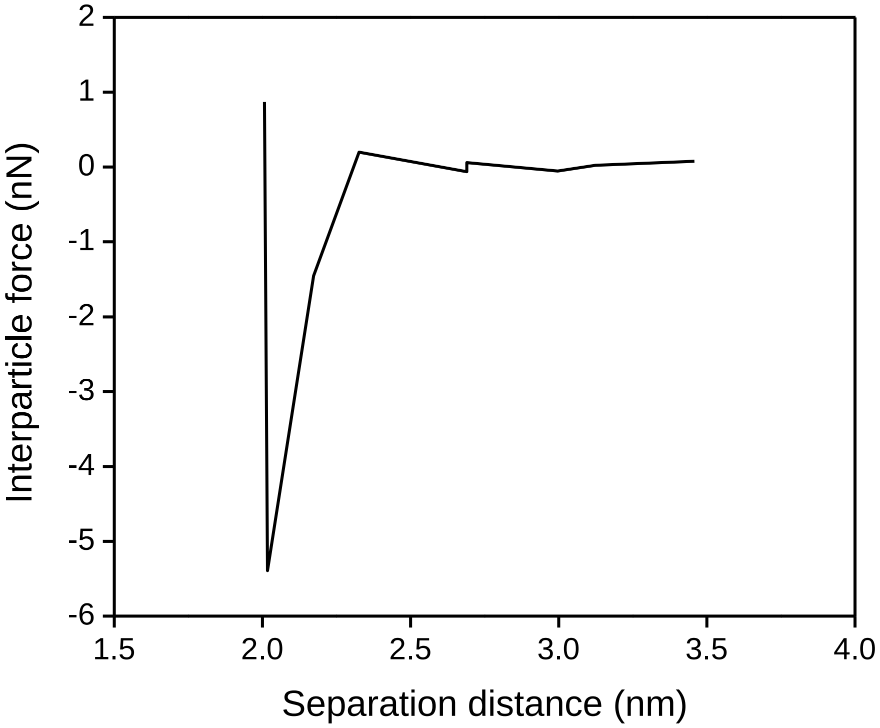

Figure 7.12 Force-displacement curves for 2nm anatase nanoparticles simulated in bulk water. Particles were constrained at their centre of masses and their atoms were allowed to rotate and distort.

7.4 Relating interparticle interactions to effective thermal conductivity

Discussions based on Figure 2.5, revealed that loosely packed aggregates within nanofluids tend to enhance thermal conductivity of the fluids since the clusters formed will have fluids flowing through the pore-like spaces of the cluster. Figure 7.13 shows a cluster of loosely packed anatase nanoparticles with water molecules and heat flowing around and across the particle surfaces and entire effective volume. The effective volume created from this cluster will enhance thermal enhancement as seen from Figure 2.5 (Wang and Mujumdar, 2007). Studies of interparticle interaction above have shown that nanoparticles (especially at small sizes) will come together without any force applied even at low temperatures (as seen at 300 K). This has been observed for vacuum and water environments. The particles are also seen to be repulsive just at initial contact. However, they are seen to stick together. Figure 7.13 shows the flow of heat through the particles and water molecules, and across the entire effective volume which will eventually lead to effective thermal enhancement of the fluid medium. The formation of clusters within the fluid is important to keep the flow of heat going.

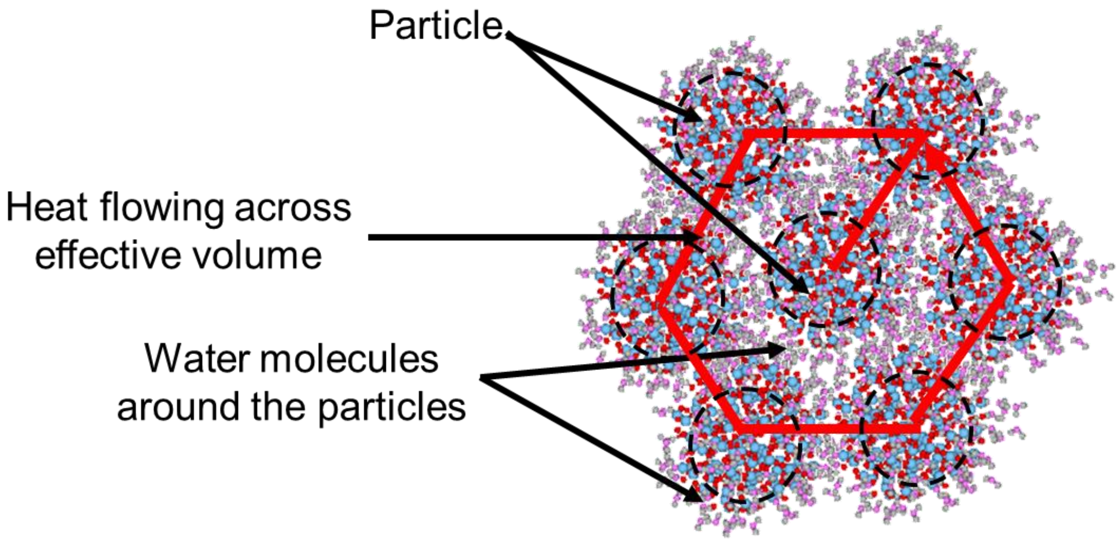

Figure 7.13 Cluster of loosely packed anatase nanoparticles with water molecules around particle surfaces and heat (in red) flowing across the effective volume.

7.5 Conclusion

Force-displacement curves have been reported above showing interparticle forces between TiO_2 nanoparticles at different sizes, at 300 K in vacuum and water environments using two approaches. Using the first approach of simulations in vacuum, it can be seen that for 2 nm anatase and rutile, the particles were in the attractive regime and highly attractive right from their original centre-centre distances (which were their original positions at the commencement of the simulations). The observed attraction is seen to reduce with increase in particle size as particles become attractive mostly at closer distances to each other. The interparticle forces for particles in both approaches were seen to be within the same order of magnitude. Also, simulations in water carried out using the first approach, showed that anatase particles tend to have earlier attractive and repulsive regime compared to rutile. Visualization of the interaction process in both environments showed that particles become repulsive when they initially touched each other. In the case of simulations using the second approach in water, the particles were seen to have later repulsive regimes, with a short centre-to-centre distance of about 2.05 nm.

Chapter 8

Conclusion and Recommendations for Future work

8 Conclusion and Recommendations for Future work

8.1 Conclusion

This work investigated physico-thermal properties of TiO_2 nanoparticles using molecular dynamics simulations. The motivation to carry out this research was derived from previous research (Wen et al., 2009) which showed that out of the four possible mechanisms proposed for explaining the enhancement of thermal conductance in nanoliquids (i.e. Brownian motion of nanoparticles in the liquid, formation of liquid layers around nanoparticles, ballistic nature of heat transport within nanoparticles, and formation of nanoparticle clusters), the formation of nanoparticle clusters is the most influential mechanism. In this research, investigations were carried out to study the influence of particle aggregation on three types of nanofluids. These nanofluids were alumina, copper oxide and titania water based nanofluids. As findings from this investigation showed the influence of particle aggregation on thermal enhancement of nanofluids, this justified further investigation to be carried out on the particle scale properties of nanoparticles (in this research, TiO_2 nanoparticle as a model nanoparticle). Particle scale properties including thermodynamic, structural, surface and inter-particle interaction force are known to influence particle interactions (Dunphy Guzman et al., 2006) and their bulk transport behaviour, and hence detailed investigations on them are performed here for TiO_2 under different environments conditions including water liquid base. Molecular dynamics simulation packages (i.e. GULP and DL_POLY) were used to investigate these particle-scale properties under vacuum and liquid environments for different temperatures. Molecular modelling provides a clearer view of atomic scale properties and interactions, as these properties influence bulk scale properties. The main conclusions from this research are summarised in the following sections.

8.1.1 Investigations on Effective thermal conductivity of model based nanofluids and the relevance of their single-particle scale properties (Chapter 3)

Investigations were conducted to study the influence of particle aggregation on the effective thermal conductivity of the model based nanofluids using the Maxwell-Garnet model, and results showed that effective thermal conductivity of the three nanofluids increased for increasing aggregate size (represented by *Rg/a*) and particle volume fraction. Results also showed that the influence of aggregate size is significant when *Rg/a* < 20. (Wen and Ding, 2005) experimentally formulated alumina-water nanofluids containing a measured aggregate size of 167.5 nm and primary particle size ranging from 10 – 50 nm. This aggregate and particle size range falls within those reported in other literature (Leong et al., 2006). This means that *Rg/a* will usually fall within a range of 16.7 to 3.35. However it is important to note that large aggregates will tend to settle within the nanofluid rather form suspensions. Since the settling of these aggregates could reduce the thermal efficiency of the fluids, an optimum aggregate size is required to achieve the desired effective thermal conductivity of nanofluids. Further investigations were carried out on the effect of fractal and chemical dimensions which were used to characterize aggregate sizes, showed that aggregation of nanoparticles in fluid bases is mostly Diffusion Limited Cluster-Cluster Aggregation (DLCCA). DLCCA is known to have a rapid aggregation process which leads to loosely packed aggregates.

Investigations carried out on the effect of particle volume fraction on effective thermal conductance showed that a significant increase in thermal enhancement began when the volume fraction was above 1%, though further enhancements were observed up to 5% volume fraction (limited to 5% due to economic considerations). Careful consideration is also required so as not to load particles above the optimum volume fraction as this will lead to a reduction in efficiency of the nanofluids, in cases such as clogging problems, pumping costs, etc.

Following findings on the influence of particle aggregation on effective thermal conductivity of nanofluids, particle scale properties of a model nanoparticle (in this work, TiO_2) were investigated using molecular modelling simulations. These properties are known to influence particle interaction and aggregation. Conclusions on these properties are summarised subsequently.

8.1.2 Performance testing of the force field for conducting molecular modelling of TiO_2, using force fitting (Chapter 5)

In this thesis, the force field of Matsui-Akaogi, widely used for carrying out molecular modelling of TiO_2, was used. This force field which is in the form of the Buckingham potential, is known to be the most suitable for carrying out molecular modelling simulations of bulk TiO_2 polymorphs for a wide range of temperatures, and reproduces the structures of the three main TiO_2 polymorphs (Koparde and Cummings, 2005, Filyukov et al., 2007, Koparde and Cummings, 2007, Matsui and Akaogi, 1991). The suitability and performance of this force field was further tested in this work by performing force field fitting using structural data in the form of elastic constant values, derived from a high level calculation (*ab initio*), CASTEP. These calculations were made as part of a separate PhD programme involving collaboration with members of a research group constituting of Professor Rick Brydson, Dr Andrew Scott and Trevor Hardcastle from the Institute of Materials and Research (IMR), University of Leeds. Force field fitting was carried out using GULP, a molecular modelling software. When fitted using elastic constants from *ab initio* calculations and experiments (Isaak et al., 1998), the fitted force fields reproduced properties of bulk TiO_2 that were well within reasonable limits when compared to properties predicted using the original Matsui-Akaogi force field. This further confirmed the suitability of the Matsui-Akaogi force field in performing molecular modelling simulations of TiO_2 bulk crystals and nanoparticles in this research.

8.1.3 Bulk properties of TiO_2 crystals using GULP for molecular modelling (Chapter 6, section 6.2 – 6.3)

Bulk properties such as lattice, surface and attachment energies, for the unrelaxed and relaxed structures of the three phases of TiO_2 (i.e. rutile, anatase and brookite), were predicted from GULP, using the Matsui – Akaogi force field, and results were presented in Table 6.1 – 6.4. In terms of the lattice energy, there was no significant change between the unrelaxed and relaxed structures for anatase. However, for rutile and brookite, a significant change in their lattice energies was observed between the unrelaxed and relaxed structures.

Surface and attachment energies of the crystal surfaces were predicted for the three phases, using a GULP visualisation interface, GDIS. It was observed that surface energies for the rutile surfaces (apart from that of (1 1 0) surfaces) was higher than the surface energies for the corresponding anatase surfaces. For example, the (0 0 1) surface energy of rutile is higher than its corresponding anatase surface by 46.28 %. Also, the (1 0 0) surface energy of rutile is higher than for the (1 0 0) anatase surface by 19.52 %. On average, anatase showed the least surface energy ($\approx$ 1.76 Jm^{-2}) compared to rutile ($\approx$ 2.05 Jm^{-2}) and brookite ($\approx$ 2.38 Jm^{-2}).

Furthermore, models of the equilibrium crystal morphology for the three phases of TiO_2 were presented in section 6.2.2. The structures were predicted using the BFDH model, and the calculated surface and attachment energies from the present study. Three morphological models were produced, one using the BFDH model, the second using the attachment and surface energies calculated for the unrelaxed crystal lattice, and the third model using those quantities calculated for the relaxed crystal lattice. For rutile, the morphology predicted using the BFDH model expressed the (1 1 0) and (0 1 1) surfaces of rutile. In the unrelaxed morphology predicted using the calculated surface energies, the (1 1 0), (0 1 1) and (1 0 0) surfaces were expressed. The (2 2 1) surface is expressed in the relaxed morphology predicted using the surface energies and is mainly due to the reduction in its surface energy upon relaxation from 3.77 Jm^{-2} to 2.12 Jm^{-2}. Also, for rutile, the unrelaxed morphology predicted using the attachment energies, expressed the (1 1 0) and (0 1 1) surfaces similar to the morphology prediction using the BFDH model. The relaxed structure obtained using the attachment energies, had a slightly squashed habit in the z direction, when compared to the unrelaxed morphology. The relaxed morphologies predicted using the surface and attachment energies are similar to that predicted using experimental data (Kostov, 1968).

In the case of anatase, the morphologies predicted using the surface and attachment energies were seen to express the (0 0 1) and (0 1 1) surfaces, similar to that predicted using the BFDH model. It was observed that the capped octahedral shape observed in the rutile morphologies is as a result of the (0 1 1) octahedral which is capped with the (0 0 1) surface. Furthermore, the anatase phase showed the least change in surface energy when comparing the unrelaxed to the relaxed surfaces. For example, the (0 0 1) showed no significant change in terms of atom relocation or relaxation.

In the case of brookite, the (0 0 1), (0 1 0), (1 0 0), (1 1 1) and (2 1 0) surfaces were expressed in all morphologies predicted using the BFDH model, surface and attachment energies. As in the case of rutile and anatase, the (0 0 1) surface formed at a cap on the orthorhombic brookite structure. The (0 1 0) formed a hexagonal protrusion on all the morphologies.

Overall, the expression of surfaces upon relaxation as a result of reduction in surface energy or increase in attachment energy, shows the relevance of surface relaxation in the prediction of a morphology structure.

8.1.4 Physico-thermal properties of TiO_2 nanoparticles using DL_POLY for molecular dynamics simulations (Chapter 6, section 6.4 – 6.5)

Investigations conducted on anatase and rutile TiO_2 nanoparticles by carrying out molecular dynamics simulation using DL_POLY showed a relationship between thermodynamic and structural properties. Parameters such as total energy, surface energy, radial distribution function and sphericity of the nanoparticles which capture the thermal and structural properties, have been predicted as a function of temperature. The melting point and the point of phase transition of the particles have been predicted through analysis of these parameters as a function of temperature. The surface energies of the crystal surfaces of the TiO_2 phases, were relatively similar to the surface energies of the nanoparticle structures and considering the fact that the crystal surfaces are the low index surfaces, this shows that both rutile and anatase nanoparticles are dominated by mostly the low index surfaces which are known for their stability.

The effect of simulation time and temperature on surface energy of the nanoparticles has also been investigated and results show a high dependence of surface energy on particle size and temperature. Surface energy of anatase nanoparticles in water is seen to be lower than that in vacuum by about 50%. In both environments, surface energy is seen to increase to a maximum (optimal value) at about 4 nm, after which no further significant increase is observed. The difference in the surface energy trend between the two phases has been attributed to the fact that anatase is more thermodynamically stable at the nanocrystalline phase, compared to rutile. In terms of temperature effects on surface energy, surface energy of anatase and rutile nanoparticles in vacuum is seen to decrease with increase in temperature until 1500 K after which a sharp increase in surface energy is observed. This has been observed especially for particle sizes between 3 and 6 nm.

The well-ordered, high temperature and liquid thermo-structural phases of anatase and rutile TiO_2 nanoparticles at temperatures between 300 and 3000 K (as shown in the radial distribution function plots) reveal that the high orderliness and coordination of titanium decreases to a point of undercoordination as the temperature increases. This was associated with visible surface disordering of the particles as temperature increased. Structural and surface properties of pure water, anatase and rutile TiO_2 nanoparticles in vacuum and water environments have also been investigated. Plots of radial distribution functions for particles in vacuum show a much higher crystallinity and coordination, with peaks of about 95% higher than that of the particles in water. Further investigation into radial distribution function plots of TiO_2 – water atom pairs show more interactions between the atoms of water and the particles at the surface than at the inner core of the particle. Also, the estimated surface tension of water is seen to agree quite well with that of experiments of 0.0725 J/m^2.

8.1.5 Force distance analysis of TiO_2 interacting nanoparticles using DL_POLY for molecular dynamics simulations (Chapter 7)

Force-displacement curves at 300 K for TiO_2 nanoparticles at different sizes under vacuum and liquid environments, have also been investigated using two approaches. In the first approach, the TiO_2 molecules in the particles were treated as rigid bodies and for a given separation distance, at each simulation time step, the interaction force was calculated as the sum of all individual forces acting on the atoms of one particle. In the second approach, the atoms in the particles were not treated as rigid bodies, but were allowed to freely rotate and distort. The particles in this approach were fixed at their centre of masses. Each simulation formed a separation distance, and the interparticle force was averaged over each simulation. Using the first approach, for both anatase and rutile at 2 nm in vacuum, the particles were seen to be in the attractive regime even from their original centre-centre distance (which was their original positions at the start of the simulations). However, this attraction was seen to reduce with increase in particle size. Visualization of the process of particle interaction during simulation showed that the particles became repulsive when they initially touched each other. The magnitude of the interparticle forces for both approaches, are seen to be within reasonable agreement. For simulations in water, the first approach involved coating the particles with water molecules. The interparticle force was calculated during a single simulation and a force-displacement curve was produced. The second approach involved constraining the particles at their centre-to-centre distance and the simulation box in which they were placed, was filled with water molecules. The interparticle force in this approach was calculated over a series of simulation, and a force-displacement curve was produced. Using the first approach, anatase particles in water were seen to have earlier attractive and repulsive regime compared to rutile. Comparing simulations of both approaches in water, in relation to their separation distances, an early repulsion was observed in the first approach. This observation is as a result of the water molecules coated around the particles, forming a neck when the particles approach each other. As a result of the neck formation, the particles were not in contact. In the second approach, it was considered, that the particles were in contact with each other, and water molecules were around them, without a neck formation. Also, it was seen that the magnitude of the interaction force in the second approach was higher than that in the first approach. This is as a result of more interactions between both particles, leading to a stronger attraction when the particles were close to each other, and repulsion, when the particles were in contact.

8.2 Recommendation for future work

This research study has provided valuable information on physico-thermal properties of TiO_2 nanoparticles as a model nanoparticle. These properties are known to influence particle aggregation in nanofluids. The aim of investigating these properties is to understand the underlying mechanisms behind particle aggregation which leads to the observed thermal enhancement in nanofluids. Further studies are required to understand the molecular scale properties of other types of nanoparticles (e.g. copper oxide, alumina) similar to the case of TiO_2 nanoparticles considered in this study. This could help scientists and engineers in future to develop clear understanding of multi-scale functional properties of different types of nanoparticles in engineering applications for example, starting from molecular scale properties of nanoparticles through their surface properties such as surface energy reported here which in turn could influence formation of particle clustering to other functional properties such as thermal conductance of nanofluids. Also, further research needs to be done on the following;

1. Testing the fitted force fields derived using the elastic constants from *ab initio* calculations and experiments (in Table 5.9) by carrying out molecular dynamics simulations of all three phases of TiO_2. Predicted properties such as surface and attachment energies of the bulk crystalline surfaces, surface energy of the nanoparticles etc, from these simulations are to be compared with those predicted using the original Matsui-Akaogi force field. This will aid in further confirming the force field that is most suitable and which has better transferability across the three polymorphs of TiO_2.
2. Identifying precisely, the surfaces of the TiO_2 phases that are most likely present on the nanoparticles as a function particle size, temperature and simulation environment (i.e. vacuum or water). This will aid in further confirming the thermodynamic stability of the phases of TiO_2, as the particles with mostly low index stable surfaces will be the most thermodynamically stable.
3. Carrying out simulations of TiO_2 nanoparticles in other liquid systems such as ethylene glycol etc., and compare predicted properties such as radial distribution functions, surface energy etc., to those for nanoparticles in water. This will provide solid understanding on nanoparticle behaviour in a wide variety of liquid systems.
4. Investigating the influence of the type of interaction forces between nanoparticles on the self-assembly and mechanical strength of nanoparticles using theories of contact mechanics. Furthermore, investigating the

directional orientation of clusters and fabric analysis with liquid systems is desired at a fundamental level.

5. Developing a robust thermal conductivity model which will incorporate surface energy of the individual nanoparticles, fractal dimension of nanoparticle clusters, as well as the structural properties of nanoparticles in relation to direction of the clusters. Development of a unified multi-scale modelling software for this would be much helpful for scientists and engineers in future.

References

A. Ahmad G. H. A., Salman Aziz 2006. Synthesis and applications of TiO_2 nanoparticles. *Pakistan Engineering Congress, 70th Annual Session Proceedings*.

Agari Y. & Uno, T. 1986. Estimation on thermal conductivities of filled polymers. *Journal of Applied Polymer Science,* 32**,** 5705-5712.

Ahdjoudj J. & Minot, C. 1997. A theoretical study of HCO_2H adsorption on TiO_2(110). *Catalysis Letters,* 46**,** 83-91.

Ahmad M. I. & Bhattacharya, S. S. 2009. Size effect on the lattice parameters of nanocrystalline anatase. *Applied Physics Letters,* 95**,** 191906-191906-3.

Akpan U. G. & Hameed, B. H. 2010. The advancements in sol–gel method of doped-TiO_2 photocatalysts. *Applied Catalysis A: General,* 375**,** 1-11.

Albers B. J., Schwendemann, T. C., Baykara, M. Z., Pilet, N., Liebmann, M., Altman, E. I. & Schwarz, U. D. 2009. Data acquisition and analysis procedures for high-resolution atomic force microscopy in three dimensions. *Nanotechnology,* 20**,** 264002.

Alimohammadi M. & Fichthorn, K. A. 2009. Molecular Dynamics Simulation of the Aggregation of Titanium Dioxide Nanocrystals: Preferential Alignment. *Nano Letters,* 9**,** 4198-4203.

Amanbayev T., Okeke, G., Afzal, M. & Antony, S. J. Modelling of bacterial growth in nano liquids. 7th International Conference on Engineering Computational Technology, ECT 2010, September 14, 2010 - September 17, 2010, 2010 Valencia, Spain. Civil-Comp Press.

Avsec J. & Oblak, M. 2007. The calculation of thermal conductivity, viscosity and thermodynamic properties for nanofluids on the basis of statistical nanomechanics. *International Journal of Heat and Mass Transfer,* 50**,** 4331-4341.

Bandura A. V. & Kubicki, J. D. 2003. Derivation of Force Field Parameters for TiO_2-H_2O Systems from ab Initio Calculations. *The Journal of Physical Chemistry B,* 107**,** 11072-11081.

Banfield J. F., Bischoff, B. L. & Anderson, M. A. 1993. TiO_2 accessory minerals: coarsening, and transformation kinetics in pure and doped synthetic nanocrystalline materials. *Chemical Geology,* 110**,** 211-231.

Barnard A. S. & Zapol, P. 2004. Predicting the Energetics, Phase Stability, and Morphology Evolution of Faceted and Spherical Anatase Nanocrystals. *The Journal of Physical Chemistry B,* 108**,** 18435-18440.

Barteau M. A. 1996. Organic Reactions at Well-Defined Oxide Surfaces. *Chemical Reviews,* 96**,** 1413-1430.

Bates S. P., Kresse, G. & Gillan, M. J. 1997. A systematic study of the surface energetics and structure of TiO_2(110) by first-principles calculations. *Surface Science,* 385**,** 386-394.

Baur W. H. 1956. Über die Verfeinerung der Kristallstrukturbestimmung einiger Vertreter des Rutiltyps: TiO_2, SnO_2, GeO_2 und MgF_2. *Acta Crystallographica,* 9**,** 515-520.

Berendsen H. J. C., van Gunsteren, W. F., Egberts, E. & de Vlieg, J. 1987. Dynamic Simulation of Complex Molecular Systems. *Supercomputer Research in Chemistry and Chemical Engineering.* American Chemical Society.

Berkovitch-Yellin Z. 1985. Toward an ab initio derivation of crystal morphology. *Journal of the American Chemical Society,* 107**,** 8239-8253.

Binnig G., Quate, C. F. & Gerber, C. 1986. Atomic Force Microscope. *Physical Review Letters,* 56**,** 930-933.

Boer-Duchemin E., Tranvouez, E. & Dujardin, G. 2010. The interaction of an atomic force microscope tip with a nano-object: a model for determining the lateral force. *Nanotechnology,* 21**,** 455704.

Boudenne A., Ibos, L., Fois, M., Gehin, E. & Majeste, J. C. 2004. Thermophysical properties of polypropylene/aluminum composites. *Journal of Polymer Science, Part B (Polymer Physics),* 42**,** 722-32.

Bréchignac C., Houdy, P. & Lahmani, M. 2008. *Nanomaterials and Nanochemistry*, Springer.

Bredow T. & Jug, K. 1995. Theoretical investigation of water adsorption at rutile and anatase surfaces. *Surface Science,* 327**,** 398-408.

Brostow W. 1977. Radial distribution function peaks and coordination numbers in liquids and in amorphous solids. *Chemical Physics Letters,* 49**,** 285-288.

Brown C. A. & Savary, G. 1991. Describing ground surface texture using contact profilometry and fractal analysis. *Wear,* 141**,** 211-226.

Bruggeman D. A. G. 1936. Calculation of various physical constants of heterogeneous substances. II. Dielectric constants and conductivity of polycrystalline and irregular systems. *Annalen der Physik,* 25**,** 645-672.

Buongiorno J., Venerus, D. C., Prabhat, N., McKrell, T., Townsend, J., Christianson, R., Tolmachev, Y. V., Keblinski, P., Hu, L.-w., Alvarado, J. L., Bang, I. C., Bishnoi, S. W., Bonetti, M., Botz, F., Cecere, A., Chang, Y., Chen, G., Chen, H., Chung, S. J., Chyu, M. K., Das, S. K., Paola, R. D., Ding, Y., Dubois, F., Dzido, G., Eapen, J., Escher, W., Funfschilling, D., Galand, Q., Gao, J., Gharagozloo, P. E., Goodson, K. E., Gutierrez, J. G., Hong, H., Horton, M., Hwang, K. S., Iorio, C. S., Jang, S. P., Jarzebski, A. B., Jiang, Y., Jin, L., Kabelac, S., Kamath, A., Kedzierski, M. A., Kieng, L. G., Kim, C., Kim, J.-H., Kim, S., Lee, S. H., Leong, K. C., Manna, I., Michel, B., Ni, R., Patel, H. E., Philip, J., Poulikakos, D., Reynaud, C., Savino, R., Singh, P. K., Song, P., Sundararajan, T., Timofeeva, E., Tritcak, T., Turanov, A. N., Vaerenbergh, S. V., Wen, D., Witharana, S., Yang, C., Yeh, W.-H., Zhao, X.-Z. & Zhou, S.-Q. 2009. A benchmark study on the thermal conductivity of nanofluids. *Journal of Applied Physics,* 106**,** 094312.

Burton W. K., Cabrera, N. & Frank, F. C. 1951. The Growth of Crystals and the Equilibrium Structure of their Surfaces. *Philosophical Transactions of the Royal Society of London. Series A, Mathematical and Physical Sciences,* 243**,** 299-358.

Carmona N., Herrero, E., Llopis, J. & Villegas, M. A. 2007. Chemical sol–gel-based sensors for evaluation of environmental humidity. *Sensors and Actuators B: Chemical,* 126**,** 455-460.

Carp O., Huisman, C. L. & Reller, A. 2004. Photoinduced reactivity of titanium dioxide. *Progress in Solid State Chemistry,* 32**,** 33-177.

Chen H., Yang, W., He, Y., Ding, Y., Zhang, L., Tan, C., Lapkin, A. A. & Bavykin, D. V. 2008. Heat transfer and flow behaviour of aqueous suspensions of titanate nanotubes (nanofluids). *Powder Technology,* 183**,** 63-72.

Chen X. & Mao, S. S. 2007. Titanium Dioxide Nanomaterials: Synthesis, Properties, Modifications, and Applications. *Chemical Reviews,* 107**,** 2891-2959.

Choi S. U.-S. 1998. *Nanofluid technology : current status and future research*.

Choi S. U. S., Zhang, Z. G., Yu, W., Lockwood, F. E. & Grulke, E. A. 2001. Anomalous thermal conductivity enhancement in nanotube suspensions. *Applied Physics Letters,* 79**,** 2252-2254.

Collins D. R., Smith, W., Harrison, N. M. & Forester, T. R. 1996. Molecular dynamics study of TiO_2 microclusters. *Journal of Materials Chemistry,* 6**,** 1385-1390.

Connolly M. 1983. Analytical molecular surface calculation. *Journal of Applied Crystallography,* 16**,** 548-558.

Das S. K., Putra, N., Thiesen, P. & Roetzel, W. 2003. Temperature dependence of thermal conductivity enhancement for nanofluids. *Transactions of the ASME. Journal of Heat Transfer,* 125**,** 567-74.

Diebold U. 2003. The surface science of titanium dioxide. *Surface Science Reports,* 48**,** 53-229.

Ding Y., Chen, H., Musina, Z., Jin, Y., Zhang, T., Witharana, S. & Yang, W. 2010. Relationship between the thermal conductivity and shear viscosity of nanofluids. *Physica Scripta,* T139 (2010).

Dobrushin R. L., Kotecký, R. & Shlosman, S. 1992. *Wulff Construction: A Global Shape from Local Interaction*, American Mathematical Society.

Docherty R. 1990. *Application of Bravais-Friedel-Donnay-Harker, Hartman-Perdok Attachment Energy and Ising Models to Predicting and Understanding the Morphology of Molecular Crystals*, Daresbury Laboratory.

Douglas B., Ho, Shi-Ming 2006. Structure and Chemistry of Crystalline Solids. *Springer*.

Dulub O., Valentin, C. D., Selloni, A. & Diebold, U. 2006. Structure, defects, and impurities at the rutile TiO_2 surface: A scanning tunneling microscopy study. *Surface Science,* 600**,** 4407-4417.

Dunphy Guzman K. A., Finnegan, M. P. & Banfield, J. F. 2006. Influence of Surface Potential on Aggregation and Transport of Titania Nanoparticles. *Environmental Science & Technology,* 40**,** 7688-7693.

Eapen J., Rusconi, R., Piazza, R. & Yip, S. 2010. The Classical Nature of Thermal Conduction in Nanofluids. *Journal of Heat Transfer,* 132**,** 102402-14.

Eastman J. A., Choi, U. S., Li, S., Thompson, L. J. & Lee, S. Enhanced thermal conductivity through the development of nanofluids. Proceedings of the 1996 MRS Fall Symposium, December 2, 1996 - December 5, 1996, 1997 Boston, MA, USA. Materials Research Society, 3-11.

Erdin S., Lin, Y., Halley, J. W., Zapol, P., Redfern, P. & Curtiss, L. 2007. Self-consistent tight binding molecular dynamics study of TiO_2 nanoclusters in water. *Journal of Electroanalytical Chemistry,* 607**,** 147-157.

Evans W., Prasher, R., Fish, J., Meakin, P., Phelan, P. & Keblinski, P. 2008. Effect of aggregation and interfacial thermal resistance on thermal conductivity of nanocomposites and colloidal nanofluids. *International Journal of Heat and Mass Transfer,* 51**,** 1431-1438.

Every A. G., Tzou, Y., Hasselman, D. P. H. & Raj, R. 1992. The effect of particle size on the thermal conductivity of ZnS/diamond composites. *Acta Metallurgica et Materialia,* 40**,** 123-129.

Feng Y., Yu, B., Xu, P. & Zou, M. 2007. The effective thermal conductivity of nanofluids based on the nanolayer and the aggregation of nanoparticles. *Journal of Physics D: Applied Physics* 40, 3164-3171.

Filyukov D., Brodskaya, E., Piotrovskaya, E. & de Leeuw, S. 2007. Molecular-dynamics simulation of nanoclusters of crystal modifications of titanium dioxide. *Russian Journal of General Chemistry,* 77**,** 10-16.

Franks A. 1987. Nanotechnology. *Journal of Physics E: Scientific Instruments,* 20**,** 1442.

Fujishima A., Rao, T. N. & Tryk, D. A. 2000. Titanium dioxide photocatalysis. *Journal of Photochemistry and Photobiology C: Photochemistry Reviews,* 1**,** 1-21.

Galasso F. S. 1970. *Structure and properties of inorganic solids,* Oxford; New York, Pergamon Press.

Gale J. & Rohl, A. 2003. The General Utility Lattice Program GULP. *Molecular Simulation,* 29(5):291-341.

Gao J.-c., Zou, J., Tan, X.-w. & Wang, Y. 2006. Characteristics and properties of surface coated nano-TiO_2. *Transactions of Nonferrous Metals Society of China,* 16**,** 1252-1258.

Garg P., Alvarado, J. L., Marsh, C., Carlson, T. A., Kessler, D. A. & Annamalai, K. 2009. An experimental study on the effect of ultrasonication on viscosity and heat transfer performance of multi-wall carbon nanotube-based aqueous nanofluids. *International Journal of Heat and Mass Transfer,* 52**,** 5090-5101.

Giessibl F. J. 2003. Advances in atomic force microscopy. *Reviews of Modern Physics,* 75**,** 949-83.

Grant F. A. 1959. Properties of Rutile (Titanium Dioxide). *Reviews of Modern Physics,* 31**,** 646.

Grimsditch M. H. & Ramdas, A. K. 1976. Elastic and elasto-optic constants of rutile from a Brillouin scattering study. *Physical Review B,* 14**,** 1670.

Guo Z. & Tan, L. 2009. *Fundamentals and Applications of Nanomaterials*, Artech House, Incorporated.

Gupta S. & Tripathi, M. 2011. A review of TiO_2 nanoparticles. *Chinese Science Bulletin,* 56**,** 1639-1657.

Hameeuw K. J., Cantele, G., Ninno, D., Trani, F. & Iadonisi, G. 2006. The rutile TiO_2 (110) surface: Obtaining converged structural properties from first-principles calculations. *The Journal of Chemical Physics,* 124**,** 024708.

Hamilton R. L. & Crosser, O. K. 1962. Thermal conductivity of hetrogeneous two-component systems. *Industrial & Engineering chemistry fundamentals,* 1**,** 187-191.

Hammond R. B., Pencheva, K. & Roberts, K. J. 2007. An examination of polymorphic stability and molecular conformational flexibility as a function of crystal size associated with the nucleation and growth of benzophenone. *Faraday Discuss,* 136**,** 91-106; discussion 107-23.

Han Y., Li, G. & Zhang, Z. 2006. Synthesis and optical properties of rutile TiO_2 microspheres composed of radially aligned nanorods. *Journal of Crystal Growth,* 295**,** 50-53.

Hart J. N., Cervini, R., Cheng, Y. B., Simon, G. P. & Spiccia, L. 2004. Formation of anatase TiO_2 by microwave processing. *Solar Energy Materials and Solar Cells,* 84**,** 135-143.

Hart J. N., Cheng, Y. B., Simon, G. P. & Spiccia, L. 2005. Challenges of producing TiO_2 films by microwave heating. *Surface and Coatings Technology,* 198**,** 20-23.

Hart J. N., Menzies, D., Cheng, Y.-B., Simon, G. P. & Spiccia, L. 2007. A comparison of microwave and conventional heat treatments of nanocrystalline TiO_2. *Solar Energy Materials and Solar Cells,* 91**,** 6-16.

Hartman P. & Bennema, P. 1980. The attachment energy as a habit controlling factor: I. Theoretical considerations. *Journal of Crystal Growth,* 49**,** 145-156.

Hartman P. & Perdok, W. G. 1955. On the relations between structure and morphology of crystals. I. *Acta Crystallographica,* 8**,** 49-52.

Haussühl S. 1974. P. Hartman (Ed.): Crystal Growth: An Introduction. North-Holland series in crystal growth Vol. 1. North-Holland Publishing Company, Amsterdam-London 1973. 531 S. *Berichte der Bunsengesellschaft für physikalische Chemie,* 78**,** 1276-1276.

Haverkamp R. G. 2010. A Decade of Nanoparticle Research in Australia and New Zealand. *Particulate Science and Technology: An International Journal,* 28**,** 1 - 40.

He Y., Jin, Y., Chen, H., Ding, Y., Cang, D. & Lu, H. 2007. Heat transfer and flow behaviour of aqueous suspensions of TiO_2 nanoparticles (nanofluids) flowing upward through a vertical pipe. *International Journal of Heat and Mass Transfer,* 50**,** 2272-2281.

Hengerer R., Kavan, L., Krtil, P. & Gratzel, M. 2000. Orientation dependence of charge-transfer processes on TiO_2 (anatase) single crystals. *Journal of the Electrochemical Society,* 147**,** 1467-1472.

Henrich V. E. 1983. The nature of transition-metal-oxide surfaces. *Progress in Surface Science,* 14**,** 175-199.

Henrich V. E. & Cox, P. A. 1994. *The Surface Science of Metal Oxides*, Cambridge University Press.

Herman G. S., Sievers, M. R. & Gao, Y. 2000. Structure Determination of the Two-Domain (1×4) Anatase TiO_2(001) Surface. *Physical Review Letters,* 84**,** 3354-3357.

Hermann K. 2011. *Crystallography and Surface Structure: An Introduction for Surface Scientists and Nanoscientists*, Wiley.

Hoang V. V. 2008. *The glass transition and thermodynamics of liquid and amorphous TiO_2 nanoparticles,* Bristol, ROYAUME-UNI, Institute of Physics.

Hong D. C., Havlin, S. & Stanley, H. E. 1985. Family of growth fractals with continuously tunable chemical dimension. *Journal of Physics A (Mathematical and General),* 18**,** 1103-7.

Horn M., Schwerdtfeger, C. F. & Meagher, E. P. 1972. Refinement of the structure of anatase at several temperatures*. *Zeitschrift für Kristallographie,* 136**,** 273-281.

Hu Y., Tsai, H. L. & Huang, C. L. 2003a. Phase transformation of precipitated TiO_2 nanoparticles. *Materials Science and Engineering A,* 344**,** 209-214.

Hu Y., Tsai, H. L. & Huang, C. L. 2003b. Phase transformation of precipitated TiO_2 nanoparticles. *Materials Science and Engineering: A,* 344**,** 209-214.

Hunter R. J. 2001. *Foundations of colloid science / Robert J. Hunter,* Oxford ; New York :, Oxford University Press.

Idriss H. & Barteau, M. A. 1996. Selectivity and mechanism shifts in the reactions of acetaldehyde on oxidized and reduced TiO_2(001) surfaces. *Catalysis Letters,* 40**,** 147-153.

Isaak D. G., Carnes, J. D., Anderson, O. L., Cynn, H. & Hake, E. 1998. Elasticity of TiO_2 rutile to 1800 K. *Physics and Chemistry of Minerals,* 26**,** 31-43.

Iuga M., Steinle-Neumann, G. & Meinhardt, J. 2007. Ab-initio simulation of elastic constants for some ceramic materials. *The European Physical Journal B - Condensed Matter and Complex Systems,* 58**,** 127-133.

Jagtap N., Bhagwat, M., Awati, P. & Ramaswamy, V. 2005. Characterization of nanocrystalline anatase titania: an in situ HTXRD study. *Thermochimica Acta,* 427**,** 37-41.

Jang S. P. & Choi, S. U. S. 2004. Role of Brownian motion in the enhanced thermal conductivity of nanofluids. *Applied physics letters,* 84**,** 4316-4318.

Jono K., Ichikawa, H., Miyamoto, M. & Fukumori, Y. 2000. A review of particulate design for pharmaceutical powders and their production by spouted bed coating. *Powder Technology,* 113**,** 269-277.

Jorgensen W. L. & Jenson, C. 1998. Temperature dependence of TIP3P, SPC, and TIP4P water from NPT Monte Carlo simulations: Seeking temperatures of maximum density. *Journal of Computational Chemistry,* 19**,** 1179-1186.

Keblinski P., Eastman, J. A. & Cahill, D. G. 2005. Nanofluids for thermal transport. *Materials Today,* 8**,** 36-44.

Keblinski P., Phillpot, S. R., Choi, S. U. S. & Eastman, J. A. 2002. Mechanisms of heat flow in suspensions of nano-sized particles (nanofluids). *International Journal of Heat and Mass Transfer,* 45**,** 855-863.

Kelly A., Groves, G. W. & Kidd, P. 2000. *Crystallography and Crystal Defects*, Wiley.

Kiejna A. & et al. 2006. The energetics and structure of rutile TiO_2 (110). *Journal of Physics: Condensed Matter,* 18**,** 4207.

Kim S. J., Bang, I. C., Buongiorno, J. & Hu, L. W. 2007. Surface wettability change during pool boiling of nanofluids and its effect on critical heat flux. *International Journal of Heat and Mass Transfer,* 50**,** 4105-4116.

Kirkby M. J. 1979. Fractals: Form, chance, and dimension, Benoit B. Mandelbrot, W. H. Freeman and Co., 1977. *Earth Surface Processes,* 4**,** 98-98.

Kittel C. 1971. *Introduction to solid state physics*, Wiley.

Klusek Z., Busiakiewicz, A. & Datta, P. K. 2006. Scanning tunnelling microscopy and spectroscopy of the reduced TiO_2 surface. *Surface Science,* 600**,** 1619-1623.

Kolb M., Botet, R. & Jullien, R. 1983. Scaling of Kinetically Growing Clusters. *Physical Review Letters,* 51**,** 1123.

Koo J. & Kleinstreuer, C. 2004. A new thermal conductivity model for nanofluids. *Journal of Nanoparticle research,* 6**,** 577-588.

Koparde V. N. & Cummings, P. T. 2005. Molecular Dynamics Simulation of Titanium Dioxide Nanoparticle Sintering. *The Journal of Physical Chemistry B,* 109**,** 24280-24287.

Koparde V. N. & Cummings, P. T. 2007. Molecular Dynamics Study of Water Adsorption on TiO_2 Nanoparticles. *The Journal of Physical Chemistry C,* 111**,** 6920-6926.

Koparde V. N. & Cummings, P. T. 2008. Phase Transformations during Sintering of Titania Nanoparticles. *ACS Nano,* 2**,** 1620-1624.

Kostov I. 1968. *Mineralogy*, Oliver & Boyd.

Kumar D. H., Patel, H. E., Kumar, V. R. R., Sundararajan, T., Pradeep, T. & Das, S. K. 2004. Model for heat conduction in nanofluids. *Physical Review Letters,* 93.

Larson I., Drummond, C. J., Chan, D. Y. C. & Grieser, F. 1993. Direct force measurements between titanium dioxide surfaces. *Journal of the American Chemical Society,* 115**,** 11885-11890.

Lazzeri M., Vittadini, A. & Selloni, A. 2001. Structure and energetics of stoichiometric TiO_2 anatase surfaces. *Physical Review B (Condensed Matter and Materials Physics),* 63**,** 155409/1-155409/9.

Lazzeri M., Vittadini, A. & Selloni, A. 2002. Erratum: Structure and energetics of stoichiometric TiO_2 anatase surfaces [Phys. Rev. B 63, 155409 (2001)]. *Physical Review B,* 65**,** 119901.

Leach A. 2001. *Molecular Modelling: Principles and Applications (2nd Edition)*, Prentice Hall.

Leach R. K. 2010. *Fundamental Principles of Engineering Nanometrology*, William Andrew.

Lee H., Lee, N., Seo, Y., Eom, J. & Lee, S. 2009. Comparison of frictional forces on graphene and graphite. *Nanotechnology,* 20**,** 325701.

Lee S., Choi, S. U. S., Li, S. & Eastman, J. A. 1999. Measuring thermal conductivity of fluids containing oxide nanoparticles. *Transactions of the ASME. Journal of Heat Transfer,* 121**,** 280-9.

Leong K. C., Yang, C. & Murshed, S. M. S. 2006. A model for the thermal conductivity of nanofluids - the effect of interfacial layer. *Journal of Nanoparticle research,* 8**,** 245-254.

Leung C., Bestembayeva, A., Thorogate, R., Stinson, J., Pyne, A., Marcovich, C., Yang, J., Drechsler, U., Despont, M., Jankowski, T., Tschöpe, M. & Hoogenboom, B. W. 2012. Atomic Force Microscopy with Nanoscale Cantilevers Resolves Different Structural Conformations of the DNA Double Helix. *Nano Letters,* 12**,** 3846-3850.

Li C. H. & Peterson, G. P. 2006. Experimental investigation of temperature and volume fraction variations on the effective thermal conductivity of nanoparticle suspensions (nanofluids). *Journal of Applied Physics,* 99, 1015-1031.

Li Y. X., Galatsis, K., Wlodarski, W., Passacantando, M., Santucci, S., Siciliano, P. & Catalano, M. 2001. Microstructural characterization of MoO_3-TiO_2 nanocomposite thin films for gas sensing. *Sensors and Actuators B: Chemical,* 77**,** 27-34.

Liang Y., Gan, S., Chambers, S. A. & Altman, E. I. 2001. Surface structure of anatase TiO_2(001): Reconstruction, atomic steps, and domains. *Physical Review B,* 63**,** 235402.

Linsebigler A. L., Lu, G. & Yates, J. T. 1995. Photocatalysis on TiO_2 Surfaces: Principles, Mechanisms, and Selected Results. *Chemical Reviews,* 95**,** 735-758.

Margolina A. 1985. The fractal dimension of cluster perimeters generated by a kinetic walk. *Journal of Physics A: Mathematical and General,* 18**,** L651.

Mark P. & Nilsson, L. 2001. Structure and Dynamics of the TIP3P, SPC, and SPC/E Water Models at 298 K. *The Journal of Physical Chemistry A,* 105**,** 9954-9960.

Matsui M. & Akaogi, M. 1991. Molecular Dynamics Simulation of the Structural and Physical Properties of the Four Polymorphs of TiO_2. *Molecular Simulation,* 6**,** 239-244.

Maxwell J. C. 1881. *A treatise on Electricity and Magnetism*, Clarendon Press, Oxford, UK.

Meakin P. 1983. Formation of Fractal Clusters and Networks by Irreversible Diffusion-Limited Aggregation. *Physical Review Letters,* 51**,** 1119.

Meakin P. 1987. Fractal aggregates. *Advances in Colloid and Interface Science,* 28**,** 249-331.

Mor G. K., Varghese, O. K., Paulose, M., Shankar, K. & Grimes, C. A. 2006. A review on highly ordered, vertically oriented TiO_2 nanotube arrays: Fabrication, material properties, and solar energy applications. *Solar Energy Materials and Solar Cells,* 90**,** 2011-2075.

Murshed S. M. S., Leong, K. C. & Yang, C. 2005. Enhanced thermal conductivity of TiO_2 - water based nanofluids. *International Journal of Thermal Sciences,* 44**,** 367-373.

Murshed S. M. S., Leong, K. C. & Yang, C. 2008. Thermophysical and electrokinetic properties of nanofluids - A critical review. *Applied Thermal Engineering,* 28**,** 2109-2125.

Naicker P. K., Cummings, P. T., Zhang, H. & Banfield, J. F. 2005. Characterization of Titanium Dioxide Nanoparticles Using Molecular Dynamics Simulations. *The Journal of Physical Chemistry B,* 109**,** 15243-15249.

Nan C. W., Birringer, R., Clarke, D. R. & Gleiter, H. 1997. Effective thermal conductivity of Particulate composites with inetrfacial themal resistance. *Journal of Applied Physics,* 81**,** 6692-6699.

Oh S. W., Park, S.-H. & Sun, Y.-K. 2006. Hydrothermal synthesis of nano-sized anatase TiO_2 powders for lithium secondary anode materials. *Journal of Power Sources,* 161**,** 1314-1318.

Okeke G., Hammond, R. & Antony, S. J. 2012. Analysis of Structural and Surface Properties of TiO_2 Nanoparticles in Water and Vacuum Using Molecular Dynamics Modeling and Simulations. *Journal of Nanofluids,* 1**,** 21-27.

Okeke G., Hammond, R. B. & Antony, S. J. 2013. Molecular Dynamics Simulation of Anatase TiO_2 Nanoparticles. *Journal of Nanoscience and Nanotechnology,* 13**,** 1047-1052.

Okeke G., Witharana, S., Antony, S. & Ding, Y. 2011. Computational analysis of factors influencing thermal conductivity of nanofluids. *Journal of Nanoparticle Research,* 13**,** 6365-6375.

Oliver P. M., Watson, G. W., Toby Kelsey, E. & Parker, S. C. 1997. Atomistic simulation of the surface structure of the TiO_2 polymorphs rutile and anatase. *Journal of Materials Chemistry,* 7**,** 563-568.

Ong Q. K. & Sokolov, I. 2007. Attachment of nanoparticles to the AFM tips for direct measurements of interaction between a single nanoparticle and surfaces. *Journal of Colloid and Interface Science,* 310**,** 385-390.

Ovenstone J. 2001. Preparation of novel titania photocatalysts with high activity. *Journal of Materials Science,* 36**,** 1325-1329.

Øye G., Glomm, W. R., Vrålstad, T., Volden, S., Magnusson, H., Stöcker, M. & Sjöblom, J. 2006. Synthesis, functionalisation and characterisation of mesoporous materials and sol–gel glasses for applications in catalysis, adsorption and photonics. *Advances in Colloid and Interface Science,* 123–126**,** 17-32.

Pak B. & Cho, Y. 1998. Hydrodynamic and heat transfer study of dispersed fluids with submicron metallic oxide particles. *Experimental Heat Transfer,* 11**,** 151-170.

Pallas N. R. & Pethica, B. A. 1983. The surface tension of water. *Colloids and Surfaces,* 6**,** 221-227.

Pang C. L., Lindsay, R. & Thornton, G. 2013. Structure of Clean and Adsorbate-Covered Single-Crystal Rutile TiO_2 Surfaces. *Chemical Reviews*.

Parker R. A. 1961. Static Dielectric Constant of Rutile TiO_2, *Physical Review,* 124**,** 1719.

Pettersson S. & Mahan, G. D. 1990. Theory of the thermal boundary resistance between dissimilar lattices. *Physical Review B (Condensed Matter),* 42**,** 7386-90.

Pitchumani R. & Yao, S. C. 1991. Correlation of thermal conductivities of unidirectional fibrous composites using local fractal techniques. *Journal Name: Journal of Heat Transfer (Transactions of the ASME (American Society of Mechanical Engineers), Series C); (United States); Journal Volume: 113:4***,** Medium: X; Size: Pages: 788-796.

Prasher R., Bhattacharya, P. & Phelan, P. E. 2005. Thermal conductivity of nanoscale colloidal solutions (nanofluids). *Physical Review Letters,* 94, 025901-1 - 025901-4.

Prasher R., Bhattacharya, P. & Phelan, P. E. 2006a. Brownian-motion-based convective-conductive model for the effective thermal conductivity of nanofluids. *Journal of Heat Transfer-Transactions of the Asme,* 128**,** 588-595.

Prasher R., Evans, W., Meakin, P., Fish, J., Phelan, P. & Keblinski, P. 2006b. Effect of aggregation on thermal conduction in colloidal nanofluids. *Applied physics letters,* 89, 1431-1438.

Prasher R., Phelan, P. E. & Bhattacharya, P. 2006c. Effect of Aggregation Kinetics on the Thermal Conductivity of Nanoscale Colloidal Solutions (Nanofluid). *Nano Letters,* 6**,** 1529-1534.

Předota M., Zhang, Z., Fenter, P., Wesolowski, D. J. & Cummings, P. T. 2004. Electric Double Layer at the Rutile (110) Surface. 2. Adsorption of Ions from Molecular Dynamics and X-ray Experiments. *The Journal of Physical Chemistry B,* 108**,** 12061-12072.

Prywer J. 2004. Explanation of some peculiarities of crystal morphology deduced from the BFDH law. *Journal of Crystal Growth,* 270**,** 699-710.

Putnam S. A., Cahill, D. G., Braun, P. V., Ge, Z. B. & Shimmin, R. G. 2006. Thermal conductivity of nanoparticle suspensions. *Journal of Applied Physics,* 99, 084508-1 - 084308-6.

R. Collins D., Smith, W., M. Harrison, N. & R. Forester, T. 1997. Molecular dynamics study of the high temperature fusion of TiO_2 nanoclusters. *Journal of Materials Chemistry,* 7**,** 2543-2546.

Ramamoorthy M., Vanderbilt, D. & King-Smith, R. D. 1994a. First-principles calculations of the energetics of stoichiometric TiO_2 surfaces. *Physical Review B,* 49**,** 16721.

Ramamoorthy M., Vanderbilt, D. & Smith, K. 1994b. First-principles calculations of the energetics of stoichiometric TiO_2 surfaces. *Physical Review B,* 49**,** 16721-16727.

Ramirez-Garcia S., Chen, L., Morris, M. A. & Dawson, K. A. 2011. A new methodology for studying nanoparticle interactions in biological systems: dispersing titania in biocompatible media using chemical stabilisers. *Nanoscale,* 3**,** 4617-24.

Ranade M. R., Navrotsky, A., Zhang, H. Z., Banfield, J. F., Elder, S. H., Zaban, A., Borse, P. H., Kulkarni, S. K., Doran, G. S. & Whitfield, H. J. 2002. Energetics of nanocrystalline TiO_2. *Proceedings of the National Academy of Sciences of the United States of America,* 99**,** 6476-6481.

Raza H., Pang, C. L., Haycock, S. A. & Thornton, G. 1999. Non-contact atomic force microscopy imaging of TiO_2(100) surfaces. *Applied Surface Science,* 140**,** 271-275.

Remy H. 1956. *Treatise on Inorganic Chemistry: Introduction and main groups of the periodic table*, Elsevier Publishing Company.

Ren Y., Xie, H. & Cai, A. 2005. Effective thermal conductivity of nanofluids containing spherical nanoparticles. *Journal of Physics D-Applied Physics,* 38**,** 3958-3961.

Reyes-Coronado D., Rodr, iacute, guez-Gattorno, G., Espinosa-Pesqueira, M. E., Cab, C., de Coss, R. & Oskam, G. 2008. *Phase-pure TiO_2 nanoparticles: anatase, brookite and rutile*.

Ribeiro C., Vila, C., Milton Elias de Matos, J., Bettini, J., Longo, E. & Leite, E. R. 2007. Role of the Oriented Attachment Mechanism in the Phase Transformation of Oxide Nanocrystals. *Chemistry – A European Journal,* 13**,** 5798-5803.

Roosen A. R., McCormack, R. P. & Carter, W. C. 1998. Wulffman: A tool for the calculation and display of crystal shapes. *Computational Materials Science,* 11**,** 16-26.

Salameh S., Schneider, J., Laube, J., Alessandrini, A., Facci, P., Seo, J. W., Ciacchi, L. C. & Mädler, L. 2012. Adhesion Mechanisms of the Contact Interface of TiO_2 Nanoparticles in Films and Aggregates. *Langmuir,* 28**,** 11457-11464.

Schaak R. E. 2006. Structure and Chemistry of Crystalline Solids By Bodie E. Douglas and Shih-Ming Ho (University of Pittsburgh). Springer Science + Business Media, Inc.: New York. 2006. ISBN 0-387-26147-8. *Journal of the American Chemical Society,* 129**,** 451-452.

Schneider J. & Ciacchi, L. C. 2010. First principles and classical modeling of the oxidized titanium (001) surface. *Surface Science,* 604**,** 1105-1115.

Segall M. D., Lindan, P. J. D., Probert, M. J., Pickard, C. J., Hasnip, P. J., Clark, S. J. & Payne, M. C. 2002. First-principles simulation: ideas, illustrations and the CASTEP code. *Journal of Physics: Condensed Matter,* 14**,** 2717.

Seo Y. & Jhe, W. 2008. Atomic force microscopy and spectroscopy. *Reports on Progress in Physics,* 71.

Shahini S., Askari, M. & Sadrnezhaad, S. K. 2011. Gel–sol synthesis and aging effect on highly crystalline anatase nanopowder. *Bulletin of Materials Science,* 34**,** 1189-1195.

Shepard M. K., Brackett, R. A. & Arvidson, R. E. 1995. Self-affine (fractal) topography: Surface parameterization and radar scattering. *Journal of Geophysical Research: Planets,* 100**,** 11709-11718.

Shuttleworth R. 1950. The Surface Tension of Solids. *Proceedings of the Physical Society. Section A,* 63**,** 444.

Singh M. R. & Ramkrishna, D. 2013. A Comprehensive Approach to Predicting Crystal Morphology Distributions with Population Balances. *Crystal Growth & Design,* 13**,** 1397-1411.

Skaarup S., West, K., Zachau-Christiansen, B., Popall, M., Kappel, J., Kron, J., Eichinger, G. & Semrau, G. 1998. Towards solid state lithium batteries based on ORMOCER electrolytes. *Electrochimica Acta,* 43**,** 1589-1592.

Smith W. 1987. The computer simulation of liquids by molecular dynamics. *Physics Education,* 22**,** 355-9.

Smith W. & Forester, T. R. 1996. DL_POLY_2.0: A general-purpose parallel molecular dynamics simulation package. *Journal of Molecular Graphics,* 14**,** 136-141.

Smith W., Forester, T. R. & Todorov, I. T. 2010. The DL_POLY_2 User Manual. *STFC Daresbury Laboratory,* Version 2.21.

Song D.-P., Liang, Y.-C., Chen, M.-J. & Bai, Q.-S. 2009. Molecular dynamics study on surface structure and surface energy of rutile TiO_2 (1 1 0). *Applied Surface Science,* 255**,** 5702-5708.

Soo-Jin Park Y. C. K., Ju Y. Park, Ed A. Evans, Rex D. Ramsier, and George G. Chase 2010. Physical Characteristics of Titania Nanofibers Synthesized by Sol-Gel and Electrospinning Techniques. *Journal of Engineered Fibers and Fabrics,* 5**,** 50-56.

Stephan K. 1985. Heat transfer fluids and systems for process and energy applications. Von J. Singh. Marcel Dekker, Inc., New York–Basel 1985. 1. Aufl., VII, 283 S., zahlr. Abb. u. Tab., geb. *Chemie Ingenieur Technik,* 57**,** 792-792.

Su C., Hong, B. Y. & Tseng, C. M. 2004. Sol–gel preparation and photocatalysis of titanium dioxide. *Catalysis Today,* 96**,** 119-126.

Subba Rao, V.;, K., Zhuo, B., Cox, J. M., Chiang, K., Brungs, M. & Amal, R. 2006. Photoinduced Bactericidal Properties of Nanocrystalline TiO_2 Thin Films. *Journal of Biomedical Nanotechnology,* 2**,** 71-73.

Sun Z. H., Wang, X. X. & Wu, H. A. 2008. Surface relaxation effect on the distributions of energy and bulk stresses in the vicinity of Cu surface: An embedded-atom method study. *Journal of Applied Physics,* 104**,** 033501.

Sunagawa I. 2005. *Crystals: Growth, Morphology, & Perfection*, Cambridge University Press.

Swamy V. & Dubrovinsky, L. S. 2001. Bulk modulus of anatase. *Journal of Physics and Chemistry of Solids,* 62**,** 673-675.

Swamy V., Gale, J. D. & Dubrovinsky, L. S. 2001. Atomistic simulation of the crystal structures and bulk moduli of TiO_2 polymorphs. *Journal of the Physics and Chemistry of Solids,* 62**,** 887-95.

Swartz E. T. & Pohl, R. O. 1989. Thermal boundary resistance. *Reviews of Modern Physics,* 61**,** 605-68.

Syrkin I. A. K. & D͡iatkina, E. 1950. *Structure of Molecules and the Chemical Bond*, Interscience Publishers.

Tang H., Berger, H., Schmid, P. E., Lévy, F. & Burri, G. 1993. Photoluminescence in TiO_2 anatase single crystals. *Solid State Communications,* 87**,** 847-850.

Tanner R. E., Sasahara, A., Liang, Y., Altman, E. I. & Onishi, H. 2002. Formic Acid Adsorption on Anatase TiO_2(001)−(1×4) Thin Films Studied by NC-AFM and STM†. *The Journal of Physical Chemistry B,* 106**,** 8211-8222.

Tao N., Zhao, J., Guo, Y., Jiang, Y., Ding, X. & Wang, Z. 2004. Preparation and characteristics of core-shell rutile titania/wollastonite at room temperature. *Materials Chemistry and Physics,* 84**,** 58-62.

Tasker P. W. 1979. The stability of ionic crystal surfaces. *Journal of Physics C: Solid State Physics,* 12**,** 4977.

Tersoff J. 1989. Modeling solid-state chemistry: Interatomic potentials for multicomponent systems. *Physical Review B,* 39**,** 5566-5568.

Testino A., Bellobono, I. R., Buscaglia, V., Canevali, C., D'Arienzo, M., Polizzi, S., Scotti, R. & Morazzoni, F. 2007. Optimizing the Photocatalytic Properties of Hydrothermal TiO_2 by the Control of Phase Composition and Particle Morphology. A Systematic Approach. *Journal of the American Chemical Society,* 129**,** 3564-3575.

Thompson T. L. & Yates, J. T. 2006. Surface Science Studies of the Photoactivation of TiO_2 New Photochemical Processes. *Chemical Reviews,* 106**,** 4428-4453.

Vittadini A., Selloni, A., Rotzinger, F. P. & Grätzel, M. 1998. Structure and Energetics of Water Adsorbed at TiO_2 Anatase (101) and (001) Surfaces. *Physical Review Letters,* 81**,** 2954-2957.

Wadell H. 1935. *Volume, Shape, and Roundness of Quartz Particles*, University of Chicago.

Waite T. D., Cleaver, J. K. & Beattie, J. K. 2001. Aggregation Kinetics and Fractal Structure of [gamma]-Alumina Assemblages. *Journal of Colloid and Interface Science,* 241**,** 333-339.

Wang B.-X., Zhou, L.-P. & Peng, X.-F. 2003. A fractal model for predicting the effective thermal conductivity of liquid with suspension of nanoparticles. *International Journal of Heat and Mass Transfer,* 46**,** 2665-2672.

Wang J., Han, X., Liu, C., Zhang, W., Cai, R. & Liu, Z. 2010. Adjusting the Crystal Phase and Morphology of Titania via a Soft Chemical Process. *Crystal Growth & Design,* 10**,** 2185-2191.

Wang X.-Q. & Mujumdar, A. S. 2007. Heat transfer characteristics of nanofluids: a review. *International Journal of Thermal Sciences,* 46**,** 1-19.

Watson G. W., Kelsey, E. T., de Leeuw, N. H., Harris, D. J. & Parker, S. C. 1996. Atomistic simulation of dislocations, surfaces and interfaces in MgO. *Journal of the Chemical Society, Faraday Transactions,* 92**,** 433-438.

Wen D., Lin, G., Vafaei, S. & Zhang, K. 2009. Review of nanofluids for heat transfer applications. *Particuology,* 7**,** 141-150.

Wen D. S. & Ding, Y. L. 2004. Experimental investigation into convective heat transfer of nanofluids at the entrance region under laminar flow conditions. *International Journal of Heat and Mass Transfer,* 47**,** 5181-5188.

Wen D. S. & Ding, Y. L. 2005. Experimental investigation into the pool boiling heat transfer of aqueous based gamma-alumina nanofluids. *Journal of Nanoparticle research,* 7**,** 265-274.

Wen D. S., Ding, Y. L. & Williams, R. A. 2006. Pool boiling heat transfer of aqueous TiO2-based nanofluids. *Journal of enhanced heat transfer,* 13**,** 231-244.

Westbrook J. H. & Fleischer, R. L. 2000. Intermetallic Compounds, Volume 2 - Basic Mechanical Properties and Lattice Defects of Intermetallic Compounds. John Wiley & Sons.

Witharana S., Haisheng, C., Musina, Z., Ding, Y. & Yi, J. Shear stability and thermophysical properties of titania nanofluids. Information and Automation for Sustainability (ICIAFs), 2010 5th International Conference on, 17-19 Dec. 2010 2010. 555-559.

Wong K.-F. V. & Kurma, T. 2008. Transport properties of alumina nanofluids. *Nanotechnology,* 19**,** 345702.

Xie H., Fujii, M. & Zhang, X. 2005. Effect of interfacial nanolayer on the effective thermal conductivity of nanoparticle-fluid mixture. *International Journal of Heat and Mass Transfer,* 48**,** 2926-2932.

Xuan Y. & Li, Q. 2000. Heat transfer enhancement of nanofluids. *International Journal of Heat and Fluid flow,* 21**,** 58-64.

Xuan Y., Li, Q. & Hu, W. 2003. Aggregation structure and thermal conductivity of nanofluids. *AIChE Journal,* 49**,** 1038-1043.

Yang J., Mei, S. & Ferreira, J. M. F. 2001. Hydrothermal Synthesis of Nanosized Titania Powders: Influence of Tetraalkyl Ammonium Hydroxides on Particle Characteristics. *Journal of the American Ceramic Society,* 84**,** 1696-1702.

Yong C. W., Smith, W. & Kendall, K. 2002. Investigation of contact interactions of (001) MgO: molecular dynamics simulations studies. *Journal of Materials Chemistry,* 12**,** 593-601.

Yoo D.-H., Hong, K. S. & Yang, H.-S. 2007. Study of thermal conductivity of nanofluids for the application of heat transfer fluids. *Thermochimica Acta,* 455**,** 66-69.

Young D. A. & Maris, H. J. 1989. Lattice-dynamical calculation of the Kapitza resistance between FCC lattices. *Physical Review B (Condensed Matter),* 40**,** 3685-93.

Zhang H. & Banfield, J. F. 2000. Understanding Polymorphic Phase Transformation Behavior during Growth of Nanocrystalline Aggregates: Insights from TiO_2. *The Journal of Physical Chemistry B,* 104**,** 3481-3487.

Zhang H., Chen, B., Banfield, J. F. & Waychunas, G. A. 2008. Atomic structure of nanometer-sized amorphous TiO_2. *Physical Review B,* 78**,** 214106.

Zhang H. & F. Banfield, J. 1998. Thermodynamic analysis of phase stability of nanocrystalline titania. *Journal of Materials Chemistry,* 8**,** 2073-2076.

Zhang X., Gu, H. & Fujii, M. 2006. Experimental study on the effective thermal conductivity and thermal diffusivity of nanofluids. *International Journal of Thermophysics,* 27**,** 569-80.

Zhu S., Jiang, B. & Cao, W. Characterization of piezoelectric materials using ultrasonic and resonant techniques. 1998. 154-162.

Zhuiykov S., Wlodarski, W. & Li, Y. 2001. Nanocrystalline V_2O_5-TiO_2 thin-films for oxygen sensing prepared by sol-gel process. *Sensors and Actuators B: Chemical,* 77**,** 484-490.

List of Publications

Okeke, G., Hammond, R. & Joseph Antony, S. 2013. Computational Studies on the effects of different phases of $\mathrm{TiO_2}$ nanoparticles on their thermo-physical properties. *To be submitted to Journal of Nanoparticle Research*

Okeke, G., Hammond, R. & Joseph Antony, S. 2013. Influence of size and temperature on the phase stability and thermophysical properties of anatase $\mathrm{TiO_2}$ nanoparticles: molecular dynamics simulation. *Journal of Nanoparticle Research,* 15**,** 1-9.

Okeke, G., Hammond, R. B. & Antony, S. J. 2013. Molecular Dynamics Simulation of Anatase $\mathrm{TiO_2}$ Nanoparticles. *Journal of Nanoscience and Nanotechnology,* 13**,** 1047-1052.

Okeke, G., Hammond, R. B. & Antony, S. J. 2012. Molecular Dynamics Study of Antase $\mathrm{TiO_2}$ Nanoparticles in Water. *Proceedings of the ASME 2012 International Mechanical Engineering Congress & Exposition, Texas, USA.*

Okeke, G., Hammond, R. & Antony, S. J. 2012. Analysis of Structural and Surface Properties of $\mathrm{TiO_2}$ Nanoparticles in Water and Vacuum Using Molecular Dynamics Modeling and Simulations. *Journal of Nanofluids,* 1**,** 21-27.

Okeke, G., Hammond, R. & Antony, S. J. 2011. Molecular Dynamics Simulation of Anatase $\mathrm{TiO_2}$ nanoparticles. *International Conference on Nanoscience & Technology, China 2011.*

Okeke G., Witharana, S., Antony, S. & Ding, Y. 2011. Computational analysis of factors influencing thermal conductivity of nanofluids. *Journal of Nanoparticle Research,* 13**,** 6365-6375.

Amanbayev, T., Okeke, G., Afzal, M. & Antony, S. J. 2010. Modelling of Bacterial Growth in Nano Liquids. *Proceedings of the Seventh International Conference on Engineering Computational Technology. Civil-Comp Press, Stirlingshire, UK, Paper 118.*

Okeke, G., Witharana, S., Antony, S. & Ding, Y. 2009. A Sensitivity Analysis of Factors Influencing Thermal Conductivity of Nanofluids. *UKHTC 2009. The Eleventh UK National Heat Transfer Conference, London, UK.*

A. Appendix A

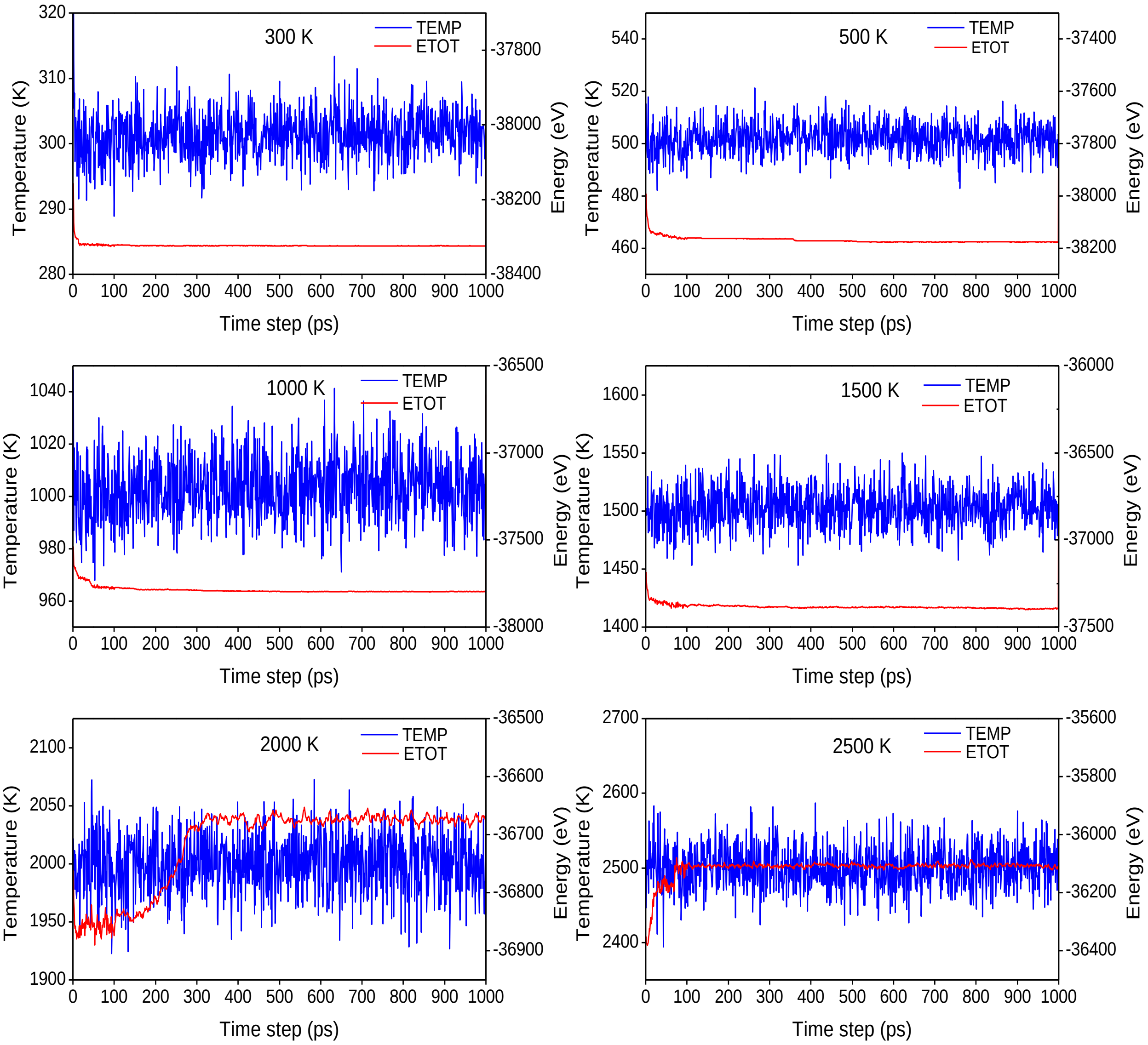

Figure A.1 Temperature and Total Energy (ETOT) plotted against time for 4nm anatase TiO_2 nanoparticles

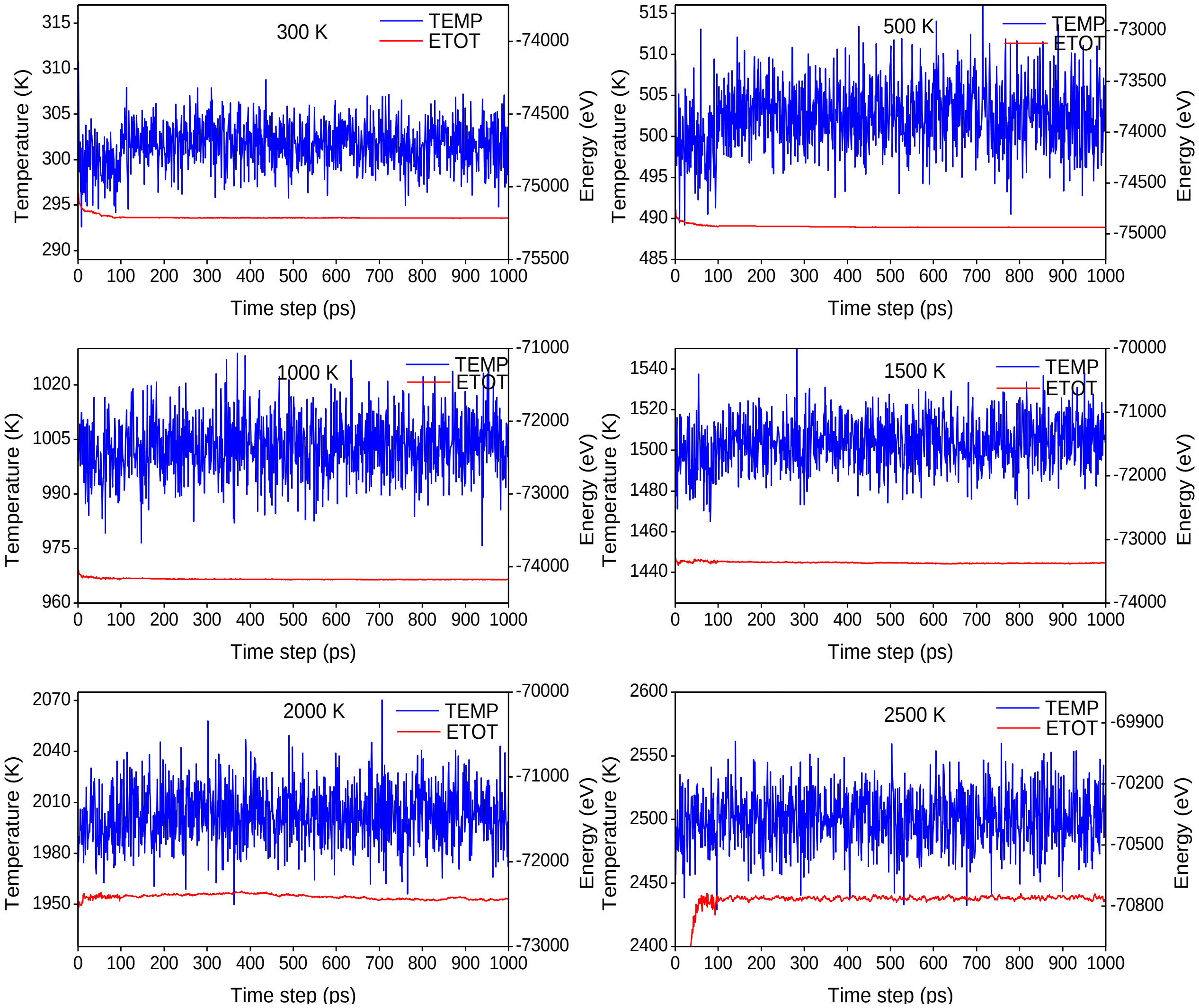

Figure A.2 Temperature and Total Energy (ETOT) plotted against time for 5nm anatase TiO_2 nanoparticles

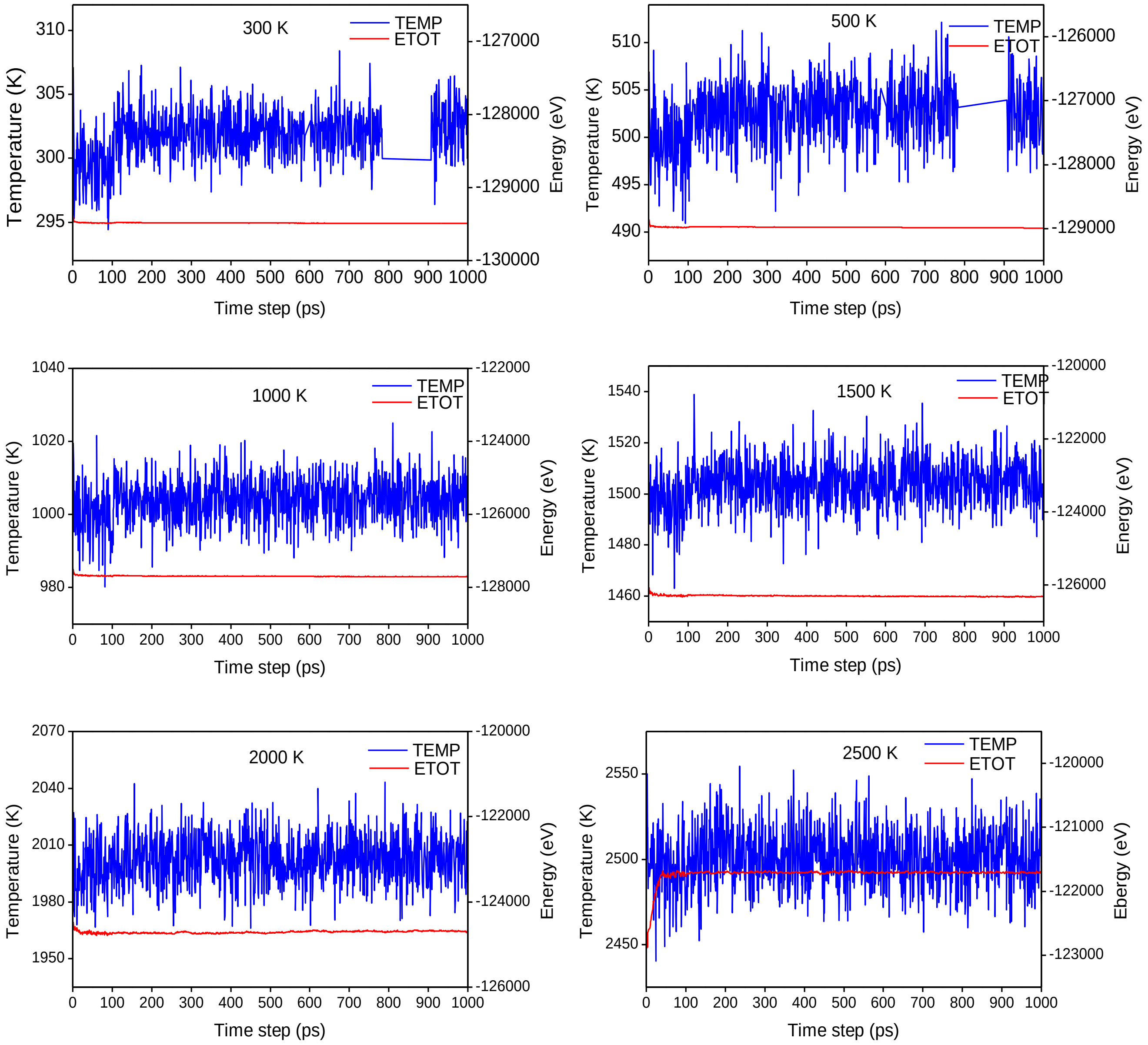

Figure A.3 Temperature and Total Energy (ETOT) plotted against time for 6nm anatase TiO_2 nanoparticles

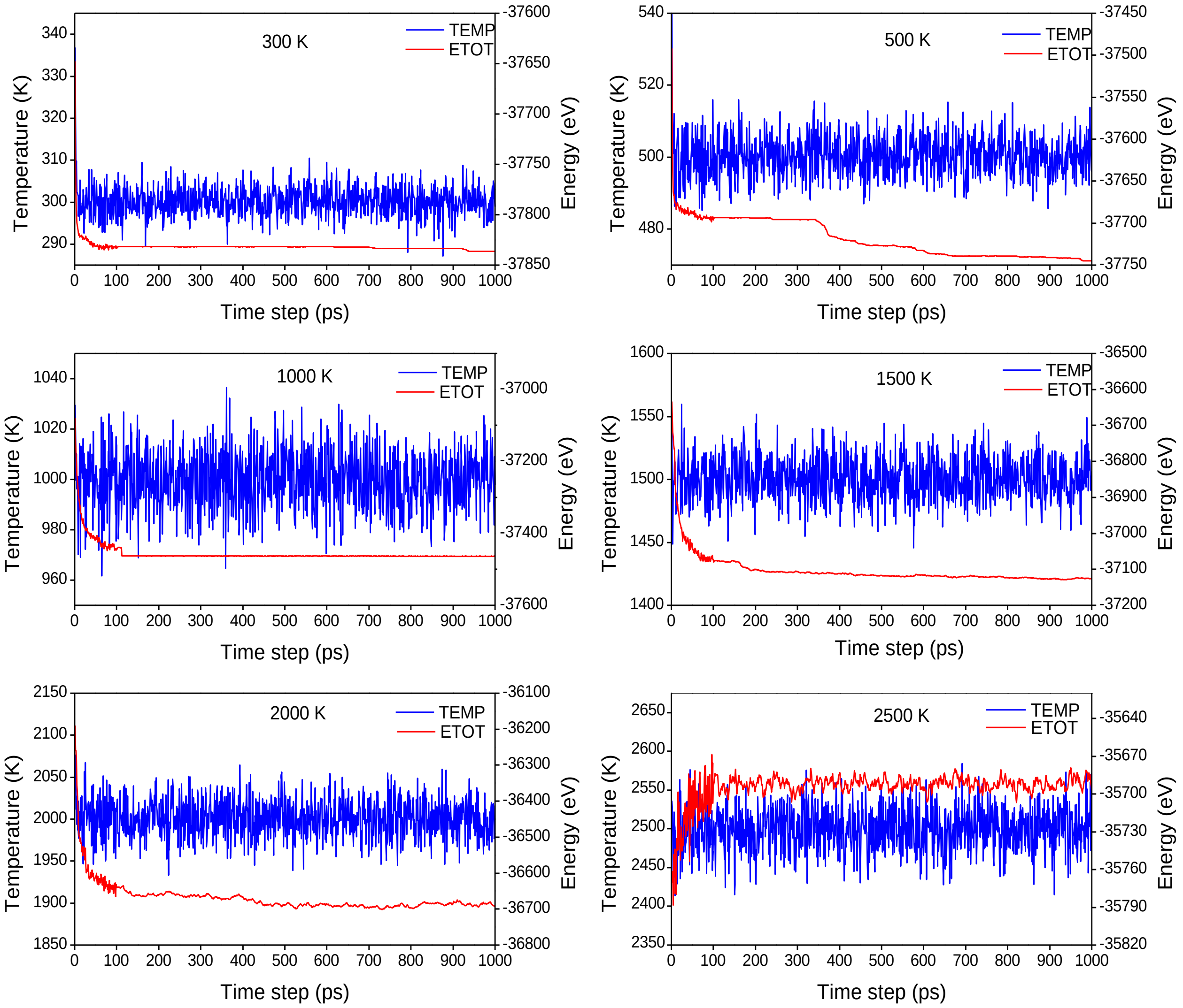

Figure A.4 Temperature and Total Energy (ETOT) plotted against time for 4nm rutile TiO_2 nanoparticles

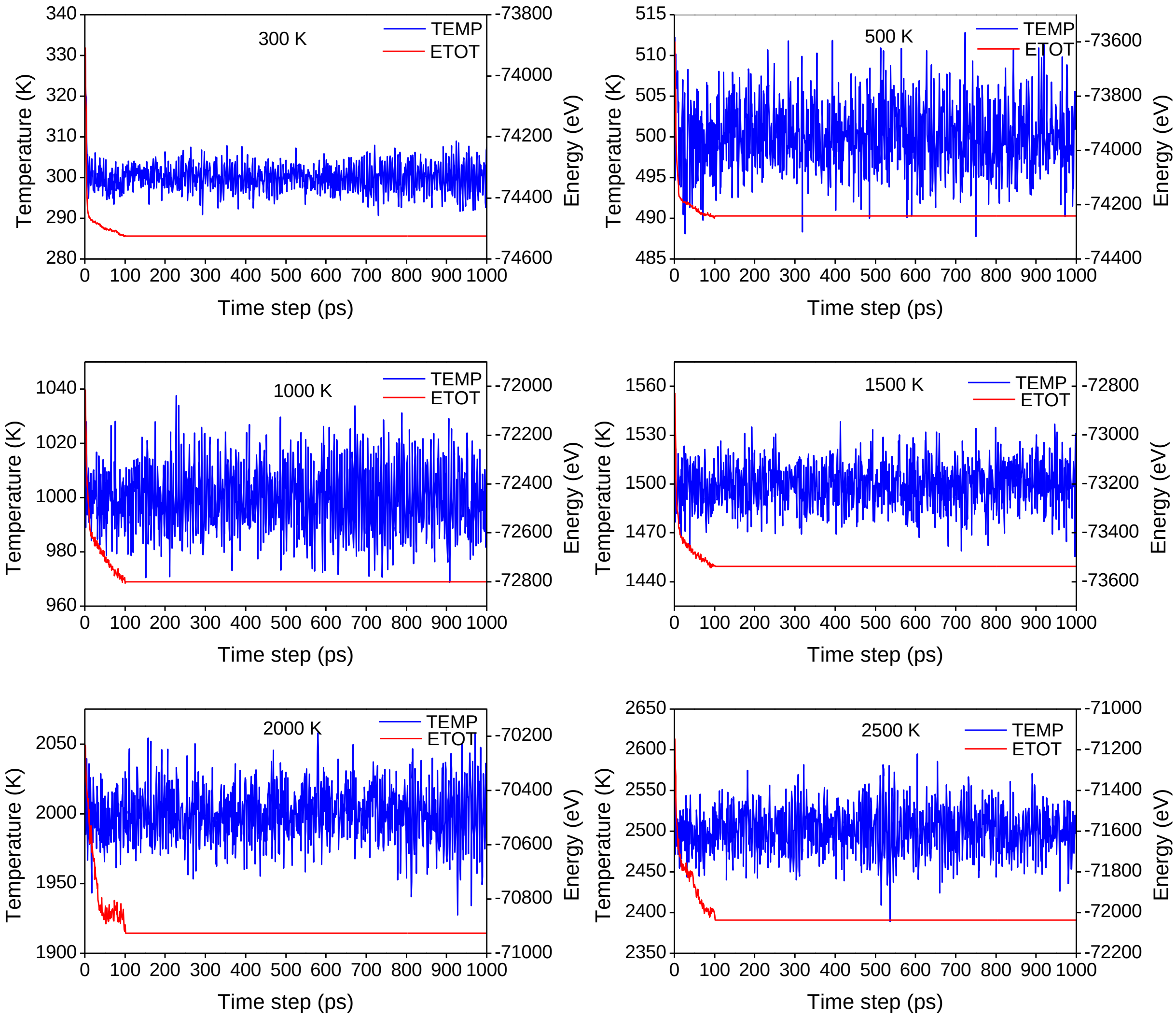

Figure A.5 Temperature and Total Energy (ETOT) plotted against time for 5nm rutile TiO_2 nanoparticles

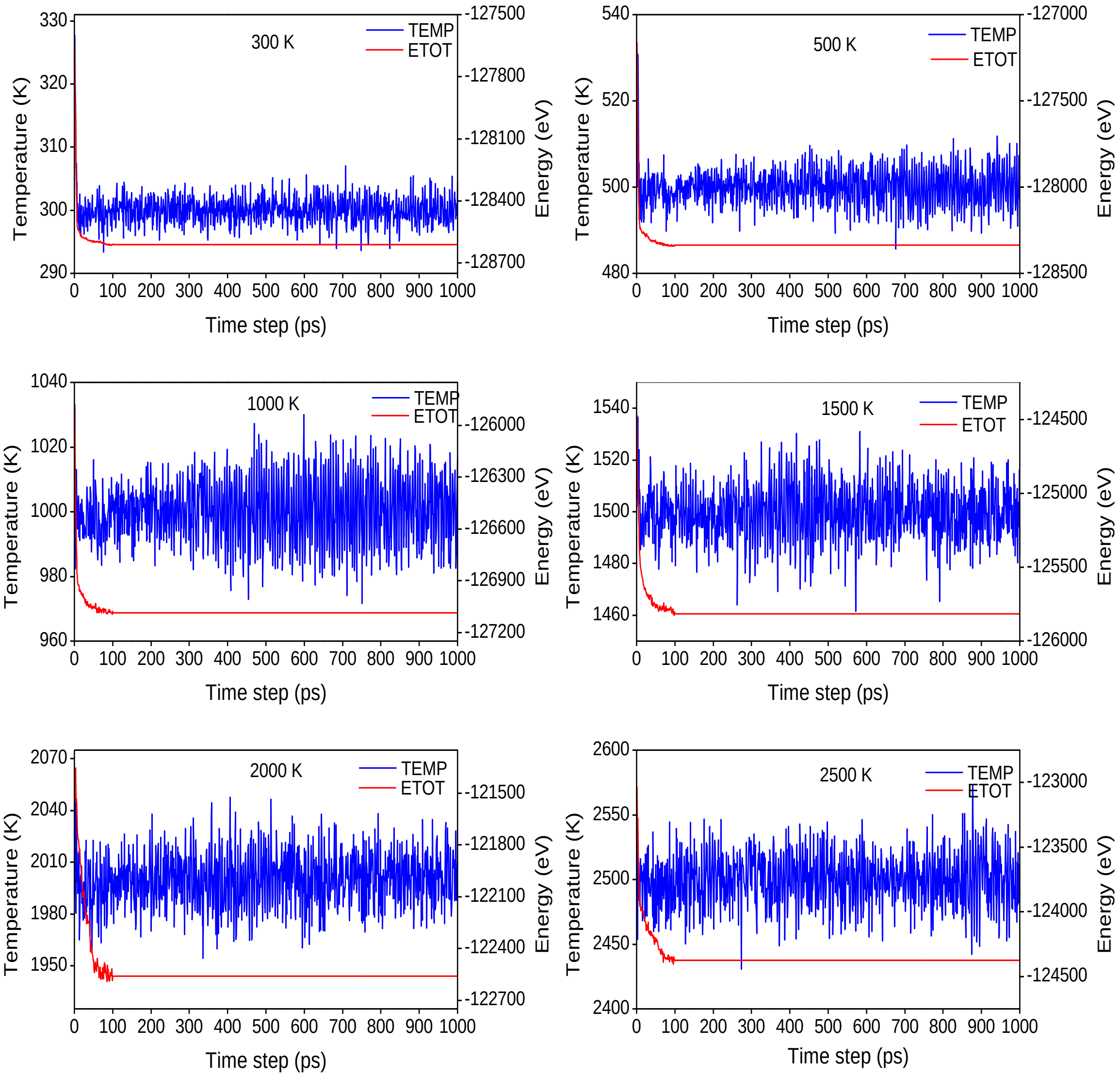

Figure A.6 Temperature and Total Energy (ETOT) plotted against time for 6nm rutile TiO_2 nanoparticles

B. Appendix B

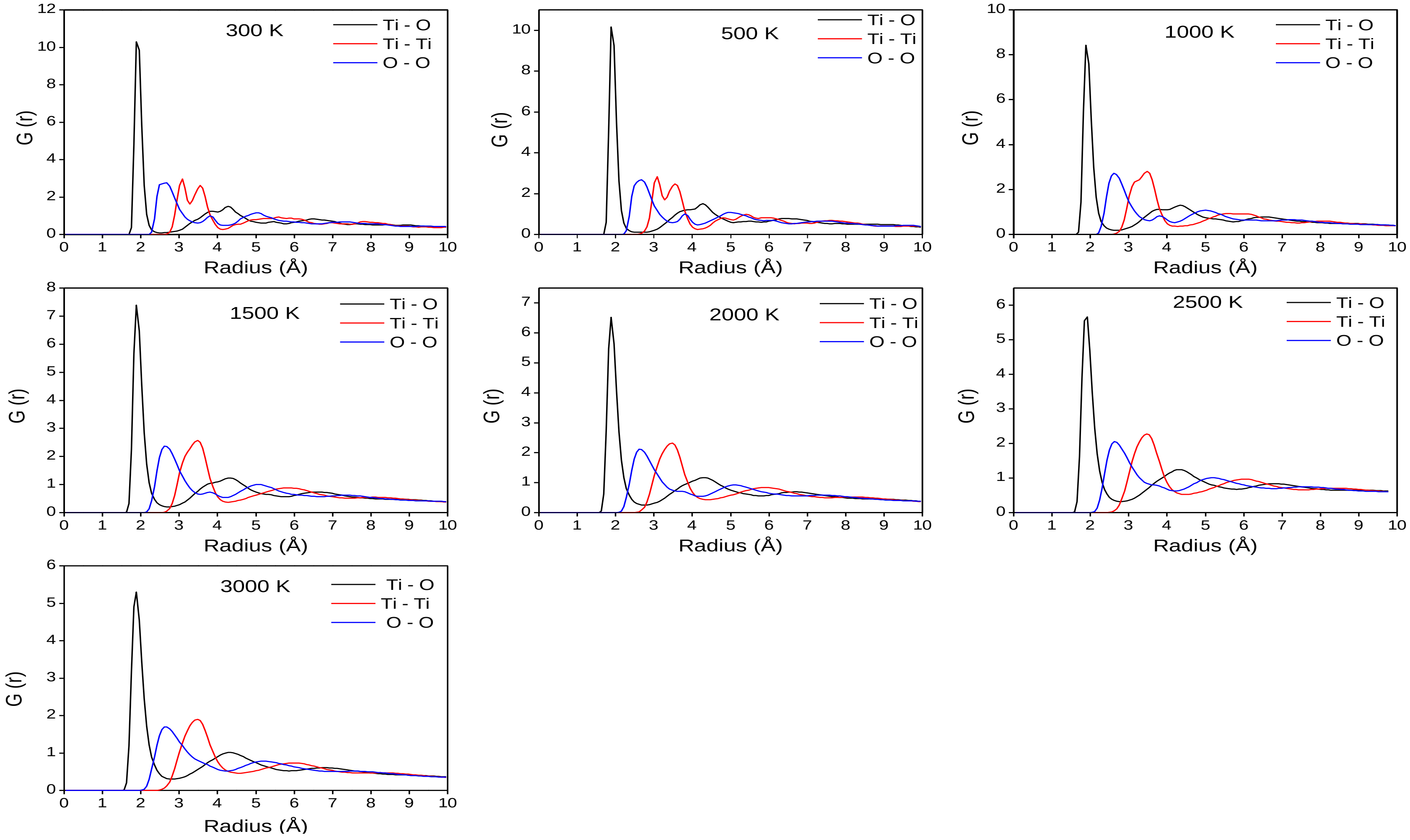

Figure B.1 RDF’s for anatase Ti – Ti, Ti – O and O – O pairs for 3 nm

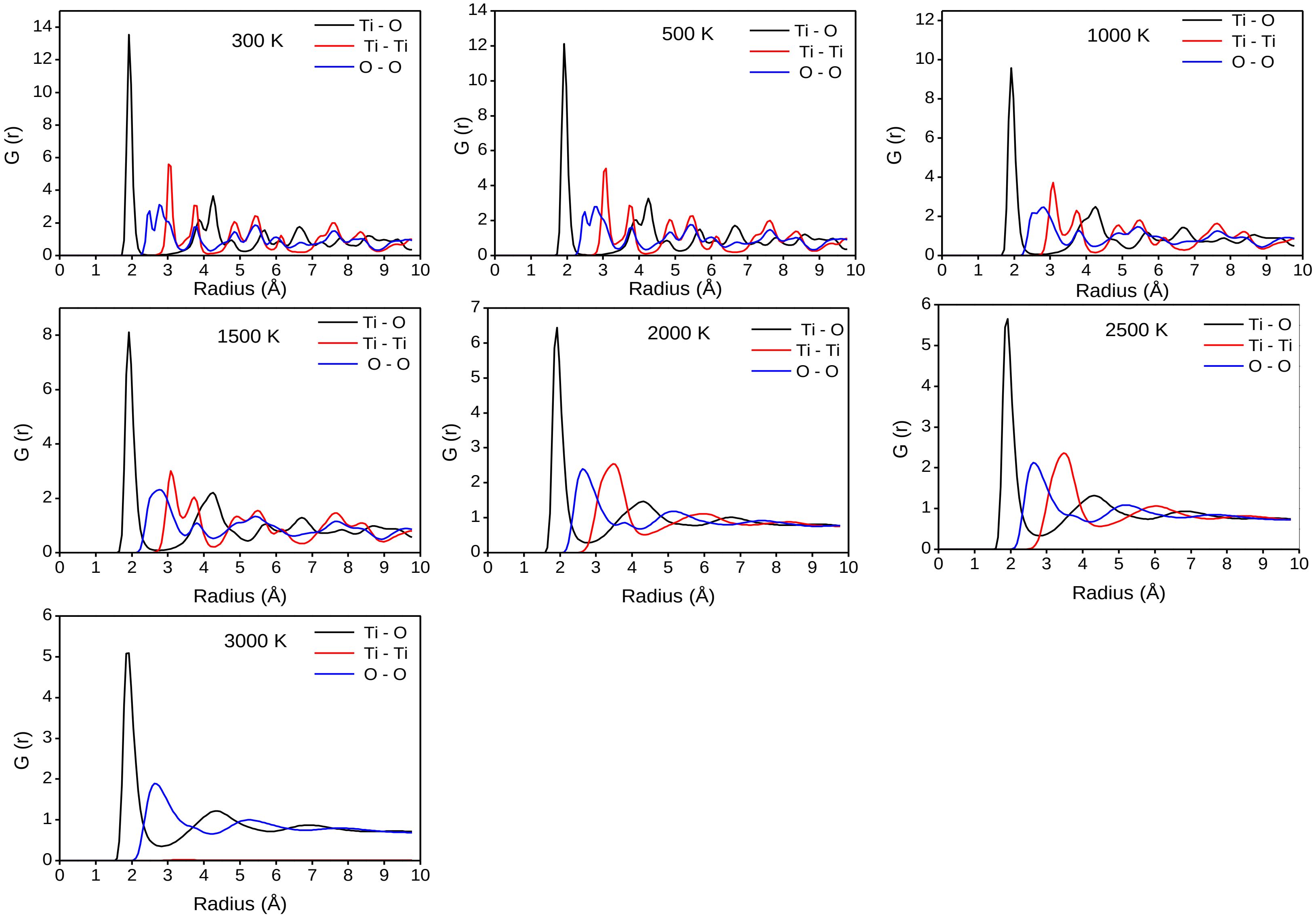

Figure B.2 RDF's for anatase Ti – Ti, Ti – O and O – O pairs for 4 nm

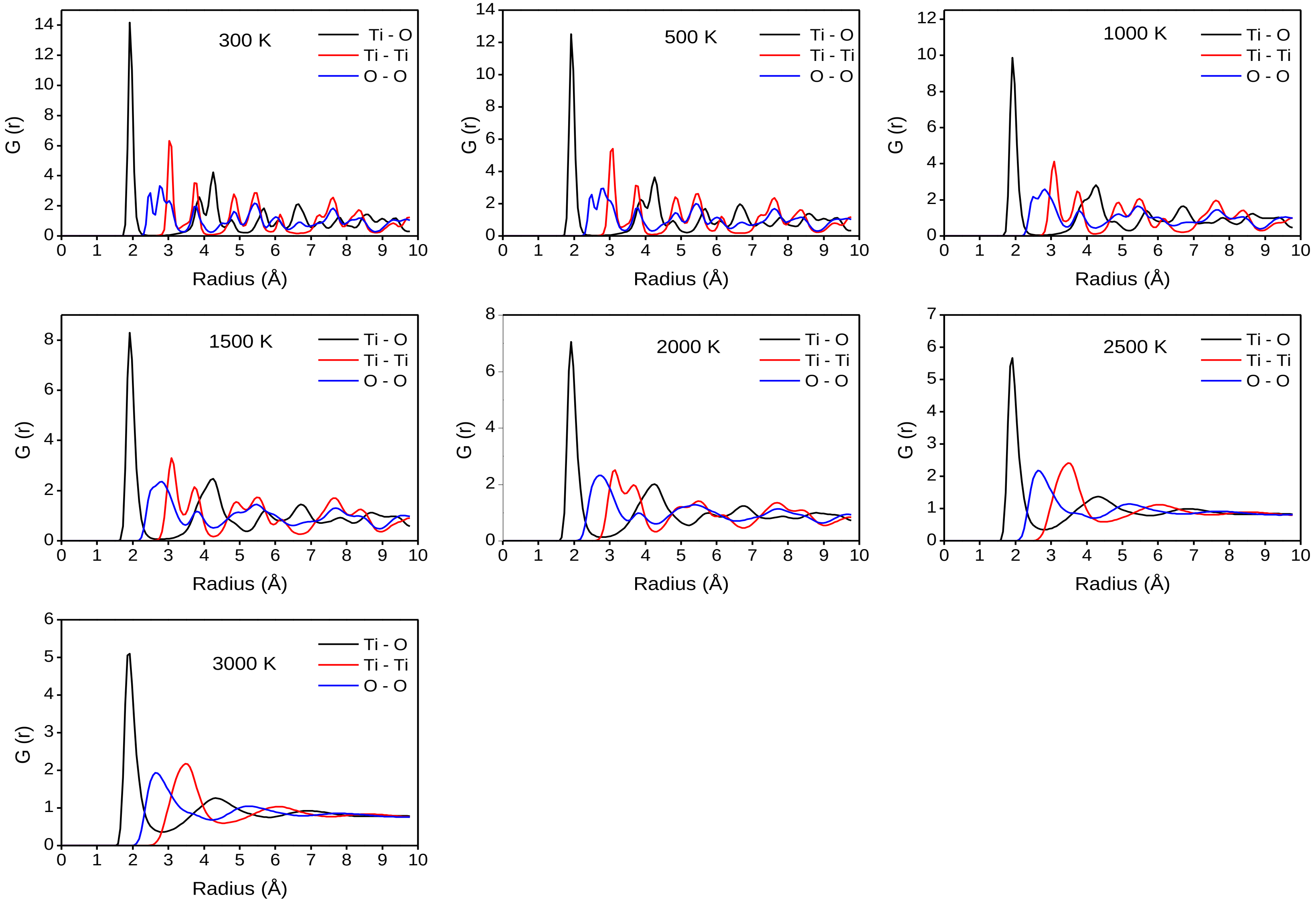

Figure B.3 RDF's for anatase Ti – Ti, Ti – O and O – O pairs for 5 nm

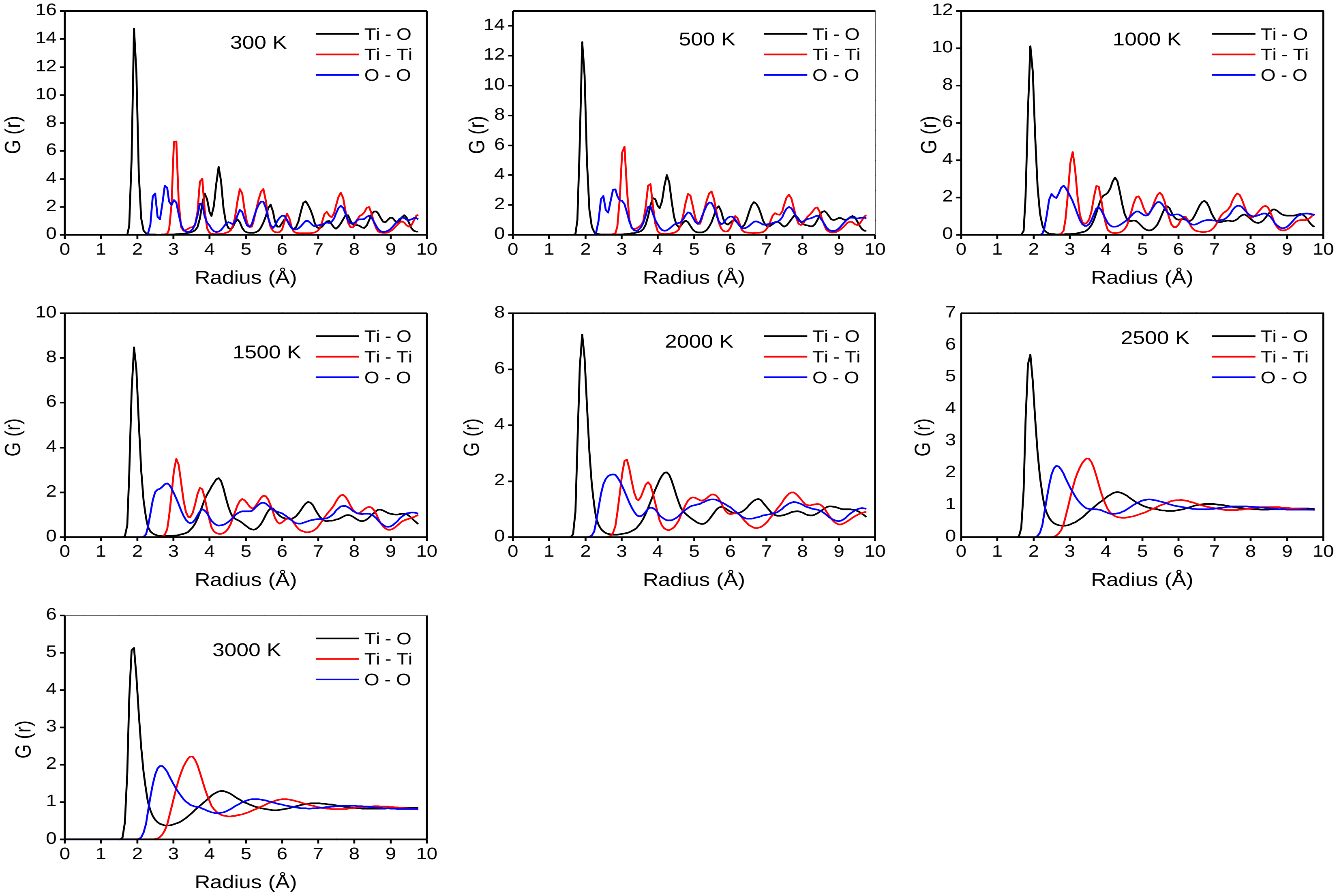

Figure B.4 RDF’s for anatase Ti – Ti, Ti – O and O – O pairs for 6 nm

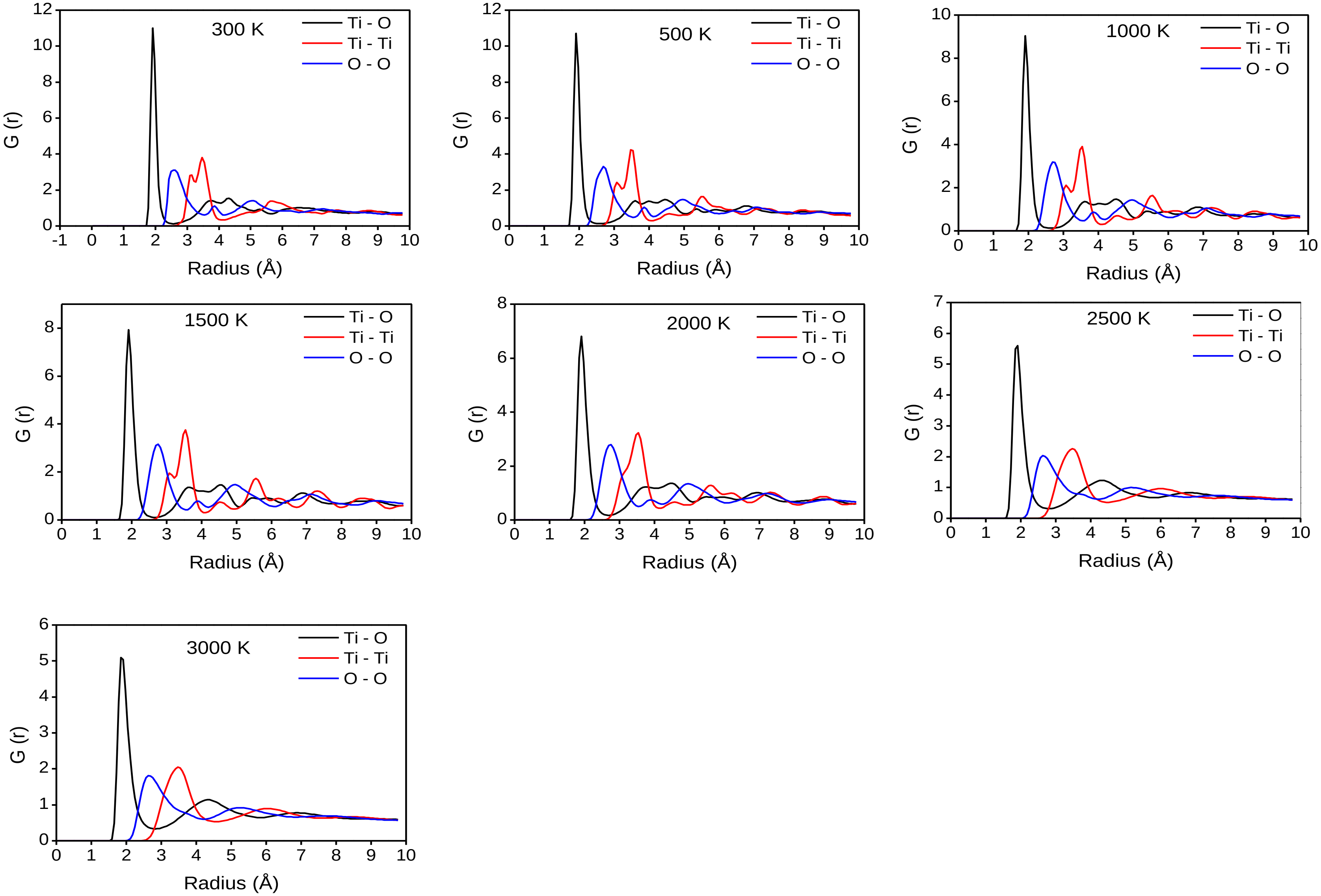

Figure B.5 RDF's for rutile Ti – Ti, Ti – O and O – O pairs for 3 nm

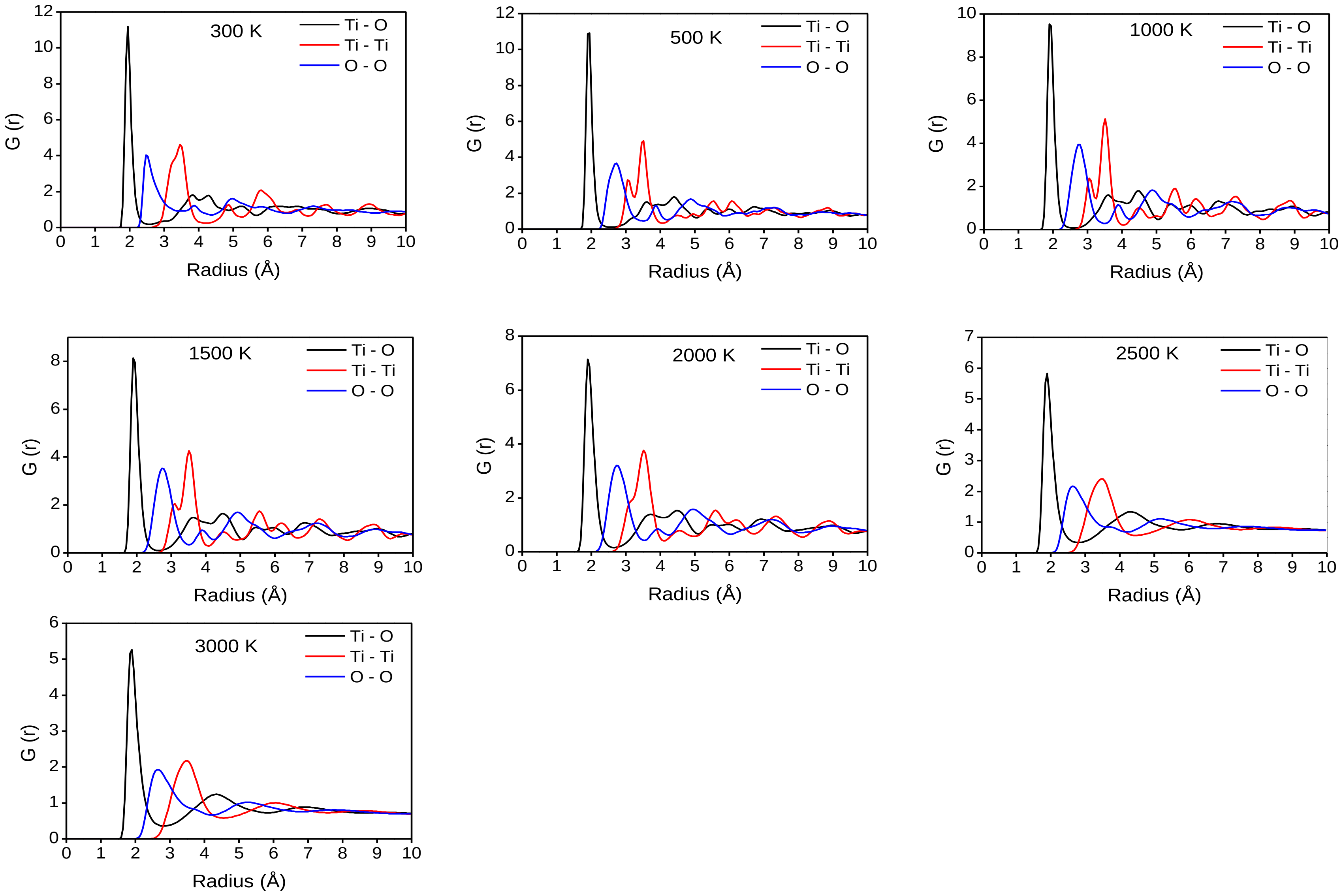

Figure B.6 RDF’s for rutile Ti – Ti, Ti – O and O – O pairs for 4 nm

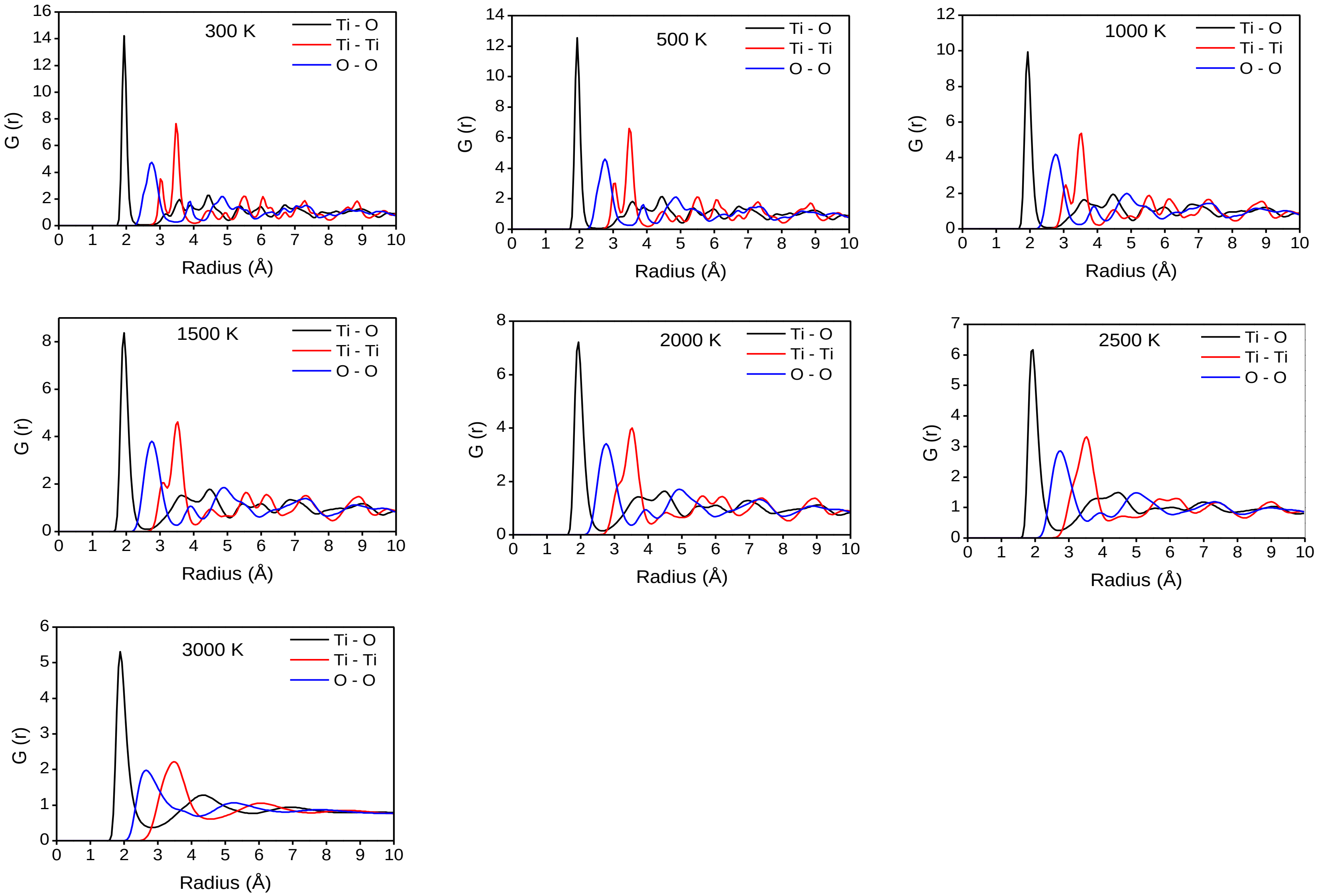

Figure B.7 RDF's for rutile Ti – Ti, Ti – O and O – O pairs for 5 nm

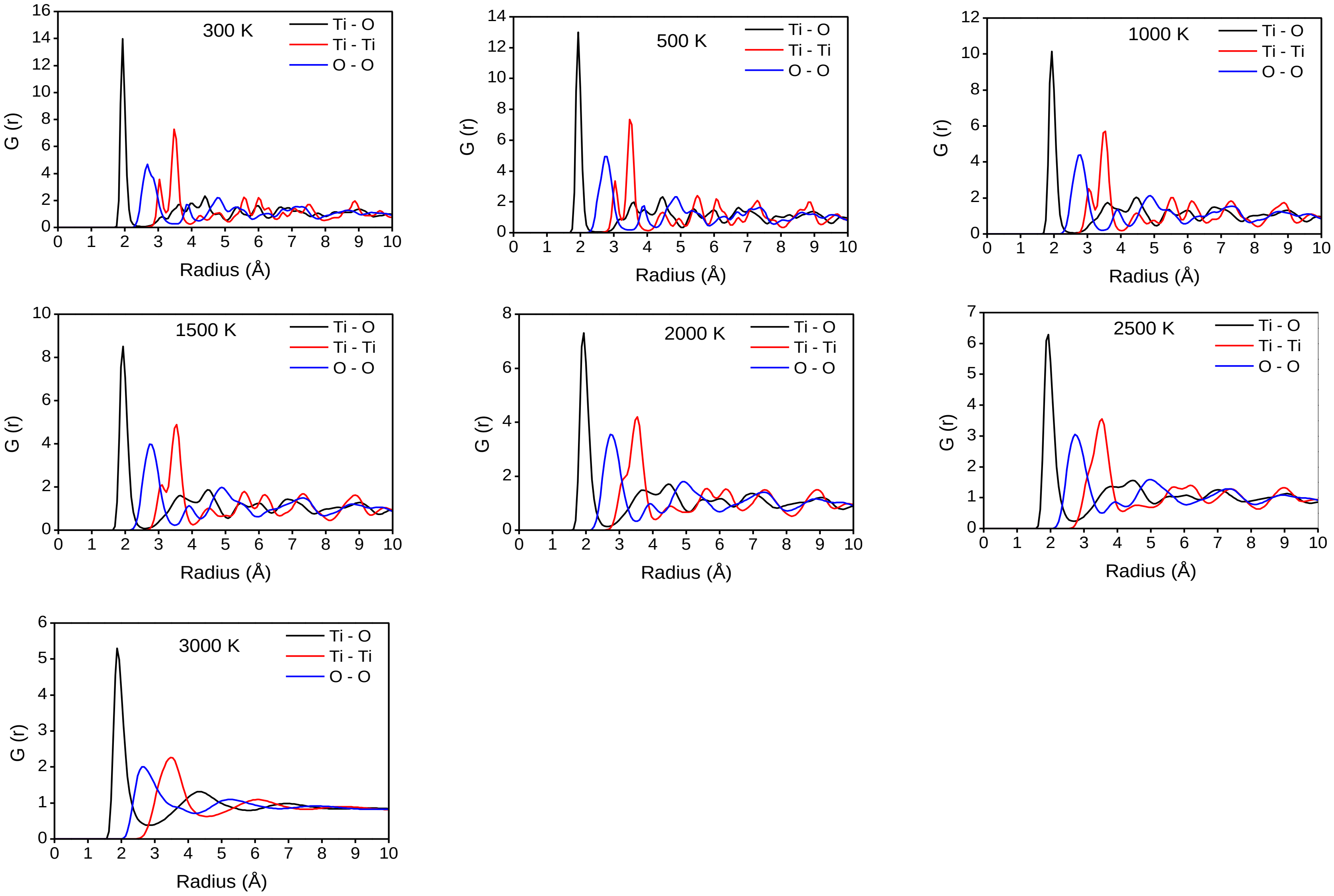

Figure B.8 RDF's for rutile Ti – Ti, Ti – O and O – O pairs for 6 nm